THE UNIVERSITY *of* EDINBURGH

Towards High Pressure Resonant X-ray Diffraction Experiments on I16

Isabel Povedano-Fuentes

Doctor of Philosophy
The University of Edinburgh
March 2020

Abstract

The investigation of the properties of electron correlated materials under pressure remains a fertile arena for the discovery of novel electronic ground states, often beyond conventional wisdom. However, direct microscopic insight into pressure-driven quantum phenomena is certainly limited to a small number of techniques and usually hampered by the lack of suitable instrumentation.

In this regard, resonant elastic x-ray scattering (REXS) is one of the best techniques that combines the elements of diffraction and spectroscopy, offering information about the atomic species, their positions in the crystal lattice and their electronic orbital configuration. Combining REXS with high-pressure (HP) presents an invaluable potential since pressure tuning of the interatomic electron-electron interactions in a crystal can be probed directly via the distortion of the lattice. Thus, HP-REXS experiments allow simultaneous observation of the crystallographic, magnetic and electronic degrees of freedom within the same experiment. This is extremely important in high-pressure studies where often inconsistencies stem from the use of different pressure devices or due to sample-dependent effects.

Nevertheless, non-trivial technological challenges need to be overcome when developing the hardware and the methodology for HP-REXS experiments, mainly dictated by two factors. Firstly, the observation of electron-electron interatomic interactions frequently requires low-temperature, where the electronic ground state is free of thermal motion and, therefore, other energy scales such as the on-site Coulomb repulsion, the crystal field splitting or the spin-orbit coupling prevail over the electronic fluctuations induced by the temperature. Secondly, the absorption cross-section of materials is severe in the range of energies demanded to excite the elementary resonant processes of interest (typically below 15 keV), making the detection of weak magnetic reflections challenging. Moreover, the

signal arising from these weak interactions gets further screened by the high-pressure device.

The aim of this work is to provide a set of instrumentation for HP-REXS experiments on I16, the beamline for materials and magnetism at the Diamond Light Source (DLS). Likewise, to establish the working methodology and to collect REXS data at HP. The thesis begins with the introduction to synchrotron radiation and the fundamentals of REXS before describing the state-of-the-art of the HP instrumentation dedicated to x-ray studies under cryogenic conditions. Then, the new setup for HP-REXS experiments is described. It consists of a membrane-driven diamond anvil cell, a panoramic dome and an optical system for *in situ* pressure measurement using the ruby fluorescence method. The membrane cell presents an asymmetric layout for operating in back-scattering geometry, with a panoramic aperture of 100 degrees. This system allows the observation of resonant signals using excitation energies at least as low as $\sim$ 8 keV, within a temperature range of 30-300 K and up to 20 GPa for anvils of 500 μm in culet diameter.

Finally, the thesis presents the results obtained from investigating the evolution of magnetic correlations in $Sr_3Ir_2O_7$ and the lanthanum doped counterpart $(Sr_{1-x}La_x)_3Ir_2O_7$ [x = 0.007(1)] upon application of hydrostatic pressure. The experimental evidence reveals the presence of long-range 3D magnetic order at up to at least 11 GPa of pressure. Combining the HP-REXS results with additional resonant inelastic x-ray scattering data and theoretical modelling a conclusion can be made about the presence of a spin-flop transition at the critical pressure of $P_c \sim$ 14 - 15 GPa, with putative short-range in-plane magnetic order above P_c.

In summary, this thesis presents a set of instrumentation and detailed methodology for conducting REXS experiments under high-pressure. The experimental results demonstrate the viability of the proposed approach and provide a notion of the extraordinarily wealth information accessible, particularly beneficial for the investigation of the electronic properties of materials.

Declaration

I declare that this thesis has been composed by myself and that it has not been submitted, in whole or in part, in any previous application for any degree or professional qualification. Except where otherwise stated, the work presented is entirely my own.

Parts of this work have been published in [1, 2]. The latter submitted for publication at the time of writing.

Isabel Povedano-Fuentes, March 2020

Acknowledgements

The work I am presenting here would not have been possible without the aid and support of a number of people. Firstly, I would like to thank my supervisors Alessandro Bombardi and Konstantin Kamenev for giving me the opportunity of doing this PhD. For the many hours shared during the experiments and for the patience and guidance. All along these years, I had the privilege of sharing my time between the University of Edinburgh and Diamond, which got me the chance to work with different people and to experience the unique dynamics of a big research facility.

From my time in Edinburgh, I would like to acknowledge the advice and help received from different people at the Centre for Science at Extreme Conditions. The realisation of core parts of this work is only possible thanks to the outstanding job done at the mechanical workshops of the school of Engineering and Physics in Edinburgh, and in particular thanks to the hands of Dave McCabe. Thanks a lot for considering all my good and not-that-good ideas, and for always giving your best to make them real.

I would like to also mention the generosity of Simon Parsons, Stephen Moggach, Jacob Shephard and Charlie McMonagle for sharing their high-pressure crystallography knowledge and lab facilities at the early stage of my thesis. My office mates Michal, Serjeis, Haoxiang and Xao provided me with a healthy amount of enjoyable chats involving life and science.

I wish to express my gratitude to the group of Des McMorrow at UCL for the collaboration in the main scientific case presented in this thesis. Thanks to James Vale, Quentin Faure and in particular to Larissa Veiga. I cannot appreciate enough the gift of finding you in this journey, the countless memories that bring me joy and make me smile wide. Thanks for your unconditional support in science

and beyond. Thanks also to Radu Coldea and Valerio Scagnoli, who provided samples for the very first HP-REXS studies conducted on I16. This was crucial to develop the right experimental procedures and to identify the main aspects hampering the success of HP-REXS experiments.

I would like to thank all members of the I16 team: Dan, Gareth, Steve, Rob and Davide. Your proactive inputs helped me to overcome many of the various challenges of this project. Thanks also to the engineers Martin Burt and Stephen Green for their assistance in the design of the cryostat dome. I must also mention the key support received from beamlines I15, I15-1, I19 and I20. Many thanks for sharing your expertise, equipment and lab space when needed. A fond appreciation goes to Simone Anzellini and Geoff Cutts, for being an excellent companion in occasional breakfasts, regular meals and anytime laughs, crucial to ease the insanity that at times surrounds a PhD. I would like to extend this to the rest of the I15-1 crew: Maria, Dean and Phil. Thanks for your company and for fuelling me with coffee in a daily basics. I am also in debt with Dominik, the first person in teaching me some of the artisan secrets of diamond anvil cell preparation.

Among all the inspiring people I have met during this thesis, I am especially grateful to my PhD colleagues in Edinburgh: Irene, Jana, Joe, Ant, Julia, Chris, Christian, Marie, Izzy, Sarah, Dan, Rebecca and Nia. I have been incredibly lucky of sharing the ups and downs of this experience with you. Thank you all for your friendship. A special mention to Jana and Irene, you two truly made my days brighter and your emotional support throughout this period is beyond words. I am also in debt with my Oxfordian family: Mara, Anna, Sara, Joao, Carolina, Rebecca, Chris, Pilar, Tatiana, Leticia... I much enjoyed the moments I shared with you. This list would be incomplete without expressing my gratitude to Paula Kayser, Miriam Marqués, Elena Blanco and Miriam Peña, who brought a piece of home to the burgh. Peña, what a journey we made side by side over the years! Thank you so much for everything. This also brings to my mind joyful memories with a bunch of people at the Universidad Complutense in Madrid. Javi, Adri, Irene, Álvaro, Berengere, Oscar, Merce, Valen and a bit up in the North, also Carlos, Toño, David, Julia and now Virginia. Thanks for playing an important part in motivating my way here.

I cannot forget *"a mis Amilayos queridos"*. Thank you all for your visits, calls, texts, trips and foremost, your anytime friendship. Also Andrea, *mi hermana de*

vida. Thanks for being there providing love, joy and support ever since I can possibly remember.

On a different note, I will always be indebted to Marta O'Kelly. Thanks for taking care of my psychological well-being. If I made it here, it is largely thanks to your labour.

Finally, a heartfelt thanks to my parents, Leo and Antonia, for giving their best to provide me comfort, encouragement and love all my life long. You have always believed in me, in spite of not understanding much of what I do. I must confess you here that sometimes I do not even know myself, but this is also one of the charming parts of science. My success is your success. My effort doing this thesis is dedicated to you both.

Lay summary

The investigation of the electronic behaviour of solids in a variety of pressure and temperature conditions opens the door to new states of matter. However, the achievement of these conditions is frequently limited by the capacity of the instruments available and therefore, the development of new technology is needed. This thesis is aimed at contributing to the design of high-pressure instrumentation for conducting resonant elastic x-ray scattering (REXS) experiments at low-temperature and at investigating the nature of electronic correlated materials in these conditions.

Below a certain temperature threshold, the unpaired electrons in the external part of the electronic cloud that surrounds atoms -otherwise disordered by the action of thermal fluctuations-, may undergo long-range correlation, in other words, to adopt fixed orientations with respect to each other giving rise to a periodic electronic order. This forms the basis of exotic physical phenomena such as superconductivity or metal-to-insulator transitions, all of them forming potential grounds for future technological outbreaks.

This thesis proposes a new set of instrumentation to study electron correlated materials under pressure by REXS, a technique that provides direct observation of different degrees of electronic order (orbital, magnetic and charge). Combining it with high-pressure conditions is an excellent path to simultaneously tracking the effect of pressure on the evolution of the crystalline structure and the electron-electron interactions. It thus provides information of enormous interest for understanding fundamental properties of solids and their potential technological application.

Contents

List of Figures

List of Tables

Acronyms and abbreviations

a	Acceleration
APD	Avalanche Photo-Diode
BA	Boehler Almax
BM	Bending Magnet
BZ	Brillouin zone
CAD	Computer Aided Design
CCD	Charge Coupled Device
CF	Crystal Field
DAC	Diamond Anvil Cell
DLS	Diamond Light Source
EDM	Electrical Discharge Machine
EM	Electromagnetic
EXAFS	Extended X-Ray Absorption Fine Structure
FCC	Face centred cubic
FWHM	Full-Width at Half Maximum
HP	High-Pressure
ID	Insertion Device
IMT	Insulator-to-Metal Transition
J_H	Hund's coupling constant
LSW	Linear spin-wave theory
LT	Low Temperature

LRO	Long Range Order
MB	Merrill-Bassett
ME	4:1 Methanol:Ethanol
PT	Pressure-Temperature
QCP	Quantum Critical Point
QPT	Quantum Phase Transition
QSL	Quantum Spin Liquid
REXS	Resonant Elastic X-Ray Scattering
RF	Radio Frequency
RIXS	Resonant Inelastic X-Ray Scattering
RMXS	Resonant Magnetic X-Ray Scattering
RPS	Ruddlesden-Popper Series
SOC	Spin-Orbit Coupling
SR	Synchrotron Radiation
SRO	Short Range Order
SW	Spin-wave
TM	Transition Metal
TMO	Transition Metal Oxide
U	Coulomb Repulsion
v	Velocity
W	Bandwidth
WC	Tungsten Carbide
WSM	Weyl Semi-Metal
XAS	X-Ray Absorption Spectroscopy
XMCD	X-Ray Magnetic Circular Dichroism
XRD	X-Ray Diffraction
Z	Atomic Number

Chapter 1

Introduction

Contents

1.1 Motivation: Why resonant elastic x-ray scattering experiments under pressure?

Resonant elastic x-ray scattering (REXS) is an outstanding technique for probing the nature of a material's Fermi surface, which in turn is crucial to understand its electronic, magnetic, optical and thermal characteristics. A plethora of phenomena such as multiferroicity [3], metal-insulator transitions [4], charge-ordering [5], solving the magnetic structure of frustrated magnets [6–8] or investigating the distribution of magnetic domains [9, 10] have been understood using the REXS technique. The nature of coupled correlated states is extremely sensitive to the spatial arrangement of the individual elements, charge, orbital or spin, giving rise to the long-range correlations present in all these phenomena. In this sense, the application of hydrostatic pressure provides the means to continuously modify, in first instance the structural order of materials, and consequently the charge, spin and orbital degrees of freedom.

REXS is a relatively young technique whose application emerged together with the materialisation of synchrotron sources in the 1980s and ever since, the scientific community has shown a growing interest in its application to investigate the nature of long range electronic interactions in solids. However, only in the last two decades its combination with high-pressure has been considered in order to expand the information accessible in this manner. The novelty of the technique together with the experimental demands, mostly comprising low-temperature and the need of specific values of excitation energy where the x-ray absorption is severe (3.5 - 15 keV), challenge the viability of HP-REXS experiments. In this respect, two scientific teams based at the Advanced Photon Source (APS) in Lemont, US [11–17] and the European Synchrotron Radiation Facility (ESRF) in Grenoble, France [18–20] started the pioneering task of overcoming these restrictions. Within this framework, the present work attempts to provide new technological means to further extend the application of HP in REXS experiments. In the following, custom-designed instrumentation will be presented to this end.

This thesis is the result of a collaborative project between The University of Edinburgh and Diamond Light Source (DLS), a 3rd generation synchrotron facility based in the UK. It is nourished by the joint expertise in the development of high-pressure instrumentation at the Centre for Science at Extreme Conditions

(CSEC) and the deep knowledge in the conduction of resonant studies and the physics of correlated materials at I16, the beamline for materials and magnetism at DLS [21].

The foremost aim of this thesis is not only limited to the design and test of HP-REXS instrumentation, but to devise the suitable methodology to conduct studies in these conditions, as well as to investigate the nature of strongly correlated materials using the technology produced. In particular, the research focus will be on the family of 5d transition metal oxides (TMO) that exhibit exotic electronic behaviours and recently captured great interest from the condensed matter community [22, 23]. This group of materials present particularly favourable conditions to be explored by REXS under pressure in terms of the excitation energy required and the rich playground of electronic behaviours shown.

In the following pages of this introduction, I will provide a brief overview to the fundamental principles behind the phenomena of electronic correlation in materials containing 5d elements. Finally, I will explain some of the most noticeable effects induced by pressure in this family of compounds.

1.2 The effect of pressure on strongly correlated materials

1.2.1 The Hubbard model: from 3d to 5d electronic correlations

Historically, the study of TMOs has been subject of intensive research in the field of condensed matter physics. TMOs exhibit a vast variety of electronic phenomena such as high-temperature superconductivity of copper oxides [24], colossal magneto-resistance in manganese oxides [25], multiferroicitiy [26] and different types of spin- and charge-correlations [27, 28], providing not only an invaluable scenario to understand the underlying physics but also potential technological applications. To a large extent, the origin of these phenomena is understood via the interplay of different energy scales that govern the electron-electron interactions: electrostatic Coulomb repulsion (U), Hund's coupling (J_H), crystal-field (CF), bandwidth (W) or spin-orbit coupling (SOC) among others. The strength of each of these interactions varies from element to element in the

series of transition metals (TM) giving rise to different electronic behaviours [22, 29].

The Hubbard model is the simplest framework that describes the nature of correlated electrons in solids [30, 31]. It considers the electron hopping and the on-site Coulomb repulsion as the two opposite tendencies that determines the conductive/insulating behaviour of condensed materials, represented in the following interaction Hamiltonian (Eq. 1.1):

$$\begin{aligned} \mathcal{H} &= H_t + H_U \\ &= -t \sum_{\langle ij \rangle, \sigma} (c^{\dagger}_{i\sigma} c_{j\sigma} + h.c.) + U \sum_{i} n_{i\uparrow} n_{i\downarrow} \end{aligned} \tag{1.1}$$

the first term (H_t) stands for the kinetic energy of electrons that allow the tunnelling or "hopping" between neighbouring sites of the lattice favouring the metallic regime, while the second term (H_U) represents the potential energy due to on-site Coulomb repulsion and aids in the localisation of the carriers. In this basis, metallic conduction occurs when the hopping term prevails over the on-site Coulomb repulsion and electrons are able to tunnel between lattice sites.

This model was first devised to describe the electronic behaviour of solids containing elements from the 3d-series of TM. However, when descending in the periodic table towards the heavier atoms in the 4d and 5d rows, additional forces come into play. The increased number of electrons in the core shells produces the screening of the nuclear force felt at the d-orbital level, allowing these bands to expand in the space and further overlap with each other. The latter directly fosters the electronic hopping and so, one could naively expect rather metallic and non-magnetic states over insulating behaviour. Strikingly, this conventional wisdom contradicts the early empirical trends observed in Sr_2IrO_4, $Sr_3Ir_2O_7$ and $BaIrO_3$ [32–37].

An additional ingredient, the SOC -largely neglected in the theoretical treatment of 3d-elements and their oxides-, gets drastically enhanced in 4d and 5d elements as a result of the increase in the atomic number (Z). The spin-orbit coupling constant (λ) scales as the square of Z for the case of the outer electrons in the valence band ($\lambda \propto Z^2$) [38]. Thus, the strength of this interaction can

be as much as an order of magnitude larger in the 5d TM respect to the 3d counterparts, $\lambda_{3d} \sim 20 - 40$ meV [39] and $\lambda_{5d} \sim 200 - 500$ meV [40]. In these conditions, additional splitting of the otherwise degenerate orbitals/bands may occur, allowing the correlation physics to step in. The simple initial Hamiltonian of the Hubbard model given in Equation 1.1, will thus be modified by the addition of the spin-orbit coupling term as:

$$\begin{aligned} \mathcal{H} &= H_t + H_U + H_\lambda \\ &= -t \sum_{\langle ij \rangle, \sigma} (c^\dagger_{i\sigma} c_{j\sigma} + h.c.) + U \sum_i n_{i\uparrow} n_{i\downarrow} + \lambda \sum_i L_i \cdot S_i. \end{aligned} \tag{1.2}$$

The resulting electronic ground state includes narrow bands with marked directionality induced by the orbital degree of freedom, where the electrostatic repulsion arising from moderate electronic correlations can be sufficient to open a small gap, giving rise to exotic non-conventional ground states as topological insulators [41–43] or Weyl semimetals [44, 45].

Other fundamental interactions such as the Hund's coupling or the crystal field, tailor the final individual electronic behaviour of each particular material. The CF energy scale gives consideration to the influence of the spatial distribution of the electric potential produced by the charge density of the anions surrounding the TM cation, whereas J_H allows for the energetic cost of the repulsion between two electrons occupying the same orbital. Thus, strong values of CF favours larger gaps and low-spin filling of the d orbitals typical of the insulating (correlated, usually antiferromagnetic) states. On the contrary, large values of J_H favours high-spin configuration, taking the system away from the insulating picture [46].

1.2.2 High-pressure novel electronic states in 5d based TMOs

Pressure has been demonstrated to be an extremely powerful tool to access novel electronic ground states in 5d TMOs, where often, the stability of the lowest-energy electronic configuration is closely interlaced with the lattice degree of freedom. An example of this behaviour can be found in the family of iridium oxides featured by a strong SOC mediated $J_{eff} = 1/2$ electronic ground

state.[1] This configuration was first identified in Sr_2IrO_4 in 2008 [34, 47, 48] and since, it has inspired an enormous body of experimental and theoretical work. On the whole, these materials exhibit complex magnetic states with high critical temperatures but low magnetic moments, and exotic insulating behaviours instead of metallic conduction [49].

A variety of iridates with different crystalline structures share this electronic configuration, each of them potential scenario for the realisation of exotic electronic behaviours. From the pyrochlore based compounds with stoichiometry $A_2Ir_2O_7$ -where A is commonly a rare earth or an alkali metal-, predicted as potential base for topological non-trivial electronic states [17, 45, 50, 51]; or the honeycomb lattice of Na_2IrO_3 or $\alpha, \beta, \gamma-$ Li_2IrO_3 depicted as a fertile ground for the realisation of non-isotropic Kitaev quantum spin liquid (QSL) [52–57]; to the layered family of the Ruddlesden-Popper series (PRS) $Sr_{n+1}Ir_nO_{3n+1}$ where the splitting of the $J_{eff} = 1/2$ and $J_{eff} = 3/2$ bands progressively narrows as a function of the dimensionality (*i.e.* n). In this series of compounds, the bandwidth gradually broadens closing the charge gap Δ, from a robust insulating state for Sr_2IrO_4 ($n = 1$) to a metallic state for $SrIrO_3$ ($n = \infty$). The intermediate member $Sr_3Ir_2O_7$ ($n = 2$), which presents weak-insulating character at ambient pressure will be the foundation of the experimental work of this thesis. Further details on the physics of this family of iridates will be given in connection with the latter in Chapter 5.

All these compounds seem to present large to moderate sensitivity to applied external pressure and indeed, some striking novel electronic states has been revealed by this means. Generally speaking, the application of external pressure is expected to enhance the electron hopping (t) via widening of the electronic bands and hence, facilitating the metallic behaviour. However, due to the rich balance between equally competing energy scales in 5d materials, more often than not, uncommon and extraordinary outcomes arise from the application of pressure.

For example in 5d honeycomb systems, pressure is predicted to aid in the achievement of the elusive QSL state promoting anisotropic magnetic exchange via structural distortion. However, the experimental observations reveal that moderate level of stress -below 5 GPa-, seem to induce dimerisation of the Ir centres, causing marked molecular electronic configurations that enter in

[1] A schematic representation of the $J_{eff} = 1/2$ ground state is pictured later in this text in Fig. 5.2.

competition with the formation of the QSL state [52, 53, 55, 56, 58–62]. Other peculiar behaviours, such as the unusual increase of the magnetic ordering temperature (T_N) upon applying pressure prior to the final vanishing of the AFM order has also been reported in the two-dimensional honeycomb materials such as Na_2IrO_3 [50, 51, 63] and α-$RuCl_3$ [64, 65]. The latter showing remarkably stable magnetoresistance up to 140 GPa [65].

In similar fashion, 1-2 GPa of pressure are enough to suppress the three dimensional counter-rotating AFM spiral order of the honeycomb iridates β-Li_3IrO_3 [54, 56, 57] and γ-Li_3IrO_3 [7, 13]. Additionally, β-Li_3IrO_3 seems to undergo a structural zig-zag dimerisation of the Ir units above 4 GPa [53, 55] in line with the observations on the two-dimensional counterparts. Evidence that suggests the dimerisation phenomena as a typical characteristic of the electronic behaviour of honeycomb 5d iridates under pressure.

The family of pyrochlores with stoichiometry $R_2Ir_2O_7$ (R = rare earth, Bi or Pb) also show exceptional behaviours under pressure. They have been pointed out as potential arena for the formation of Weyl semi-metals (WSM) and non-trivial topological effects [66]. They are characterised by a diamond-like crystalline structure and general insulating all-in-all-out (AIAO) magnetic behaviour, with the exceptions of the semimetal $Pr_2Ir_2O_{7-\delta}$ [67] and the metallic $Pb_2Ir_2O_7$ [68] and $Bi_2Ir_2O_7$ [69]. The latter, exhibits unusual pressure induced electronic localization in the shape of a metal-to-insulator transition above 0.48 GPa [70]. Recently, this abnormal phenomena has been also observed in the hyper-kagome iridate $Na_3Ir_3O_8$, where the application of 2 GPa of pressure is sufficient to turn the semimetallic nature of this system into a robust insulating state that stays correlated up to the megabar regime [62].

Despite other pyrochlores do follow the expected trend towards metallic conduction, they are not exempt from added exceptional electronic behaviours induced by pressure. This is the case of $Eu_2Ir_2O_7$, which exhibits an unconventional negative temperature coefficient of resistivity upon applied pressure above 6 GPa [71], or $Nd_2Ir_2O_7$ that presents evidence of WSM behaviour induced by pressure [72]. It is worth mentioning the singularity of the Os^{5+} ($5d^3$) based pyrochlore $Cd_2Os_2O_7$, with electronic configuration t_{2g}^3 e_g^0, that presents a continuous quantum phase transition (QPT) above 35.8 GPa where magnetic and structural transformations occur concurrently with the charge gap collapse, a typical sign of three-dimensional quantum criticality [12].

Finally, I will only briefly mention here the group of layered-perovskite iridates $Sr_{n+1}Ir_nO_{3n+1}$, since more details of their HP behaviour are given in Chapter 5. This family of materials displays a rich variety of exotic electronic, structural and magnetic transitions induced by pressure.

All these thrilling discoveries, often compromise the conventional knowledge on the hierarchy between energy scales that govern 5d electron correlated materials and represent a source of exciting intellectual challenge both theoretically and experimentally. The materials mentioned hitherto are only a very small selection of the large number of systems that could be addressed by HP-REXS. On this subject, the present work aims to explore alternative technical approaches to overcome the experimental factors that hamper their investigation by HP-REXS. Likewise, to shed light on the physical nature of the conspicuous electron-electron interactions in 5d TMO.

1.3 Thesis outline

This thesis is organised as follows:

- Chapter 2 provides a brief introduction to synchrotron radiation and its unique properties, prior to describe the fundamental principles of resonant elastic x-ray scattering (REXS). The formalisms and definition of the parameters of relevance for the design of high-pressure instrumentation are discussed is Section 2.3. The theoretical concepts required for understanding the scattering interaction of x-rays with magnetic materials are also explained. In Section 2.2, the two laboratories where most of the experiments of this thesis were conducted, beamlines I16 and I19 at DLS, are described. Finally, a concise subsection provides the details from the sample pre-characterization routines followed in preparation for the experiments conducted and further discussed in Chapter 5.

- Chapter 3 starts by offering a general insight into the historical evolution of high-pressure science. It will then focus on the state-of-the-art of HP devices especially dedicated to conduct x-ray experiments under cryogenic conditions. Section 3.3 describes the main parts of a diamond anvil cell and its basic handling, providing some practical recommendations for the

conduction of REXS experiments. Lastly, I provide a description of the HP setups employed for the studies presented in Chapter 5.

- Chapter 4 presents a novel setup to conduct HP-REXS experiments on I16, which includes a diamond anvil cell, a panoramic dome and an optical system for *in situ* measurement of the level of pressure at low-temperature. In the first place, I will explain the general experimental constrains for the combination of HP and REXS techniques, as well as, the particular experimental conditions required in I16. Then, the HP-setup is described providing details of each component and its use. The results from the experimental tests conducted for characterization of the system are also reported in this section. A final view of the various prototypes considered throughout the designing process is given in the last part of the chapter.

- In Chapter 5, I will present an analysis of the experimental results obtained investigating the magnetic properties of $Sr_3Ir_2O_7$ and its electronically doped counterpart $(Sr_{1-x}La_x)_3Ir_2O_7$ by HP-REXS. A collaborative analysis of REXS, RIXS and computational data reveals a potential spin-flop transition from collinear to canted AFM order at a critical pressure of *ca.* 18 GPa for $Sr_3Ir_2O_7$.

- Finally, Chapter 6 summarises the information reported in this thesis. Firstly, the technological outcomes for the realisation of HP-REXS experiments on I16 are explained, highlighting the possible directions for further development of HP devices for resonant x-ray studies. Secondly, the most significant findings from the experimental investigation of $Sr_3Ir_2O_7$ and $(Sr_{1-x}La_x)_3Ir_2O_7$ [x = 0.007] are also summarised.

Chapter 2

Resonant magnetic scattering of x-rays

Contents

In an effort to make this thesis self-contained, in this chapter I provide an introduction to the basic theoretical concepts behind synchrotron radiation and REXS, the core technique employed in this work, that will aid in the design of high-pressure instrumentation. Firstly, I will explain the main properties of synchrotron light and the particular working parameters of the DLS, which are important not only for REXS, but also for a large number of new experimental techniques only viable thanks to the unique properties of synchrotron radiation [73–75]. Secondly, I discuss qualitatively the nature of the REXS process and the associated cross-section. The complete mathematical derivation of the scattering cross-section is beyond the scope of this thesis and the interested reader is referred to [76–81] for further details.

2.1 Synchrotron radiation

The linear trajectory of a charged moving particle can be modified by means of the interaction with a magnetic or electric field. When the particle is moving in the relativistic regime and experiences acceleration perpendicular to its velocity ($a \perp v$), it loses energy in the form of light known as synchrotron radiation (SR). This phenomenon was predicted in 1944 [82] and first observed at the General Electric Research Laboratory in New York by Elder *et al.* [83] three years later. SR can be produced in a broad range of the electromagnetic spectrum, from microwaves to hard x-rays and it is extensively used for scientific purposes.

Fig. 2.1 shows a scheme of the main components of a synchrotron facility: electron gun, linac, booster, storage ring and beamlines. The first step to produce synchrotron radiation is the generation of a source of electrons, which takes place by thermionic emission in an electron gun. A high-voltage cathode is heated under vacuum giving the electrons enough energy to escape the material. Then, the ejected particles are accelerated from 90 keV to 100 MeV in a linear particle accelerator (LINAC). In the LINAC, the beam of charged particles passes through several radio-frequency (RF) cavities. In them, the electromagnetic radiation transfers energy to the electrons that, leads to an increase in their acceleration, pushing them forward along the tunnel. Right after is the booster, a ring made of alternated bending magnets (BM) and RF cavities where the electrons are further accelerated reaching maximum energies in the GeV regime (3 GeV at DLS).

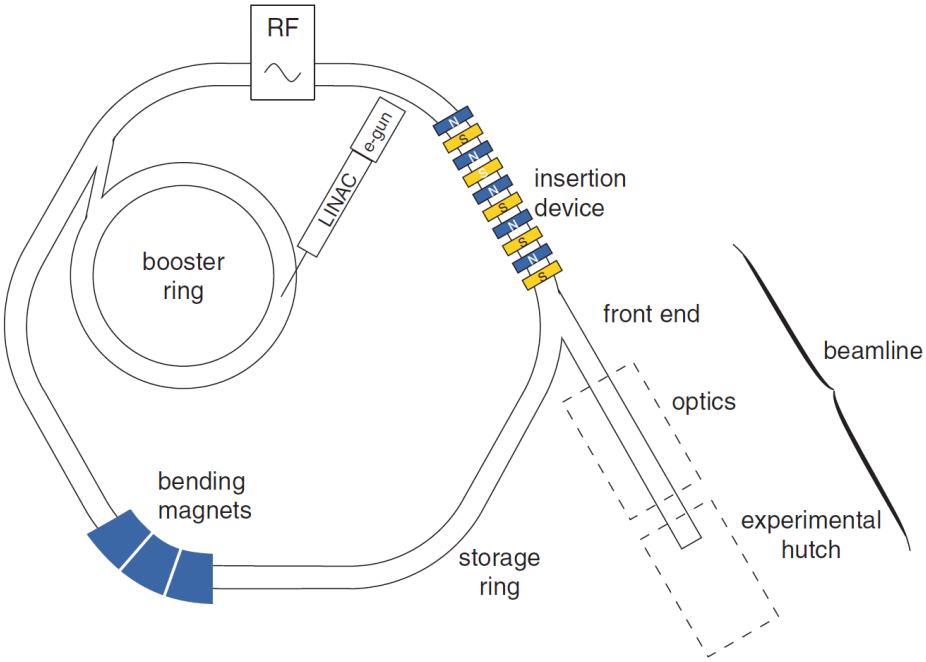

Figure 2.1 *A schematic diagram of the most important components of a modern synchrotron source: electron gun (e-gun), linear particle accelerator (LINAC), booster ring, storage ring and beamline. From [74].*

Once the particles have reached the target energy, they are injected into a larger storage ring. At DLS, this is a closed loop of 562 m in circumference made of 24 straight sections connected by 48 bending magnets. Small amounts of electrons are injected from the booster into the storage ring quasi-continuously following the so-called "top-up" process that allows experiments to run with no interruptions. Particles in the storage ring circulate generating SR when feeling the proximity of the magnetic field exerted by bending-magnets (BM) and insertion devices (ID). The first ones provide the perpendicular driving force needed to define the arc between straight sections of the storage ring. BM are used mainly when a broad section of the electromagnetic spectrum is required, as it is the case of some spectroscopic techniques. However, ID in the shape of wigglers and undulators produce much brighter light (see Eq. 2.1) and are most commonly used. Both, wigglers and undulators, are made of arrays of alternated magnets located in straight sections of the storage ring that force the beam to wiggle or undulate making it even brighter. These are distinctive of the so-called 3rd generation synchrotrons and produce the most intense artificial synchrotron light.[1] Depending on the periodic spacing between the magnets in the array,

[1]Synchrotron light can be also produced naturally by astronomical objects such as nebulae or pulsars [84, 85].

different photon energies are produced.

Finally, the beam of light enters the beamline through the so-called *front end* that connects the storage ring to the beamline space. Here, the beam is cleaned, monitored and optically prepared. Following the front end is the experimental hutch where the experiments are carried out and next to it, the control room, from where users command all the experimental parameters. From the electron gun to the optical front, the entire travelled path is maintained under high-vacuum conditions to minimise the scattering of electrons by air molecules and the beam absorption.

In summary, SR presents the following properties:

– *High Flux* and *High Brilliance*. The flux can be defined as the number of photons per second and per band width unit (usually 0.1%) passing through a defined area. Whereas brilliance makes reference to the spatial and angular distribution of the beam, *i.e.* the smallest spot onto which the beam can be focused. It is defined as

$$Brilliance = \frac{Photons/second}{(mrad)^2(mm^2\ source\ area)(0.1\%\ bandwidth)}. \tag{2.1}$$

In a synchrotron, the size of the beam after focusing is within the range of microns and the flux of photons is proportional to the square of the electron acceleration. Therefore, a very large flux of photons is confined in a very small spot that consequently results in an extremely brilliant beam. This allows much more rapid experiments than ordinary laboratory sources and it is key for highly demanding photon techniques as REXS, aimed to observe diffraction signals orders of magnitude weaker in intensity than ordinary charge peaks.

– *Broad Spectrum*. Fig. 2.2 displays the power distribution provided by a BM of constant field and different values of ring current. The radiation generated in each case covers a range of energy of several orders of magnitude. Nevertheless, the flux of photons is only high within a small region, mostly concentrated in the x-ray spectrum and shifts towards higher values of energy as the ring current increases.[2] For this reason, most of the experiments conducted in synchrotron facilities exploit x-ray radiation.

[2]This same effect could be attained by increasing the field strength. However, the maximum field in BM is technologically limited to ~ 1 T [74, 86].

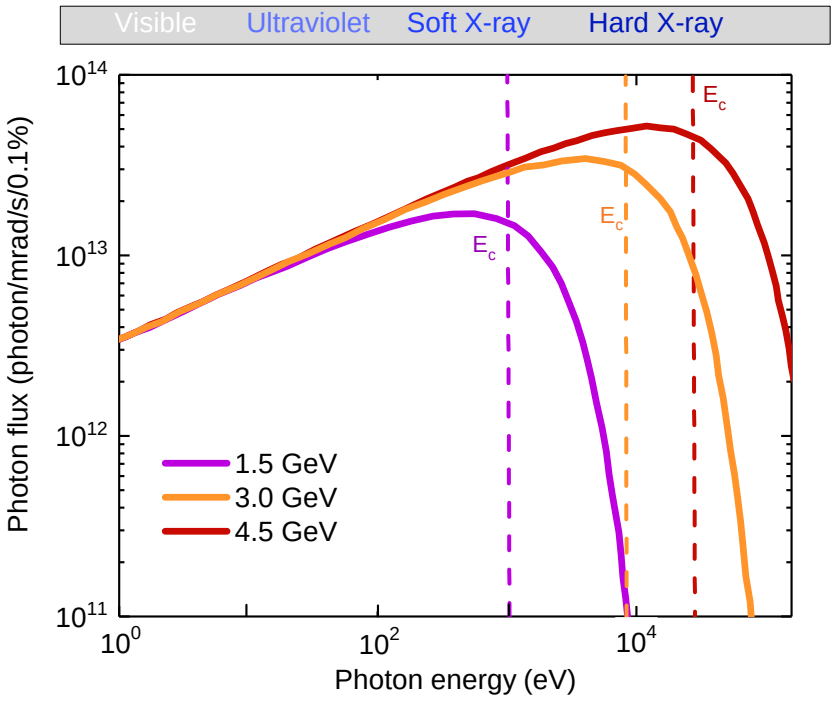

Figure 2.2 *Power distribution of the synchrotron radiation generated by a BM of identical magnetic field and different values of ring currents (1.5, 3.0 and 4.5 GeV). Dotted vertical lines stand for the value of the critical energy E_c defined in Eq. 2.2 for each case. In the top, details of the corresponding spectral energy range are displayed.*

In order to take full advantage of the SR, a useful parameter to evaluate the energy at which the flux of photons is at its maximum is the critical energy E_c represented by dashed vertical lines in Fig. 2.2. E_c is proportional to the product between the electron beam energy ε and the external magnetic field B as detailed in Eq. 2.2. It divides the spectral distribution into two parts of equally radiating power and lies just above the energy at which the flux of photons is at its maximum. This is an important parameter to consider when planning a synchrotron experiment, since ideally the maximum flux should lie close to the excitation energy required. As an example, for the REXS studies conducted during this thesis (see Chapter 5), only the sources with ring current above 3 GeV provide a large flux of photons in the proximity of the absorption edge exploited (Ir $L_3 \sim 11.217$ keV) (see Fig. 2.2).

$$E_c = \hbar\omega_c[keV] = 0.665\varepsilon^2[GeV]B[T]. \tag{2.2}$$

– *Polarization.* Both linear and circular polarization can be obtained depending on the position of observation with respect to the horizontal plane of the storage ring. When the line of sight is in-plane with the storage ring, electrons appear to oscillate linearly. If the observer is above/below the horizontal plane of the ring, electrons seems to follow an elliptical orbit.[3] This particular aspect is utilised in techniques as x-ray magnetic circular dichroism (XMCD) that takes advantage of the difference in absorption of some magnetic materials when exposed to left and right circularly polarized light.

– *Pulsed Time Structure.* The radio frequency power supply that restores the energy loss of the particles circulating in the storage ring, also modulates the final pulsed structure of the electrons in it. It defines packets or 'bunches' of electrons separated by tens of picoseconds that make possible time resolved studies on the same time scale.

For all reasons mentioned, synchrotron light is extensively used for diffraction, scattering, spectroscopy and imaging purposes by an ever-growing community since the first facilities where constructed to our days. In the next section, the beamline where most of the experimental work of this thesis was conducted is described.

2.2 I16 - Materials and magnetism beamline at DLS

I16 is the beamline for Materials and Magnetism at DLS especially designed for REXS studies [21]. Fig. 2.3 contains a schematic illustration of the setup. In I16, a diamond U27 undulator device (27 mm period) provides x-ray radiation in the range of energy between 3.3 and 15 keV, with the possibility of extending these limits up to 25 keV and down to 2.7 keV using a different optical configuration and minimizing the absorption from air. The experimental energy is selected by means of a liquid nitrogen cooled monochromator sandwiched between two gas bremsstrahlung collimating units. The latter gets rid of the gamma rays produced when electrons collide to each other, causing noise and parasitic high energy radiation in the beam. The monochromator includes three sets of crystals: a channel-cut Si (111) and two double-crystals of Si (111) and Si (311). For ease

[3] Circular polarization can be also obtained in helical undulators when the photon energy is within the soft x-ray regime < 2.5 keV [86].

of use and beam stability, the single channel-cut crystal is the one normally in place. This crystal produces small shifts of the beam height when changing energy and that is taken into account by adjusting the height of all the downstream components from this point.

Once the suitable energy is selected, the monochromatic beam is focused by a pair of 1.2 m mirrors. The first one is a 96 mm radius sagittal cylinder responsible for the vertical focus, while the second, is a flat mirror that presents a mechanical bender (tangential radius $\sim$ 5.8 km) and provides horizontal focus. The first is coated with Rh whilst the second one can be used either on a Si or a Rh outer cover in order to provide better harmonic rejection. At the focal point, the beam spot has a Gaussian profile with full-width at half maximum (FWHM) of 20 $\times$ 200 μm^2 (V $\times$ H).

The sample under study is mounted on a 6-axis Newport N-6050 kappa diffractometer that allows to conduct experiments in vertical and horizontal geometries and to accommodate different experimental environments. The particular experiments carried out during this thesis were done in a vertical configuration using two different cooling systems: a 4 K closed-cycle cryostat (D-202N) and a nitrogen Cryojet from Oxford Instruments. Additionally, the application of external electric and magnetic fields is also possible.

In this geometry, four angles named ω, χ, ϕ for the sample and δ for the detector arm define the possible motions (see Fig. 2.4). A set of unitary vectors u_1, u_2 and u_3 define the system of reference for the scattering coordinates following the description by Blume and Gibbs [78] as illustrated in Fig. 2.5. In it, the polarization of the incident and scattered beams is expressed in terms of the ϵ_{in} and ϵ_{out} polarization vectors with orthogonal basis perpendicular (σ) and parallel (π) to the scattering plane.

Finally, the detection of the diffracted peaks is done at the detector arm unit equipped with 5 point detectors, a Pilatus 100 K area detector and a polarization analyser. The point detectors available are an APD - Avalanche Photodiode, a Si drift detector, a Scintillator, a PIN diode and a High-resolution Imager. The Pilatus 100k is offset by 9 degrees with respect to the main axis of the arm (blue box in Fig. 2.3) and allow the collection of signals in a large solid angle. This is particularly useful for the alignment and mapping of the samples.

The polarization analyser consists of a set of crystals that presents a Bragg

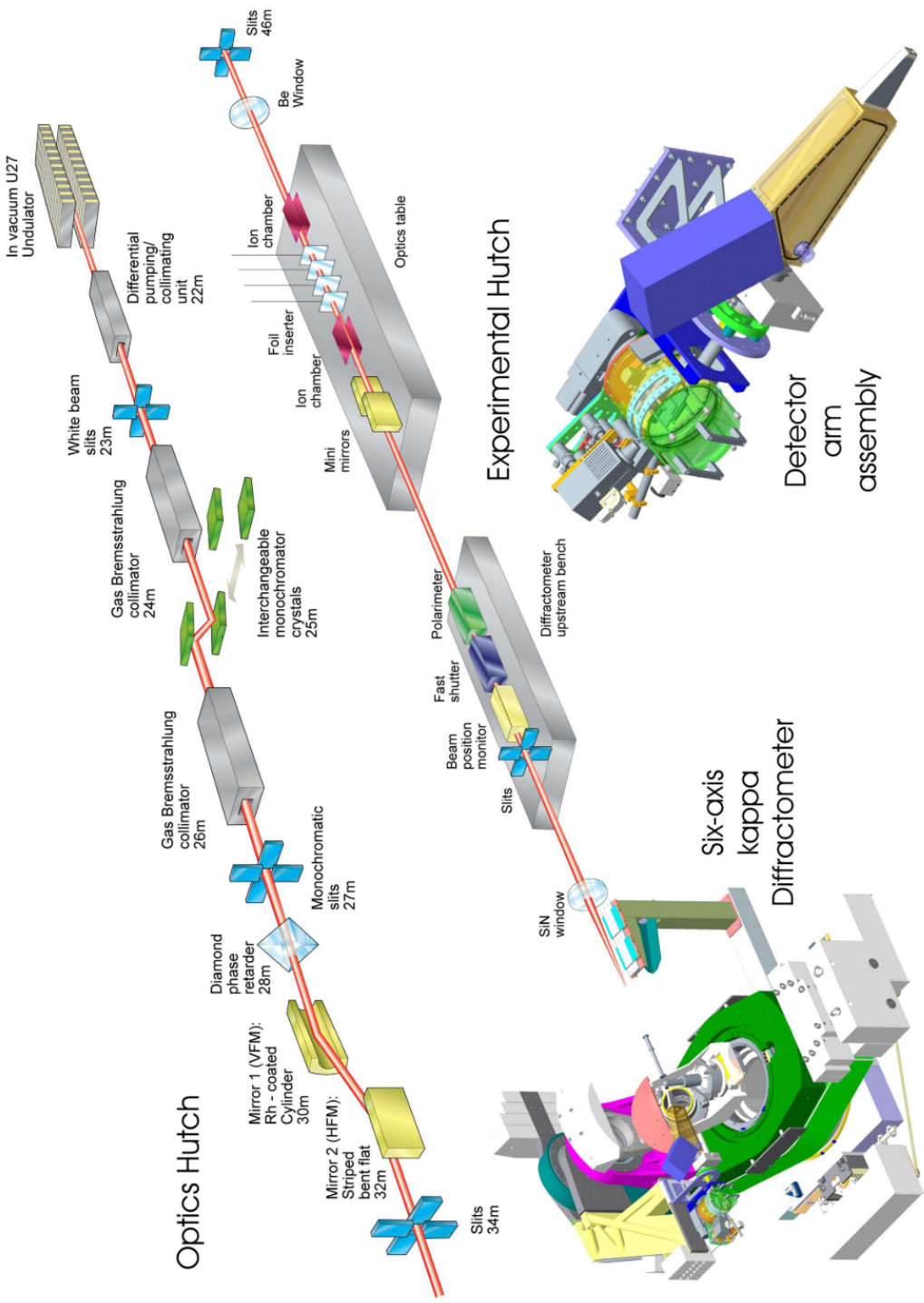

Figure 2.3 *Schematic view of the optics and experimental hutch layouts on I16 at DLS. Detail of the 6-axis kappa diffractometer with the closed-cycle cryostat mounted on the goniometric stage and the detector arm. Figure adapted from [21].*

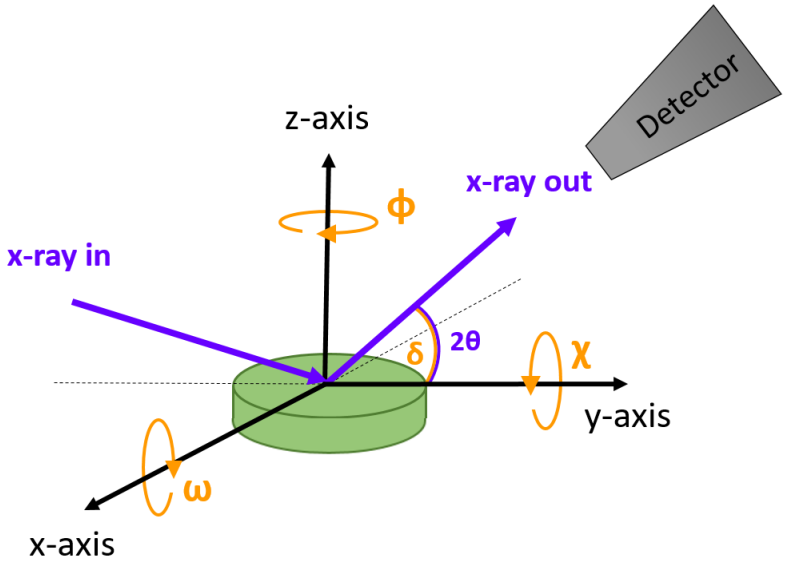

Figure 2.4 *Illustration of the beam path and the different goniometer motions in a 4 axis diffractometer.*

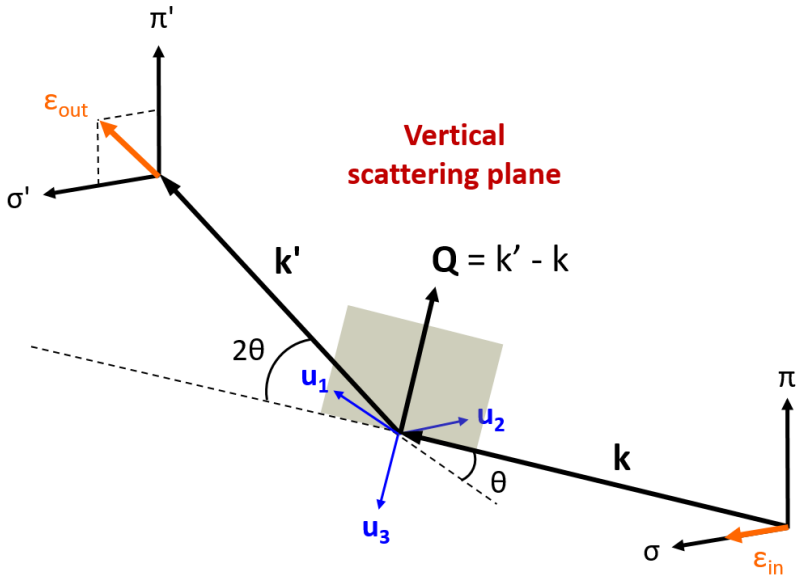

Figure 2.5 *Schematic drawing of the vertical scattering configuration in a REXS experiment. The unitary vectors (u_1, u_2, u_3) define the system of reference for the scattering process. Linearly polarised beams defined in terms of the polarization basis σ and π, perpendicular and parallel to the scattering plane respectively.*

reflection at $\theta \sim 45^{o}$ at the operating energy, such as only polarization perpendicular to the scattering plane can be diffracted and reach the detector. Thus, by rotating the whole crystal-detector assembly around the scattered beam direction, it is possible to select the linear component σ' and π' of the scattered beam. For instance, at the Ir L_3 absorption edge, polarization analysis is frequently done using the scattering planes (333) from Au ($\theta \sim 45^{o}$) or (008) from graphite ($\theta \sim 41^{o}$).

2.3 Resonant elastic x-ray scattering in magnetic materials

2.3.1 The scattering interaction

The Hamiltonian (H') describing the scattering interaction between the electromagnetic radiation and the electronic charge density in a crystalline material can be expressed in terms of the theory of perturbation as resulting from three independent contributions [81, 87]:

$$H' = H_{el} + H_{rad} + H_{int} \tag{2.3}$$

where H_{el} describes the electronic state of the system, H_{rad} stands for the Hamiltonian representing the electromagnetic wave and H_{int} characterises the scattering interaction between the previous two. This last term can be further divided in

$$
\begin{aligned}
H_{int} &= H_1 + H_2 + H_3 + H_4 = \\
&= \underbrace{\sum_i \frac{e^2}{2m}[\mathbf{A}(\mathbf{r}_i,t)]^2}_{e^- \text{ charge + EM wave}} - \underbrace{\sum_i \frac{e^2\hbar}{2m^2c^2}\mathbf{s}_i \cdot \left[\frac{\partial \mathbf{A}(\mathbf{r}_i,t)}{\partial t} \times \mathbf{A}(\mathbf{r}_i,t)\right]}_{\text{spin-orbit interaction}} - \\
&\underbrace{- \sum_i \frac{e}{m}[\mathbf{A}(\mathbf{r}_i,t) \cdot \mathbf{p}_i]}_{e^- \text{ charge + EM wave}} - \underbrace{\sum_i \frac{e}{m}\mathbf{s}_i \cdot [\nabla \times \mathbf{A}(\mathbf{r}_i,t)]}_{e^- \text{ spin + } \mathbf{B} \text{ EM wave}}
\end{aligned}
\tag{2.4}
$$

where $\mathbf{s}_i$, $\mathbf{r}_i$ and $\mathbf{p}_i$ are the spin, position and momentum of the i-electron in the system and $\mathbf{A}$ is the position and time-dependent vector potential of the EM wave. The terms H_1 and H_3 arise from the interaction between the electronic charge and the EM field, H_2 represents the spin-orbit interaction and H_4 stands for the interaction between the electronic spin and the magnetic field ($\mathbf{B}$) of the incident EM wave.

Under this consideration, the scattering mechanism can be described as a two-photon process between the eigenstates of H_{el} and H_{rad} induced by the perturbation H_{int}. Thus, an incident photon with polarization $\boldsymbol{\epsilon}$ and wave vector $\mathbf{k}$ is scattered by the initial state $|g\rangle$ (ground state) to a final state $|f\rangle$ transferring momentum $\mathbf{p} = \hbar\mathbf{k}$ to the system. Then, a second photon ($\boldsymbol{\epsilon}'$, $\mathbf{k}$') of the same energy ($|\mathbf{k}| = |\mathbf{k}'|$) is emitted. This process is schematically illustrated in Fig. 2.6. The probability of this transition to happen is given by the Fermi's golden rule of time-dependent perturbation theory to second order:

$$
w = \frac{2\pi}{\hbar}\left|\langle F|H_1 + H_2|G\rangle + \sum_n \frac{\langle F|H_3 + H_4|n\rangle\langle n|H_3 + H_4|G\rangle}{E_G - E_n}\right|^2 \delta(E_F - E_G) \tag{2.5}
$$

where $|G\rangle = |g;\mathbf{k},\boldsymbol{\epsilon}\rangle$ is the initial state of the whole system with energy $E_G = (E_g + \hbar\boldsymbol{\omega}_{\mathbf{k}_{in}})$, energy of the ground state (E_g) plus the energy of the incoming photon ($\hbar\boldsymbol{\omega}_{\mathbf{k}_{in}}$). $|F\rangle = |f;\mathbf{k}',\boldsymbol{\epsilon}'\rangle$ and $E_F = (E_f + \hbar\boldsymbol{\omega}_{\mathbf{k}_{out}})$ are the corresponding counterparts for the final state, and E_n is the energy of the intermediate state

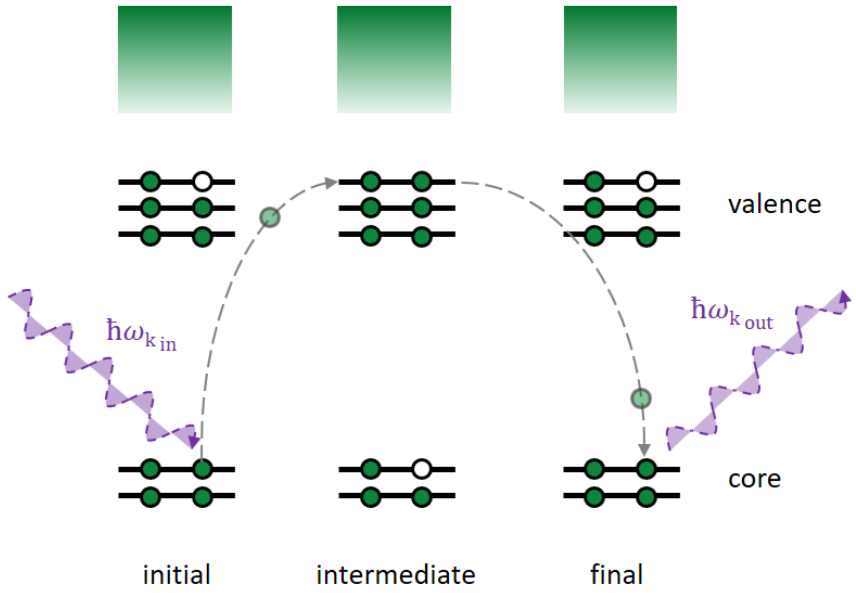

Figure 2.6 *Illustration of the two-photon scattering process of x-rays. In the first step, an incident photon promotes a core electron to the valence band. In the second step, another electron decays from the valence band filling the core hole and a second photon is emitted. When the energy of the incident and scattered photons are the same ($\boldsymbol{\omega}_{\mathbf{k}_{in}} = \boldsymbol{\omega}_{\mathbf{k}_{out}}$) the interaction is considered elastic.*

where no photons are involved.

The scattering cross-section is the magnitude directly measured during a scattering experiment, defined as the probability for a particle of incident energy E_g to be scattered along a given direction, into an unitary solid angle $\Delta\Omega$, with a final energy E_f. For the coherent elastic x-ray scattering in single crystals ($\hbar\boldsymbol{\omega}_{\mathbf{k}_{in}} = \hbar\boldsymbol{\omega}_{\mathbf{k}_{out}}$ and $E_g = E_f$), the differential cross-section can be expressed as the product between the square of the absolute structure form factor and the square of the Thomson scattering length $r_0 = e^2/mc^2 \sim 2.88 \cdot 10^{-5}$Å,

$$\frac{d\sigma}{d\Omega} = r_0^2 \left| \sum_j e^{i\mathbf{Q}\cdot\mathbf{R}_j} f_j(\mathbf{k}, \mathbf{k'}, \boldsymbol{\epsilon}, \boldsymbol{\epsilon}', \hbar\boldsymbol{\omega}_{\mathbf{k}}) \right|^2 . \tag{2.6}$$

The terms in the sum comprising the structure form factor consider the phase differences between the scattered x-rays by the j-electrons at different positions $\mathbf{R}_j$ of the crystal for a given scattering vector $\mathbf{Q} = (\mathbf{k} - \mathbf{k}')$, and the *total scattering amplitude* $f_j(\mathbf{k}, \mathbf{k'}, \boldsymbol{\epsilon}, \boldsymbol{\epsilon}', \hbar\boldsymbol{\omega}_{\mathbf{k}})$ that results from the angular dependence of the scattering amplitude due to the spatial distribution of the local electron density of

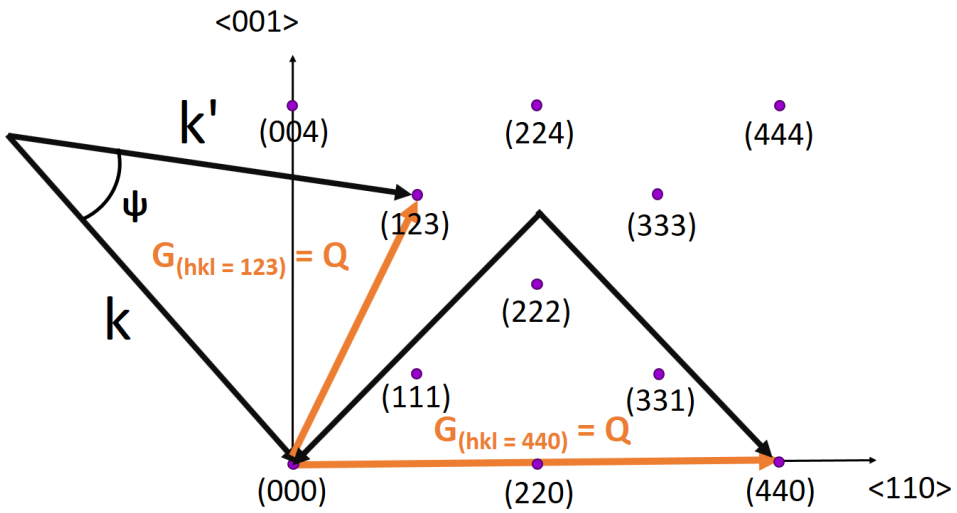

Figure 2.7 *Schematic illustration of the Laue condition. Only when the scattering vector* ***Q*** *is coincident with the lattice vector* ***G*** *at a given hkl, the scattering intensity is maximum.*

each atom. The differential scattering cross section is maximum when $\mathbf{Q}$ coincides with any given reciprocal lattice vector $\mathbf{G}_{hkl}$ and the scattering intensities are non-vanishing due to constructive interference. This is known as the Laue condition illustrated in Fig. 2.7.

In the presence of magnetically ordered spins and as a function of the excitation energy, the shape of the total scattering amplitude becomes more complex in order to account for the magnetic, absorption and resonance phenomena. In these conditions, three main contributions can be distinguished in the scattering amplitude following the formalism in [87]:

$$f_j = (f_j^{Thom.}(\mathbf{Q}) + f_j^{magn.}(\mathbf{Q}) + f_j'(\hbar\boldsymbol{\omega}) + i f_j''(\hbar\boldsymbol{\omega})) \tag{2.7}$$

$$\begin{aligned} f_j^{Thom.}(\mathbf{Q}) &= \left\langle \Psi_g^j \,\middle|\, H_1 \,\middle|\, \Psi_g^j \right\rangle \\ f_j^{magn.}(\mathbf{Q}) &= \left\langle \Psi_g^j \,\middle|\, H_2 \,\middle|\, \Psi_g^j \right\rangle \\ f_j'(\hbar\boldsymbol{\omega}) + i f_j''(\hbar\boldsymbol{\omega}) &= \sum_n \frac{\left\langle \Psi_g^j \,\middle|\, H_3^* + H_4^* \,\middle|\, \Psi_n^j \right\rangle \left\langle \Psi_n^j \,\middle|\, H_3 + H_4 \,\middle|\, \Psi_g^j \right\rangle}{\hbar\boldsymbol{\omega} - (E_n - E_g) + i\frac{\Gamma}{2}} \end{aligned} \tag{2.8}$$

where Ψ_g^j is the core state centred at site j, Ψ_n^j are all possible intermediate states that can be reached by the virtual absorption/emission process characterized by an energy E_n and a lifetime $\sim \hbar/\Gamma$, and H_i correspond to the interaction Hamiltonian terms defined in Eq. 2.4.

The first two energy-independent terms, are dominant when the incident photon energy $\hbar\boldsymbol{\omega}_\mathbf{k}$ is well above the absorption edges. The first term is the so-called Thomson scattering amplitude $f_j^{Thom.}(\mathbf{Q})$, associated with the isotropic distribution of the local charge density, and the second is the non-resonant magnetic scattering amplitude $f_j^{magn.}(\mathbf{Q})$, associated with the orbital and spin density distributions. The real and imaginary terms $f_j'(\hbar\boldsymbol{\omega})+if_j''(\hbar\boldsymbol{\omega})$, also named anomalous or dispersive terms, respond for the resonant contribution due to the core hole transitions into available electronic states just above the Fermi level when the excitation photon energy lies near an elementary absorption edge (i.e. K, L, M...).

In these conditions ($\hbar\boldsymbol{\omega}_\mathbf{k} \sim$ K, L, M...), the coherent interference between the resonant scattering amplitudes from different sites of the crystal, provides sensitivity to the long range electronic order and results in a significant enhancement of the intensity of specific reflections as a function of the symmetry and the multipole character of the electronic levels involved in the transition. In this manner, remarkably weak electronic correlations become visible.

2.3.2 Resonant magnetic scattering amplitude

The specific scattering amplitude of a resonant transition can be calculated by considering the symmetry relationships between the magnetic atoms in the unit cell and by using a tensorial description to the resonant terms in Eq. 2.8. A powerful way to express the REXS amplitude as a scalar product of two spherical tensors is [88]:

$$f^{REXS} = \sum_{p,m} (-1)^{p+m} X_{-m}^{(p)} F_m^{(p)}(j;\omega) \tag{2.9}$$

where the $X_{-m}^{(p)}$ depends on the incident and scattered polarization and the wavevector, and $F_m^{(p)}(j;\omega)$ is associated to the tensorial properties of the j-atom that can be expressed in terms of a multipole expansion. Thus, Eq. 2.9 separates

the contributions from the radiation and the crystalline structure respectively. A detailed derivation of these terms is far from the scope of this thesis and it can be found elsewhere [88–91].

Nevertheless, it is worth highlighting that the tensorial nature of f^{REXS} has important consequences in the scattering cross-section, since forbidden lattice reflections involving magnetic states become visible at resonance. In the proximity of an absorption edge, additional terms appear in the anisotropic susceptibility tensor (ATS) that provide sensitivity to aspheric modulations in the local electron density. Frequently, the site symmetry of the resonant ion is distorted by small atomic displacements via bonding/hybridisation by the crystalline electric field of surrounding atoms or the presence of punctual defects and thermal motion [92–95]. In these conditions, forbidden reflections can appear in non-cubic[4] environments as a result of dipole resonant transitions (E_1), since the symmetry equivalence between resonant species is broken and the extinction rules tabulated for glide planes and screw axes [99] are violated.

Figure 2.8 displays an schematic illustration of this idea, where the lower and high symmetry cases are represented by ellipsoids and spheres respectively. If we compare the positions labelled as A and B in each case, related by a glide transition, they do not cancel when added with the phase in the elliptical case. As a consequence, the extinction rules applying on the spheric and aspheric scenarios are different and forbidden reflections can come into sight.

In a magnetic material, the local magnetic axial vectors are also able to cause anisotropy in the electron density and so, magnetic information becomes accessible via dipole E_1 and quadrupole E_2 electric transitions.[5] This sensitivity arises thanks to the joint effect of the Pauli exclusion principle and the SOC interaction.

On the one hand, the exclusion principle determines the availability of intermediate states near the resonance energy. The population imbalance between spin-up and spin-down semi-occupied levels gives rise to the so-called *magnetic polarisation* of the surrounding empty states in the valence band. Thus, by

[4] ATS reflections are also possible in systems with cubic symmetry when excited through quadrupole (E_2) [96] and mixed dipole-quadrupole (E_1 - E_2) [97, 98] transitions in account of the local chirality of the crystal [98].

[5] The selection rules for dipole E_1 transitions are $\Delta J = 0, \pm 1$ and $\Delta L = \pm 1$, where J is the total angular momentum ($J = L + S$) and L and S are the orbital and spin quantum numbers respectively. For the quadrupole E_2 counterpart $\Delta J = 0, \pm 1, \pm 2$ and $\Delta L = 0, \pm 1$ apply.

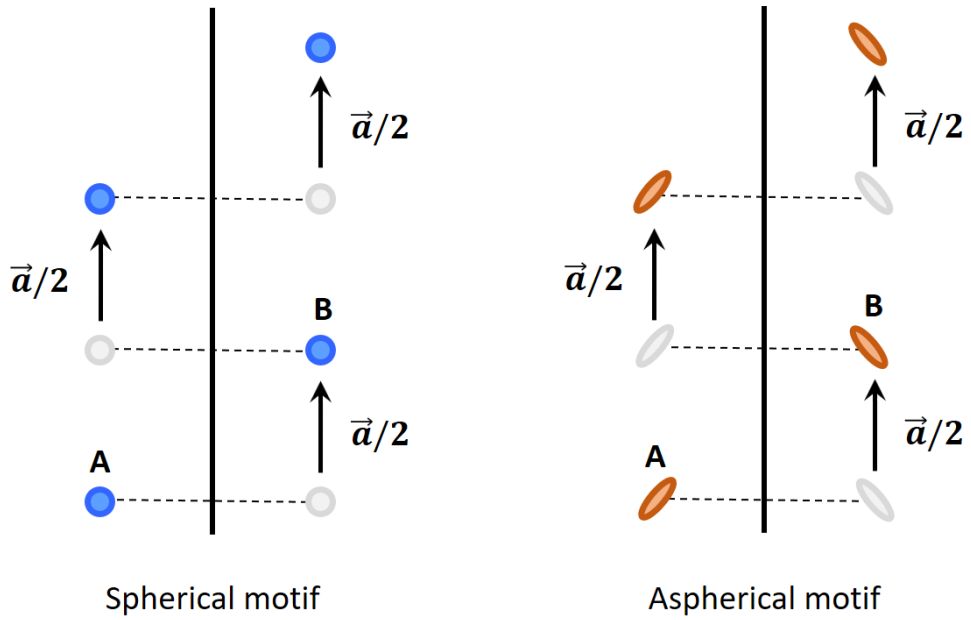

Figure 2.8 *Glide translation on spherical (high-symmetry) and aspherical (low-symmetry) motifs. The operations of symmetry relating ellipsoids and spheres after a glide translation are not equivalent since the former presents site directionality (local anisotropy).*

the exclusion principle and considering that the spin is conserved in optical transitions, the promotion of core spins into magnetically polarised levels near the Fermi energy is favoured for those spins counteracting the resulting local magnetic moment.

On the other hand, since sizeable SOC occurs in electronic levels with $l \neq 0$, *i.e.* non-spherical orbitals, it represents a source of directionality/spatial anisotropy for the electrons taking part in the resonant process. This is, in fact, the ultimate reason why E_1 and E_2 transitions are sensitive to the magnetic order in spite of being purely electric. The splitting of the electronic levels with non-vanishing orbital moment ($l \neq 0$), either in the core or the valence band, entails certain relaxation in the selection rules for the corresponding multipolar excitation.[6] This produces an unbalance in the magnitude of the transition matrix elements generating net magnetic scattering amplitude [29, 79, 88].

This is the case of the magnetic reflections observed in $Sr_3Ir_2O_7$, the main system studied in this thesis. In this compound, the Ir 5d orbitals are responsible for the

[6]The spin selection rule strictly applies only when the electron spin is a good quantum number, i.e. in the case of negligible SOC.

magnetic interactions. Among other energy scales, the SOC induces the splitting of the 5d levels generating a $J_{eff} = 1/2$ ground state magnetically ordered below 285 K at ambient pressure (see Chapter 5 for further details). The resulting magnetic moment leads to magnetic polarisation of the non-occupied surrounding orbitals, which can be accessed via optical dipole transitions from the $2p_{1/2}$ (Ir L_2 edge) and $2p_{3/2}$ (Ir L_3 edge) core levels.

A different aspect is the strength of the resonant enhancement, which mainly responds to the cooperative action of three factors: the magnitude of the transition matrix element, the difference in the density of polarised states above the Fermi level and the strength of the SOC. In general, dipole transitions ($\Delta L = \pm 1$) are stronger than the quadrupole counterparts ($\Delta L = \pm 2$), producing transition matrix elements of larger magnitude. Likewise, the broad overlapping of the electronic levels involved also favours large transition matrix elements. From the point of view of the density of intermediate states available, the larger is the unbalance of polarised states near the resonance energy, the larger is the intensity of the resonant reflections. Third and final, strong SOC splitting of the core and/or the intermediate states produce large unbalance in the transition matrix elements and therefore, larger magnetic scattering amplitude.

Table 2.1 shows a summary of the most common absorption edges exploited in REXS experiments adapted from [88]. The specific electronic levels involved in each transition, the multipolar character, the energy range and the estimated values for the resonant magnetic scattering amplitudes are listed in this table. The most important edges for hard REXS lie within energy range 3.5 - 15 keV, which includes K-edges of transition metals (TM), the L-edges and M-edges of rare-earths and both the L-edges and M-edges of actinides.[7] Inspection of table 2.1 reveals that the maximum enhancement occurs in strongly spin-orbit coupled shells and for dipole E_1 transitions, in line with the criteria just explained. Likewise, the transitions involving 1s core levels ($l = 0$) are significantly weaker than those presenting non-vanishing orbital moment ($l \neq 0$).

In practice, REXS is a complementary technique to neutron scattering for the study of magnetic materials. Despite neutron scattering is the time-honoured procedure for solving magnetic structures, the use of x-rays presents a number

[7]The L-edges of 3d TM and the M-edges of rare earths despite presenting a huge resonant enhancement, lie within the soft x-ray regime E < 2.5 keV where the scattering conditions are not fulfilled for most of the magnetic structures. Atomic resolution cannot be obtained at wavelengths of 12 to 30 Å under normal conditions.

Table 2.1 *Common absorption edges exploited in REXS with detail on the magnitude of the energy (keV), wavelength λ (Å), the allowed transitions between electronic shells, the multipolar character (type), and the estimated resonant magnetic x-ray scattering (RMXS) amplitudes expressed in r_0 units [88].*

Series	**Abs. edge**	**Energy** (keV)	λ (Å)	**Shells**	**Type**	**RMXS** (r_0)
3d	$\mathbf{L_{2,3}}$	0.4 - 1.0	12 - 30	$2p \rightarrow 3d$	E_1	~ 100
	K	4.5 - 9.5	1.3 - 2.7	$1s \rightarrow 4p$	E_1	~ 0.02
				$1s \rightarrow 3d$	E_2	~ 0.01
5d	$\mathbf{L_{2,3}}$	5.4 - 14	0.9 - 2.2	$2p \rightarrow 5d$	E_1	~ 1 - 10
4f	$\mathbf{L_{2,3}}$	5.7 - 10.3	1.2 - 2.2	$2p \rightarrow 5d$	E_1	~ 0.10
				$2p \rightarrow 4f$	E_2	~ 0.05
	$\mathbf{M_{4,5}}$	0.9 - 1.6	7.7 - 13.8	$2d \rightarrow 4f$	E_1	~ 100 - 200
5f	$\mathbf{L_{2,3}}$	17 - 21	0.6 - 0.7	$2p \rightarrow 6d$	E_1	~ 0.05
				$2p \rightarrow 4f$	E_2	~ 0.01
	$\mathbf{M_{4,5}}$	3.5 - 4.5	2.7 - 6	$3d \rightarrow 5f$	E_1	~ 10

of advantages. Firstly, REXS allows the study of materials containing strong neutron absorbing elements such as Gd, Sm, Eu, B, Cd, Dy, Os and Ir. Secondly, x-rays can be easily collimated down to small spots comparable to the typical size of a single crystal (< 100 μm) while keeping an elevated flux of scatterers[8]. This, automatically translates into higher momentum resolution and the possibility of investigating smaller samples, even surface magnetism in thin films or molecular magnets [100–102]. Both bulk and surface states can be selectively probed as a function of the scattering geometry. In normal conditions, the penetration depth of x-rays in the proximity of 10 keV is approximately 50 μm, while typical values for an equivalent neutron beam are in the order of cm (same ratio applies for the beam spot size).

The superior momentum-space resolution of REXS is particularly suitable to investigate incommensurate electronic correlations where the signals get typically broaden [7, 103] or for the accurate refinement of magnetic structures initially investigated by neutron scattering. In addition, when in resonance, the

[8]The flux of neutrons in a spallation source is not larger than $2{\times}10^3$ neutrons $\cdot$ cm^{-2}s^{-1} or $1.5{\times}10^5$ neutrons $\cdot$ cm^{-2}s^{-1} for a nuclear reactor, which implies big samples of several mm^3 not always affordable in single-crystalline form.

interaction of x-rays and matter is much stronger than with neutrons, which is especially beneficial for studying antiferromagnetic materials presenting small magnetic moments and propagation vector k $\neq$ (0,0,0).[9]

The resonant nature of REXS also provides sensitivity to specific elements and electronic states. It is possible to probe different magnetic species separately and disentangle their individual contribution to the global magnetic behaviour. Likewise, it can differentiate between oxidation states of the same element via shift of its inner core levels. Finally, since the promotion of electrons in REXS occurs between specific orbitals, it grants information from the orbital state of the system.

As drawbacks, the scattering cross section of the resonant phenomenon is several orders of magnitude weaker than the corresponding for ordinary charge scattering. An estimation of the approximate ratio between these two quantities can be obtained as

$$\frac{\sigma_{mag}}{\sigma_{charge}} \propto \left(\frac{\hbar\omega_k}{mc^2}\right)^2 \left(\frac{Z^{mag}}{Z}\right)^2 \langle M\rangle^2 \left(\frac{f_m}{f}\right)^2 \tag{2.10}$$

where f and f_m are the magnetic and charge form factors and $\langle M\rangle$ is the magnetic order parameter, whose value is 1 when the system is magnetically saturated at low temperature. Whereas the magnetic scattering cross-section σ^{mag} involves only the electrons occupying partially filled shells (Z^{mag}), σ_{charge} is extended to all electrons in the core and valence bands (Z). Additionally, the energy dependence of the resonant magnetic scattering further diminish their relative value in a factor of $\hbar\omega_k/mc^2$. For this reason, only the significantly larger flux of photons achieved in a synchrotron source can compensate for the weak resonant scattering-cross section, making possible the conventional application of this technique in the investigation of magnetic materials.

A further consequence of the small resonant cross-section is manifested in the form of strong sample dependency. High crystalline quality crystals that maximise the number of spins interacting coherently with the x-ray beam are crucial. In

[9] In the case of ferromagnetic structures or antiferromagnets with propagation vector at the gamma point, x-rays will not see the magnetic signal, since the magnetic contribution is too weak compared to the charge one and both peaks are coincident in the reciprocal space. In this matter, neutron scattering is a superior probe, the comparable magnitude of nuclear and magnetic scattering allows the discrimination of overlapping peaks.

other respects, quantitative analysis of the scattering intensity is rather complex as for any second order perturbation process. Frequently, computational aid is needed to quantify the individual contribution of the different factors affecting the observed peak intensities.

Chapter 3

High-pressure instrumentation for x-ray experiments

Contents

In this chapter, I will begin by presenting a general view on the evolution of high-pressure science and continue by describing the state of art of HP instrumentation dedicated to x-ray experiments. In Section 3.3, I will explain the general considerations for the preparation of HP diamond anvil cells and the particular procedures followed in the REXS experiments conducted in this thesis. A brief description of the two HP setups employed in the experiments presented in Chapter 5 is also provided in the last section of this chapter.

3.1 A brief introduction to the high-pressure field

The field of high-pressure physics started to catch the attention of the scientific community in the last decades of the 19th century when some geologists were interested in reproducing the formation conditions of minerals in the laboratory. It was in the first years of the 20th century when the field blossomed thanks to the prolific work of Percy W. Bridgman [104]. The American scientist was a pioneer in developing novel instrumentation to study the behaviour of matter up to pressures 10,0000 times larger than the value we experience in our living room. He came up with a system of two opposed anvils in contact through a small flat area that were pressed against each other by actuating firstly a lever-arm, and lately, an hydraulic press (see Fig. 3.1). Using this system, Bridgman was able to evaluate volumetric properties, equations of state, thermal-conductivity, viscosity or the electrical resistance of different materials under pressure [104]. His remarkable contribution setting-up the foundations of the high-pressure research was recognised by The Royal Swedish Academy of Science with the Nobel Prize in Physics in 1946 [105].

A new exciting scientific field was born and ready to be explored. Since the discovery in 1797 that diamond was made of pure carbon [107], chemists tried to find the procedure to synthesise diamond in the laboratory out of graphite. This goal became one of the main targets of the high-pressure field during its first decades of life. It was in the mid-twentieth century thanks to the technological outbreaks that led to the construction of the large-volume press, when two independent research groups succeeded at the General Electric Company (GE) in the United States and the ASEA (Swedish Electrical Company). The obtention of synthetic diamonds was accomplished very close in time by the two teams, nevertheless it was first claimed by the GE group in 1955 [108, 109].

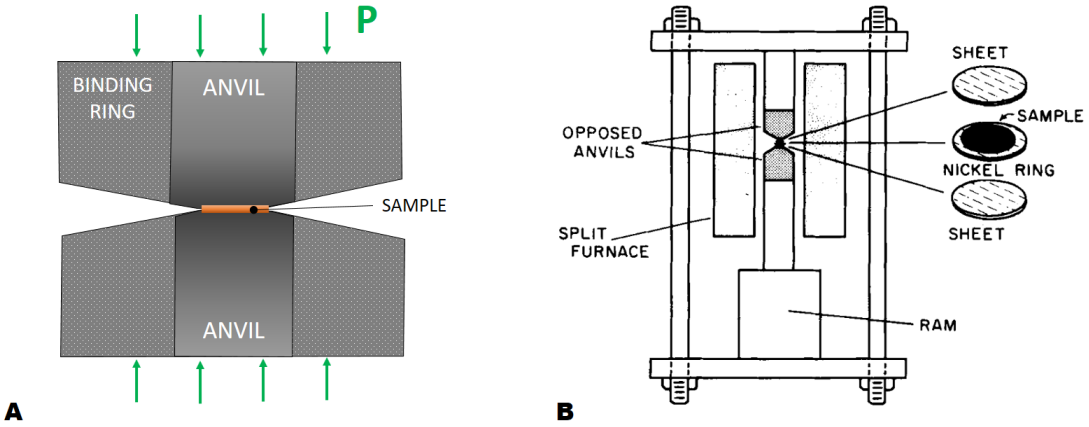

Figure 3.1 *Schematic drawings of A. Bridgman anvils and B. Bridgman hydraulic press with detail of the different components from [106]. The anvils, made of tungsten carbide (WC) are placed between the pistons of an hydraulic press. The sample assembly is composed of a nickel sample ring (0.25 mm thick) sandwiched in between two platinum-rhodium sheets (0.02 mm thick).*

The possibility of producing synthetic diamonds in a controlled form, made it affordable to replace the original tungsten carbide anvils from Bridgman's apparatus with diamonds. In 1959, once again, two separate teams at the National Bureau of Standards (NBS) [110] and the University of Chicago [111] presented the first Diamond Anvil Cell (DAC). In this new device, a solid sample was placed between the flat tips of two opposed diamonds with brilliant cut and a lever-arm mechanism was used to generate pressure. Fig. 3.2 shows a schematic diagram of the device to illustrate the mechanism and a picture of the original DAC created at the NBS [110, 112]. The use anvils made of the hardest natural material known to the date, allowed to expand the pressure limit up to 40 GPa in the early 70's [113, 114]. Additionally, diamonds are not only good at conveying pressure, they also are excellent optical windows highly transparent in a wide range of the electromagnetic spectrum. In particular, their optical transparency in the visible allowed to position the sample by direct observation under the microscope, likewise improving the alignment (parallelism of the anvils) and to use a number of spectroscopic techniques as diagnostic tools.

Initially, a solid sample was directly placed between the two flat surfaces of the anvils but soon A. Van Valkenburg introduced the idea of using a perforated gasket made of a soft material to prevent the sample from extruding out of the area of contact and to be able to study liquid and gas materials [115, 116]. The use of gaskets also provides a more even distribution of pressure along the sample chamber. When the anvils touch directly, "*dry contact*", a pressure gradient

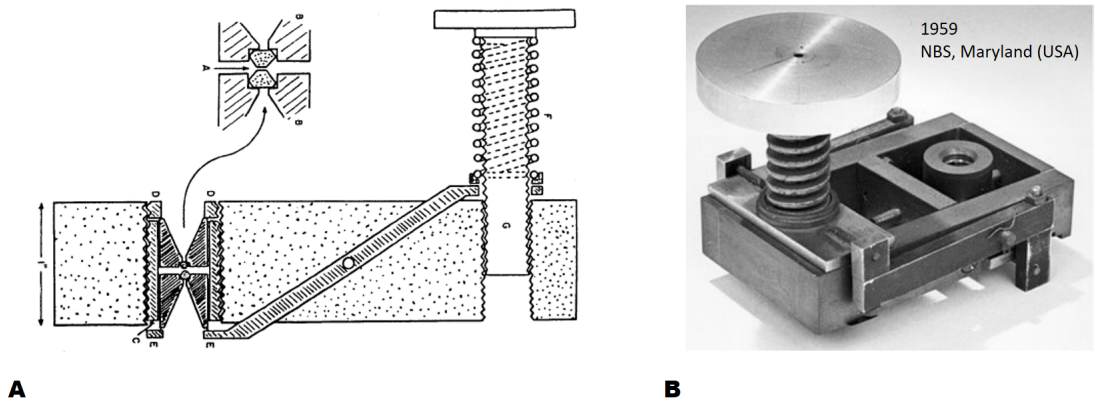

Figure 3.2 *A. Schematic cross-section diagram of the original diamond "squeezer" for infrared transmission studies up to 3 GPa created at the NBS by Weir, Lippincott, Van Valkenburg, and Bunting in 1959 [110]. B. Picture of the real device now on display at the National Institute for Standards and Technology (NIST). Pictures taken from [112].*

appears radially to the direction of compression with the maximum value in the centre of the cullet (see Fig. 3.3). In this situation pressure is considered uniaxial along the direction of the applied force. A different case occurs when using a metallic gasket with a small hole sandwiched between the tips of the anvils creating a small chamber. This space is filled with the sample and a pressure transmitting media (PTM), a substance that conveys pressure and avoids the collapse of the cavity when compressing. In these conditions the pressure profile along the sample chamber is uniform and the system is considered quasi-hydrostatic.

Hydrostatic pressure is a thermodynamic quantity extensively covered in most text books, whose effect is intrinsic to the material and can be described theoretically. It is crucial to keep the system as close as possible to the ideal hydrostatic regime in order to evaluate correctly the effects of pressure. In this respect, a key finding was done by G. J. Piermarini *et al.* in 1973, who discovered that the mixture 4:1 Methanol-Ethanol remains hydrostatic up to 10 GPa at room temperature [117]. A few years later, in 1979 helium gas was also found to be an excellent PTM [118]. Hydrostaticity is not only important to reproduce correctly the experimental observations using theoretical calculations, but to accurately measure the level of pressure in the sample chamber, since most pressure scales are sensitive to the normal and shear stresses generated in non-hydrostatic conditions [119].

In parallel to these discoveries, great effort was also made from the designing

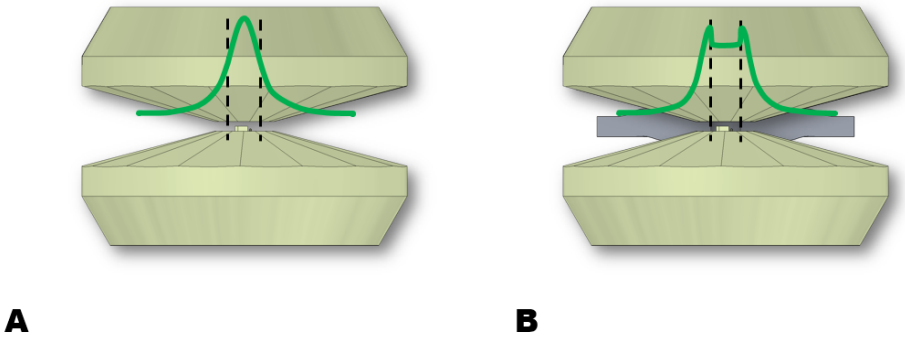

Figure 3.3 *Pressure distribution across the diamond anvils in A) uniaxial and B) hydrostatic conditions (green line). In absence of gasket, there is a gradient of pressure across the diamond culet with the maximum value in the centre of the anvil. When using a gasket the pressure profile is constant along the sample chamber.*

point of view to extend the range of pressure accessible using DACs. In 1978, H. K. Mao and P. M. Bell presented a novel cut for diamond anvils with bevelled tips [120], which combined with a piston-cylinder cell [121], pushed the pressure limit up to the megabar regime. Using this system, A. L. Rouff was able to reach a record pressure of 416 GPa in 1990 [122]. More recently, following the same inspiration, alternative anvil designs proved that it is still possible to extend the pressure limit even further. In 2016, N. Dubroviskaia claimed to reach static pressures beyond 1 TPa using a double-stage diamond anvil cell [123]. In the double stage set-up two opposed nano-polycrystalline diamond (NPD) semiballs are placed on top the cullet of the main anvils and pressed against each other through the spheric surface (see Fig. 3.4). However, despite the remarkably high value of pressure, it is substantially difficult to reproduce this method consistently [124]. Alternatively, last year two independent works presented by A. Dewaele [125] and Zs. Jenei [126] proposed the use of anvils with a toroidal cut in the tips that provides a more stable tension in the central area of the culet and prevents the gasket outflow. The toroidal cut allows one to reach static pressures above 600 GPa. A schematic view of the different diamond anvil geometries mentioned in this text can be seen in Fig. 3.4.

To summarise the information provided in this brief introduction, a timeline comprising the main milestones of the high-pressure field is illustrated in Fig. 3.5. In the following section, an overview of the state of the art of the HP

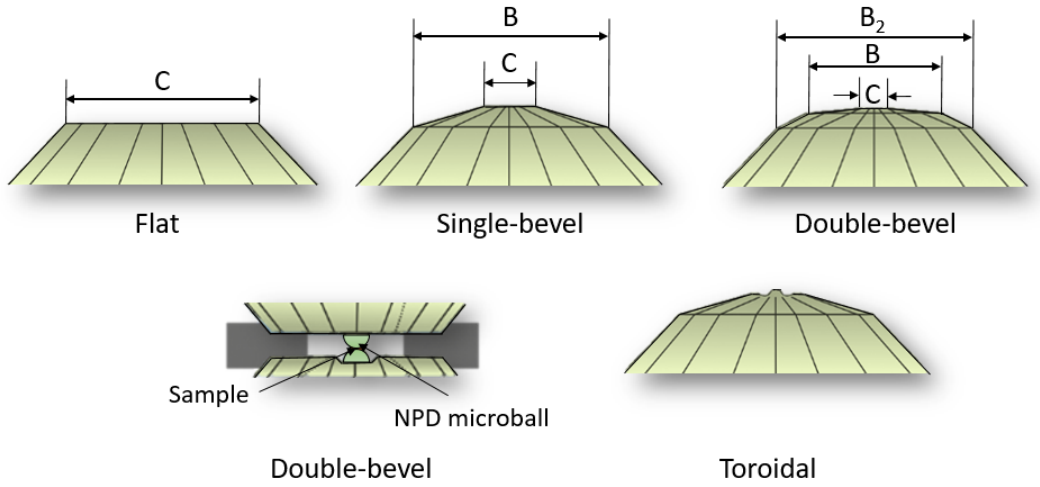

Figure 3.4 *Schematic diagram of the different geometries for diamond anvil culets mentioned in this text adapted from [127].*

instrumentation dedicated to x-ray experiments is given.

3.2 Review on high-pressure instrumentation for x-ray experiments

x-rays have been one of techniques most widely used to track the alterations induced by pressure in matter. Structural transitions towards new crystalline or amorphous arrangements take place upon applying pressure and in many cases, the resulting structure can be solved by analysing the diffraction pattern produced from the interaction with x-rays. Keeping this idea in mind, even previous to the invention of the DAC, scientists attempted to study the crystalline structure of different materials under pressure using anvils made of light elements (low Z), that poorly interact with the x-ray radiation [128]. At this stage, beryllium was the most common material, a steel-grey, strong, light-weight ($Z = 4$) and brittle alkali earth metal, highly transparent to the x-ray radiation that allowed the collection of the scattered diffraction peaks passing through. However, beryllium is toxic and does not allow optical visualization of the sample. For these reasons, in the early 1950s, it started to get substituted for diamond anvils [129], remaining just as a material for seats, gaskets or body parts in HP instruments.

A BRIEF HISTORY OF

HIGH-PRESSURE RESEARCH

The field of **high-pressure** emerges in the first decades of the 20th century trying to recreate the conditions of formation of minerals in the laboratory.

1946

Nobel Prize in Physics **P.W. Bridgman**: "for the invention of an apparatus to produce extremely high pressures, and for the discoveries he made therewith in the field of high pressure physics." Bridgman anvils - **10 GPa**[1].

1955

1st Synthetic Diamonds at **GE** (General Electric) [2,3] and 1953 - the ASEA (Swedish Electrical Company). Not reported until 1980.

1959

First DAC at the NBS[4] (National Bureau of Standards) and The University of Chicago[5].

1964-65

Metal gasket with a **hole** to create a sample chamber that could be filled with a solid or gas sample[6,7].

1967-75

Perfect alignment of the anvils. Pressure limit **40 GPa**[8,9].

1972

Ruby gauge[10].

1973

4:1 Methanol -Ethanol as PTM[11]. Hydrostatic conditions up to 10 GPa at room temperature.

1978

Bevelled anvils. Extended the pressure range **above 100 GPa**[12]. Maximum P of 416 GPa (Ruoff. 1990).

1979

Helium and other gases as PTM[13,14].

2016

TPa limit using **double-stage anvils**[15].

2018

Toroidal anvils[16,17] New anvil geometry by Dewaele and Jenei. Maximum pressure 5.5-6 Mbar.

[1] P. W. Bridgman, Harvard University Press (1964)
[2] F. P. Bundy *et al.*, Nature, 365, 19 (1955)
[3] H. P. Bovenkerk et al., Nature, 365, 19 (1993)
[4] C. E. Weir et al., J. Res. Nat. Bur. Stand. A, 63, 55, (1959)
[5] J. C. Jamieson et al., Rev. Sci. Instrum. 30, 1016 (1959)
[6] A, Van Valkenburgh, Diamond Res., 17, (1964)
[7] A, Van Valkenburgh, Conf. Procc., France, (1965)
[8] G. J. Piermarini et al., Rev. Sci. Instr., 46, 973-9 (1975)
[9] W. A. Bassett et al., Rev. Sci. Instr., 38, 973-9 (1967)
[10] R.A.. Forman et al., Sci., 176, 284-5 (1972)
[11] G.J. Piermarini et al., J. App. Phys., 44,5377-82 (1973)
[12] H. K. Mao and P. M. Bell., Sci., 206, 1145-7, (1978)
[13] J. M. Besson and J. P. Pinceaux, Sci., 206,1073-5, (1979)
[14] H. K. Mao and P. M. Bell., Carnegie Inst. W. Year-Book, 78, 659-60, (1979)
[15] N. Dubrovinskaia et al., Sci. Adv. 2, e1600341 (2016)
[16] A. Dewaele et al., Nat. Commun. 9, 2913 (2018)
[17] Zs. Jenei et al., Nat. Commun. (2018)

Figure 3.5 *Timeline of the key milestones of the high-pressure research field.*

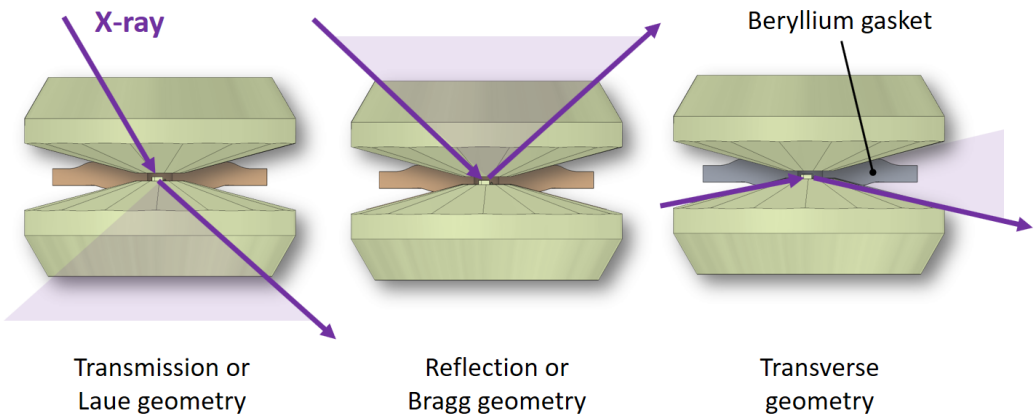

Figure 3.6 *Possible scattering geometries for x-ray experiments using DACs. From left to right, transmission or Laue geometry, reflection or Bragg geometry (backscattering) and transverse geometry. For this last, the gasket material traditionally employed is beryllium. Shaded area represents the scattering angle allowed for the outgoing beam.*

The first x-ray experiments under pressure were conducted on polycrystalline samples directly compressed between the anvils with no gasket [110–113, 130]. In these studies, x-rays with different scattering orientations, were passed through one or both of the anvils (transverse and transmission geometry, see Fig. 3.6), and the diffracted peaks were collected using a photographic film. Most of the DACs employed at that time were able to operate at several tens of kilobars, reaching a record pressure of 300 kbar (30 GPa) using the design proposed by William A. Bassett in 1967 [113]. This cell included a novel rocking mechanism in one of seats supporting the anvils that allowed to adjust the parallelism between the culets and therefore, to take full advantage of the mechanical strength of diamonds (see Fig. 3.7).

Experiments on single crystals arrived together with the introduction of metallic gaskets. Besides the possibility of compressing materials in gas and liquid phase, the use of gaskets threw the doors wide open to the study of single-crystals thanks to the hydrostatic conditions provided by PTM. Using this methodology, in 1965, Block, Wier and Piermarini were able to grow a single crystal of the phase VI of water under pressure and solve its structure using x-ray diffraction [132]. This same team, a few years later, proposed a version of the NBS-DAC (Fig. 3.2) entirely made of Beryllium that allowed to collect diffraction peaks from a wider section of the reciprocal space up to 4 GPa [133]. Since then, a number of designs

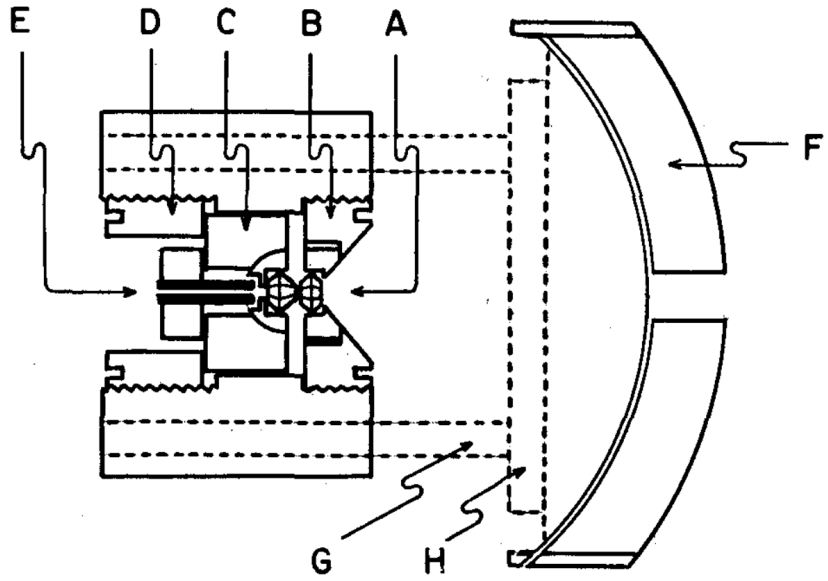

Figure 3.7 *Cross section of the diamond anvil press by Bassett et al. from [113]. A - diamond anvils; B - stationary piston; C - sliding piston; D - driver screw; E - collimator; F - film cassette; G - cassette mounitng rods; H - cassete tranlating bars.*

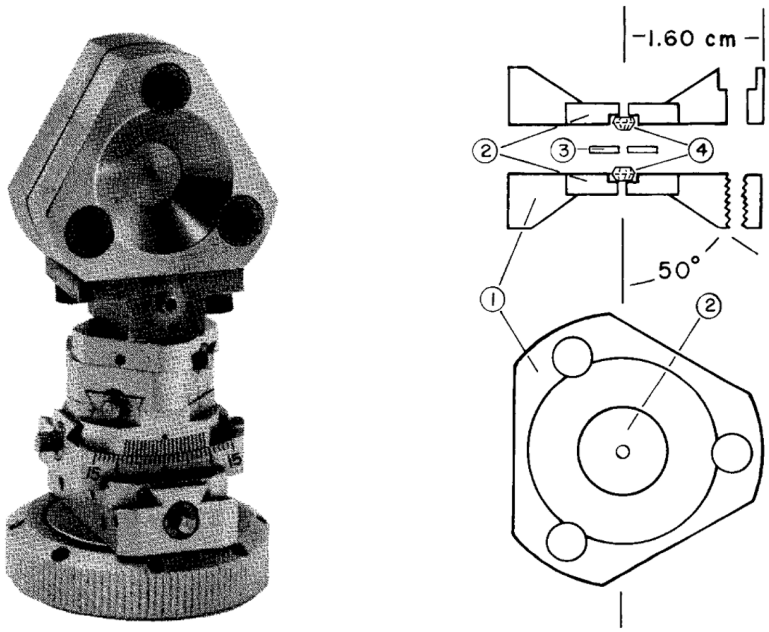

Figure 3.8 *A. Merrill-Bassett DAC mounted on a goniometric head to couple with an x-ray diffractometer. B. Diagram of the cell with detail of the different parts. (1) - Stainless steel platens; (2) - Beryllium disks; (3) - Inconel gasket; and (4) - diamond anvils. Image from [131].*

have been proposed to perform single crystal HP x-ray experiments [134–138].

Among all these pressure cells, Leo Merrill and William A. Bassett published one of the designs most widely used for HP x-ray experiments up to our days [131]. Unlike previous cells where the alignment was based on piston-cylinder mechanisms, the Merrill-Bassett cell (MB) presents three pins that links the two body parts hosting the diamonds, limiting the relative displacement with respect to each other (see Fig. 3.8). The cell is locked by tightening three screws, that also provide the driving force to increase pressure. In this design, the absence of concentric cylinders to define the position of the anvils or lever-arm mechanisms to generate pressure, leads to a significantly lighter and smaller body, with a wider opening angle that maximizes the access to the reciprocal space in transmission geometry. In the original version of the MB cell, the anvils were glued directly on the surface of two flat beryllium seats with no additional mechanism for rocking alignment and optical access was provided through a small perforation in the centre of the seats. This cell is been extensively used to study single-crystals under moderate pressures since its invention to the present day.

The next advance of special interest for the design of HP-REXS instrumentation is the introduction of cryogenic conditions. In order to operate at low-temperature, the pressure cell needs to be located inside a cryogenic vessel and it requires mechanisms to be actuated remotely. Different factors such as the thermal expansion, the thermal conductivity or the increased friction of the materials at LT become significant and need to be considered in the design of dedicated HP instrumentation.

Already in the mid 70s, different research groups tried to obtain information about the behaviour of matter at LT. The first attempt in this direction was performed using Bridgman anvils actuated mechanically by an assembly of rods and lever arms [139]. The set-up published in 1974 by Hawke *et al.*, was initially designed for optical measurements through a sapphire anvil, but soon K. Syassen and collaborators presented a new version adapted for x-rays [140], with anvils made of tungsten and boron carbide and the scattering plane perpendicular to the direction of compression (see Fig. 3.9).

More or less in the same space of time, a different actuating approach was adopted by D. U. Gubser and A. W. Webb, in order to study the effect of pressure in the superconducting transition of Aluminium [141]. This study was conducted by

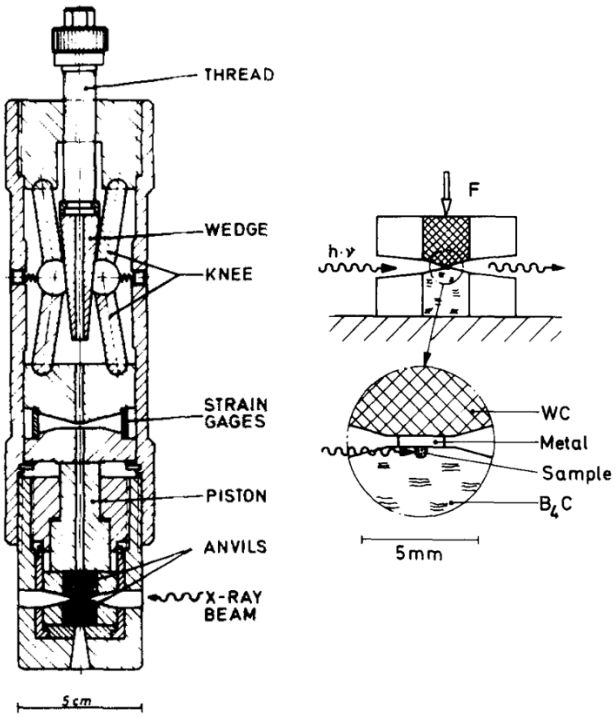

Figure 3.9 *First mechanically driven high-pressure cell for x-ray experiments at low-temperature proposed by Syassen in 1978 [140].*

using a DAC integrated in the circuit of a dilution refrigerator. The pressure cell was hydraulically actuated by circulating liquid ^{4}He through a system of bellows that generates more or less force depending on the amount of flow passing through. Although this setup did not allow optical observation of the sample and did not involve the use of x-ray radiation, together with the example just mention before set the foundations for the actuating mechanisms employed to operate high-pressure cells at LT, mechanical (gear box, lever arms and rods) and pneumatic/hydraulic (membranes, bellows and diaphragms). Since then, several design variations have been proposed based on these mechanisms and a number of cells have been built to operate at low-temperature [142–148]. In the following, a brief description of the most relevant examples of DACs that have been of inspiration for the present work is provided.

The first example of this list is the design proposed by R. Le Toullec and collaborators in 1991 [149, 150], a pneumatically-driven DAC able to reach 15 GPa of pressure at temperatures as low as 45 K using flat diamond anvils. Later, using bevelled anvils, this cell has been employed successfully at higher pressures in a number of studies [151–153]. Le Toullec's cell mirrors the MB design with four

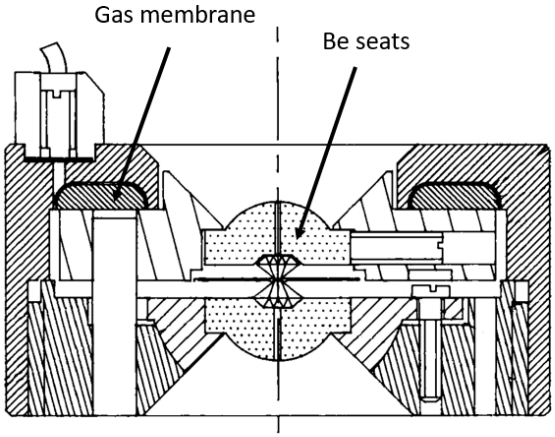

Figure 3.10 *Le Toullec's membrane-driven DAC [149]. In this cell a metallic membrane made of a rigid frame and a flexible metallic sheet was used to generate pressure at low-temperature.*

guiding pins for alignment and four screws as locking mechanism (see Fig. 3.10). It presents a symmetric aperture of 90 degrees in both sides with the diamond anvils glued onto beryllium seats. Despite the scattering angle is similar to the one from the original MB cell, in this case the beryllium seats present a semi-spherical shape in order to generate a more homogeneous path for the incident and diffracted beams. In this way, regardless the angle, the thickness of material crossed by the beam remains constant and the absorption corrections employed to process the peak intensities can be applied more accurately.

In Le Toullec's design, the gas membrane -consisting in a rigid frame and a flexible metallic sheet- is externally attached against the cell using a can-type enclosure that covers most of the cell body. Then, by inflating the membrane with helium gas, an axial thrust is generated that pushes the moving half of the cell body against the fixed one. The major issue of this design may arise from the fact that the can-type enclosure represents a big increase of the overall mass of the cell inside the cryostat, limiting the minimum temperature reachable. In addition, the friction arising from a possible contact between the moving half the body and the internal wall of the can, could result in a dissipation of the transmitted force reducing the efficiency of the actuating mechanism.

Turning now into a higher regime of pressure, anvil cells based on the Mao-Bell design seems to be more stable than the multi-pin DACs. The original

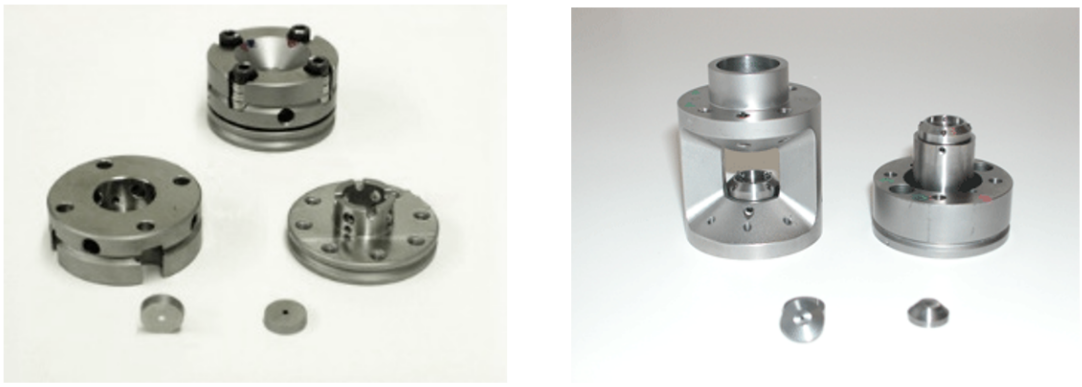

Figure 3.11 *Images of the short-cylinder (left) and panoramic (right) variations of the Mao-Bell DAC design. Images adapted from [156].*

design proposed by H.K. Mao and P. M. Bell [120], based on a piston cylinder mechanism for alignment, has been modified in different ways in order to make it more suitable for x-ray experiments. The most popular variations introduced for this purpose are the so called *panoramic* and *short cylinder* DACs (see Fig. 3.11). The *panoramic*-DAC [148, 154], presents a number of radial apertures along the cylinder section that allow a large access to the reciprocal space in transverse geometry. A recent example of this design, specially built for LT nuclear resonant inelastic x-ray scattering (NRIXS) [155], presents two radial apertures, each with 140 degrees equatorial angle and 68 degrees along the DAC axis, that allow continuous access to a wide portion of the reciprocal space using beryllium gaskets (see Fig. 3.12). Pressure can be modified either by tightening the locking screws or by coupling a gas membrane, and values up to 1.4 Mbar can be reached. The cooling power is given by a flow of helium circulating through the holder hosting the cell in the cryostat that is able to to reach temperatures below 10 K at the sample level. In parallel to the panoramic design, another variation of the Mao-Bell cell especially suitable for x-ray experiments in transmission through the anvils, consist in shortening the piston-cylinder length to symmetrically enlarge the scattering solid angle (see left picture in Fig. 3.11).

A different design approach was recently adopted by Jin *et al.* [157], inspired in the miniature turn-buckle cells used for HP measurements in commercial magnetometers [158, 159]. This pressure cell presents remarkably compact dimensions, 9 mm of diameter and 7 mm of height, and it can be operated in transmission and reflection geometries through a symmetric solid angle of 80

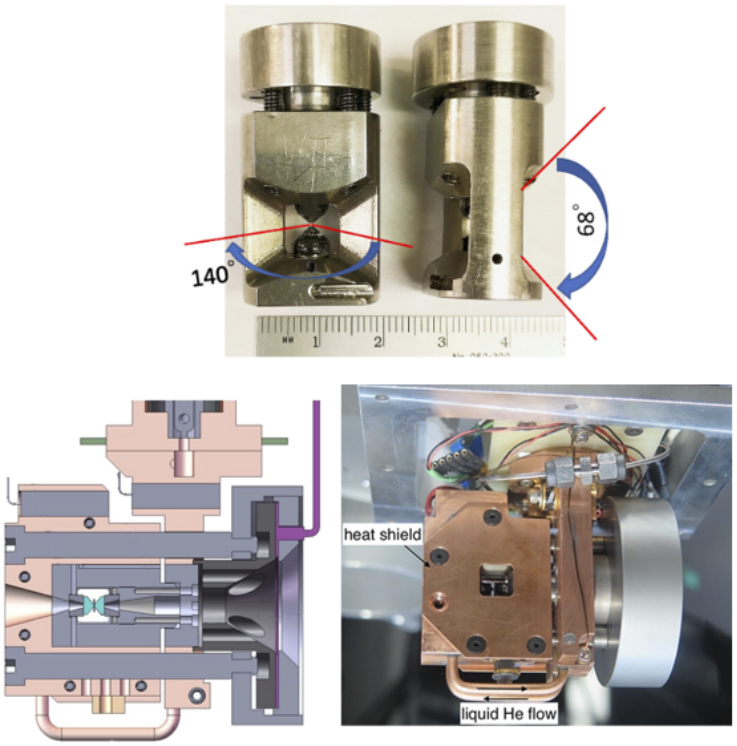

Figure 3.12 *Panoramic DAC for low-temeperature nuclear resonant inelastic x-ray scattering by Zhao et al. [155].*

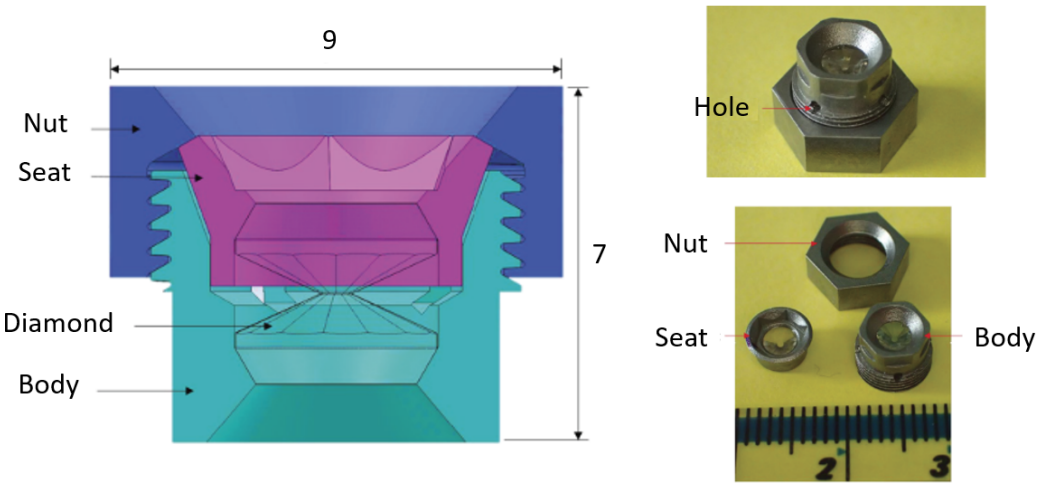

Figure 3.13 *Miniature x-ray DAC by Jin et al. [157]*

degrees reaching a maximum pressure of 15 GPa (see Fig. 3.13). Thanks to its small size, it is possible to couple with an Oxford cryostream device that allows fast temperature adjustment down to 100 K [160]. From our particular experience, this is a very efficient setup when moderate values of pressure and temperature are needed. However, the formation of ice below 150 K might become a recurrent problem when the nitrogen flow gets disturbed by the cell rotation during the experiment. Additionally, pressure tuning cannot be done remotely, it requires one to dismount the cell from the goniometric head and realign the sample every time we need to modify the pressure value. A version of this cell machined in a NiCrAl alloy, has been used to obtain some of the experimental data shown in Chapter 5.

Finally, narrowing down to specific designs for x-ray resonant experiments, two approaches can be found in the literature differing in the strategy employed to overcome the critical absorption from the diamond anvils. This is a crucial aspect in the design, since for anvils of standard thickness the transmission below 7 keV is only marginal (see Fig. 3.19). The first example makes use of a pair of wide-angle partially perforated diamonds with a solid angle of 60 degrees [11]. The second approach exploits the partial transparency of beryllium working in reflection geometry through the gasket [18]. In the first case, the wide partial perforation reduces the total thickness of diamond crossed by the x-ray beam under 1 mm, which in turn allows the use of excitation energies below 7 keV otherwise restricted. A schematic diagram of these anvils can be seen in Fig. 3.14. This is the approach adopted at the Advanced Photon Source (APS) in the USA. They employ a can-type membrane DAC similar to Le Toullec's cell (see Fig. 3.10), that allows one to reach remarkably high-pressures around 17 GPa for anvils of 800 μm of culet size [11]. This cell can be integrated into a Gifford-McMahon 4K-cryocooler for temperature regulation.

The second approach was proposed by by Kernavanois *et al.* [18] and it is mainly employed at the ESRF in France. It consists in a multi-pin anvil cell machined in a CuBe alloy and designed for operating in reflection geometry through a beryllium gasket (see Fig. 3.15). In this configuration, the scattering plane lies within the equatorial section of the gasket and it is only limited by the three pillars responsible from the alignment. However, in the axial direction the scattering window is restricted to $\pm$ 2-3 degrees respect to the gasket plane in order to avoid absorption from the diamonds. For this reason, the position

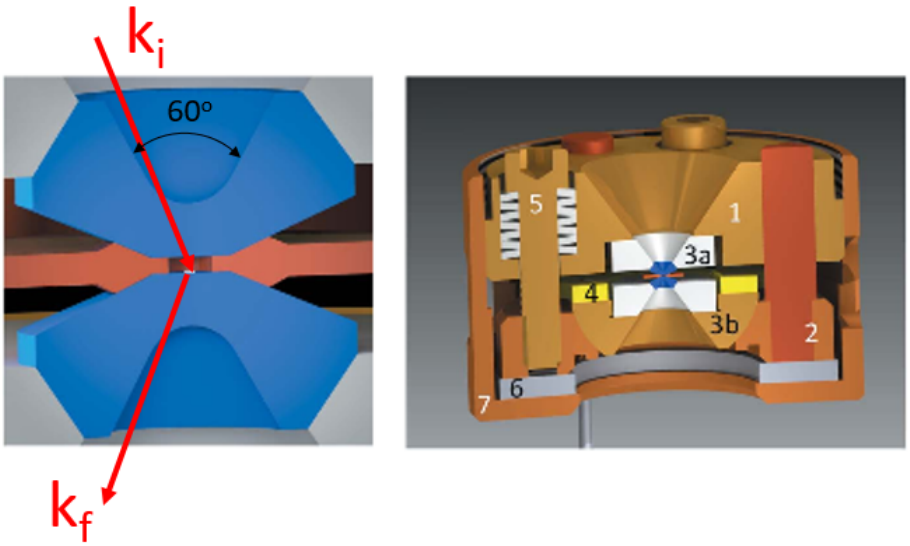

Figure 3.14 *Wide angle partially perforated anvil and pressure cell for resonant x-ray experiments by Feng et al., adapted from [11]. Detail of the incoming and outgoing scattering wavevectors k_i and k_f.*

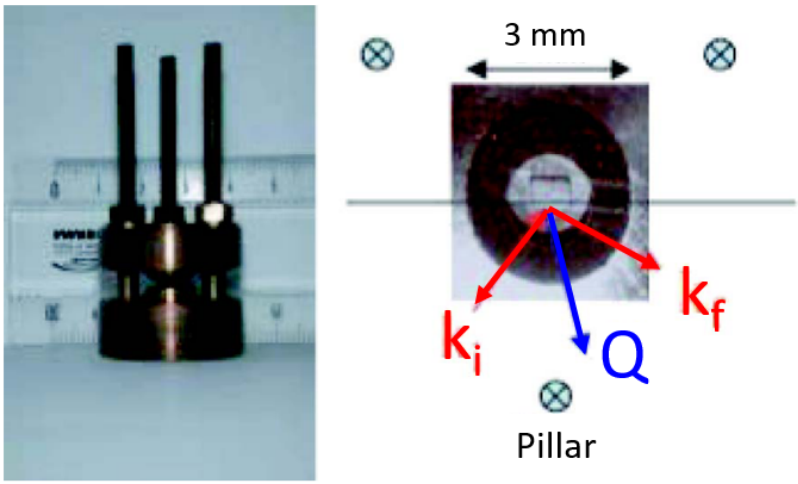

Figure 3.15 *Diamond anvil cell for RMXS experiments in reflection geometry through the beryllium gasket. Images adapted from [18]. Detail of the incoming and outgoing scattering wavevectors k_i and k_f respectively, and the scattering vector Q.*

Table 3.1 *High-Pressure cell designs for x-ray diffraction experiments at low temperature and principal characteristics (pressure range (P_{range}), actuation mechanism, scattering geometry, opening angle and minimum operational temperature (T_{min}).*

Pressure cell		P_{range}	Actuation	Scatt. Geometry	Op. Angle	T_{min}
Bridgman type	*Syassen* [140]	6 GPa	Mechanical	Transverse		mK
Mao-Bell	Panoramic *Zhao* [155]	Mbar	Membrane	Laue/Bragg	140° Equatorial 68° axial	< 10 K
	Short piston	Mbar	Membrane	Laue/Bragg		< 10 K
Multi-pin	*Le Toullec* [149, 150]	50 GPa	Membrane	Laue/Bragg	90°	46 K
	RMXS-*Kernavanois* [18]	3 GPa	Mechanical	Transverse	120° Equatorial 4° axial	1.4 K
	RXS-Anvil perforation [11]	17 GPa	Membrane	Bragg	60°	4 K
	m-RXS (this work) [1]	20 GPa	Membrane	Bragg	100°	30 K
Miniature DAC	*Jin* [157]	15 GPa	Mechanical	Laue/Bragg	80°	80 K

of the reflections of interest needs to be carefully considered during the sample preparation and the cell loading, so the scattering condition is coincident with the narrow axial aperture. Thick crystals and large anvils are needed in order to maximise the surface of sample scattering the x-ray beam and therefore to amplify the magnetic amplitude, which limits the maximum pressure achievable.

Kernavanois' cell is designed to couple with a modern version of the Orange cryostat originally designed at the Institut Laue-Langevin (ILL) in France [161]. In this cryostat, a system of rods allows continuous tuning of pressure up to 3 GPa in the whole range of temperature between 300 and 1.4 K using big Moissanite anvils 2 mm in culet diameter.

To summarise, the key characteristics of the pressure cell designs mentioned in this text are listed in table 3.1. In the next section, I will describe the main steps followed in the preparation of HP-REXS experiments.

3.3 Main parts and basic handling of diamond anvil cells for REXS experiments

From the information provided so far, one can deduce that the essential components common to all the pressure cells based on the opposed-anvil mechanism are: the anvils (diamonds in many cases, but also some softer

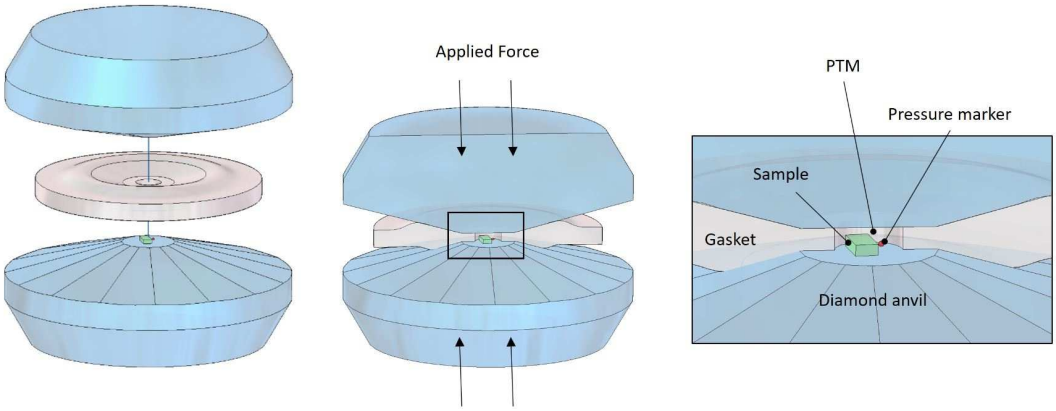

Figure 3.16 *From left to right, illustration of the assembly of the main components of a diamond anvil cell: opposing diamond anvils, metallic gasket and sample space. Far right, detail of the elements placed in the sample chamber: sample, PTM and pressure marker.*

materials such as sapphire or moissanite that can be used for moderate pressures), the baking seats, the gasket and the cell body. Likewise, one can see that the general idea behind its operational mechanism is to create a cavity between the flat tips of the anvils by sandwiching a hole drilled in the centre of the indentation of a metallic gasket (see Fig. 3.16). This cavity is filled with sample, pressure transmitting media and pressure gauge, and compressed by bringing the two anvils together using different mechanisms. The criteria followed for the selection and preparation of each component are detailed in the following.

Anvils selection. The first aspect to consider when planning a HP-REXS experiment is the selection of the anvils based on the experimental environment and the demands of the probing technique. There are different anvil-cut geometries in the market in order to satisfy the needs of different experimental conditions [162]. For x-ray experiments in transmission geometry, the so-called Boehler-Almax (BA) cut [163] is particularly beneficial for two reasons. This anvils present conical support that reduces its thickness and enlarges significantly the scattering angle. Both parameters crucial in HP-REXS experiments. In Fig. 3.17 is a schematic representation of anvils of standard and BA cut for clarity.

The maximum value of pressure achievable is largely dictated by the size of the culet. Considering the definition of pressure P = F/A, where F is the force applied perpendicular to a surface of area A, the smaller the culet the higher is

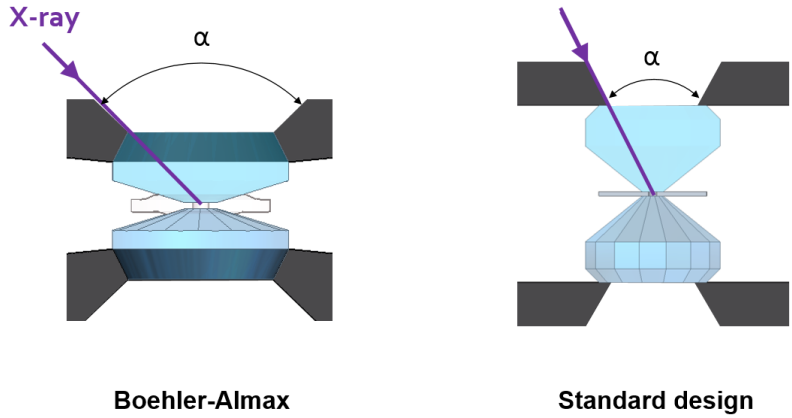

Figure 3.17 *Geometry of the standard design and the Boehler-Almax (BA) cut for diamond anvils. The conical support of BA anvils reduces the anvil thickness and enlarges the scattering angle (α).*

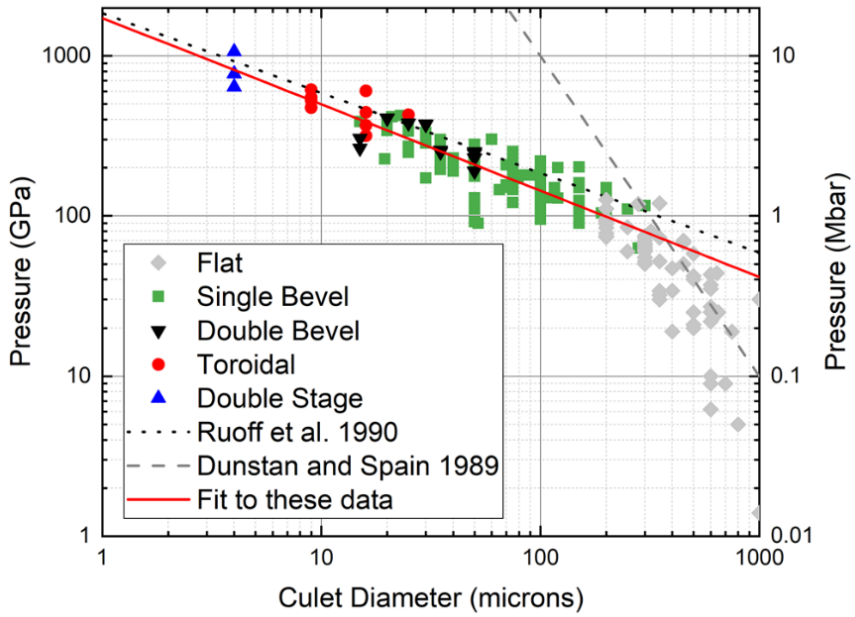

Figure 3.18 *Maximum pressure as a function of culet diameter. The dashed line refers to the fit of Dustan and Spain [164], the dotted line refers to the fit of Ruoff et al. [122] and the red line to the fit of O'Bannon et al. [127] from where this figure is adapted.*

the pressure achieved for the same value of applied force. But not only the culet dimensions, also the shape of the tip is a conclusive factor. Bevelled, double-stage and toroidal anvils are able to withstand higher values of pressure than flat anvils. One can find some examples in the literature analysing the dependency of the culet area and the maximum pressure reachable [122, 127, 164]. In Fig. 3.18 are represented the results obtained recently by O'Bannon *et al.* [127] that reviewed the maximum pressure achieved and the culet size of 224 high-pressure experiments from the last 50 years. By fitting this set of data the authors obtained the expression:

$$P_{max}(GPa) = 1727d(\mu m)^{-0.54} \tag{3.1}$$

where d is the diameter of the culet in microns and P_{max} in GPa is the maximum value of pressure reached. This equation can be used as a guide in order to choose suitable dimension of the anvils for our pressure experiment. The authors observed a deviation from the fitting for culet diameters > 400 μm, attributed to the fact that for this size of anvils, diamonds are reused in several experiments and not taken up to their pressure limit.

In x-ray experiments, the most important interaction between anvils and radiation arise in the form of absorption and diffraction. Diamond is highly transparent to the x-ray radiation in the range of energy typically used for conventional HP diffraction experiments (20-200 keV). However, below 7-8 keV the absorption becomes high enough to compromise the viability of HP-REXS studies. This regime of energy is particularly important for x-ray spectroscopy techniques such as x-ray absorption scattering (XAS), x-ray magnetic circular/linear dichroism (XMCD/XMLD respectively) or resonant x-ray scattering (RXS). In these cases, the energy of the incident beam is tuned to the absorption edge of the elements involved in the phenomenon of interest, many times below the threshold imposed by the diamond absorption. In Fig. 3.19, we can see the transmission of x-ray radiation through diamonds of different thickness in the range of energy between 6 and 15 keV [165, 166]. The dotted vertical lines represent the value of the energy of the absorption edge of some common elements of interest for this thesis. The total thickness of diamond crossed by the x-ray beam is double of the thickness of one anvil (incoming and outgoing beam). Thus, for standard anvils 2 mm thick, the x-ray beam would cut a total length of 4 mm

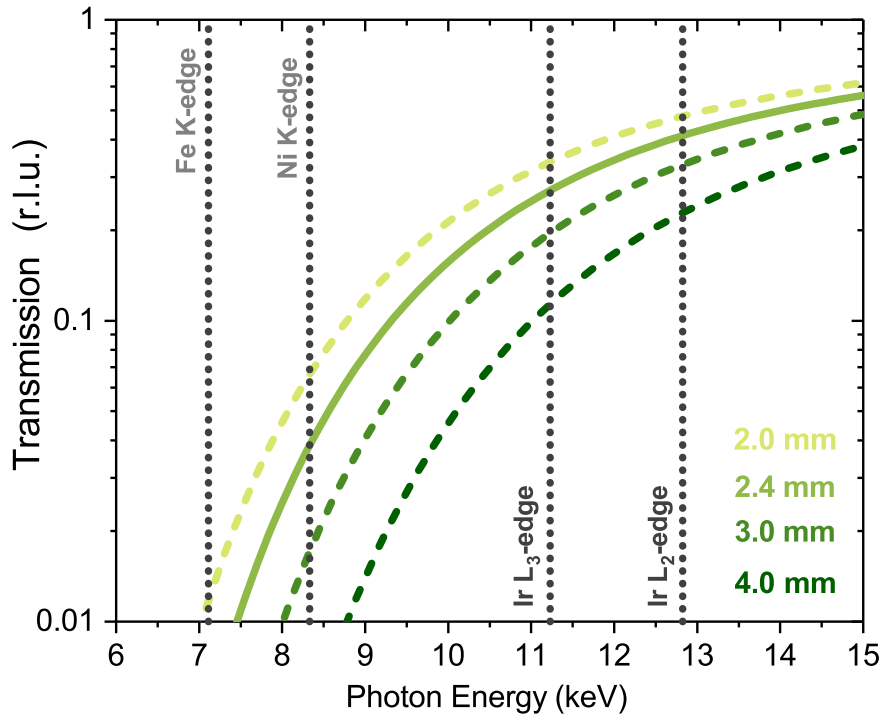

Figure 3.19 *In logarithmic scale, x-ray transmission through diamond anvils of thickness between 1.0 and 2.0 mm for the range of energy between 6 and 15 keV calculated from [165, 166]. The solid line represents the thickness of the anvils employed in the pressure cell proposed in this work. The dotted vertical lines represent the energy values of some absorption edges relevant for the studies carried out during this thesis.*

of anvil material and the transmission would become critical below 9 keV.

This problem can be mitigated by decreasing the thickness of the anvils at the expense of weakening their strength, as shown previously for the partially perforated diamonds. Similar setups combining a partially perforated anvil and a fully perforated one that acts as backing seat of a small anvil glued on top, have been also extensively used in XMCD experiments [167].

The second challenge to be overcome is the overlap of the Bragg peaks from diamond with the diffraction pattern of the sample that induces severe distortion of the signals. Different strategies have been tried in order to correct this issue, from rotating the pressure cell so the Bragg peaks from diamond do not meet the diffraction conditions any more, to the use of complex masking post-processing procedures. Recently, a better solution was found in the use of poly-

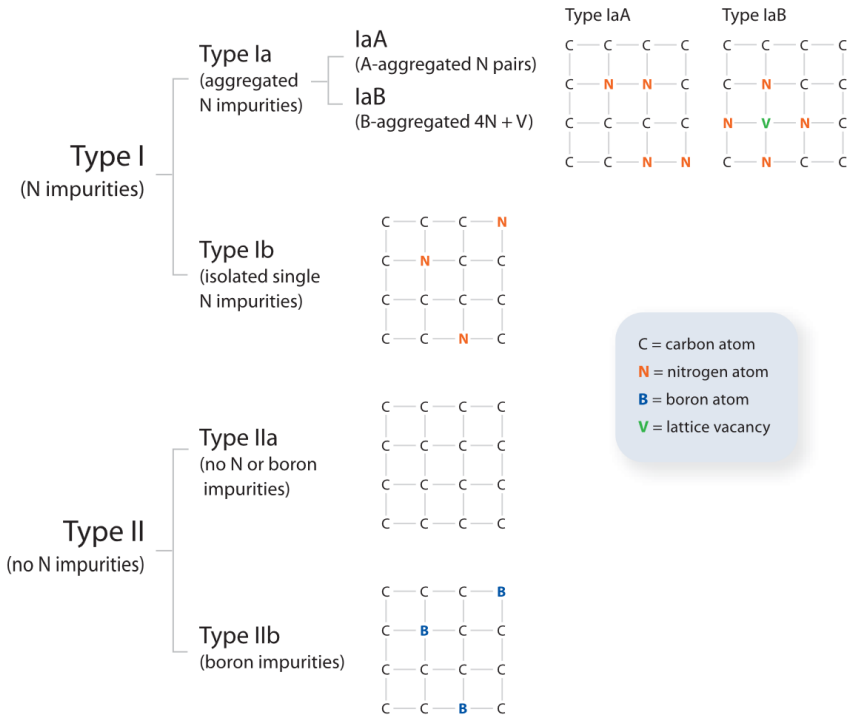

Figure 3.20 *Diamond-type classification based on the presence or absence of nitrogen and boron impurities and their configurations within the diamond lattice.*

crystalline nanodiamonds [168, 169]. This kind of anvil consists of randomly oriented diamond grains of tens of microns in size, so that Bragg's law is always satisfied for any angle and photon energy. Thus, they provide a smooth glitch-free background resulting from the average of all the diamond grains in random orientations. This solution has been exceptionally beneficial in XAS and EXAFS (Extended x-ray Absorption Fine Structure) experiments. For the case of REXS, thanks to the spatial resolution of small area detectors, usually it is possible to discriminate between peaks separated by 1 degree in the reciprocal space, which makes a small rotation of the cell sufficient to displace the diamond peak out of sight.

Finally, possible internal defects or impurities in the crystalline structure of diamonds may cause stress and failure. Diamonds present particularly high compression strength along the crystallographic direction [100], hence this is the preferred orientation with the culet of the anvil perpendicular to it. However, the presence of defects or impurities can act as a centre of nucleation for cracks under compression. Diamonds can be classified into two types (I and II) based on the presence or absence of nitrogen impurities, and further subdivided according to

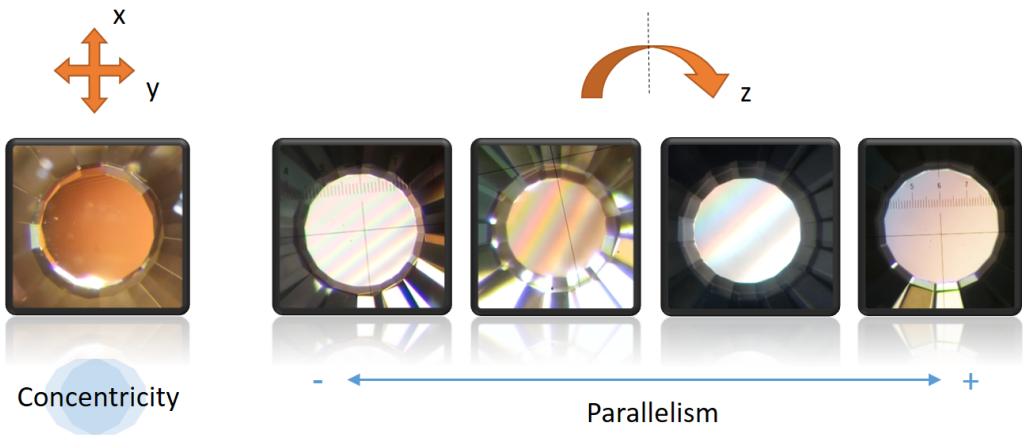

Figure 3.21 *Anvils alignment process. Good alignment is accomplished when the anvils are concentric and parallel. On the far left, view under the microscope of non-concentric anvils. On the right, different stages improving the parallelism from left to right until full alignment is completed (far right).*

the arrangement of nitrogen atoms (isolated or aggregated) and the occurrence of boron impurities (see Fig. 3.20). In general, pure synthetic diamonds (type IIa) present superior optical and mechanical properties, however for some experimental environments, e.g. high temperature, the presence of isolated single nitrogen impurities (Ib) can be beneficial in terms of mechanical strength. The specific optical and mechanical properties of each type can be found elsewhere [162, 170, 171].

Anvils gluing and alignment. Once the suitable anvils are chosen, the next step is to mount them on the backing seats. The seats are the pieces directly supporting the diamonds, usually made of hard materials such as tungsten carbide (WC) or alloys as Inconel. This is an important part of the pressure cell. The quality of the contact between anvil and seat is key to reach a good pressure distribution and to avoid punctual stress that may cause failure. It is very important to ensure that the surface of contact between seat and anvil is completely clean. The seats present a conical aperture in the side opposite to the anvil that will determine the angular access to the sample chamber. They are moving parts responsible of the fine alignment of the anvils in the pressure cell. In some cases, one of them presents hemispherical shape in order to provide an extra degree of freedom to adjust the axial parallelism (rotation around z), whereas the other seat is usually cylindrical and allow the adjustment in the x

Figure 3.22 *Jigs for anvils gluing.*

and y directions using a set of precision screws located in the cell body. The alignment of the anvils consist in making them parallel and concentric respect to each other. This process needs to be done under the microscope by observing the lateral match of the tips and the birefringence lines (interference of light) that appear when the culets are close together. As the parallelism of the anvils increases, the interference lines get broader until disappearing as shown in Fig. 3.21.

Prior to the alignment, the anvils need to be fixed onto the seats using glue. It is important to ensure that the culet is parallel to the base of the seat, especially for cells with no hemispherical adjustment. In order to do so, one can use a jig, a mechanical clamp to temporarily fix the position of the anvil on the seat during the gluing process. This accessory allows the free movement of the anvil and seat under the microscope to check their relative position. This is particularly beneficial when using anvils with BA cut, where the conical shape of the support usually allows slight tilts when mounting the anvils. Figure 3.22 shows a picture of the jigs employed for the preparation of the experiments conducted in this thesis.

Different glues can be used for this purpose. Some of the most common are: Hysol-9514, Araldite-Rapid, Stycast-2851, Stycast-1266 or Loctite Double-Bubble. The particular properties of each of them can be found elsewhere [172–175]. Hysol-9514 and Araldite-Rapid showed the best performance in cryogenic

conditions. Stycast-1266, which is specially formulated for working at LT, presents very low viscosity and it easily runs between anvil and seat during the gluing process.

Gasket. Once the anvils are aligned, the next step is the preparation of the gasket. The selection of the material and its thickness is crucial, since it plays a key role in the maximum pressure achievable. Additionally to the encapsulation of the sample, gaskets also provide lateral support thanks to friction with diamonds, without which the anvils would not survive above 30-40 GPa of pressure [171].

The gasket material selection is based on the range of pressure, the hardness of the anvils and the background signal. The ideal material needs to be softer than the anvils, but sufficiently hard to prevent them from getting in touch at the highest pressure. In compression, the gasket undergoes plastic deformation reducing its thickness and "work-hardening". The latter consists in the increase of the yield strength induced by the accumulation of crystalline dislocations that prevent the nucleation of new defects. This is the process occurring during the indentation that limits the extent of further gasket deformation during the real experiment. In a large percentage, the materials employed as gaskets are metals. Nevertheless, some applications demand insulating, non-magnetic or x-ray transparent gaskets. In these cases, the addition of non-conducting inserts (MgO, Al_2O_3, cBN) can provide insulation for the introduction of electrical contacts in the sample chamber. Materials such as high-strength beryllium [148], amorphous boron epoxi [176] or kapton belts [177] have been used for x-ray transparency, and in the case of magnetic measurements, CuBe is widely employed. Table 3.2 shows an overview of materials commonly used for gaskets along with the value of some of the mechanical properties of interest for this purpose: shear modulus, bulk modulus, yield strength and ultimate tensile strength (UTS).

For the experiments conducted in this thesis, stainless steel was found to meet the mechanical properties needed while, showing minimal interaction with the x-ray beam. The emission lines of Fe, $K_{\alpha 2}$ (6.390 keV) and $K_{\beta 1}$ (7,057.98), are far enough from the Ir L_3 absorption edge (11.215 keV) employed as the excitation energy in our experiments. Thus, it is possible to discriminate completely the fluorescence arising from the gasket material using the detector energy threshold. Other materials as tungsten (W) or rhenium (Re) were tried, finding that the first becomes brittle at low temperature and the second provides intense fluorescence

Table 3.2 *Gasket materials and values of the correspondent mechanical properties of interest for this purpose. Shear modulus, bulk modulus, yield strength and ultimate tension strength (UTS) from [178].*

Material	Shear Modulus (GPa)	Bulk Modulus (GPa)	Yield strength (MPa)	UTS (MPa)
Stainless-Steel 301-FH	78.0	200	965	1276
Tungsten	156	400	750	980
Rhenium	176	469	290	1070
Berylco25	50	130	1130	1310
Beryllium I-220H Grade 2	135	303	345	448
Inconel X750		210	850	1250

hampering the detection of the magnetic signals.

Indentation. The typical initial thickness of a gasket foil is 0.2 - 0.3 mm. In first place, the metallic sheet is compressed between the anvils reducing its width and undergoing plastic deformation and hardening.

In order to make the indentation of gaskets a reproducible process, it is possible to use different methods to track the degree of indenting following the pressure on the culet using ruby chips, measuring the force applied using a load cell, checking reduction in thickness of the cell using micrometers or inspecting visually the growth of the indentation walls under the microscope.

This process is traditionally done using the actual cell that will be employed later in the pressure experiment. In these conditions, the anvils work within the 'dry contact' regime and are exposed to a pressure gradient from the edge to the centre of the culet as shown in Fig. 3.3. In this situation, the anvils can be exposed to much higher pressure than in the real experiment using a drilled gasket (especially for big culets), which may lead to failure. This problem can be solved by using indenters with anvils made out of hard materials such as tungsten carbide that makes the process faster and do not put the diamonds at risk.

In Fig. 3.23 is the indenter employed for preparing the gaskets used in the miniature x-ray DAC [157]. In this case, a SPECAC press [179] and a load cell [180] were used to generate and track the uniaxial force applied. An average force of 1.8 - 2.1 kN was enough to obtain consistent indents of 100 μm out of steel sheets 250 μm thick in origin.

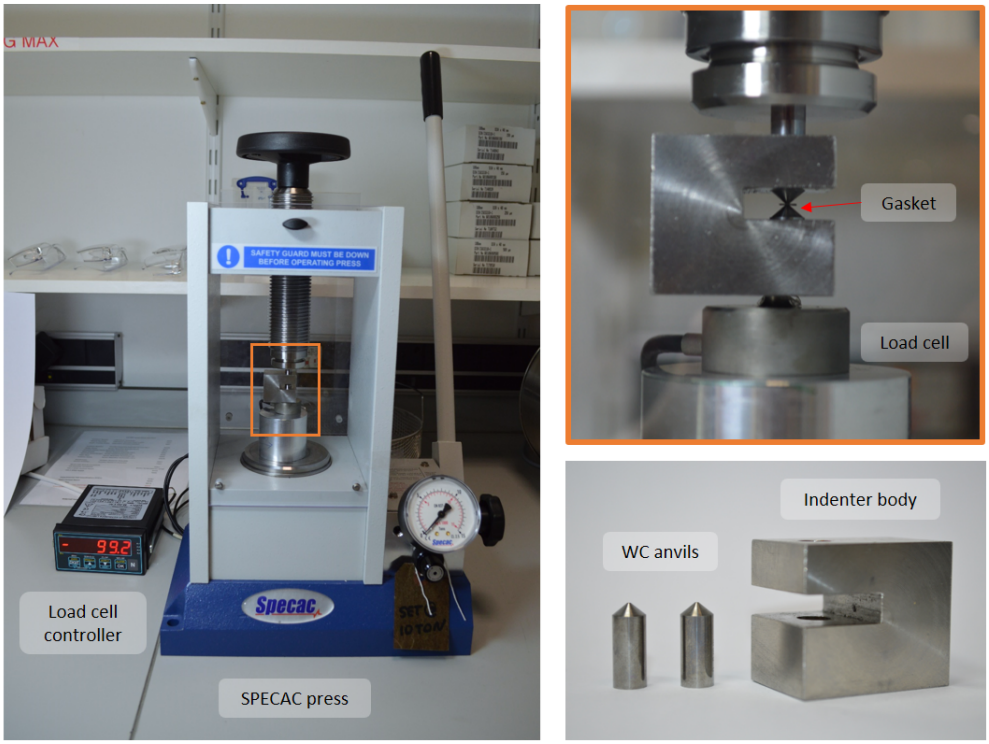

Figure 3.23 *Set-up for gasket indentation. Left: SPECAC press, and load cell assembly. Top-right, detail of the indenter set-up and the load cell employed to measure the force. Bottom-right, detail fo the tungsten carbide anvils and the indenter body.*

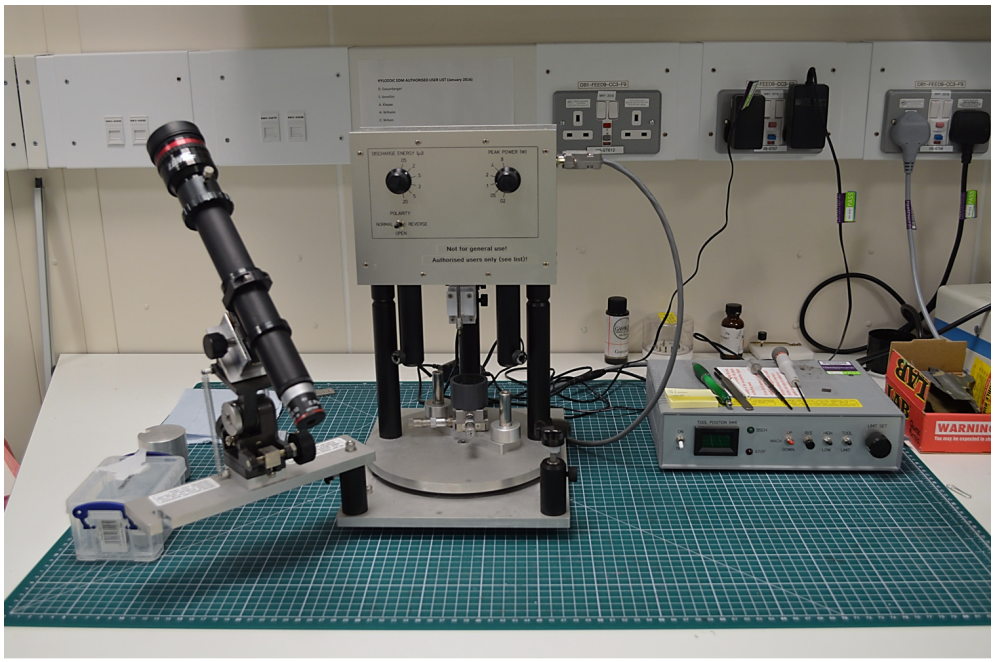

Figure 3.24 *Spark-eroder machine for gasket drilling from Hylozoic Products.*

Drilling. Drilling a hole in the centre of the indentation, one can create a cavity that will host the sample. The size of this hole should be between 1/2 and 1/3 of the size of the culet and it must be centred in both sides of the indentation. Off-centred holes mean either bad anvil alignment or non-perpendicular drilling, both potential causes of uneven gasket deformations and experimental break down.

Different methods can be employed for hole drilling, from mechanical manual drill to laser cut, or sparking erosion. This last is perhaps, the most used for experiments in a moderate regime of pressure where the final thickness of the indentation is above 50 μm. Laser drilling may be more convenient for gaskets with very thin indentations employed in the megabar regime. For the experiments conducted in this thesis, the sparking-erosion setup in Fig. 3.24 was employed for gasket preparation.

Cell loading. Once the gasket is drilled, it is mounted on top of the bottom anvil, if possible keeping the same orientation as when indented for better match with the anvil shape and better sealing. Then, it is time to start the loading of single-crystal, pressure medium and pressure gauge in the sample chamber.

Pressure transmitting media. The pressure transmitting medium (PTM) can be a soft solid, a liquid or a condensed gas. Under enough compression all of them eventually go solid, giving rise to anisotropic mechanical properties, i.e. strain inhomogeneity, pressure gradient and non-hydrostaticy. The ideal PTM needs to be soft enough to fully mould the shape of the sample chamber and to keep isotropic properties in a wide range of pressure/temperature conditions, which can be particularly challenging in the cryogenic regime.

Solid media such as NaCl, KCl or KBr present lower hydrostatic limit in comparison with liquid or condensed gases. However, they are widely used in laser heating experiments where thermal insulation from the anvils is needed. Mixtures of organic fluids such as 4:1 Methanol-Ethanol (ME), 16:3:1 Methanol-Ethanol-Water or 1:1 n-Pentane-isopentane present higher hydrostatic pressure limits at room temperature, 10.4, 14 and 7.5 GPa respectively [181, 182].

The group of condensed gases includes He, Ne, Ar or N_2. Gases are highly compressible, for this reason, they need to be loaded either pre-compressed using special equipment or condensed at low-temperature (cryo-loading). In order to

load pre-compressed gases, the cell slightly opened is introduced in a gas chamber perfectly sealed that is filled with the pressurized gas. Then, once the gas has diffused into the sample chamber, the cell is closed remotely using a gear box. The use of this equipment is particularly delicate due to the risk associated to the handling of a relatively large volume of compressed gas. In the case of the cryo-loading, the cell is immersed in the condensed gas at low temperature and closed remotely in the same way (membrane or gear box).

4:1 ME and Helium are the PTM most commonly used nowadays. 4:1 ME is a liquid in room conditions and is available in most of laboratories making it particularly easy to employ, whereas the principal benefit of helium is that it remains hydrostatic in a significantly large range of pressure at ambient temperature [117, 183]. At 5 K, both become solid at above 0.02 GPa of pressure and present similar in-homogeneity up to 20 GPa [184]. Thus, under cryogenic conditions, it is not clear that one presents superior hydrostatic properties over the other. Feng *et al.* also found that a large chamber-to-sample ratio ($\sim$ 100:1) is crucial in order to keep the quality of single-crystalline samples under pressure [184, 185]. Since 4:1 ME presents lower compressibility, the volume of the sample chamber remains bigger than for an equivalent loading made with helium and consequently, it might be a better media for HP-REXS experiments [11, 185–187].

A final consideration regarding the chemical inertness of the PTM needs to be done. Since the absorption cross section depends on the energy of the exciting radiation and the atomic number Z of the absorber as

$$\sigma_a \propto \left(\frac{1}{\varepsilon^3}\right)\left(Z^4\right) \tag{3.2}$$

for the range of energy employed in REXS, typically below 15 keV, the probability of an absorption process to happen is higher than in ordinary HP x-ray experiments typically conducted at higher energy. The absorbed radiation may produce the excitation of atoms heating the medium, inducing chemical changes, atomic displacements, etc. From our experimental experience, it is particularly crucial to attenuate the intensity of the beam in order to prevent photo-induced chemical reactions in the media. Fig. 3.25 shows some of the photo-induced chemical reactions observed in the sample chamber as a consequence of non-attenuated beam exposition.

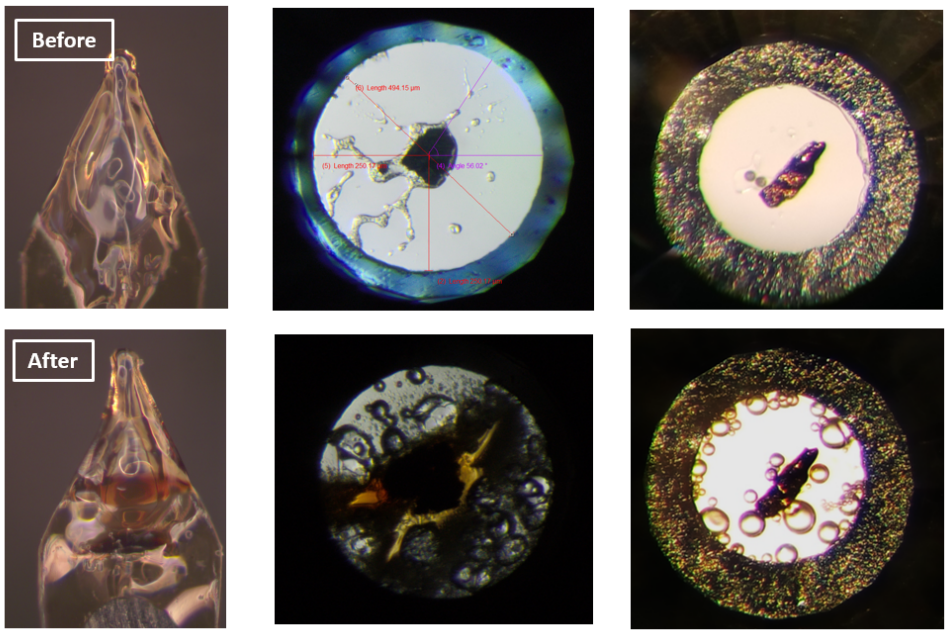

Figure 3.25 *Pictures of the photo-induced reactions observed in the different components of the pressure chamber after exposition to the x-ray radiation. From left to right, kapton pin impregnated in Vaseline, single-crystal of $AgNiO_2$ loaded with 4:1 ME as PTM, and crystal of $NaOsO_3$ loaded in the same conditions.*

Pressure gauge. Different methods are available for pressure measurement based on the dependency of a physical variable with pressure. Some examples of this are the shift of the luminescence bands of Ruby or Sm:YAG, the variations in resistivity of the Manganin alloy or the contraction of the lattice parameters of NaCl, Au, Ag or Pt upon applied pressure.

The shift of the luminescence bands R_1 and R_2 of Ruby upon compression is perhaps, the method most commonly used for experiments with DACs. Ruby, 0.5 wt% Cr^{3+} doped Al_2O_3, presents a robust corundum structure free of structural transitions up to 80 GPa [188]. The crystal field splitting of local Cr^{3+} energy levels generates electronic transitions from the doublet ^2E to the ground state $^4A_2$ that give rise to the luminescence bands R_1 and R_2 (see Fig. 3.26). The position of these lines presents a linear dependency with pressure up to 20 GPa, and more complex sub-linear relationship above that have been described by several authors [188]. Not only the position of the R lines is of interest as pressure manometer, but also the splitting and width of the bands are sensitive to the stress distribution and can be used as an indicator of the level of hydrostaticity.

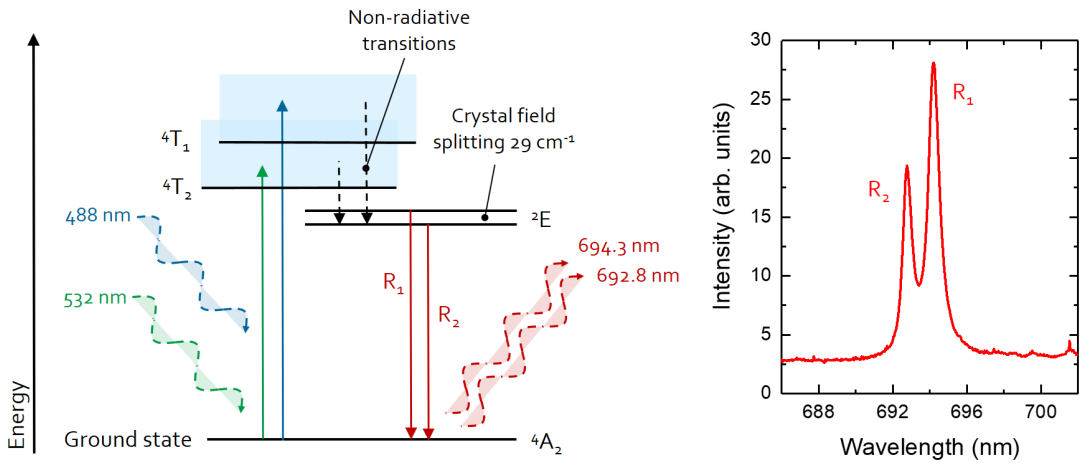

Figure 3.26 *Luminescence diagram of Ruby and fluorescence spectra of the R lines at ambient conditions.*

The position of these lines also varies with temperature. With decreasing temperature, the R-bands shift to higher energy, their widths decrease, and the R_2/R_1 intensity ratio decreases as well [189–191]. The interplay of these effects with pressure, despite it has been reviewed by several authors, is still poorly understood, specially at low temperature and for pressures above 15 GPa [184, 192–197]. Alternatively to Ruby, other optical sensors based on doped oxide garnets such as Sm:YAG or Sm:SrB_4O_7 seems to show larger temperature independence [191, 198].

A different calibration method based on the equation of state (EOS) of crystalline materials is particularly useful for experiments involving x-rays. The materials employed for this purpose are mostly ionic salts and metals such as Ag, Au, Pt or NaCl [199–201]. In the case of the ionic salts, they can play a double role as PTM and pressure gauge. By calculating the volume of the unit cell out of the diffraction pattern of the standard, the EOS of the material can be used as pressure gauge. This method is preferred over the ruby fluorescence scale for pressures above 50 GPa, where the first seems to underestimate the value of pressure [200]. However, a correction has been proposed based on this finding by Dewaele *et al.* [200] that extends the range of accuracy of the ruby scale up to 100 GPa. Above this value, the fluorescence lines becomes weak and alternative methods are required.

For experiments where optical access is not possible and no x-rays are involved, other parameters as the significant increase of the electrical resistivity of a

Manganin coil upon increasing pressure can be used as gauge [202, 203]. This secondary pressure scale is widely used nowadays in dynamic compression experiments in order to track continuously the evolution of pressure during the period of action of the shock-wave.

3.4 High-pressure experimental setups

Two different high-pressure setups were used in the experiments conducted in this thesis. The first one is the m-RXS DAC described in detail in Chapter 4, which present an asymmetric design for operation in back-scattering geometry and an opening angle of 100 degrees. This cell is membrane-driven and can be coupled with a 4K-close cycle refrigerator (CCR) reaching a minimum temperature of $\sim$ 30 K and maximum pressure of 20 GPa when fitted with diamond anvils of 500 μm culet.

The second setup consists in a Russian alloy (CrNiAl) version of the miniature turn-buckle cell by Jin *et al.* [157]. This cell is approximately 9 mm $\times$ 7 mm (diameter and height) and presents symmetric apertures of 80 degrees. It can be coupled with a nitrogen 700 series cryo-stream cooler from Oxford-Cryosystems [204] for temperature regulation between 100 and 400 K. In Fig. 3.27, it can be seen a picture of the cell and the cryo-jet mounted on the diffractometer in one of the experiments conducted on I16.

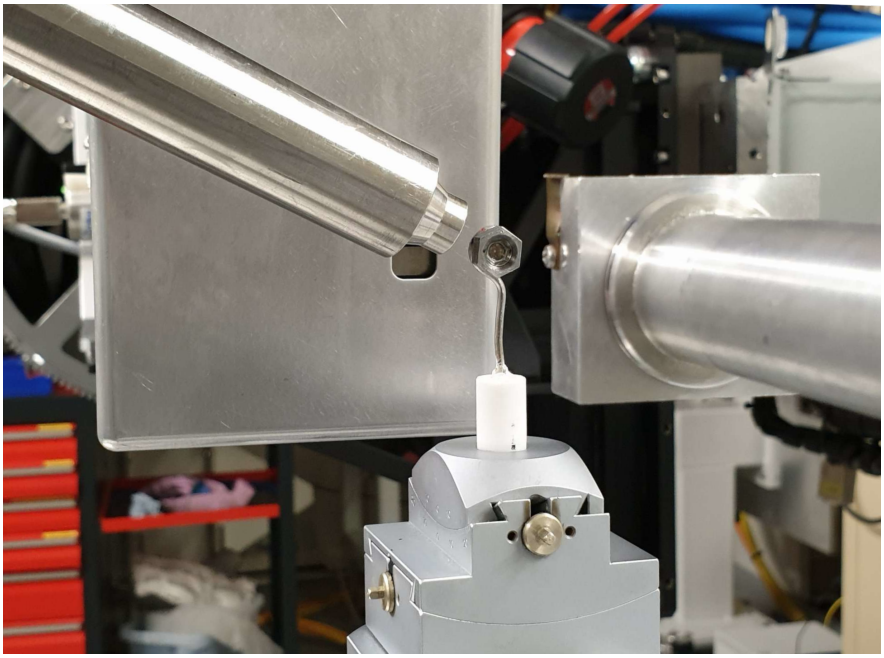

Figure 3.27 *Image of the TB-DAC mounted on the goniometric head on I16. Incoming x-rays approach the cell through the pipe on the right and scattered light is measured at the detector behind in transmission geometry. On the back of the cell, is the set of slits situated at the detector entrance (square metallic device). On the top-left corner is the nozzle of the cryo-stream cooler.*

Chapter 4

Design of Diamond Anvil Cells for HP-REXS Experiments

Contents

This chapter presents the design of a HP setup for REXS experiments that comprises a membrane-driven diamond anvil cell, a panoramic dome and an optical system, which enables the measurement of pressure *in situ* under cryogenic conditions. The proposed setup allows performing HP-REXS experiments in back-scattering configuration up to moderate pressures of $\sim$ 20 GPa and temperatures as low as 30 K. It is especially designed to get coupled with the cold finger of a 4K-CCR (close-cycle refrigerator) unit and to be operated remotely by pressurising helium gas into a thin metallic membrane. In the first section of this chapter, the different factors considered for the design of the HP-REXS setup will be discussed, prior the description of the final design and the evolution of the different prototypes considered during the designing process. All the computer aided design (CAD) drawings shown in this thesis have been generated using the Solid Edge CAD software from Siemens [205].

4.1 Design motivation

As pointed out throughout this thesis, the powerful combination of spectroscopic information via the access to the specific projection of the electronic density of states, and crystallographic capability via the sensitivity to periodic arrangements of electrons and magnetic moments in crystalline materials, provides a unique source of information that has proven invaluable in understanding many complex electronic phenomena. The introduction of pressure opens a new athermal route to explore exotic electronic behaviours as quantum criticality, which otherwise would only be accessible by chemical doping or applied external magnetic field. Moreover, it represents an additional thermodynamic dimension to explore the phase diagram of different materials. Despite the promise of a fertile field of research, the lack of commercial instrumentation able to fulfil the experimental demands of HP-REXS experiments results in a rather small number of HP-REXS studies published in the literature [11–13, 186]. The following section will start discussing the main sources of complexity for the conduction of HP-REXS experiments.

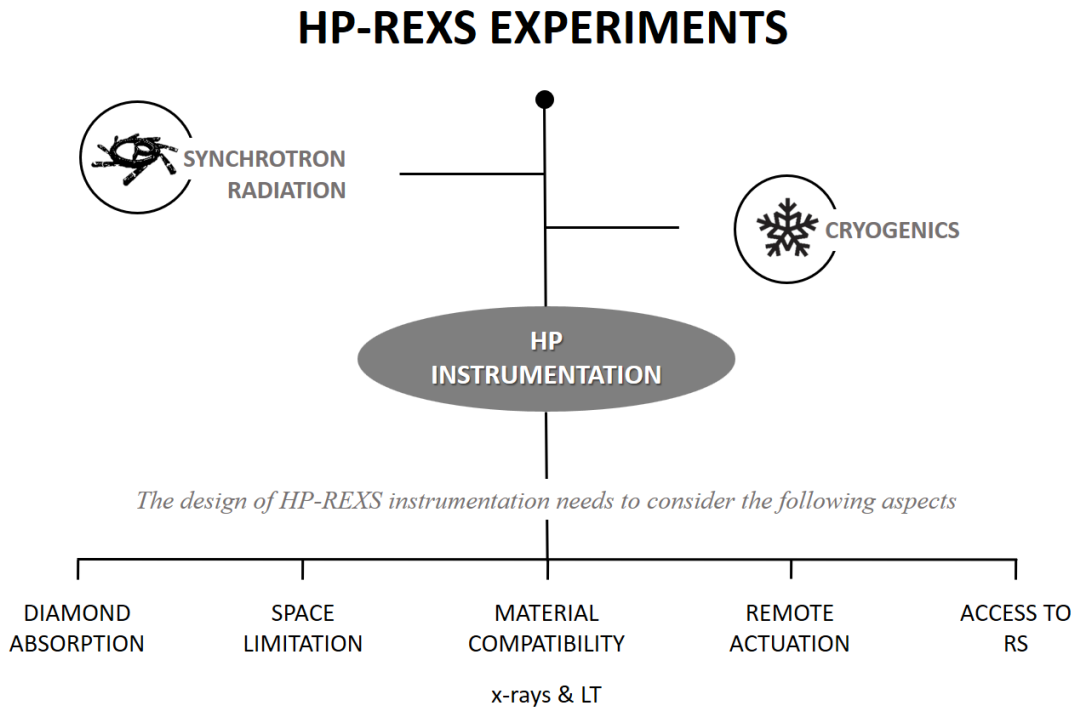

Figure 4.1 *Flowchart highlighting the main aspects considered in the design of HP-REXS instrumentation: diamond absorption, space limitation, material compatibility (x-ray interaction/low-temperature performance), remote actuation and access to the reciprocal space (RS).*

4.1.1 Experimental enviroment and demands for HP-REXS experiments

The realisation of HP-REXS experiments requires the synergic cooperation of three elements: synchrotron radiation, high-pressure instrumentation and cryogenic conditions. Figure 4.1, summarises the different aspects to be considered in the design of HP devices for REXS experiments that will be explained in detail in the following lines.

As mentioned earlier in Chapter 2, the scattering-cross section arising from a periodic correlation of electrons is several orders of magnitude weaker than the correspondent for ordinary Thomson scattering. Only with the advent of second- and third-generation synchrotron radiation sources that provide higher flux of photons, did the study of correlated materials by REXS became possible [20, 76–78, 80, 206]. In a REXS experiment the energy of the incident beam is dictated by the elementary absorption edge that allows probing electronic levels in the proximity to the Fermi surface. Typical values of excitation energy are 3 - 15

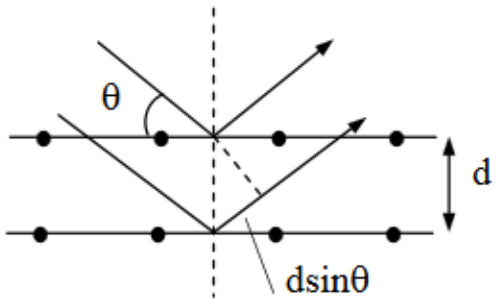

Figure 4.2 *Bragg diffraction. Two beams with identical wavelength and phase approach a crystalline solid and are scattered off two different atoms within it. The lower beam traverses an extra length of* $2d\sin\theta$*. Constructive interference occurs when this length is equal to an integer multiple of the wavelength of the radiation (n).*

keV, where the absorption edges of elements such as Ru (L_2 2.97 keV), Fe (K 7.11 keV), Ni (K 8.33 keV), Os (L_1 12.97 keV, L_2 12.38 keV) or Ir (L_2 12.84 keV, L_3 10.87 keV) lie. Within these limits, the transmission through diamond anvils of standard thickness becomes critical for excitation energies below 9 keV (see Fig. 3.19). Thus, the observation of resonant reflections below this energy value is restricted under high-pressure.

Additionally, the energy of the incoming beam is not only important from the absorption point of view, it also plays an important role in determining the portion of the reciprocal space (RS) accessible in the DAC. Bragg's law establishes the conditions for a set of crystalline planes to diffract as follows:

$$2d\sin\theta = n\lambda. \tag{4.1}$$

The path difference between x-rays interacting with successive crystallographic planes $2d\sin\theta$ (see Figure 4.2), where d is the distance in the reciprocal space between consecutive lattice planes and θ is the Bragg angle, must be an integer number (n) of wavelengths (λ) for the x-rays to interact at the strongest constructive interference.

Thus, it is possible to establish a relationship between the d-spacing and the excitation energy of the radiation:

$$d = \frac{n\lambda}{2\sin\theta} \tag{4.2}$$

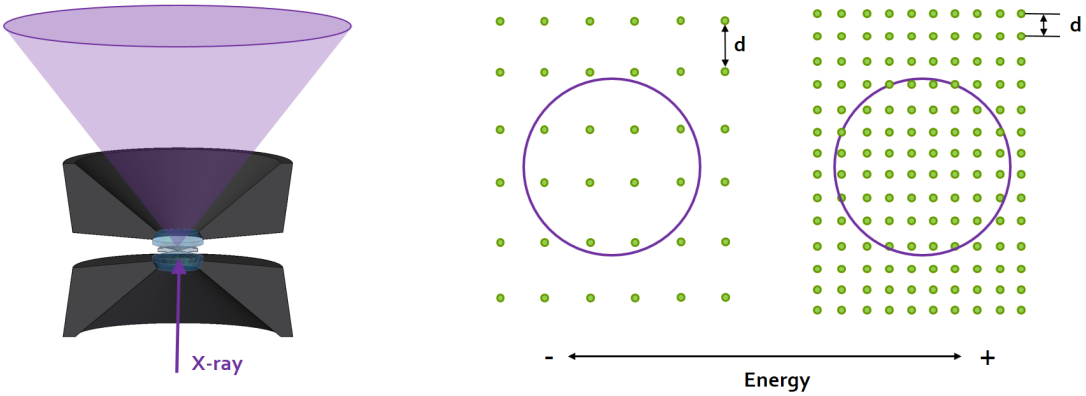

Figure 4.3 *Energy and d-spacing dependency in x-ray diffraction experiments. According to Bragg's law (Eq. 4.1), the higher the energy, the smaller the d-spacing and the larger is the portion of the reciprocal space accessible.*

$$E = h\nu = \frac{hc}{\lambda} \quad \Rightarrow \quad \lambda(\text{Å}) = \frac{12.4}{E(keV)} \tag{4.3}$$

$$d \times \left(\frac{1}{E}\right). \tag{4.4}$$

By substituting λ from Eq. 4.3 in Eq. 4.2, one can see that the magnitude of the d-spacing is in inverse proportion to the energy and therefore, the lower the energy the larger is the d-spacing, and smaller is the portion of the RS that fits in the solid angle defined by the cell body. Figure 4.3 illustrates this phenomenon. Therefore, a compromise needs to be reached to maximise the opening angle without jeopardising the mechanical strength of the DAC.

Leaving aside the excitation energy and the access to the RS, the third element to consider when designing HP-REXS instrumentation is the frequent demand of cryogenic conditions. In many cases, the energy scale of the interactions that govern electronic ordering phenomena, lies within the range of tens of meV. By using the correspondence between energy and temperature $E = K_B T$, one can see that 1 K = 0.0862 meV and therefore, room temperature conditions are usually enough to break these weak to moderate electronic interactions via thermal fluctuations. Very often, it is necessary the use cryogenic equipment in order to study these phenomena, which implies additional space restrictions and the need of mechanisms for remote actuation in order to operate the instrument at low-temperature. From this point of view, it is also very important to minimize

the mass of the instrumentation inside the cryogenic device as much as possible, in order to reduce the thermal inertia and the time required to reach the thermal equilibrium. Ideally, the bulk of the pressure device should be machined in a material that presents high thermal conductivity and low thermal expansion, while keeping good mechanical properties at low temperature. Finally, the possibility of tuning pressure *in situ* saves considerable time, allowing one to maximise the collection of data during the experiment. This key aspect is highly desirable for experiments conducted in large facilities as synchrotrons where beamtime allocation is precious.

4.1.2 Material selection

One of the main difficulties in the design of high-pressure and low-temperature instrumentation is the selection of the construction material. Most metals and alloys typically employed for machining high-pressure devices become brittle under cryogenic conditions [171, 207]. Thermo-mechanical properties such as the tensile strength or the degree of plasticity at low temperature become critical. Additionally, other thermal parameters such as thermal diffusivity or thermal contraction must be considered carefully to ensure the suitable operation and achievement of the target experimental conditions. For example, unforeseen contraction (or expansion) of a material when cooling, could end in the obstruction of the moving parts of the instrument and unwanted pressure gradients. Likewise, the use of materials with low thermal conductivity may affect drastically the time needed for reaching the thermal equilibrium at the sample stage.

One can find in the literature a number of materials employed in the construction of high-pressure cells for low-temperature studies: BeCu [18, 145, 146, 159, 208], 316L steel [157], 52RC Maragin Steel [149], silicon aluminium bronze C64200 [11, 185], Vascomax 360 [155], MP35N Ni-alloy [209, 210] or CrNiAl (Russian alloy) [171, 211] among others. In table 4.1 are listed the values of the mechanical and thermal properties of some of these materials.

Cooper-Beryllium (CuBe) is perhaps, the most popular alloy employed for HP-LT instrumentation. In particular, the alloy containing 2% of beryllium intercalated in the fcc crystalline lattice of cooper, presents exceptional mechanical properties that can rival with high-tensile steels. It is easy to machine and commercially

Table 4.1 *Mechanical and thermal properties of different materials employed in the design of HP-LT instrumentation. Chemical composition, ultimate tensile strength (UTS), coefficient of thermal expansion (CTE) and thermal conductivity coefficient (λ). Magnitudes measured at room temperature (295 K) unless specified. Data from [171, 178, 212–215].*

Material	Chemical Composition	UTS (GPa)	CTE ($\mu m/m^oC$)	λ ($W/m.K$)
Steel 316L UNS S31603	Fe (61-72%) Cr (16-18%) Ni (10-14%) Mo (2-3%)	0.55	15 - 18	13 - 17
Russian Alloy CrNiAl	Cr (40%) Al (5.5%) Ni (BAL)	2.35 (at 295 K)	-	-
Co-Ni Alloy MP35N	Ni (35%) Co (35%) Cr (20%) Mo (10%)	1.60 - 1.90 (at 295 K) 2.00 - 2.50 (at 77 K)	12.8 (range 21 - 93 ^oC)	11.2 (at 295 K) 6.5 (at 100 K)
Berylco 25 BeCu-25	Cu (> 99.5%) Be (1.8-2.0%) Co (< 0.3%) Co+Ni+Fe (< 0.6%)	1.3 (at 295 K) 1.5 (at 20 K)	17.3 (range 20 - 200 ^oC)	80 - 130 (at 295 K)
Si-Al Bronze C64200	Cu (91%) Al (7%) Si (2%)	0.6 - 0.7 (at 295 K)	45 (at 200 ^oC)	18 (at 295 K)

available in different degrees of hardening reached through thermal-treatment [216, 217]. It presents an exceptional mechanical behaviour at low-temperature, increasing its plasticity and tensile strength in a 15% at 20 K over the corresponding values at ambient temperature [171, 216]. This, together with outstanding thermal properties, low coefficient of thermal expansion (CTE) and good thermal diffusivity, makes it ideal for HP-LT applications.

Other materials, also used in the manufacturing of pressure devices for cryogenic conditions, are the alloys MP35N and CrNiAl - Russian alloy (40HNU-VI), both showing higher values of tensile strength than BeCu at LT. These are particularly tough alloys providing exceptional mechanical stability under compression. However, from the thermal point of view, MP35N presents a considerably lower thermal conductivity coefficient (λ) that would result in longer cooling rates and larger temperature gradients. For the case of the Russian alloy, little quantitative information is officially published about its thermal behaviour. Nevertheless, it has been extensively used in the fabrication of HP-LT devices in the former Soviet Union and different notes in the literature evidence its positive performance [171, 207, 210, 215]. Our personal experience using a CrNiAl version of the miniature-DAC designed by Jin *et al.* [157] also supports this thesis. Unfortunately, this alloy is difficult to obtain and it is only commercially available in small amounts.

Finally, it is important to mention that the chemical composition of the material

employed must also be considered to avoid unforeseen interactions with the probe employed. In principle, the small spot and the low divergence of the x-ray beam in 3rd generation synchrotron facilities will be enough to avoid cutting the cell body. In this sense, unlike in neutron experiments where the beam can be barely focused, the chemical composition of the cell parts is not as decisive (a different scenario occurs when choosing the gasket material as we discussed previously in Section 3.3).

4.2 m-RXS diamond anvil cell

4.2.1 Design concept

The whole setup proposed here is designed for use with the instrumentation currently available on I16, in particular a 4 K closed-cycle refrigerator (D-202N) mounted on a Newport 6-circle kappa goniometer (see Section 2.3 and appendix E for further details). Keeping in mind the geometrical constraints arising from the limited space available inside the cryostat and the position (height) of the centre of rotation, the setup proposed here consists in a membrane-driven DAC (in the following m-RXS), a panoramic dome and an optical system that allows the measurement of pressure *in situ* under cryogenic conditions.

The m-RXS DAC is inspired by the Merrill-Basset idea [131] with three pins for alignment and three screws as the locking mechanism. In Figure 4.4, we can see cross-sectional and exploded views of the CAD model numbering the different parts of the cell. Despite the instrumentation developed during this project is based solely on the generation of high-pressure conditions, the application of an external magnetic field concurrently with high-pressure could be also attractive for future experiments. For this reason, only non-magnetic materials such as CuBe, MP35N or the Russian alloy (CrNiAl) were finally considered for building the cell. Based on the discussion held in the previous section, the material chosen was the CuBe alloy BERYLCO-25® manufactured by NGK-Berylco France [216]. Upper and lower body, piston and cryostat holder, parts 10, 3, 6 and 2 respectively from Figure 4.4, are machined in this material.

This cell presents an asymmetric design, with a panoramic aperture of 100 degrees in the top part and a bottom half dedicated to the regulation and measurement of

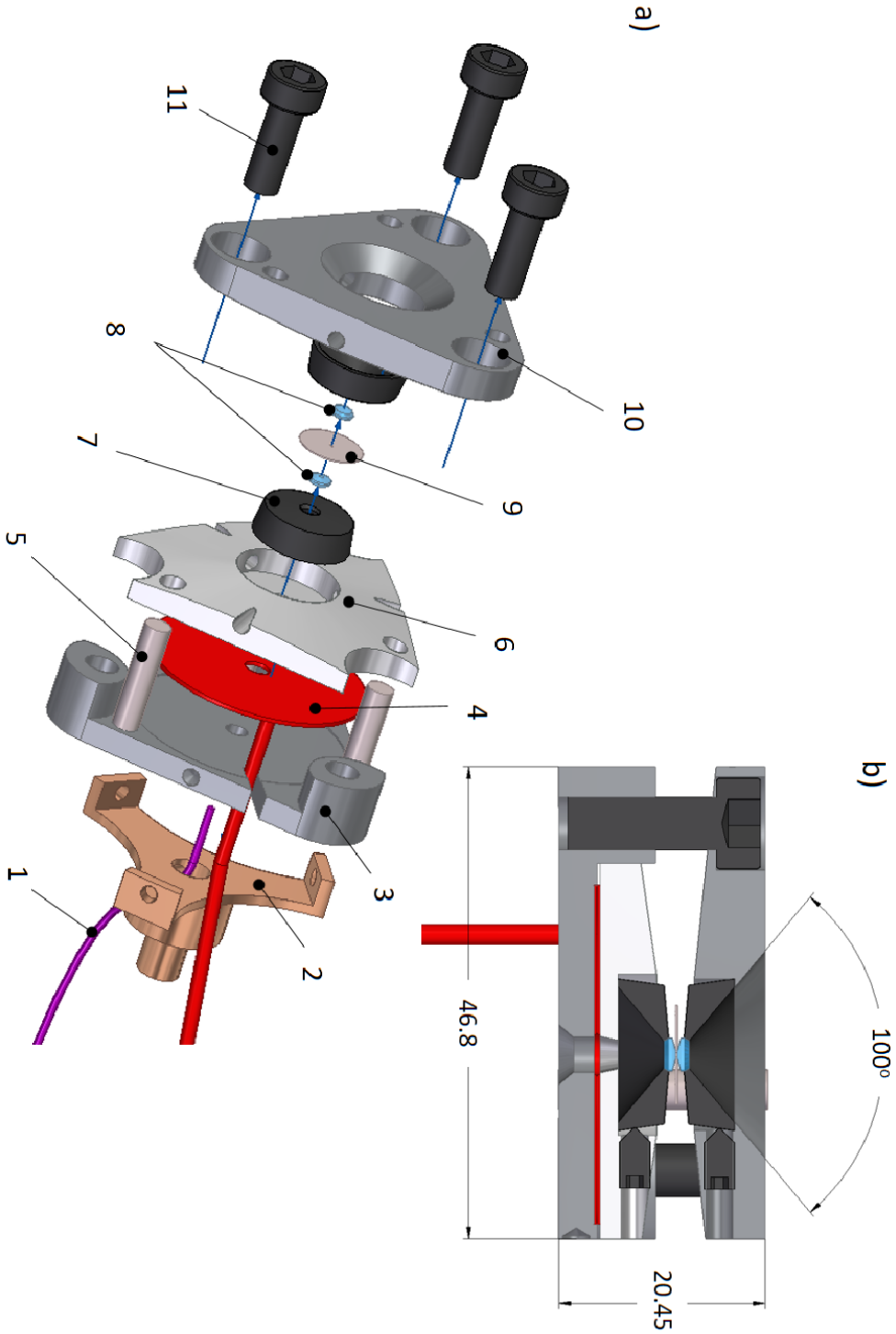

Figure 4.4 *a) Exploded view of the CAD model of the m-RXS cell. (1) Fiber optic, (2) Cryostat adapter, (3) Lower-body, (4) gas-membrane, (5) alignment pin, (6) piston, (7) tungsten carbide seats, (8) diamond anvils, (9) gasket, (10) Upper-body and (11) M5 locking screws. b) Section view of the cell with key dimensions in mm (opening angle in degrees).*

pressure. Unlike the original Merrill-Basset cell, where the force is generated by tightening the locking screws (11 in Figure 4.4), our cell relies on an alternative mechanism to produce pressure. When helium gas is introduced in the membrane (4), the collision between the molecules confined in it exerts a force that elastically deflects its walls. This deflection is enough to produce a sizeable movement of the piston (6) that pushes the lower anvil against the upper one (fixed) and results in the compression of the sample cavity. The gas-membrane is hosted within the bottom half of the cell body avoiding the use of any additional fastening mechanism that would increase the overall thickness of the cell. When assembled, the cell is approximately 20 - 21 mm high, with an external diameter of 57 mm (circumference tangential to the triangular profile). This last dimension is largely imposed by the area required by the membrane to reach the target pressure in the sample chamber.

In order to obtain a rough estimation for the membrane size in the first prototype of the cell, the relation between pressure (P), force (F) and area (A) $P = F/A$ was considered for a target pressure of 16 GPa at the anvils, 120 bar of pressure for the gas in the membrane (36% below the safe limit of the gas controller, 190 bar) and oversized culets of 900 microns (12% larger than the largest anvils considered for the real experiments) to compensate for the loss of force due to the friction between the different parts of the cell body. In this way, we obtained the corresponding area of the membrane and optimised the value of the external diameter (33.5 mm) and the central aperture (4 mm). Using these dimensions, a set of membranes was built by welding together the edges of two circular stainless steel foils 200 μm thick, and attaching a metallic capillary (1 mm outer diameter) to one of the faces. The pristine membranes present a thickness $\sim$ 0.45 mm which after use, increases to 0.5 - 0.7 mm. This design is similar to the American style of double-sided diaphragms [144, 218].

In order to assess the safe pressure limit of the membranes, a controlled burst test was conducted and found a failure pressure value of 850 bar, more than 600 bar over the maximum working pressure employed during our experiments.

Moving now onto the scattering geometry two options were considered, both of them with the scattering plane crossing through the diamond anvils. For the first one, known as reflection or back-scattering geometry, the scattered x-rays are collected through the same side of the cell through which the incident beam hits the sample (see Fig. 4.5 left). For the second one, so called transmission or Laue

geometry, the diffracted light is collected from the side opposite to the exciting beam (Fig. 4.5 right). Both configurations present drawbacks and positive points.

In Bragg geometry, it is possible to use thicker samples than in transmission, since the re-absorption of the scattered light by the sample in reflection is less severe. Thicker samples are also easier to prepare and handle. However, in back-scattering the alignment of the crystal in the centre of rotation of the diffractometer is more challenging than in transmission geometry. The drop in the diffuse scattering from diamond when mapping the sample cavity with the x-ray beam is not as well defined as in Laue configuration (precise details on the alignment procedure are given in Section 4.2.2). A different point to consider is the fact that back-scattering configuration leaves free the bottom face of the cell, which can be employed for hosting the optics needed for the pressure measurement using the ruby fluorescence method [114]. In transmission geometry, these optics need to be mechanically positioned in-and-out the beam path each time the pressure is measured.

However, the decisive factor that conditioned the final choice in this case was the small space available between the top of the cold-finger head in the cryostat and the centre of rotation of the diffractometer. Given the membrane size required to achieve the target pressure, only back-scattering configuration was found to be suitable in order to keep the design as compact as possible. In transmission geometry a larger central aperture in the membrane is needed to maximise the scattering angle and therefore, a larger external diameter to maintain the same membrane area. This would displace the sample position up in the vertical direction above the centre of rotation. See the diagram in Figure 4.5 for clarity. For this reason, a back-scattering configuration was preferred. Additionally, the number of diffraction peaks accessible in backscattering is significantly larger than in transmission geometry, given the absence of effective form factor in resonant conditions and the larger density of reflections at high angle (2θ).

Then, an optical system was developed to measure the pressure level *in situ* using the fluorescence of ruby as gauge [114]. It can be divided in two sections. In the external part of the cryostat, a bifurcated fibre from Ocean-Optics made out of six individual Lab-grade cores 300 μm in diameter 2.5 m long, assembled in two legs (5+1). The three ends of the bifurcated fibre are connected through SMA connectors to a 532 nm diode laser, a portable spectrometer from Ocean Optics (MayaPro4000) and a single core fibre inside the cryostat. The latter is a

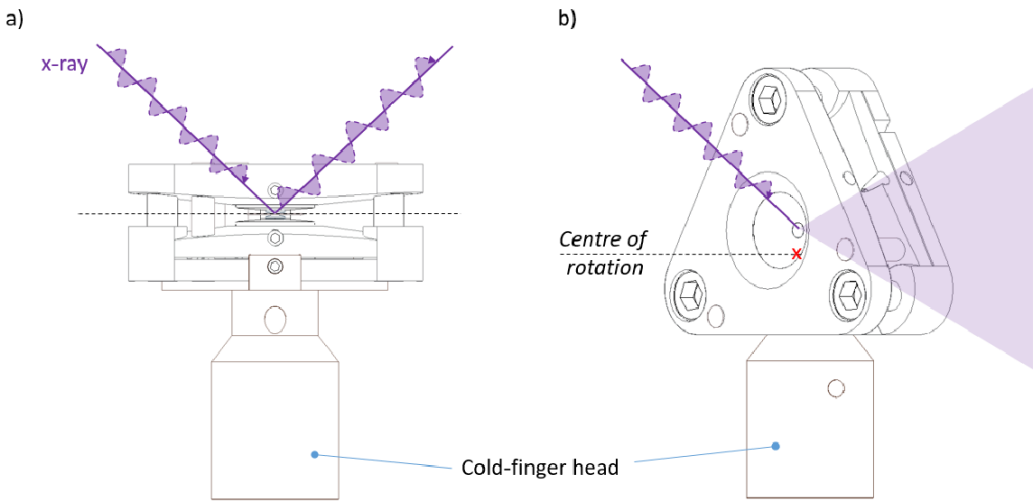

Figure 4.5 *Schematic view of the two experimental scattering geometries considered for the HP-REXS experiments: a) Reflection or back-scattering and b) transmission or Laue geometry.*

continuous bare fibre 1 mm thick, whose inner end in the proximity of the sample chamber is fitting-free and manually polished.

A number of alternative models for the optical setup including additional mirrors and collimation lenses were tested. However, the loss of light due to the transfer between different optical elements was found to be larger than for the system just described above. A brief discussion on the alternatives considered is held in Section 4.3.

In addition to the pressure cell and the optical system, a panoramic dome has been designed specifically for the HP-REXS experiments using the CCR unit. The dome is machined from steel 304L, it presents a cylindrical structure divided in three sections with a total height of 27.3 cm over the base of the cryostat and 10.2 cm in diameter. The possibility of assembling the dome in three separate parts, allows easily replacing its top section to accommodate different experimental geometries. In Figure 4.7 can be seen a CAD model with some of the main features of the design.

In this first version, the upper section of the dome is specifically designed for experiments in back-scattering with three Kapton windows: a panoramic aperture at the top for the scattering of the x-rays and two lateral windows for optical access. Kapton and beryllium are the only reliable materials employed for

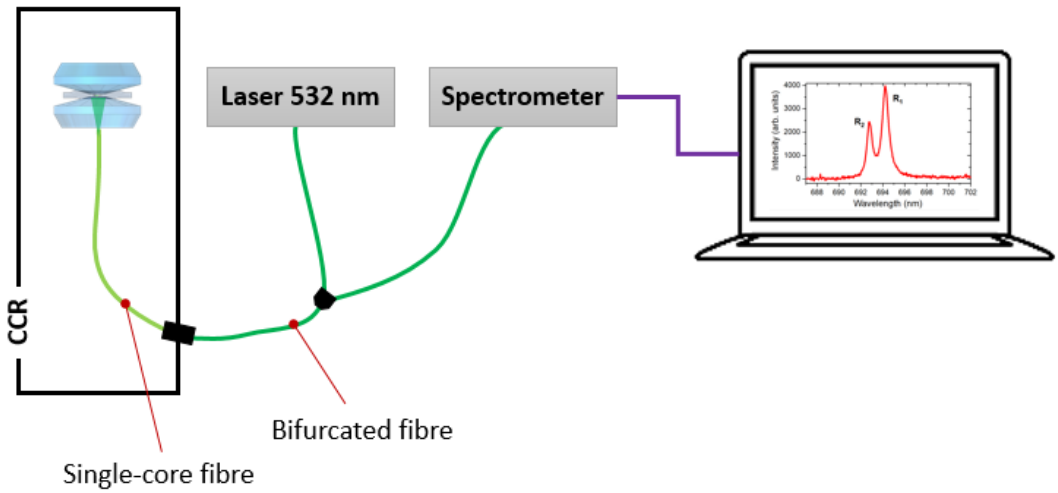

Figure 4.6 *Schematic view of the optical system designed for measurement of the pressure level in HP-REXS experiments using the membrane-DAC. This system consists in a single-single core fibre inside the cryostat and a bifurcated fibr outside that connects the former one with a 532 nm laser and a Maya-4000Pro spectrometer.*

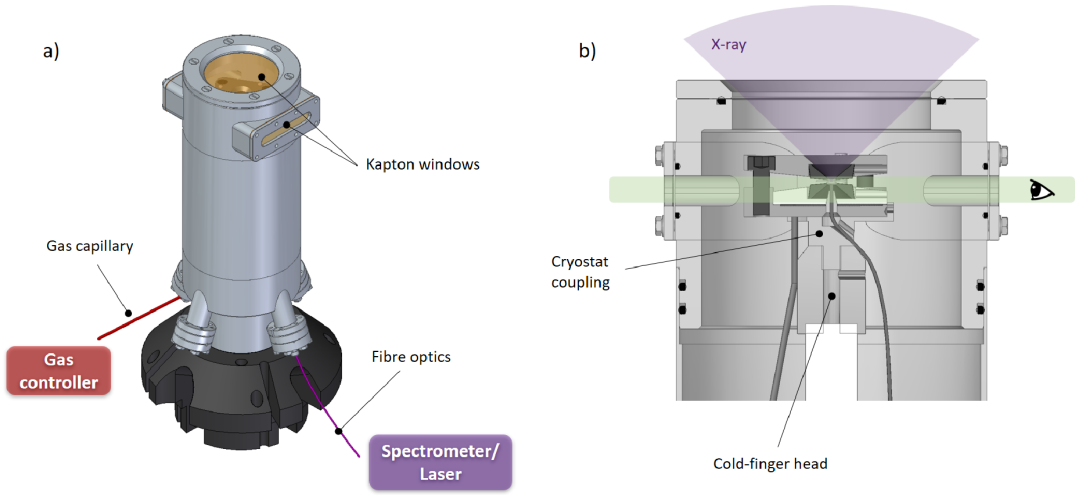

Figure 4.7 *CAD model of a) the cryostat dome with detail of the feed-throughs dedicated to the gas capillary and the fibre optics and the different optical windows. b) Section view with details of the interior of the cryostat in the proximity of the pressure cell. Shaded areas represent the scattering angle at the top and lateral optical access at the bottom.*

windows in x-ray cryogenic devices due to the their low absorption. Kapton was chosen for this first version, since is cheaper than beryllium and allows visual examination of the cell while showing a reasonable durability and transmission above 7 keV.

The lower section of the dome presents four fitting ports, two of them dedicated to the insertion of the gas capillary and the fibre optics. In order to prevent big oscillations of temperature when pumping gas into the membrane, the gas capillary is attached to the first stage of the cryostat so the gas is pre-cooled before reaching the cell body. In Figure 4.8, it can be seen a picture of the real dome, cell and optical system mounted on the diffractometer on I16. Further details of the dimensions an morphology of the different parts that comprise this setup can be seen in the technical drawings provided in appendixes A and E.

4.2.2 Operation

After the loading is completed, the cell can be mounted on the cryostat and aligned in the centre of rotation of the diffractometer. In a first approximation, while the cryostat is open as in Fig. 4.8 b), the sample position is optically adjusted using a set of video-cameras located in the experimental hutch. Then, using the x-ray beam, the gasket hole is scanned along the 3 directions of the space x, y and z, looking for a drop in the diffuse scattering from diamond due to the presence of the sample. In order to look along the z axis (see the system of coordinates in Figure 4.8 c)), assuming the sample is flat and parallel to the diamond tips, the cell is rotated $\pm$ 5 degrees around an axis normal to z. Then, with the sample tilted, a scan along the z axis reveals the position of maximum absorption, which must be corrected to coincide with the centre of rotation.

Thus, once the sample is centred, it is time to start searching for diffraction peaks by scanning in reciprocal space. The correct identification of a couple of reflections with their (hkl)-index is enough to build the orientation matrix, which allows navigating in reciprocal space and reaching the position of interest. The success of REXS experiments relies strongly on the crystalline quality of the single-crystals. The spatial resolution achieved in a synchrotron source is significantly superior than in an ordinary x-ray lab unit and the observation of additional weak reflections arising from secondary grains can be deceptive when trying to find the correct orientation matrix. It is highly recommended to pre-

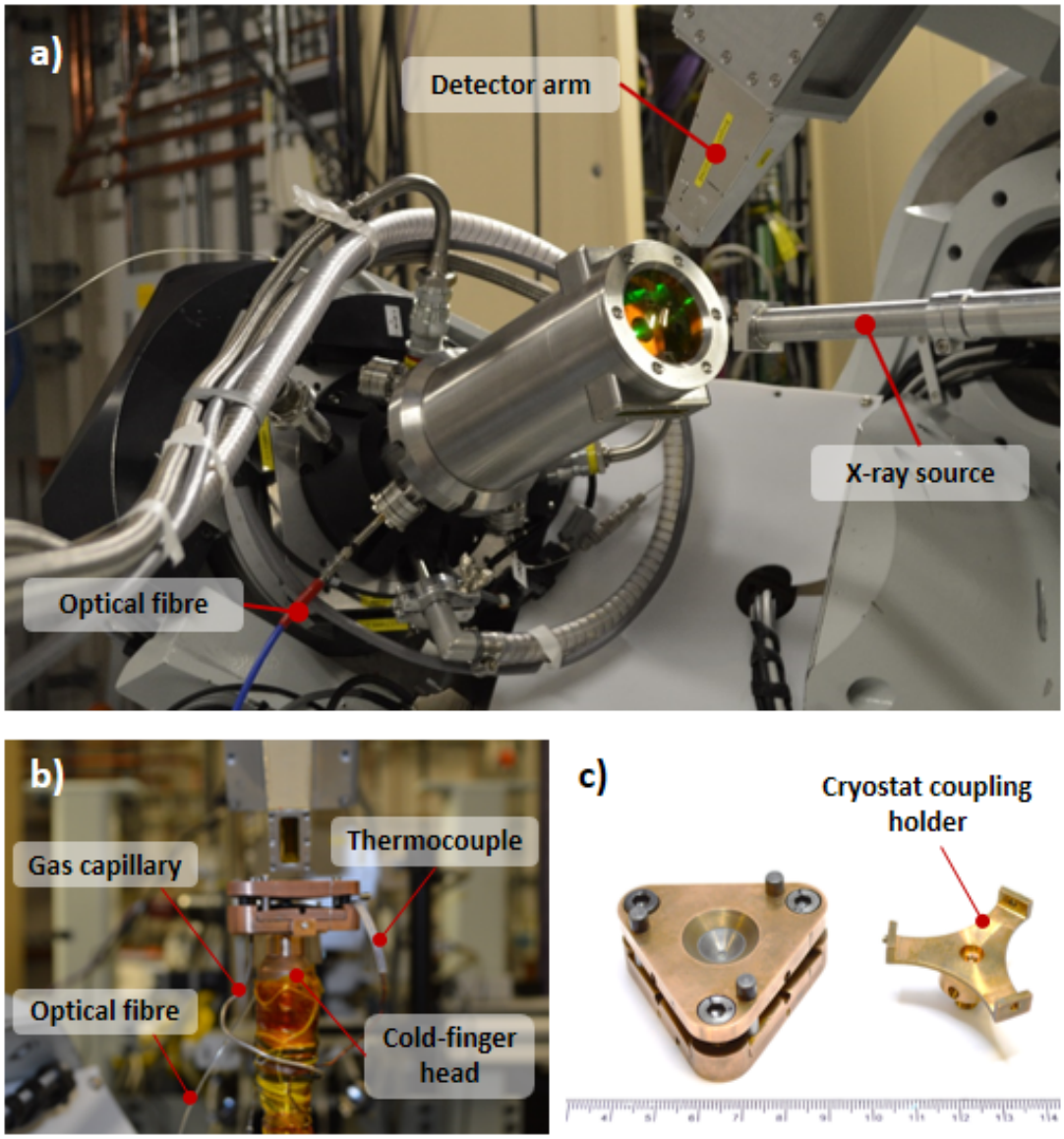

Figure 4.8 *Pictures of the setup for HP-RXS experiments. a) Pressure cell mounted on the cold finger. Detail of the thermo-couple, optical fibre, gas capillary and cold-finger head. b) Pressure cell and cryostat coupling piece. c) HP-RXS setup on I16. Detail of the x-ray source, optical fibre and detector.*

screen the crystals in a lab x-ray diffractometer to select the ones with better quality and to have an estimation of the crystalline orientation. Samples showing well-defined symmetric sharp peaks and low values of mosaicity are preferred.

After aligning the sample and finding the correct UB-matrix at ambient temperature, the cryostat is closed and the system is cooled down to the base temperature. During the cooling process, the height of the sample changes due to the thermal contraction of the different parts of the cryostat. This height variation is reproducible, so it is possible to estimate a correction based on the temperature measured at the sample-stage. In order to produce a reliable temperature variation throughout the whole experiment, the cryostat is held constantly at the base temperature while the sample stage is thermalised using a local heater. Therefore, even for the cases where particularly low temperature is not required, initially, the system needs to be cooled to base temperature to start the experiment.

Once the target temperature is reached at the sample position, a final fine alignment is conducted repeating the x, y, z scans described above around the peak of interest maximising its intensity.

In situ pressure regulation can be achieved by pumping helium gas into the membrane using a GE Druck PACE5000 unit. Temperature values above 50 K need to be reached in order to actuate the membrane. Below this value, the presence of impurities within the gas capillary may block the flow of helium. In the future, a mechanism for vacuum pumping the gas circuit prior to the connection to the helium cylinder, may allow the adjustment of pressure with no temperature limitation. Nevertheless, the present pumping mechanism ensures pressure regulation *in situ* and quick realignment in comparison with other methods, since the sample position is only slightly different after the pressure change.

4.2.3 Characterization tests

Different characterization tests were conducted in order to assess working parameters of the system such as the minimum temperature of operation, the maximum pressure reachable, or the method employed for pressure measurement.

Due to the limited space inside the cryostat the CCR is operated without any sort

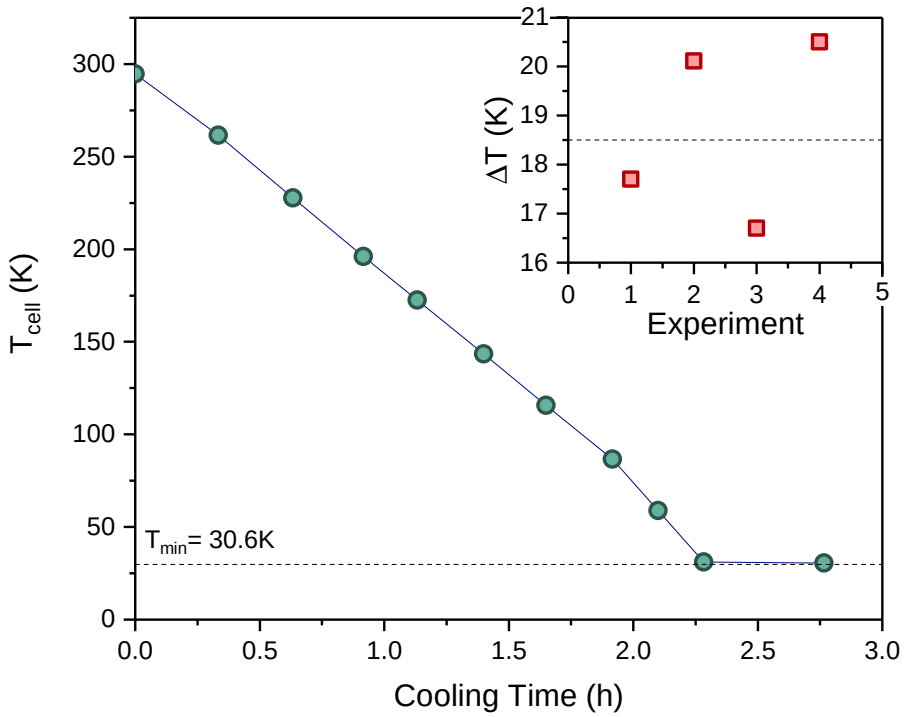

Figure 4.9 *Cooling time of the m-RXS cell mounted inside the cryostat from ambient to base temperature. Dashed line stands for the minimum temperature reached. Inset shows the temperature difference between the top of the cold finger and the cell body for different experiments. Dashed line in the inset for the average value of the temperature variation.*

of thermal shielding but the actual walls of the dome. This limits the minimum temperature reachable to 30.5 K, with an approximate cooling time of 2.5 hours (see Figure 4.9). The higher value of base temperature with respect to the regular 6 K reached in ordinary ambient pressure experiments, is partly due to the absence of shielding but also the increase of mass inside the cryostat and the presence of the large kapton windows. A temperature gradient is observed between the head of the cold finger and the cell body (see inset in Fig. 4.9).

In order to evaluate the maximum pressure that can be reached using this system, two pressure tests were performed using thin anvils with culets of 500 microns (see appendix B), 4:1 Methanol-Ethanol as pressure transmitting media and a steel gasket (initially 200 μm thick) pre-indented down to 107 μm of thickness. The cell was loaded with Ruby at an initial pressure of 1 GPa and mounted on the cryostat. Then, temperature was first stabilised at 74 K and pressure

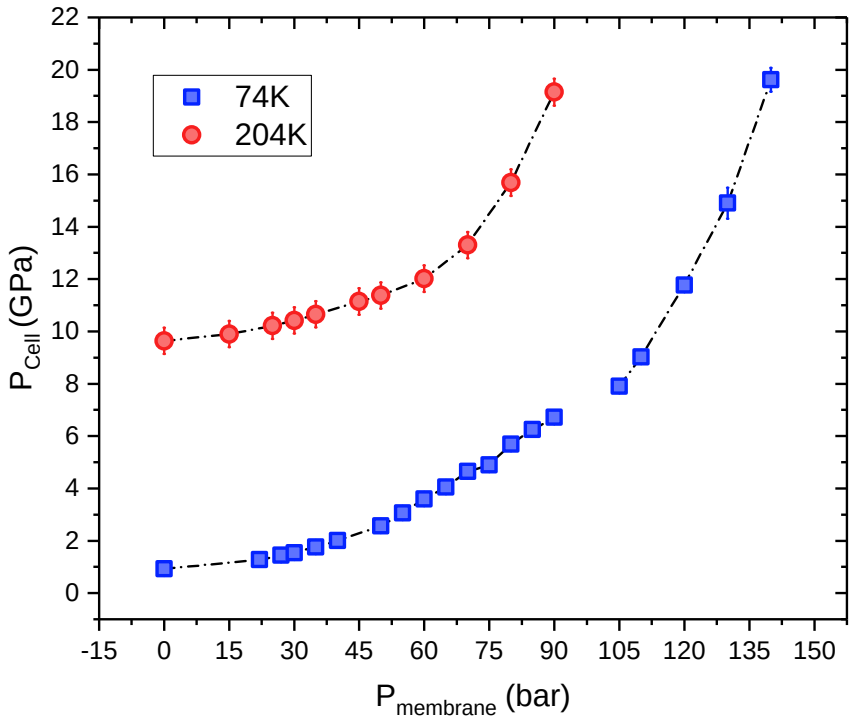

Figure 4.10 *Results of the pressure test performed at 74 K and 204 K with blue squares and red dots respectively. Pressure in the cell in GPa as a function of the pressure in the membrane in bars. The first determined using the ruby fluorescence technique, the second regulated using a GE Druck PACE5000 gas controller. The cell was prepared using 4:1 Methanol-Ethanol as pressure transmitting media and it was closed initially at 1 GPa. The test was done in first place at 74 K reaching maximum pressure close to 20 GPa. Then the pressure in the membrane was released and the test was repeated at 204 K.*

was increased reaching a maximum value close to 20 GPa measured by the ruby fluorescence method and corrected to the actual temperature. After that, the pressure in the membrane was released and the test was repeated at 204 K.

In Figure 4.10, we can see the evolution of the level of pressure in the cell against the pressure in the membrane at these two different temperatures. In both cases, we found a deterioration of the ruby signal (broadening of the peaks and lost of intensity) at the same critical pressure that can be attributed to the lost of hydrostaticity in these conditions and to the fact that the sample chamber is further away from the tip of the fibre optics as we keep on increasing pressure by inflating the membrane.

Additionally to the off-line pressure experiment, extra tests were performed in order to further develop the correct experimental methodology, determining the time required to stabilize the system when doing small variations of temperature and to explore the possibility of using the equation of state of gold as an alternative method for pressure determination. In order to do so, an on-line test was conducted on I16, using the membrane cell equipped with 800 μm culet anvils, a steel gasket indented down to 116 μm and drilled with a 500 μm hole in the centre of the indentation. Then, the cell was loaded with gold and ruby using 4:1 Methanol-Ethanol as PTM. Several pressure-temperature points were reached observing that for temperature increments of 5-10 K a stabilization time of 35-40 min is required in order to reach the thermal equilibrium. This long stabilisation time is an expected consequence of the temperature gradient observed between the head of the cold-finger and the cell body (see Fig. 4.9 inset). This could be mitigated to some extent by using better insulation from the exterior, increasing the thermal contact between the cell and the cold finger or trying to reduce the cell mass.

For several of the experimental P,T-points reached, the level of pressure was measured using the dependence of the ruby fluorescence shift applying the temperature correction from [191] and the equation of state of gold from [199]. The results obtained can be seen in Fig. 4.11. For the case of the gold scale, each pressure value was obtained by averaging the lattice parameters calculated from the position of the reflections (511), (531) and (442). Then, using the unit cell volume, the level of pressure was calculated applying the equation of state.

Both scales provide reasonably similar values of pressure up to 4 GPa, from where an underestimation of pressure from the ruby method respect to the gold scale was observed. This discrepancy might be the result of a combination of factors. First of all, deviatoric stress may appear as a consequence of the loss of hydrostaticity of the PTM at low temperature. In these conditions, the mixture 4:1 Methanol-Ethanol becomes solid at relatively low pressure [181], which may translate into inhomogeneity along the sample chamber. For this reason, it is possible that the two pressure markers might be exposed to slightly different level of stress [120]. In addition, for the ruby scale, the effects of temperature and pressure in the shift of the R1 mode are considered separately and added as the sum of two independent phenomena. This assumption has been questioned for pressures above 4 GPa [191]. The largest deviation between the two scales occurs for the pressure points

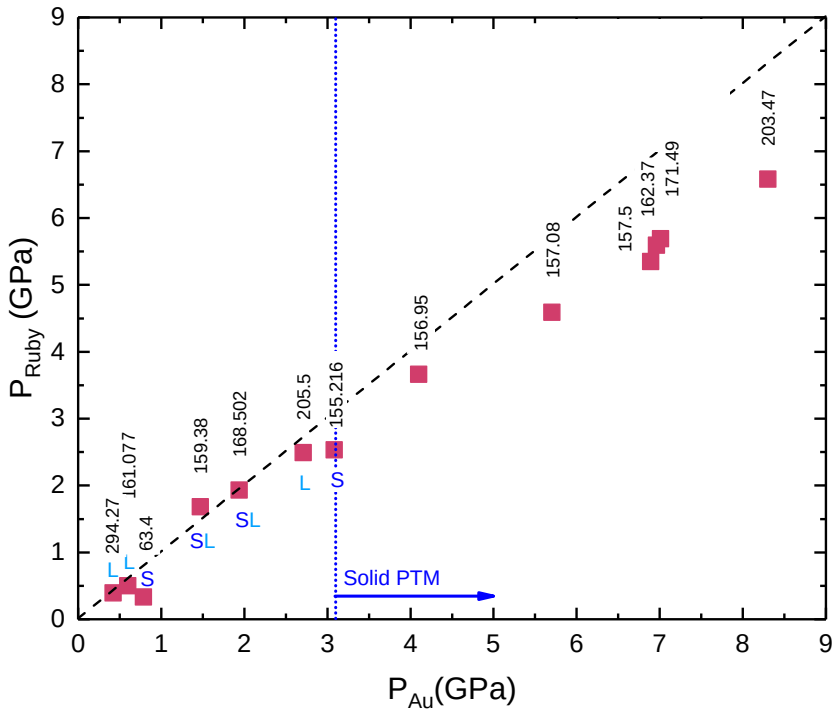

Figure 4.11 *Comparative measurement of pressure at different experimental conditions using the pressure-shift of the R1 luminescence line of ruby [191] and the equation of state of gold from [199]. All the pressure points were acquired using the same loading in different temperature and pressure conditions. Temperature of each point in vertical above the data. 'S' and 'L' stands for the state of the pressure media (4:1 Methanol-Ethanol), 'solid' or 'liquid' respectively.*

above this value, where the pressure transmitting media is solid. Nevertheless, any variation of pressure arising from this origin should equally affect both scales.

Additionally for the gold gauge, at each temperature point it is necessary to optimise the alignment around the peaks considered, in order to not to induce systematic errors. Due to the limited time available for this particular experiment, this procedure was not followed consistently for all pressure points. Nevertheless, this potential source of error could be easily amended following carefully the aligning procedure.

In favour of experimental simplicity, the ruby gauge is more convenient. At the moment, the gas control unit for the membrane is placed inside the experimental hutch and cannot be controlled remotely from the control room. Therefore,

pressure-tuning requires switching off the beam, entering the hutch and manually operating the gas membrane. Once we are inside the hutch, whereas the ruby method allows estimating the level of pressure directly in a few seconds, the use of gold requires exiting the hutch once again, interlocking, switching on the beam, aligning at the gold position and acquiring the diffraction pattern. In some cases, one may need to repeat this sequence of steps several times until reaching the aimed level of pressure, increasing significantly the time employed (from minutes to hours comparing with the ruby method). A second aspect that makes the use of gold less suitable, is the fact that the addition of extra components in the sample chamber represents an extra source of background noise that in some cases may be critical when trying to detect particularly weak resonant signals. For our particular experimental conditions and for the reasons just mentioned, the ruby fluorescence method is a better approach to estimate pressure.

Finally, as mentioned in Section 3.3, during the first attempts to conduct HP-REXS experiments, some photo-induced chemical reactions were experienced in the sample chamber when exposed to the x-ray radiation. On several occasions the sample quality degraded and the observation of the signals of interest was not possible (see Fig. 3.25). Different loading combinations of PTM (4:1 Methanol/Ethanol, 1:1 n-pentene/isopentane, Silicone oil, Daphne oil 7373, NaCl, KCl) and sample fixer (Vaseline, vacuum grease, G-varnish and super-glue) were tried,but only the attenuation of the beam was effective in preventing the chemical reactions from happening. In the energy range typically employed in our experiments (8-13 keV), the absorption cross-section of x-rays is larger than for higher energies (see Eq. 3.2), making the lighter elements in the transmitting media more prone to undergo chemical reactions. Attenuation of the incident beam down to 1% of the full intensity seems to be enough to amend this problem.

4.3 Early designs

During the design process, several iterations were needed until reaching the final version of the m-RXS DAC presented here. In this section, I give some brief details from earlier prototypes highlighting the features improved until reaching the final design. Additionally, a completely different cell based on a wedge-driven mechanism was also contemplated for operating in transmission geometry.

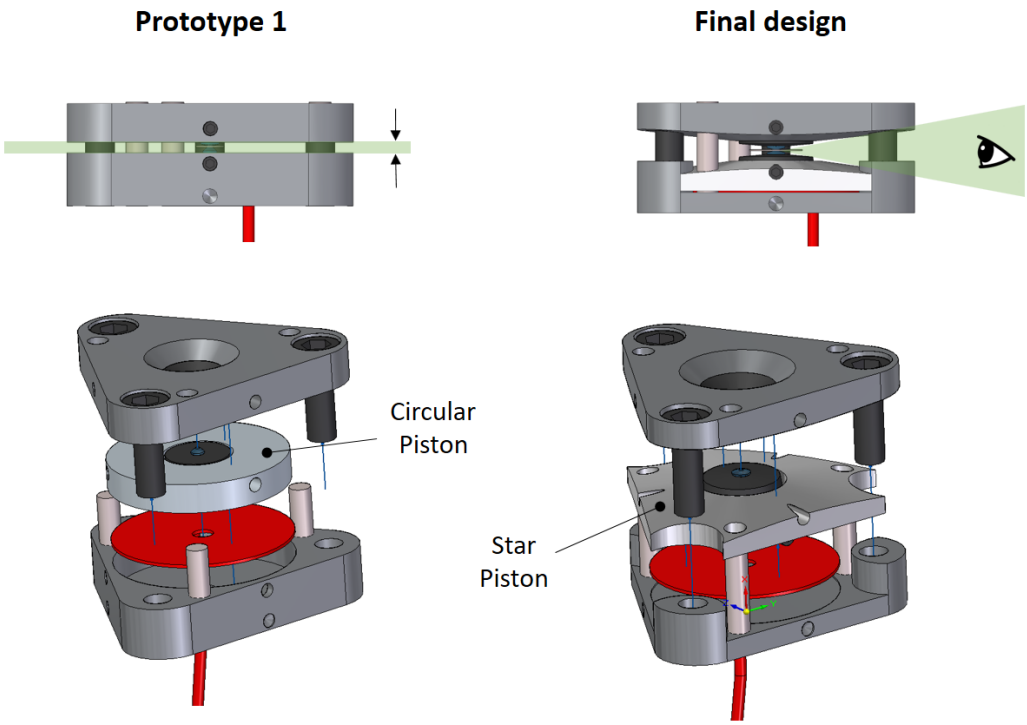

Figure 4.12 *Lateral and extruded views of the CAD model of the inital prototype and final design of the m-RXS. Detail of the different piston shapes and green shaded areas highlighting the lateral access.*

4.3.1 m-RXS first prototype

The fundamental idea behind the design of the m-RXS cell remained the same since the initial sketches. Nevertheless, two main parts were modified until reaching the final version. In the first m-RXS, a circular piston would convey the force generated by the membrane and provide alignment for the lower anvil (see Fig. 4.12). The tolerance between the moving disc and the hosting cavity restricts the movement of the lower anvil to the axial direction of the cell body, keeping it steady within the range of pressure aimed.

However, after the first tests in the beamline, lateral visualisation of the anvils was found to be very helpful to facilitate the alignment of the sample in the centre of rotation of the diffractometer. Unfortunately, direct observation through the cell's side was quite restricted in this prototype. In order to fix this, a lighter cell body with tapered inner faces and a star-like piston was developed. In this case, the piston is inserted in the same three pins than the upper body that provide alignment. This design presents an additional advantage since the reduction of the

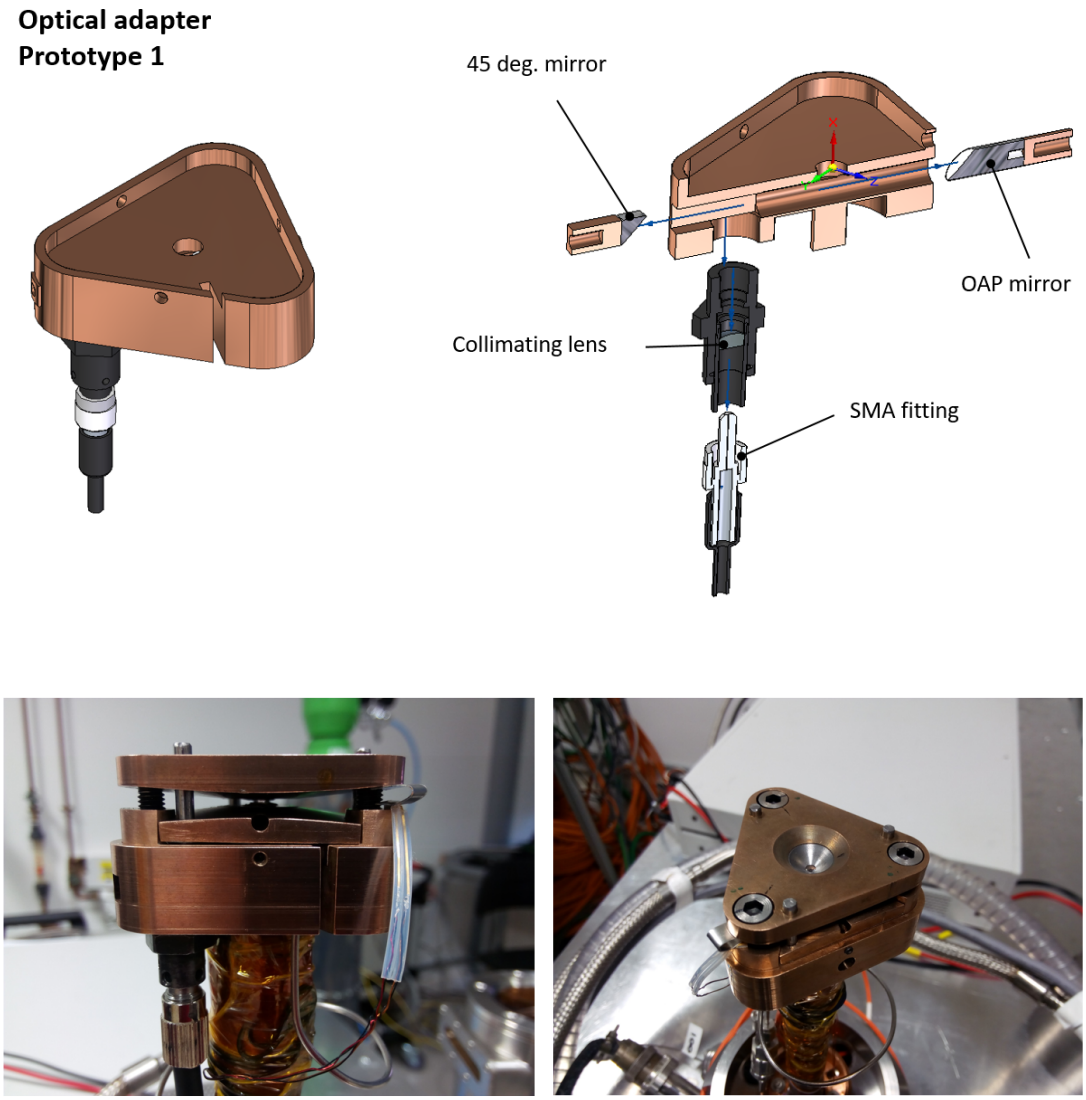

Figure 4.13 *Top - CAD model of the initial optical setup for HP-REXS experiments with detail of the main components: OAP mirror, 45 deg. mirror, collimating lens and fibre optics. Bottom - Pictures of the real optical holder with the mRXS cell, mounted on the cryostat.*

mass inside the cryostat translates in an increase of the cooling rate and a decrease of the thermal stabilisation time. Figure 4.12 shows a comparative view of the lateral and extruded CAD models of these two cells for easier comprehension of the differences mentioned.

The second upgrade with respect to the initial version of the HP-REXS setup involves the optical system. The first option considered in order to measure

the fluorescence of ruby under cryogenic conditions was a more complex optical setup which included a collimating lens, a 45 deg. mirror and a 45 deg. off-axis parabolic (OAP) mirror in addition to the fibre optics. All these elements were hosted by the piece acting as a holder that supports the pressure cell on the cold-finger head. In Figure 4.13 we can see the CAD model and some pictures of the initial optical holder and the m-RXS cell mounted on the cryostat. Despite presenting finer control of the laser beam in terms of collimation and focusing, the loss of light due to the transfer between different optical elements was found to be larger than for the single bare fibre finally employed (see Section 4.2.1).

4.3.2 Wedge-driven DAC prototype

In addition to the membrane design, a completely different idea was considered to perform HP-REXS experiments in transmission geometry. A diamond anvil cell mechanically actuated through a wedge mechanism was machined inspired on similar actuating ideas found in the literature [146, 171, 219]. In this cell, the generation of pressure relies on the sliding of a wedge piece aided by two sets of bearings made of ruby spheres 1.5 mm in diameter. Fig. 4.14 shows an image of the front and back of the real cell and the different parts that make up its body. It is machined in CuBe alloy, Berylco25 [216], and it presents two large scattering apertures of 92 and 100 degrees offering wide access to the reciprocal space in transmission geometry. The approximate dimensions of the cell body are $25 \times 32 \times 14$ mm. Figure 4.15 shows a CAD section view of the assembled body for better understanding of the functioning mechanism and dimensions. The red arrows in this view, indicate the direction of displacement of the moving parts that result in the compression of the sample chamber.

Once installed on the cryostat, two sources of actuation were considered in order to displace the wedge: a motor located on the external part of the cryostat and an internal piezo-electric unit. The piezo-electric approach was quickly discarded mainly due to the fact that at low-temperature the expansion provoked by the alignment of electric domains in the material is quite small and large piezo-electric units are needed in order to generate sufficient force.

Thus, the motor strategy seems to be more convenient. However, as the motor would be placed outside the cryostat it would be also important to thermally isolate it in order to not to create a thermal bridge with the exterior that would

Figure 4.14 *Real image of the wedge-DAC prototype. Front and back views of the cell assembled and views of the individual parts disassembled. Blue scale bar on the right for size appreciation.*

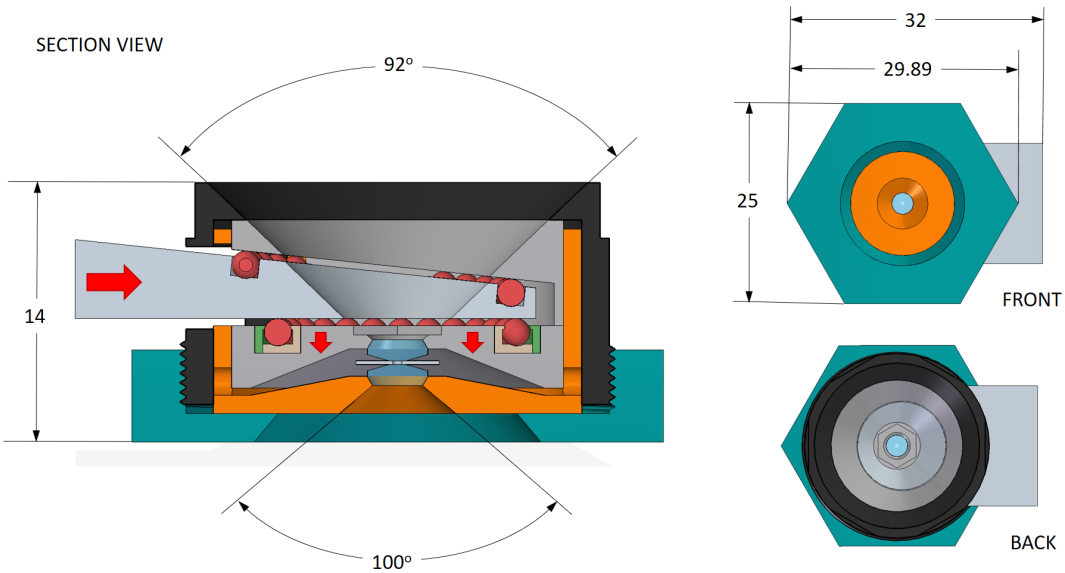

Figure 4.15 *Section-, back- and front-views of the CAD model of the wedge-DAC for HP-REXS experiments in transmission geometry. Red arrows in the section view indicate the direction of displacement of the moving parts. Dimensions in mm and degrees.*

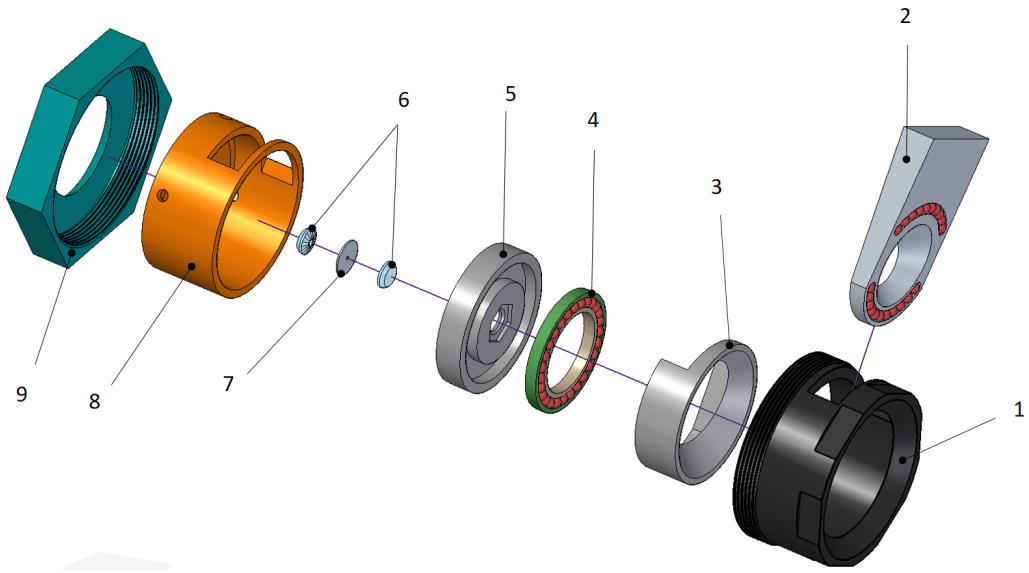

Figure 4.16 *Exploded CAD model of the wedge-DAC. (1) Outer-body, (2) lower-wedge, (3) upper-wedge, (4) bearing, (5) piston, (6) diamond anvils, (7) gasket, (8) lower-body and (9) nut.*

prevent the system from reaching the target temperature.

Further development and testing of this cell was not accomplished mainly due to the time restrictions of the project. The implementation of this setup, would require an important re-modelling of the cryostat dome, including the opening of additional radial windows for transmission geometry and the development of an external and more complex optical system as previously mentioned in Section 4.2.1. For all these reasons, priority was given to the m-RXS pressure cell.

Chapter 5

High-Pressure Resonant X-ray Studies on I16

Contents

In this chapter, I am focusing more on the research part of this thesis. A number of materials were considered as possible subjects of investigation for developing the experimental methodology and testing the instrumentation designed. The selection was made based on their suitability for HP-REXS studies and their specific scientific interest. Initial tests were conducted on materials such as $NaOsO_3$ and $AgNiO_2$ that aided in the assessment of the experimental capabilities and the conception of the right experimental procedures described in Section 4.2.2. Among the studies attempted, I am presenting here the most successful results obtained form investigating the magnetic properties of one of the iridium based systems introduced in Ch. 1, $Sr_3Ir_2O_7$ and its electronically doped counterpart $(Sr_{1-x}La_x)_3Ir_2O_7$.

This chapter is organised in three main blocks as follows. After a brief review of the experimental techniques employed, I will outline the key properties of $Sr_3Ir_2O_7$ at ambient pressure and discuss the theoretical motivation to investigate the evolution of its properties under compression. Then, I will enumerate the main findings reported under high pressure conditions in the system, before presenting the principal breakthroughs from studying the evolution of the magnetic ordering and the crystalline structure of $Sr_3Ir_2O_7$ upon applying pressure and at low-temperature by REXS and single-crystal XRD.

In the second part of this chapter, the synergy between hydrostatic and chemical pressure in samples of $(Sr_{1-x}La_x)_3Ir_2O_7$ containing 0.7% of La [x = 0.007] is investigated. A general overview of the effect of lanthanum substitution is provided as introduction, followed by the exposition of the experimental evidences obtained from the HP-REXS study.

Finally, a joint discussion of the results procured from REXS and the additional RIXS and computational modelling results provided by our collaborators is presented. In the last part of the chapter, the most speculative, I will discuss the theoretical model used to describe the experimental results.

Analysis of the experimental evidence obtained from REXS experiments was carried out in collaboration with Dr L. S. I. Veiga and Dr J. G. Vale at UCL in London (UK), who provided experimental support and performed theoretical calculations respectively, and Dr Matteo Rossi and Dr Mario Moretti-Sala at the ESRF in Grenoble (France), who conducted HP-RIXS experiments on $Sr_3Ir_2O_7$.

5.1 Experimental methods

5.1.1 Synchrotron experimental setups

Beamlines I16 and I19

Most of the experimental work of this thesis was conducted on I16, the beamline for materials and magnetism described in detail in Section 2.2 [21].

Additionally, in order to carefully track the evolution of the crystalline structure of $Sr_3Ir_2O_7$ upon applied pressure at low-temperature, a HP single-crystal XRD study was also conducted on beamline I19 at DLS [220]. I19 is based on a linear undulator that provides a large flux of photons in the hard x-ray regime (5 - 28 keV) and a Si 111 double-cut monochromator that selects the incident energy. A pair of bimorph mirrors are used for focusing and harmonic rejection. The experiments presented in this thesis were conducted in the experimental hutch 2 (EH2) equipped with a Newport 4-cycle diffractometer with sphere of confusion < 60 μm. All sets of diffraction data acquired were integrated and reduced using the CrysAlis^{Pro} software [221], which includes masking procedures to omit areas in the detector shaded by different elements of the DAC. Final refinement and modulation of the thermal parameters was done using Jana2006 software [222]. Further details from the specific experimental conditions of these studies are given in Section 5.2.4.

5.1.2 Synthesis and sample pre-characterization techniques

Single-crystal growth methods

Single-crystals of $Sr_3Ir_2O_7$ and $(Sr_{1-x}La_x)_3Ir_2O_7$ were synthesised by our collaborators via flux technique using Pt crucibles. For the obtention of pure crystallites of $Sr_3Ir_2O_7$, a mixture of $SrCO_3$, IrO_2 and $SrCl_7$ was used in a molar ratio 1.35:1:7.5. The crucibles were sealed and heated to 1220 °C, fired for 12 h and slowly cooled at 4 °C/h (see further details in [223]). La-doped samples containing 0.7 % of La, were obtained by mixing 1.30 (0.99 $SrCO_3$ + 0.005 La_2O_3) : IrO_2 : 7.5 $SrCl_2$. The mixture was heated to 1200 °C for 12 h,

cooled to 1100 °C in 18.75 h, and then cooled to 900 °C for 1 h before allowing the samples to furnace cool to room temperature (see detailed description in [223]). The crystalline quality of all the samples employed for the high-pressure experiments was assessed by single-crystal XRD. Additional energy dispersive x-ray spectroscopy (EDX) analysis was used to verify the stoichiometry of the La doped crystals.

XRD - Single-crystal x-ray diffraction

The crystalline quality of all the samples was checked using the Supernova XRD lab source at the facilities of the Research Complex at Harwell (RCaH). This diffractometer provides dual Cu/Mo x-ray sources and detection by means of a 135 mm Atlas CCD unit. It allows collecting diffraction data within a variable range of temperature (90-490 K) by coupling an Oxford Instruments cryojet [204].

The Mo-K_α source (λ = 0.7093 Å) was the excitation of choice in this case. It provides enough resolution ($d_{\text{min}} \sim 0.7$ Å) and allows reaching higher level of completeness for an equivalent number of frames with respect to the Cu-K_α source. Due to the relationship between the excitation energy and the d-spacing (see Eq. 4.4), the Mo-K_α source (17.479 keV) allows observation of a larger portion of reciprocal space for the same number of frames than the Cu-K_α source (8.047 keV). Three-dimensional analysis of individual reflections and refinement was performed using CrysAlis$^{\text{Pro}}$ [221] and Jana2006 [222] software packages respectively. Only samples showing clean and intense peaks (I $\geq$ 40000 counts), low-mosaicity and a refinement R_{wp}-factor below 6% were selected[1]. The orientation of each crystal was also assessed in order to ensure that the reflections of interest lie within the aperture of the DAC and to facilitate the orientation process during the REXS experiment (*i.e.* initial ub-matrix definition).

[1]The R-factor provides an estimate of the agreement between the observed and calculated diffraction patterns. The magnitude considered in all the datasets refined is the so called *weighted profile R-factor* (R_{wp}), which is the weighted sum of the squared difference between the observed and the calculated diffraction peak intensities: $R_{wp}^2 = \sum_i w_i(y_{c,i} - y_{o,i})^2 / \sum_i w_i(y_{o,i})^2$, where w_i is a weight factor equal to $1/y_{o,i}$, $y_{o,i}$ is the observed intensity at the ith step and $y_{c,i}$ is the calculated intensity at the ith step. A perfect fit would have an R_{wp} value equal to zero but in reality a R_{wp} value of less than $\sim$ 7% equates to a good fit [224].

EDX - Energy dispersive x-ray spectroscopy

Energy dispersive x-ray spectroscopy (EDX) is used to determine the chemical composition of a material by shooting electrons at its surface and analysing the emission lines arising at different wavelengths for each particular element. The incident flux of electrons generate core-hole unstable states followed by recombination and emission of x-ray radiation. During this process, x-ray emission occurs at a specific wavelength characteristic of each element as a function of the energy difference between the electronic level of the electron undergoing recombination and the level hosting the hole. By analysing the position of these lines and the intensity ratio between them, it is possible to determine the specific stoichiometry of samples as small as few cubic micrometers. This technique was used to determine the doping level of all the crystals of $(Sr_{1-x}La_x)_3Ir_2O_7$ used for the experiments described in Section 5.3.2. All samples were superficially cleaved in order to discard any possible artificial contamination of the surface, which could potentially mask the real composition of the crystal.

5.2 Electronic behaviour of $Sr_3Ir_2O_7$ under pressure

5.2.1 Introduction: electronic and magnetic properties of $Sr_3Ir_2O_7$ at ambient pressure

The Ruddlesden-Popper (RP) series of compounds with stoichiometry $Sr_{n+1}Ir_nO_{3n+1}$ presents a rich landscape of electronic behaviours largely influenced by the dimensionality of their crystalline structure [33, 48, 225, 226]. This family of materials crystallise into perovskite-like structures with the alkaline earth metal Sr^{2+} occupying the A-sites -tetrahedral oxygen interstices- and the transition metal Ir^{4+} in octahedral coordination with 6 oxygen atoms at the B-positions. Figure 5.1 shows an illustration of the crystalline unit cell of the members n = 1, 2 and ∞ of this series, where the subscript n refers to the number of layers of Ir-O sandwiched by layers of Sr-O.

From the insulating character of the monolayered Sr_2IrO_4 (n = 1) [34, 47, 48, 227] to the metallic nature of $SrIrO_3$ (n = ∞) [48, 228], the intermediate member $Sr_3Ir_2O_7$ (n = 2) presents weakly-insulating behaviour in the proximity of an

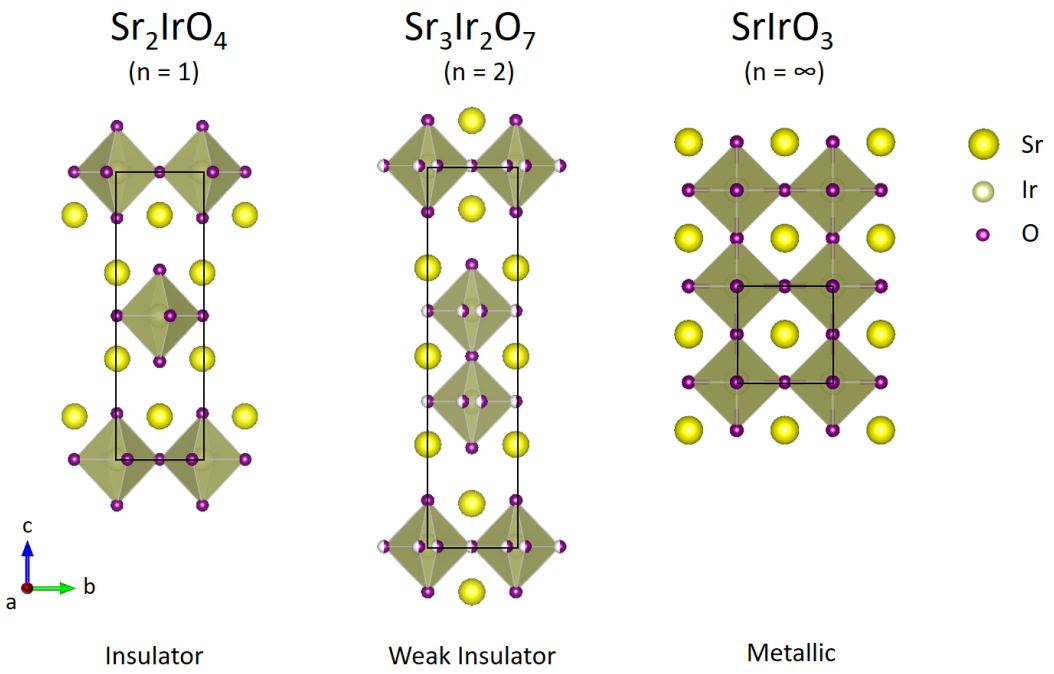

Figure 5.1 *Ruddlesden-Popper series of iridates $Sr_{n+1}Ir_nO_{3n+1}$. Evolution of the electronic and structural properties for the cases $n = 1, 2$ and ∞ of the series. Half-coloured atoms in $Sr_3Ir_2O_7$ indicate the partial occupancy of some of the oxygen atomic positions.*

insulator-to-metal transition (IMT) [48, 229–231] and will be the main subject of study in the present work.

However, not only structural diversity but also the strong spin-orbit coupling (SOC) interaction characteristic of 5d transition metals (TM) is the foremost reason behind the rich electronic landscape of the RP iridates. 5d elements present a strong SOC within the electronvolt range, matching the energy scale of the crystal field (CF). Ding *et al.* [232] estimated a value of 10Dq $\sim$ 2.8 eV for the CF gap in $Sr_3Ir_2O_7$, similar in magnitude to the spin-orbit coupling constant λ_{SOC} $\sim$ 1.9 eV deduced from RIXS measurements [232]. The balance between these two interactions tailors the electronic ground state of this compound as illustrated in Figure 5.2. In first place, the cubic crystal field interaction splits the atomic 5d orbitals of Ir^{4+} into a t_{2g}^5 and an e_g^0 manifolds, occupied in low-spin configuration as a result of the prevalence of CF over Hund's coupling (10Dq $> 3J_H$). Then, the SOC lifts the orbital degeneracy of the t_{2g}^5 orbitals into a fully-occupied $J_{eff} = 3/2$ quartet and a half-filled $J_{eff} = 1/2$ doublet. In these conditions, a weak Coulomb repulsion U is sufficient to open a gap in the $J_{eff} = 1/2$ band and form a so-called

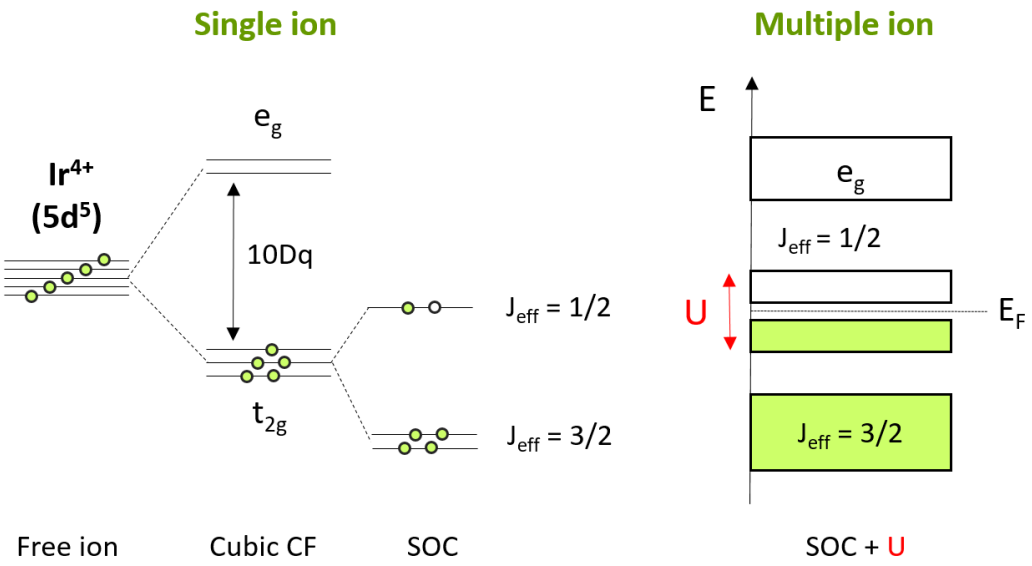

Figure 5.2 *Electronic ground state diagram of $Sr_3Ir_2O_7$ (and Sr_2IrO_4) in the single and multiple ion models. The equal footing between the SOC and the cubic CF lifts the degeneracy of the t_{2g} manifold into a $J_{eff} = 3/2$ quartet and a half filled $J_{eff} = 1/2$ doublet. Thus, when moving into a periodic array of cations (crystalline structure - multiple ion model), Coulomb repulsion is strong enough to open a gap in the $J_{eff} = 1/2$ band that explains the insulating behaviour in $Sr_3Ir_2O_7$ and Sr_2IrO_4.*

spin-orbit Mott insulator ground state [34, 47].

The $J_{eff} = 1/2$ picture is common for both $Sr_3Ir_2O_7$ and Sr_2IrO_4, differing only in the magnitude of the electronic gap ~ 0.1 and ~ 0.4 eV respectively [33, 229, 230, 233–236]. This situates $Sr_3Ir_2O_7$ in a particularly interesting position as weak insulator in the proximity of a transition towards metallic conduction that can be accessed either, via chemical doping [225, 237–239] or applied hydrostatic pressure [232, 237, 240, 241].

Additionally, the unpaired electrons occupying the $J_{eff} = 1/2$ band give rise to G-type antiferromagnetic ordering in $Sr_3Ir_2O_7$ below 285 K with the magnetic spins aligned with the c-axis [242]. Two magnetic domains A and B, illustrated in Fig. 5.3, have been described with magnetic wave vectors $k_1 = (1/2, 1/2, 0)$ and $k_2 = (1/2, -1/2, 0)$ respectively [243]. Evidence from an anomalous net ferromagnetic moment $\sim 0.04\ \mu_B$ per Ir atom in the basal plane can be also found in the literature [32, 244], in contrast with the magnetic structure just described. This can be explained as a consequence of a monoclinic distortion reported by Hogan *et al.* [245], where a rather modest out-of-plane tilt $\phi \sim 0.2^o$

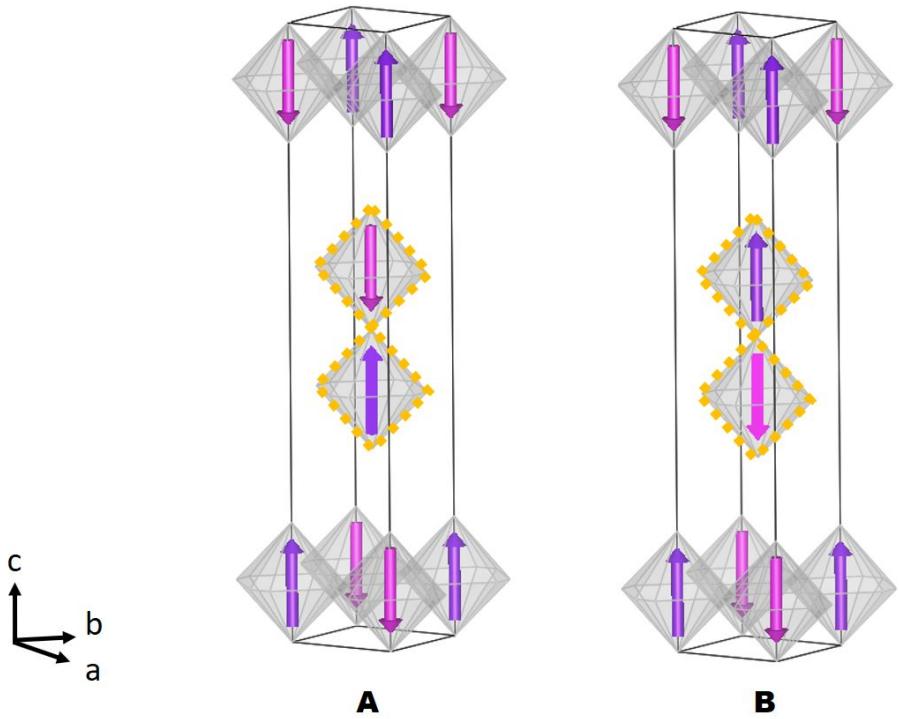

Figure 5.3 *The c-axis G-type magnetic structure of $Sr_3Ir_2O_7$ for the magnetic domains A and B defined within the I4/mmm space group by the ordering wave vectors k_1 = (1/2, 1/2, 0) and k_2 = (1/2, -1/2, 0) [242, 243]. Yellow dashed lines highlighting the variations in spin orientation between domains.*

of the octahedral units would be sufficient to produce a small projection of the total magnetic moment over the ab-plane (see ϕ in Fig. 5.4).

Indeed, certain debate is still active around the crystalline structure of $Sr_3Ir_2O_7$. Subramanian *et al.* [246], first described it within the tetragonal space group I4/mmm (No. 139), with lattice parameters c = 20.892 Å, a-b = 3.896 Å and a possible non-correlated rotation of the octahedral units of $\alpha \sim 12^o$ about the c-axis (see α in Fig. 5.4). The absence of additional super-lattice reflections, perhaps too weak to be observed under their experimental conditions, is indicative of a state of rotational disorder rather than a coordinated movement of the IrO_6 units. Nevertheless, more recent studies found evidence of these additional reflections suggesting an orthorhombic twinned structure (Bbcb) [32, 247], where neighbouring octahedra undergo coordinated counter rotation. Additionally, the monoclinic distortion mentioned before, further lowers the crystalline symmetry down to the (C2/c) space group and explains the existence of the basal magnetic moment observed in $Sr_3Ir_2O_7$ [245].

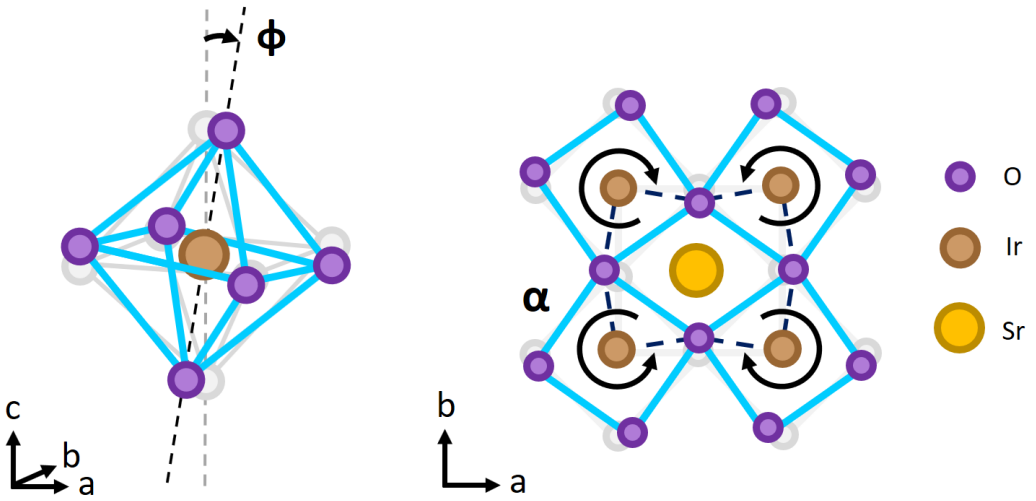

Figure 5.4 *Schematic representation of the rotational angles affecting the IrO_6 units in $Sr_3Ir_2O_7$ referred in the main text. Left - Out-plane rotation ϕ of the IrO_6 units that leads to the monoclinic distortion C2/c space group [245]. Right - Counter in-plane rotation α about the c-axis of the neighbouring octahedral units in the basal plane of the unit cell that leads to the orthorhombic space group Bbcb [32, 247].*

For the aim of this study, primarily focused on the evolution of the magnetic properties of $Sr_3Ir_2O_7$ under pressure, the higher symmetry approach, space group I4/mmm, results adequate when indexing the magnetic reflections, and will be the notation adopted for most of the results shown here.

5.2.2 Pressure induced phases in $Sr_3Ir_2O_7$

The application of hydrostatic pressure seems to be a successful method to explore charge, spin, orbital and lattice degrees of freedom in $Sr_3Ir_2O_7$. A number of exotic structural, electronic and magnetic transitions induced by pressure have been reported in the literature. Ding *et al.* [232] described the realisation of a confined metal state above 59.6 GPa at room temperature, where $Sr_3Ir_2O_7$ becomes metallic in the a-b plane and remains insulator along the c-axis. This result obtained from a single crystal, is consistent with additional resistivity measurements published by different authors on samples of the same nature [240, 241]. Slightly different critical transition parameters have been observed in studies conducted on polycrystalline samples. Li *et al.* reported a significant drop in the electrical resistivity of 6 orders of magnitude at much lower pressure

($\sim$ 13.2 GPa) and low-temperature, not reaching the full collapse of the electronic gap up to 35 GPa [237].

More recent evidence of a concurrent magnetic and structural transformation at 14.4 GPa, decoupled from the insulating-to-metal transition (IMT) can be also found in the literature [241]. In this paper, Zhang *et al.* observed a softening of the predominant single-magnon mode by Raman scattering and the appearance of two weak low-frequency magnetic signals above the mentioned critical pressure. The simultaneous magnetic and structural transitions evidence yet again, the intimate interplay between lattice and super-exchange interactions, suggesting the potential realisation of an alternative magnetic ground state mediated by the crystalline lattice. This same study also provides resistivity measurements up to 16.5 GPa that confirm the insulating character of $Sr_3Ir_2O_7$ well above the mentioned transitions. Thus, the magnetic and structural transitions observed by Raman spectroscopy seem to be decoupled from the IMT reported by Li *et al.* in the same region of pressure [237].

Different studies reported pressure-induced structural transformations involving a monoclinic distortion as a result of the correlated rotation of the octahedral IrO_6 units [232, 248]. Some disparity regarding the critical PT values at which this transformation occurs is yet to be addressed. Not only in the proximity of 14 GPa [241, 249], but also at higher pressure, close to 60 GPa (critical value for the IMT) different studies provided evidence of a structural distortion [232, 248]. Although it is not possible to discard other factors, the difference in sample dimensionality between poly- and single-crystals may be partially responsible for the inconsistency between investigations.

In addition to the crystalline lattice, other factors may influence the transition towards metallic conductivity in $Sr_3Ir_2O_7$. Signs of bandwidth broadening (W), increase of the electronic-hopping (t) and variation in the strength of the CF interaction are also important factors to consider. HP-SAXS experiments probing the ratio between the L_3 and L_2 of Ir, suggest a decrease of the SO interaction potentially caused by bandwidth broadening and hybridization of the E_g and $J_{\text{eff}} = 3/2$ levels [250]. RIXS experiments also revealed spin-waves noticeably gapped ($\sim$ 90 meV) along the entire Brillouin zone [251, 252] and softening of the magnetic mode upon applied pressure at a rate of ~ 1.5 meV GPa^{-1} [253], that predicts the full suppression of the magnetic interactions around 60 GPa. This value is in good agreement with the critical pessure for the structural transition

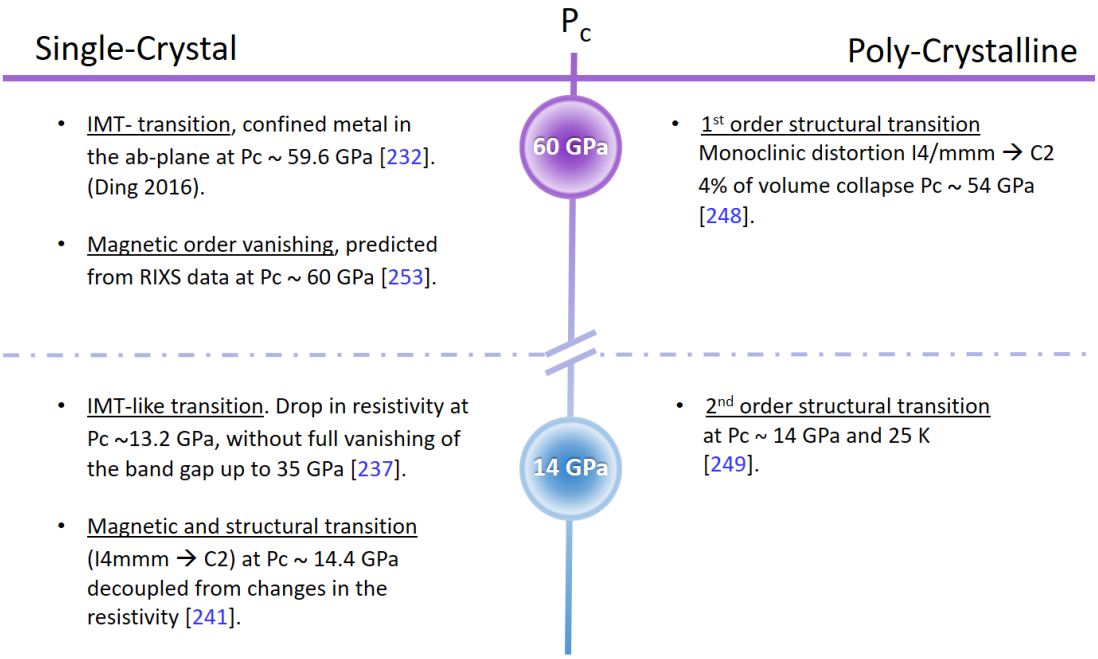

Figure 5.5 *Summary of the main transitions induced by pressure in $Sr_3Ir_2O_7$ for single-crystals and poly-crystalline samples reported in the literature, in the two regions of criticality around 14 and 60 GPa [232, 237, 241, 248, 249, 253].*

observed on poly-crystalline samples [248]. Unfortunately, to date, there are no theoretical models able to validate the full set of experimental observations [236, 252, 254]. Some of the discrepancies observed can be related to the different ratio between surface and volume in poly-crystalline and single-crystal materials. However, small stoichiometric variations could also play an important role. Other questions as what is the nature of the intermediate magnetic ground state between the transition described by Raman spectroscopy and the IMT, are yet to be solved. A summary of the main effects induced by pressure in $Sr_3Ir_2O_7$ is shown in Fig. 5.5.

In an attempt to further clarify the magnetic behaviour of $Sr_3Ir_2O_7$ in the proximity of the first region of criticality comprising 10-15 GPa of pressure, HP-REXS experiments were conducted on I16. The principal findings obtained from this investigation are reported in the next section.

5.2.3 Evolution of the magnetic ordering of $Sr_3Ir_2O_7$ under pressure by REXS

We studied the evolution of the magnetic ordering temperature T_N upon increasing pressure in $Sr_3Ir_2O_7$ by REXS. A progressive decrease of $T_N(P)$ was observed, in good agreement with the values deduced from the softening of the one-magnon band revealed by Raman spectroscopy [241]. Three-dimensional magnetic order is stable up to at least 11.7 GPa of pressure in $Sr_3Ir_2O_7$. We also estimated a 50% reduction of the magnetic moment upon increasing pressure between 2.2 and 6.6 GPa, given the decrease in the intensity ratio between magnetic and charge peaks. Above a critical pressure $P_c \sim 12$ GPa, a consistent degradation of the sample was noticed in several experiments.

Experimental parameters

REXS experiments were conducted in the beamline I16 at DLS [21] (full description provided in Section 2.2). The energy of the incoming beam was tuned to the Ir L_3 absorption edge (11.217 keV) using a Si (111) single-cut monochromator. The beam-size was focused down to a spot of 20 × 200 μm^2 (V×H) at the sample position by means of a set of parallel mirrors. At room pressure, magnetic domains of *ca.* 20 × 20 μm^2 have been described for $Sr_3Ir_2O_7$ [242]. In principle, this size of beam spot allows obtaining averaged information from the two domains. Nevertheless, the application of pressure may shift the domain walls altering their average size. Both, a Pilatus 100k area detector and an avalanche photo-diode (APD) were used to detect the scattered signals. The incident beam was carefully attenuated down to 1% of the full beam intensity in order to prevent radiation damage caused by the interaction of the beam with the pressure transmitting medium (PTM) and to reduce charging of the sample, which causes its movement. A set of slits at the entrance of the detector were used in order to minimize most of the non-sample scattering background, increasing the signal-to-noise ratio. However, given the close proximity of the diamonds with the sample not all of this scattering was eliminated.

Single crystals of $Sr_3Ir_2O_7$ were flux grown following the procedure in ref. [246] and several were cleaved under the microscope down to an average size of (100 × 60 × 20) μm. Their crystalline quality was individually checked following the

methodology detailed in Section 5.1.2.

Selected samples were loaded in the two HP-environments described in Section 3.4, with the [00l] direction perpendicular to the culet face and fixed using a small drop of Vaseline. For the backscattering geometry, the m-RXS DAC [1] was fitted with Boheler-Almax (BA) diamonds (type 1a), 1.25 mm thick and 500 μm in culet diameter (see appendix B for detailed dimensions). In transmission, the miniature TB-DAC [157] was fitted with BA anvils (type 1a) of standard thickness and 600 μm of culet diameter. In both cases, stainless steel gaskets 250 μm thick were pre-indented down to *ca.* 100 μm and EDM-drilled in the centre of the indentation, creating a sample cavity 200-250 μm wide. Gaskets for the TB-DAC were prepared using the indenter-device from Figure 3.23. Ruby spheres $\sim$ 20 μm in diameter were also placed in the sample cavity and used as pressure gauge [114]. Finally, a mixture of 4:1 Methanol:Ethanol (ME) was employed as a PTM.

Results

The temperature dependence of the intensity of magnetic reflections (0.5, 0.5, 2), (1.5, 1.5, 2) and (0.5, 0.5, 34) was collected from various samples of $Sr_3Ir_2O_7$ at different values of applied pressure. Fig. 5.6 shows the results obtained at each pressure point. As expected from a magnetic material, upon increasing temperature the scattering intensity of the magnetic reflections decreases from saturation until eventually disappearing at a critical value T_N. The temperature dependence of the magnetic reflections shows the characteristic behaviour of a second-order phase transition. The application of external pressure induces a linear shift of T_N downwards in temperature (*ca.* -10 K/GPa) up to 11.7 GPa. Above this pressure value, consistent degradation of the samples occurred in all experiments conducted impeding further observation of magnetic reflections.

Additionally to the shift downwards in temperature induced in T_N, a decrease in the relative intensity of the magnetic peak (0.5, 0.5, 2) with respect to the charge counterpart (1, 1, 2) was noticed upon increasing pressure. A reduction of 50% in intensity of the magnetic signal was quantified between 2.2 and 6.6 GPa (see inset in Figure 5.7). This drop in intensity could have its origin in a reduction of the ordered magnetic moment, potentially caused by structural distortions or by changes in the orientation of the magnetic spins.

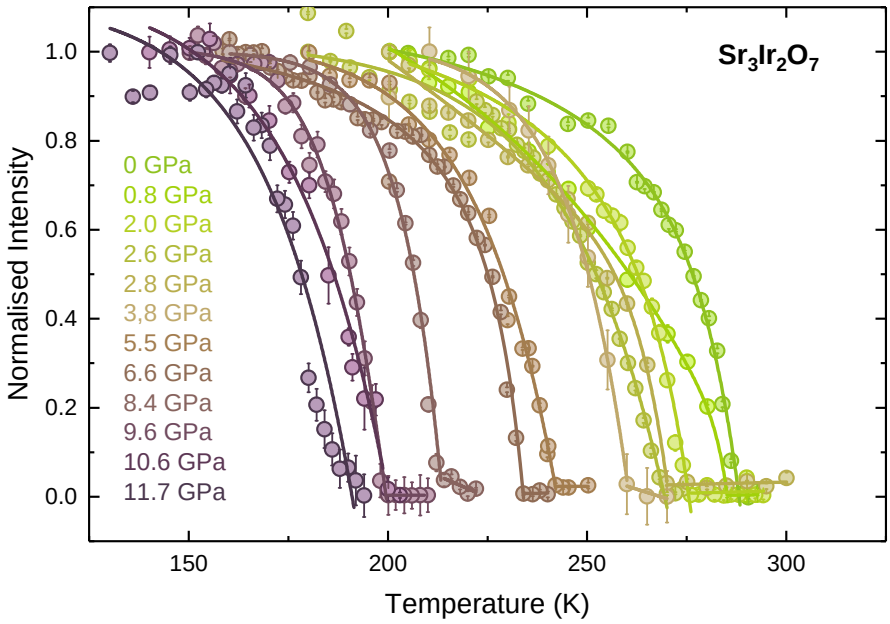

Figure 5.6 *Temperature dependence of the magnetic scattering intensity at positions (0.5 0.5 2), (1.5 1.5 2) and (0.5 0.5 34) for different applied pressures in $Sr_3Ir_2O_7$, normalised to the intensity recorded at the lowest temperature measured.*

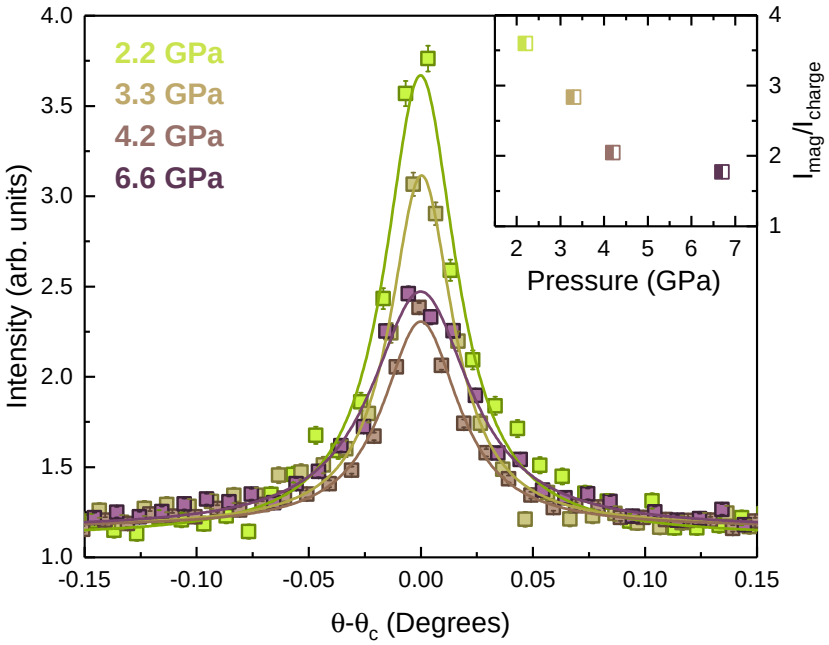

Figure 5.7 *Reciprocal space scans around the magnetic reflection (0.5 0.5 2) at different values of applied pressure in $Sr_3Ir_2O_7$. Inset: Pressure evolution of the ratio between the intensities of the magnetic reflection (0.5 0.5 2) (I_{mag}) and the charge peak (1 1 2) (I_{charge}).*

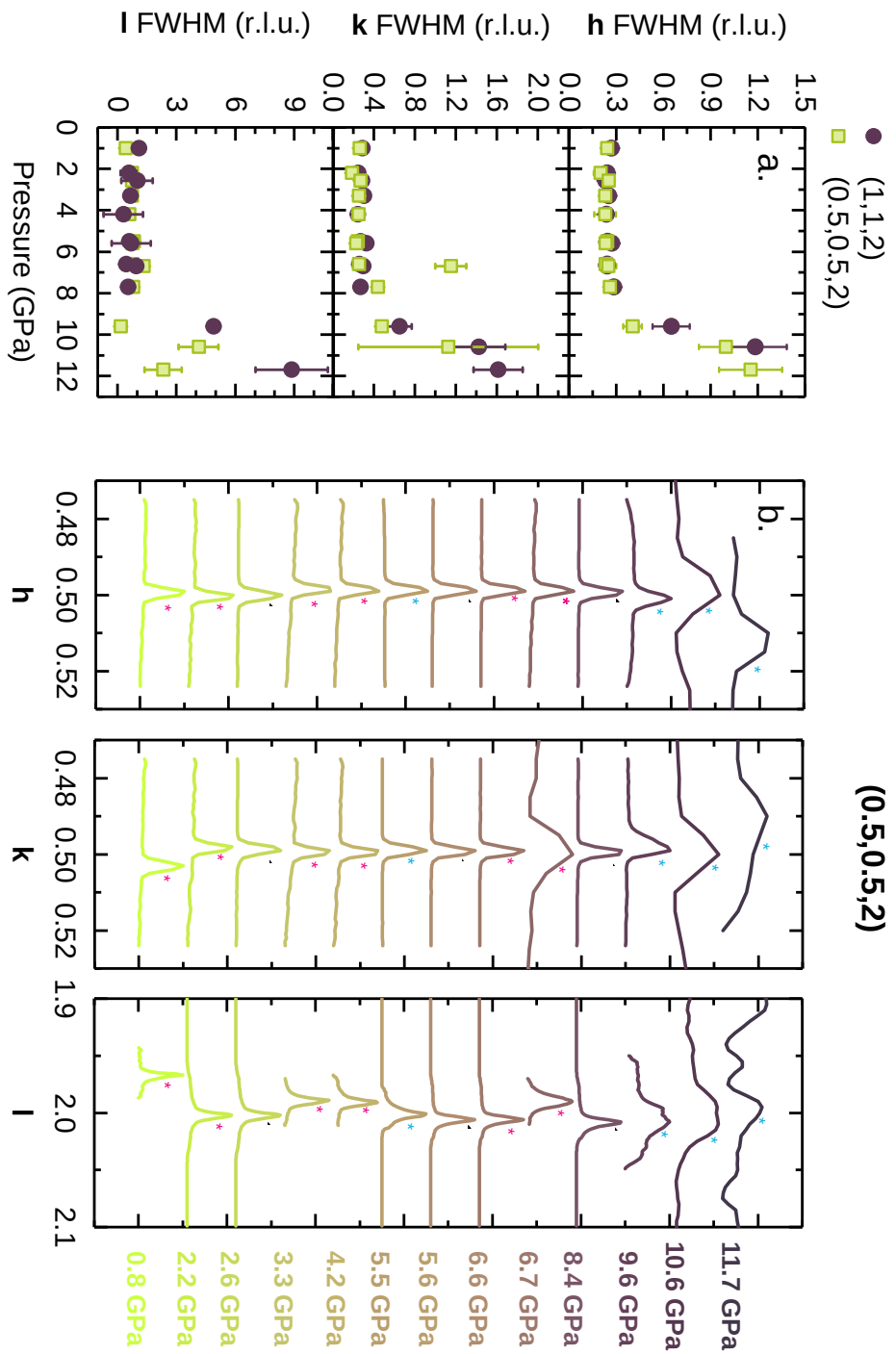

Figure 5.8 ***a)*** *Three-dimensional analysis of the full-width at half maximum (FWHM) against applied pressure of the magnetic reflection (0.5, 0.5, 2) and the charge peak (1, 1, 2) along the h-, k-, l-directions of the reciprocal space in $Sr_3Ir_2O_7$.* ***b)*** *h-, k-, l-scans of the magnetic peak (0.5, 0.5, 2) upon applied pressure. Symbols by the reflections indicating sets of data obtained from the same sample.*

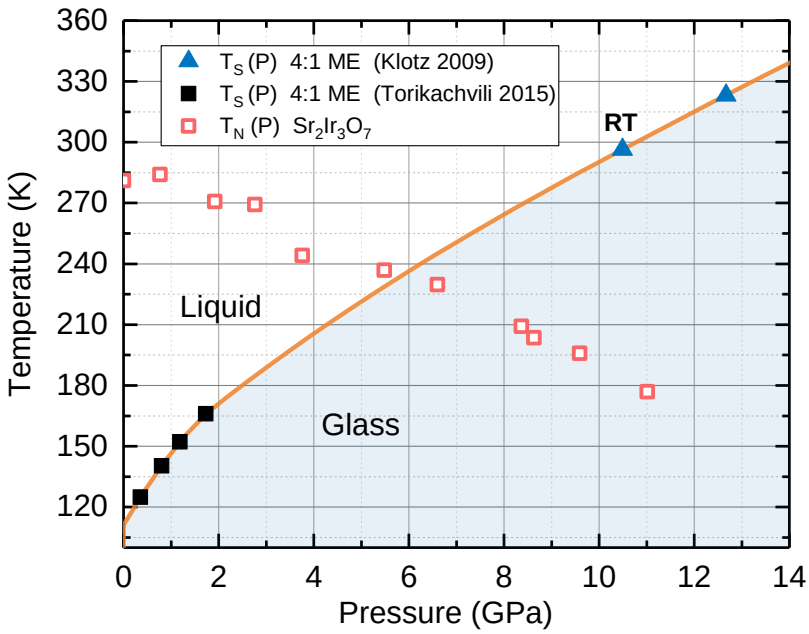

Figure 5.9 *Pressure dependence of the solidification temperature $T_S^{ME}(P)$ of the mixture 4:1 Methanol-Ethanol (orange line) extrapolated using the experimental values obtained by Torikachvili (black squares) and Klotz (blue triangles) [181, 182]. Empty pink squares represent the experimental values for the magnetic ordering temperature $T_N(P)$ of $Sr_3Ir_2O_7$ obtained by REXS in this work.*

In order to figure out whether this relative weakening in the intensity of the magnetic reflections was related to a loss of coherence that would manifest in a broadening of the magnetic peaks, we performed a three-dimensional analysis of the full-width at half maximum (FWHM). We found that the FWHM remains nearly constant for both, magnetic and charge peaks, up to 8 GPa of pressure in the three directions of the reciprocal space (hkl) (see Figure 5.8). In such situation, either the loss of coherence is so abrupt that we do no see any emerging tail, which is possible given the weakness of the peaks, or the moment rotates coherently towards the ab-plane. Above 8 GPa, both signals get progressively broaden following the same trend. This confirms the overall deterioration of the samples in the proximity of the critical pressure $P_c \sim 12$ GPa, while no sizeable alteration of the magnetic peak positions was found.

At low temperature, solidification of the PTM (4:1-ME) could result in stress inhomogeneity across the sample chamber and loss of hydrostaticity, causing uneven strain and eventual fracture of the crystal. In order to figure out whether this is the reason behind the sample deterioration, Fig. 5.9 displays the

overlap between the solidification line of 4:1 ME adapted from [181, 182] and the experimental values of $T_N(P)$ obtained in this work. From inspecting this figure, one can deduce that the mixture 4:1-ME is an amorphous glass for all pressure points above 5.5 GPa, well below the band broadening observed above $\sim$ 8 GPa of applied pressure. Therefore, not supporting the non-hydrostatic hypothesis.

Alternatively, the IrO_6 octahedra units of $Sr_3Ir_2O_7$ are prone to rotate around the c-axis [232, 248]. This rotation induced by pressure, could explain to a certain extent both, the loss of crystalline quality and the reduction of the magnetic moment. In fact, structural transitions in the proximity of 14 GPa, not far from our critical pressure value, have been described by different authors [241, 249]. However, whether applied pressure primarily induces alterations in the structure and that, in turn, change the magnetic order or whether the process occurs in the opposite direction (*i.e.* magnetically mediated crystalline distortion) is yet an open question.

Another source of sample deterioration could be the 'bridge' or direct contact of the crystal with the two diamond anvils upon the gasket gets thinner when increasing pressure. The thickness of the sample and the gasket was compared after every experiment to discard this possibility.

In order to obtain a clearer understanding of the structural variations taking place in $Sr_3Ir_2O_7$ within the PT-range explored during the REXS experiments, we conducted the HP-LT single-crystal XRD investigation reported in the next section.

5.2.4 Evolution of the crystalline structure of $Sr_3Ir_2O_7$ under pressure by single-crystal x-ray diffraction (XRD)

Experimental parameters

HP single-crystal XRD experiments were conducted in beamline I19 at DLS [220]. Excitation energy was driven to the Ag K-edge (25.514 keV, $\lambda = 0.4859$ Å) and the incoming beam was focused down to a spot (130 $\times$ 185) μm at the sample position. Diffraction patterns of $Sr_3Ir_2O_7$ under pressure were collected at 200 K in transmission geometry by means of a Dectris Pilatus 300K photon-counting detector, using the x-ray TB-DAC described in Sec. 3.4 [157].

Table 5.1 *Results obtained from the refinement of XRD data collected on $Sr_3Ir_2O_7$ at 200 K upon applied pressure in the crystallographic space group I4/mmm (No. 139).*

Space group: Tetragonal I4/mmm (No. 139)						
T = 200 K λ = 0.4859 Å I19 beamline						
P(GPa)	1.6	3.7	4.9	7.0	8.0	11.0
a(Å)	3.9036	3.8812	3.8695	3.8580	3.8570	3.8407
c(Å)	21.04	20.906	20.851	20.883	20.75	20.486
V(Å^3)	320.61	314.92	312.20	310.91	308.69	302.1
R$_{wp}$ (%)	2.4	2.3	1.6	6.1	7.7	7.9

The crystal of $Sr_3Ir_2O_7$ chosen for this experiment was (114 x 110 x 26) μm in size and presented an initial R-factor of 4.73% after XRD characterization in the I4/mmm space group (see pre-characterisation criteria and procedure in Sec. 5.1.1). Analogous loading to the one described for the REXS experiment in Sec. 5.2.3 was followed. The diamond anvil cell was initially closed at 0.6 GPa and diffraction pasterns of $Sr_3Ir_2O_7$ were collected at several pressure points reaching a maximum value of 11 GPa.

Results

The principal aim of this experiment was the determination of potential rotational changes in the IrO_6 units of $Sr_3Ir_2O_7$ induced by pressure at low-temperature, which potentially could explain the structural collapse of the samples and the progressive reduction of the magnetic moment observed by REXS. Since the oxygen atoms are considerably weaker x-ray scatterers than the much electronically denser elements Ir and Sr, the crystallographic refinement of the former is not trivial. Indeed, detailed analysis of the different sets of frames collected did not allow finding a combination of parameters to refine freely and anisotropically the oxygen sites, while keeping positive values for the atomic displacements within the I4/mmm space group. As an alternative, refinement of the data within the monoclinic distortion described by [245] (a = 20.917(3), b = 5.5080(1), c = 5.4995(7) and β = 90.069º) provided similar inconclusive results.

The crystallographic information from the analysis at each individual pressure point within the I4/mmm space group is provided in table 5.1 and illustrated in Figure 5.10. A reduction in the unit cell volume of 5.7% respect to the first point

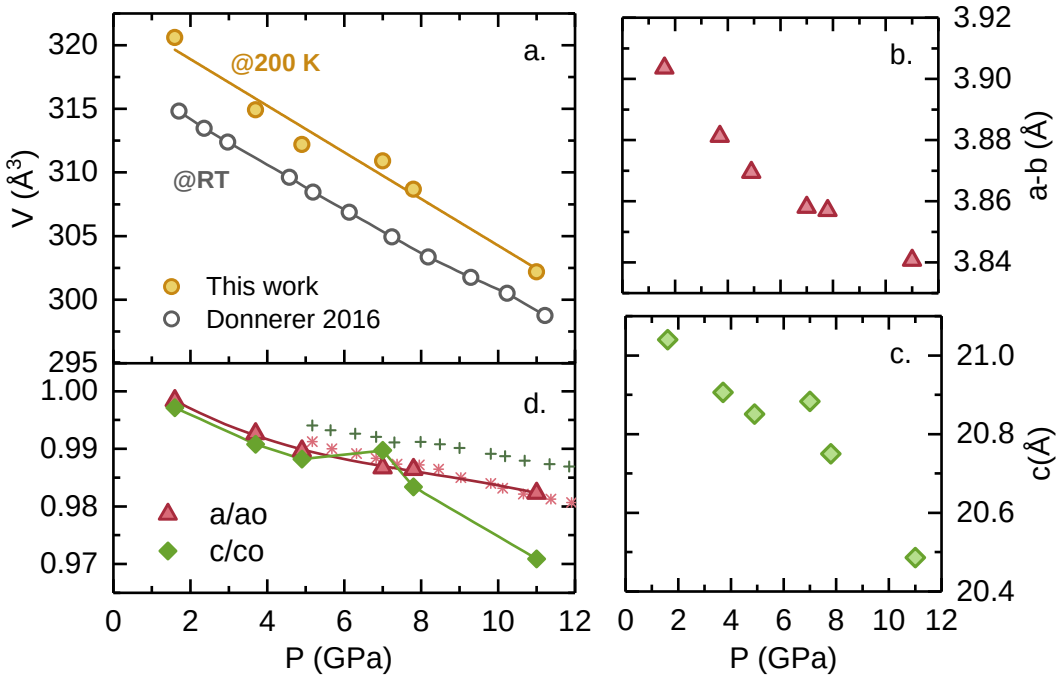

Figure 5.10 *Lattice parameters of $Sr_3Ir_2O_7$ as a function of pressure at 200 K.* ***a)*** *Evolution of the unit cell volume upon applied pressure at low and room temperature (RT), yellow circles and grey squares respectively. Data at RT was obtained from poly-crystalline samples and adapted from [248].* ***b)*** *and* ***c)*** *lattice parameters and* ***d)*** *normalised lattice constants as a function of pressure. Asterisks and crosses represent the values for a/a_0 and c/c_0 respectively, obtained from polycrystalline samples at 20 K from [248]*

of pressure collected at 1.6 GPa was observed, in line with the results obtained on polycrystalline samples at room temperature by Donnerer *et al.* [248] (see Fig. 5.10 a)). The evolution of the normalised lattice parameters follows the same trend for the a/a_0 axis in poly- and single-crystalline systems. However, larger relative compression is observed in the c/c_0 direction on single crystals respect to the data collected at 20 K in the poly-crystalline sample (see Fig. 5.10 d)).

Despite free anisotropic refinement of the oxygen positions was not possible, selective locking of the conflicting atomic displacement parameters (ADPs) into positive values, provided a rough estimation of the rotational tendency of the octahedral units displayed in Fig. 5.11. Given the magnitude of the error bars, careful examination of this set of data suggests marginal changes occurring in the Ir-O_3-Ir angle.

Further inspection of the precession images obtained at different values of

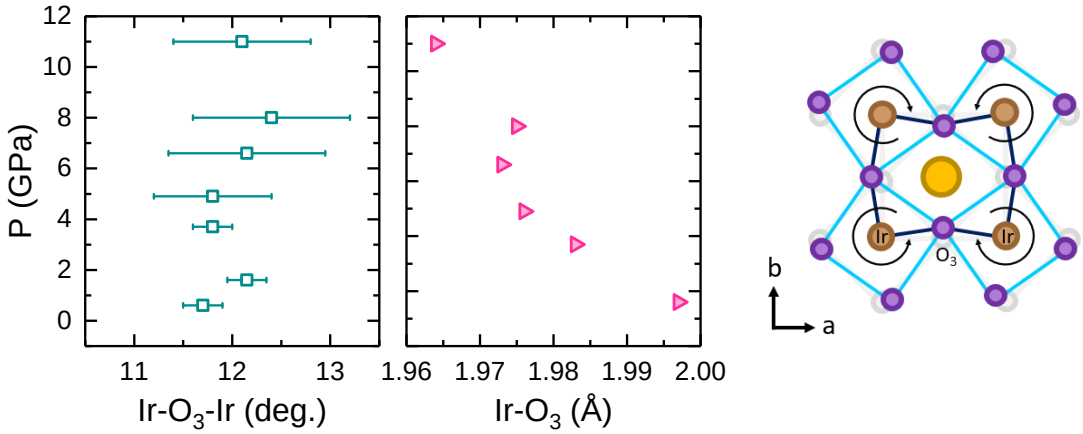

Figure 5.11 *Pressure dependence of the (Ir-O_3-Ir) angle in degrees and the distance (Ir-O_3) in angstroms. Schematic illustration of the in-plane IrO_6 octahedra rotation mechanism.*

pressure, reveals that the main source of structural distortion upon applied pressure occurred along the c-axis. The reconstruction of these images, depicted in Fig. 5.12, provides direct observation of the reciprocal space along planes (0lk), (h0l) and (hk0) after indexing in the I4/mmm space group. Above 5 GPa, a progressive asymmetric elongation in the peaks' profile can be seen along the c-axis in the images corresponding to the (0kl) and the (h0l) planes, while the crystalline order along the a-b directions remains in good shape (kh0 plane). Because of the large c/a ratio, one could expect the c-axis to undergo further adjustment upon compression than the a-b counterparts.

Unfortunately, the early mentioned limitations in the refinement and the limited access to the reciprocal space in the pressure cell, make difficult to provide a more sustained explanation for the local structural drift observed along the c-axis. Lack of hydrostaticity is discarded as potential cause, since the solidification of 4:1-ME at 200 K occurs at a critical pressure of $\sim$ 3.5 GPa (see Fig. 5.9), well below the starting point observed for the peak profile elongation (P $>$ 5 GPa).

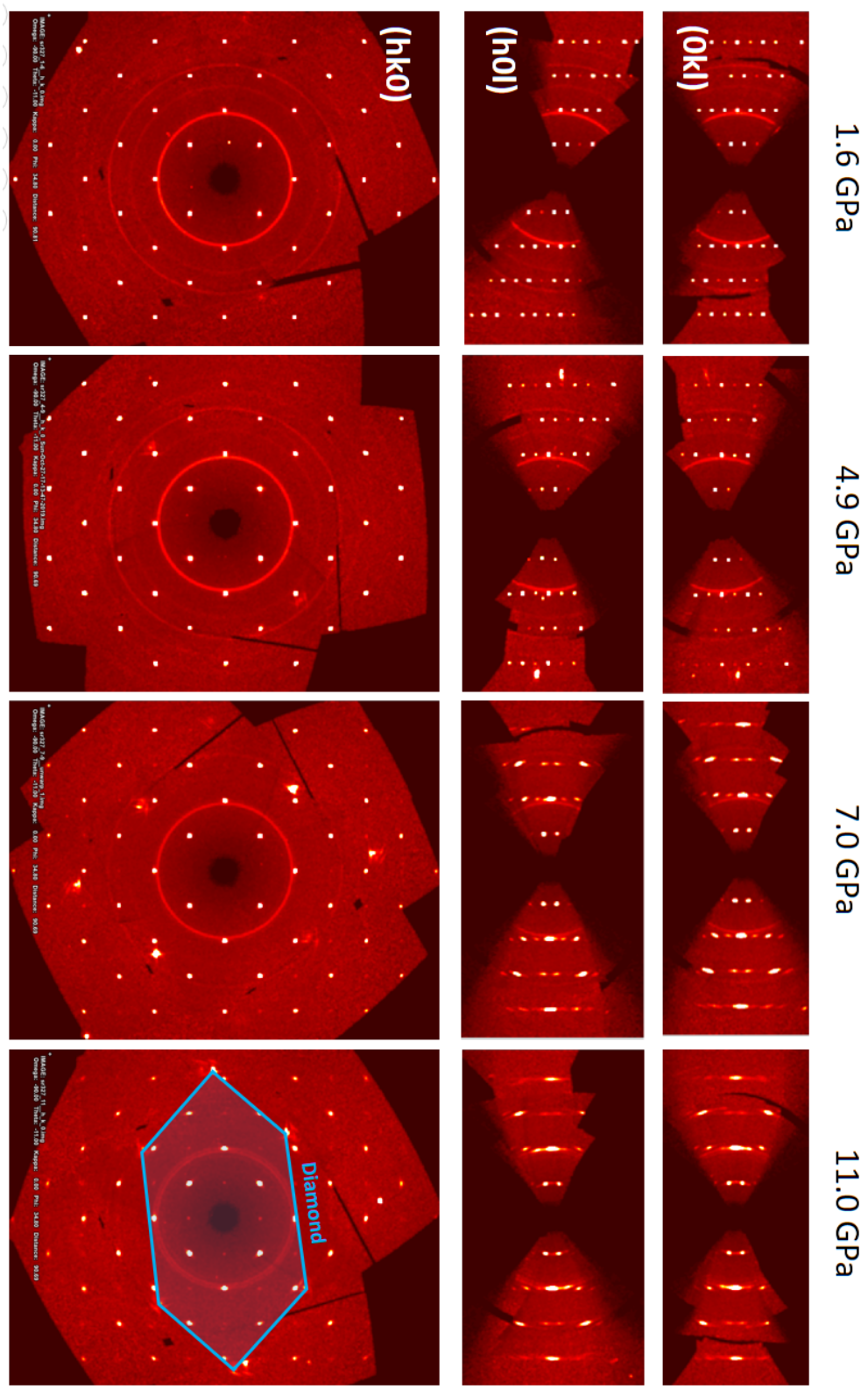

Figure 5.12 *Procession images of the planes (0kl), (h0l) and (hk0) reconstructed from diffraction data at different pressure values and 200 K on $Sr_3Ir_2O_7$. Detail of the diffraction peaks from diamond highlighted in blue in the image corresponding to the (hk0) plane at 11 GPa.*

5.3 Synergy between physical and chemical pressure: The case of $(Sr_{1-x}La_x)_3Ir_2O_7$

5.3.1 Introduction: Effect of La doping in $(Sr_{1-x}La_x)_3Ir_2O_7$

Elementary ionic substitution have been extensively used as an alternative method to recreate similar conditions to those attained through application of hydrostatic compression. Lattice parameters can be modified via exchanging ions with different atomic radius generating the so-called, positive (or negative) chemical pressure. However, the effects of these two methods are not always analogous. On the one hand, deviations from perfect crystalline order in the shape of higher mosaicity or structural defects are found to be more frequent in doped samples than in pure crystals. On the other hand, additionally to the structural degree of freedom, chemical substitution is frequently accompanied by alterations in the electronic density of the material as a result of the different number of electrons (Z) of the exchanged species. This often leads to the development of tails in the electronic gap, which in turn may facilitate the transition towards metallic character.

In the case of $Sr_3Ir_2O_7$, substitution of Sr^{2+} (Z = 38) with La^{3+} (Z = 57) has been proven to be a successful method to induce metallic behaviour [239]. Different experimental and computational studies are consistent in reporting that $\sim$ 5% of La doping is enough to fully close the electronic gap and induce an insulator-to-metal transition (IMT) in $(Sr_{1-x}La_x)_3Ir_2O_7$ [237, 238]. This IMT seems to be accompanied by a significant weakening of the magnetic order, yet not reaching full vanishing of the magnetisation even well into the metallic state [237]. By contrast, the insulating character of the pure system is more robust upon application of hydrostatic pressure, only achieving metallic conductivity in the proximity of 60 GPa [232, 240, 241]. Rather small distortions of the crystalline lattice were observed upon lanthanum doping [223], in contrast to the lattice contraction and octahedral rotation reported after the application of hydrostatic pressure [232, 241, 248, 249]. On account of these facts, it is reasonable to think that the IMT may be mediated by different mechanisms in pure and doped systems, based on structural distortions and due to a richer concentration of electrons respectively.

Despite the mentioned differences, both methods seem to be valid in order to drive $Sr_3Ir_2O_7$ into new exotic ground states. The synergic cooperation between electronic doping and the application of hydrostatic pressure could be an interesting via for probing the magnetic behaviour of this iridate in the proximity of the IMT. An increase in the density of electronic carriers potentially lowers the amount of hydrostatic pressure required to suppress T_N, providing suitable conditions to explore the vicinity of potential region of quantum criticality. Moreover, the requirement of lower values of pressure would reduce the risk of sample deterioration, key aspect given the structural distortions observed in the previous REXS and XRD experiments on $Sr_3Ir_2O_7$.

5.3.2 Evolution of the magnetic ordering of $(Sr_{1-x}La_x)_3Ir_2O_7$ under pressure by REXS

Experimental parameters

Samples of $(Sr_{1-x}La_x)_3Ir_2O_7$ were synthesised and characterised as explained in Sec. 5.1.2. Despite lower values of crystallinity were observed in the doped crystals with respect to the pure samples of $Sr_3Ir_2O_7$, several crystallites with R values below 5% were found suitable for the experimental requirements. Crystals showing EDX elementary emission lines of intensity corresponding to the stoichiometry $(Sr_{1-x}La_x)_3Ir_2O_7$ [x = 0.007(1)] were selected for the experiment (see Sec. 5.1.2 for details of the EDX characterization). Analogous loading and experimental parameters as for the REXS experiments on $Sr_3Ir_2O_7$ described in Sec. 5.2.3 were followed.

Results

The evolution of the magnetic ordering temperature of $(Sr_{1-x}La_x)_3Ir_2O_7$ [x = 0.007(1)] was explored upon increasing pressure on I16. At each pressure point, the intensity of the magnetic reflections with wave-vectors (0.5 0.5 2) and (1.5 1.5 2) was tracked upon progressive increase of temperature, using the ordinary charge peaks (110) and (112) as control references. Figure 5.14 a) illustrates a set of individual scans acquired during one of these temperature dependences at 6.3 GPa on the magnetic peak (0.5 0.5 2). The full set of data covering the pressure

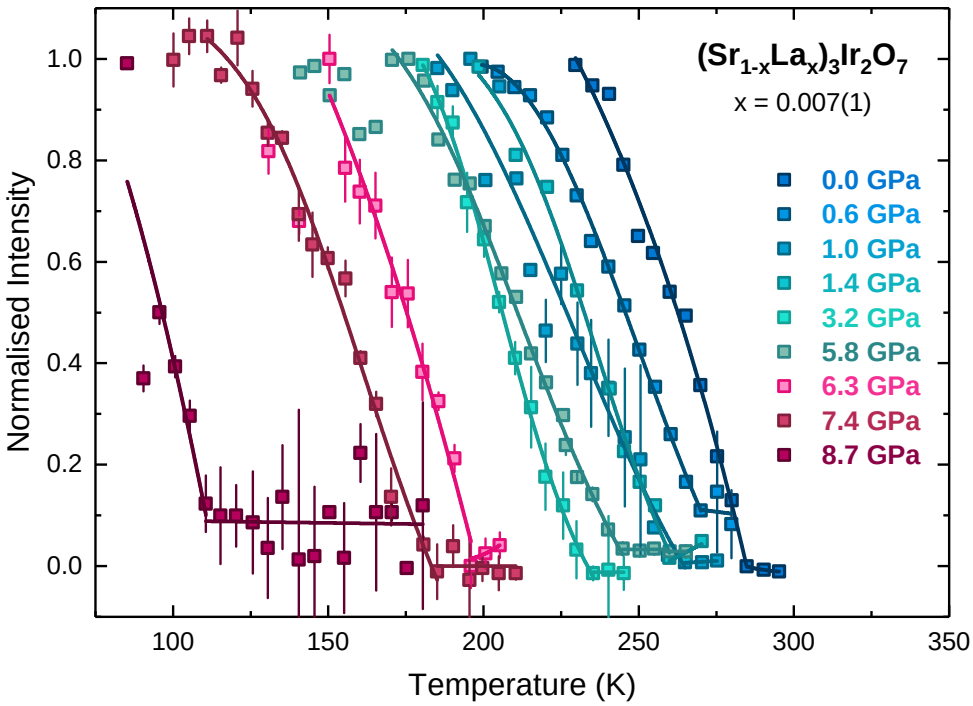

Figure 5.13 *Temperature dependences of the magnetic scattering intensity at different applied pressures in $(Sr_{1-x}La_x)_3Ir_2O_7$ [$x = 0.007(1)$], normalised to the intensity recorded at the lowest temperature measured.*

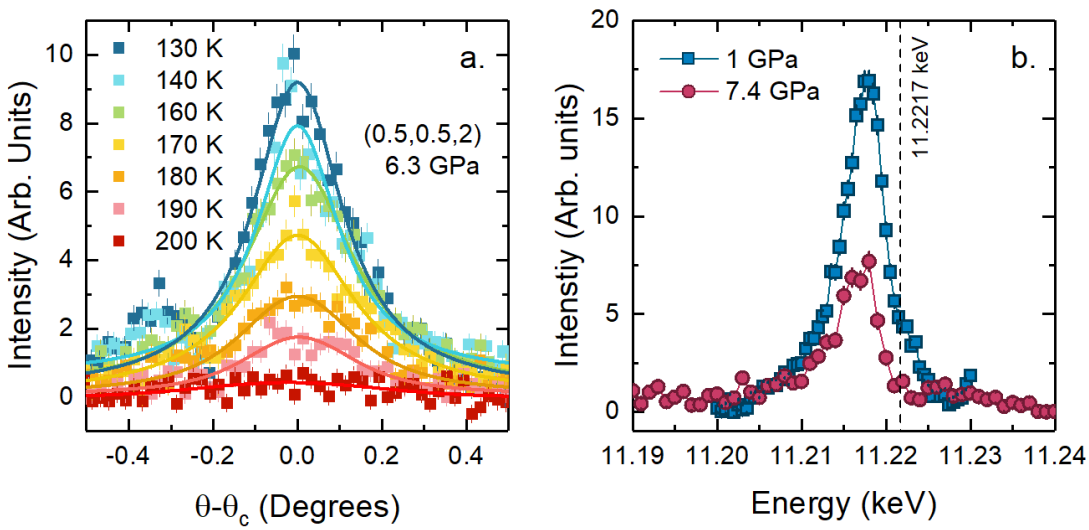

Figure 5.14 *a) Temperature dependence of the scattering intensity at the magnetic position (0.5,0.5,2) at 6.3 GPa of pressure. b) Scans of the incident photon energy on the same reflection at 1.0 and 7.4 GPa. Dotted bar at 11.2217 keV represents the white line.*

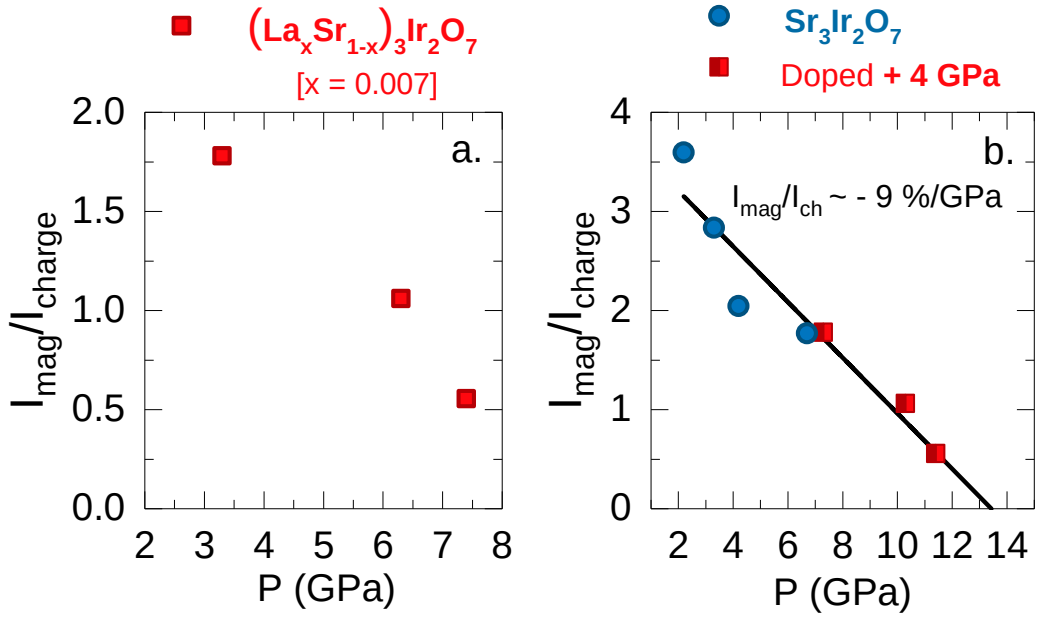

Figure 5.15 *a) Evolution of the ratio I_{mag}/I_{charge} upon applying pressure on $(Sr_{1-x}La_x)_3Ir_2O_7$ [x = 0.007(1)]. b) Joint representation of the I_{mag}/I_{charge} ratio obtained for the undoped and the doped system + 4 GPa shift.*

range between ambient up to 8 GPa is represented in Fig. 5.13. Scans of the incident photon energy at 1 and 7.4 GPa at the magnetic peak (0.5 0.5 2) are also shown in Fig. 5.14 b). At this position the resonance maximum occurs 3 eV below the white-line represented by the dashed vertical bar at 11.2217 keV.

Inspection of the data suggests that a doping level of [x = 0.007(1)] entails a linear shift of T_N(P) of *ca.* 20 K downwards in temperature with respect to the pure system. This variation is analogous to the suppression attained by applying $\sim$ 4 GPa of pressure on $Sr_3Ir_2O_7$. We observed a monotonic reduction of T_N(P) upon increasing pressure, which considering the mentioned adjustment (4 GPa shift), is remarkably symilar to the T_N variation in the undoped data.

From these results, we can confirm the persistence of three-dimensional long-range order up to at least 8 GPa of pressure. Above this value, the crystalline quality became consistently worse hindering the observation of magnetic reflections. It is important to remark the fact that the deterioration of the crystals started at a similar effective pressure in doped and pure systems on account of the 4 GPa conversion. This fact further supports the independence from the PTM of the structural and magnetic alterations encountered in $Sr_3Ir_2O_7$ and $(Sr_{1-x}La_x)_3Ir_2O_7$ [x = 0.007(1)].

Similarly to what occurred in the pure system, the application of pressure also induced a reduction in the magnetic ordered moment of $(Sr_{1-x}La_x)_3Ir_2O_7$ [x = 0.007(1)] illustrated in Fig. 5.15 a). The ratio between the magnetic reflection (0.5 0.5 2) and the charge peak (1 1 0) was calculated from sets of data obtained from the same crystal upon increasing pressure. Interestingly, a 4 GPa shift upward in pressure of the observed values for equivalency with the pure system, results in the linear decrease of the I_{mag}/I_{charge} ratio represented in Fig. 5.15 b). According to this data, the magnetic moment decreases at a rate of $\sim$ - 9-10% per GPa of applied pressure and complete vanishing of the magnetic order is expected to occur in the proximity of 14 GPa. This compares well with critical pressure of the magnetic transition described by Raman spectroscopy on $Sr_3Ir_2O_7$ [241].

5.4 Discussion

The analysis and discussion of the sets of data presented in this chapter has been done within the framework of a collaborative project comprising additional HP-RIXS experiments and computational modelling as explained in the introduction of this chapter. Joint examination of experimental and simulated data, suggests the realisation of a potential spin-flop magnetic transition for $Sr_3Ir_2O_7$ at P $\sim$ 15 GPa, indicative of a change of effective dimensionality of the magnetic interactions from 3D to 2D. Characteristics of quantum criticality have also been observed and will be discussed in the following.

Figure 5.16 summarises the results obtained from all sources of data considered during the analysis in the shape of a P-T electronic phase diagram for $Sr_3Ir_2O_7$. As it can be seen, our experimental values of T_N(P) obtained by REXS on La-doped and pure $Sr_3Ir_2O_7$ are in remarkably good agreement with the trend followed by the values obtained by Raman spectroscopy [241] and RIXS measurements.

High-pressure RIXS examination of $Sr_3Ir_2O_7$ revealed an unusually large spin-wave gap ($\sim$ 90 meV) along the entire Brillouin zone (BZ) and the splitting of acoustic and optic branches up to 12 GPa of pressure [2]. Above this value, the sample broke in a similar fashion to what happened during REXS experiments in doped and undoped systems. Softening of the acoustic branch occurs more rapidly than in the optic counterpart towards the maximum value of pressure as

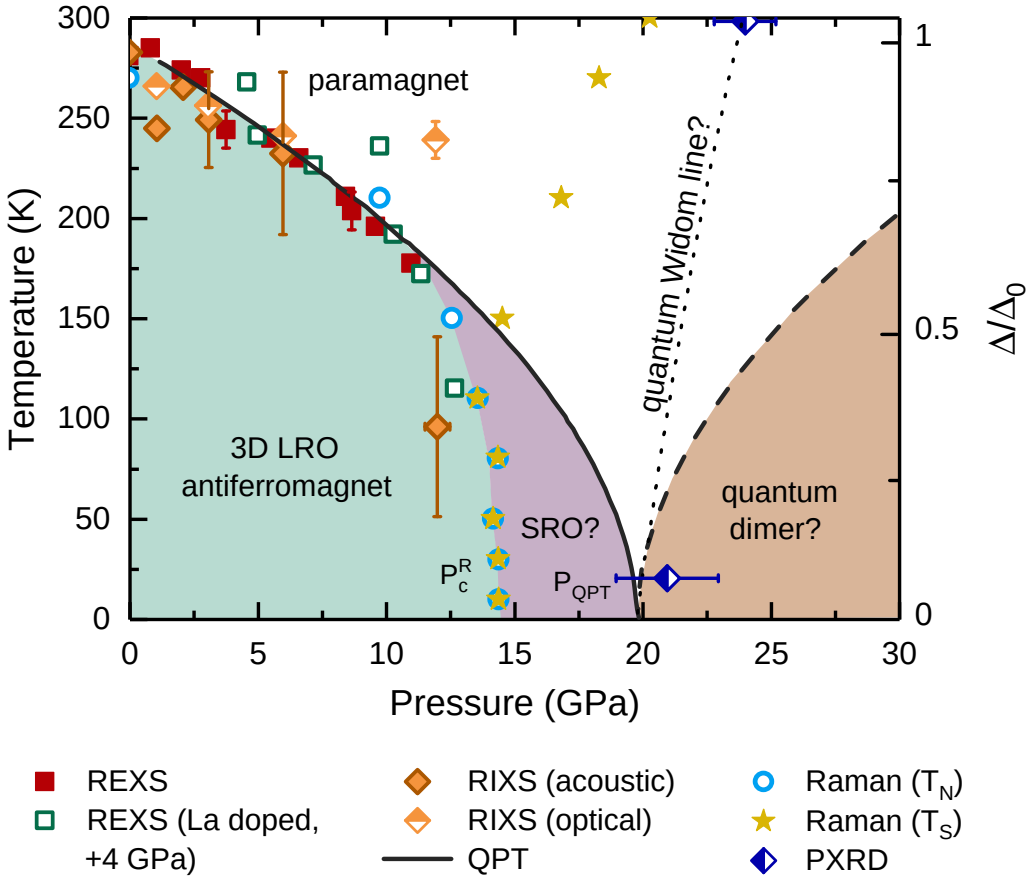

Figure 5.16 *Combined P-T electronic phase diagram for $Sr_3Ir_2O_7$ including data obtained by the different techniques mentioned in the main text [241, 253]. Scale on the right vertical axis stands for the the acoustic and optical spin wave energies Δ normalized by their ambient pressure values Δ_0. Abbreviations LRO and SRO for long- and short-ranged order.*

shown in Figure 5.16.

Analysis within the linear spin-wave theory (LSW) allows establishing a model where the numerous coupling parameters considered can be expressed as a function of four terms: the octahedral rotational angle α, the ratio between the Hund's coupling and the on-site Coulomb interaction $\eta = J_H/U$, a d-d transfer integral including the oxygen between two Ir positions (t), and an effective anisotropy term θ, which in turn contemplates the magnitude of the spin-orbit coupling and the crystal field splitting [251, 255, 256]. In a qualitative approach, the evolution of these four terms upon increasing pressure is expected to act as follows. Since the Hund's coupling J_H is mostly an atomic parameter, η is assumed to be independent of pressure. An increase in the spin-wave energy is

expected in the central (π, π) and boundary $(\pi,0)$ positions of the BZ as a function of increasing t and/or θ. Finally, small variations in the angular rotation α of the IrO_6 units are not expected to modify the SW dispersion significantly.

By applying this model to the values obtained for the spin wave energy at HP in the central (π, π) and boundary $(\pi,0)$ positions of the BZ, we found that only simultaneous increase of t, and decrease of θ, fits the experimental data. Figure 5.17 illustrates the results of this analysis. In the first panel (Fig. 5.17 a)), we can see the fitted values of spin wave energies for different values of pressure, overlaid with the theoretical dispersion that best matches the experimental data at 0 and 12 GPa, where solid and dashed lines correspond to acoustic and optical branches respectively. In the remaining panels is represented the individual theoretical evolution of θ, α and t upon applied pressure. Increase of electron hopping is expected as a result widening in the electronic bands ($W \propto 2zt$), which in turn favours the orbital overlapping. α suffers rather small variations upon applied pressure, in broad agreement with the experimental values for the angle of rotation obtained from the single crystal XRD experiment reported in Section 5.2.4 (open symbols in Fig. 5.17 c). Finally, θ is expected to decrease as pressure builds up.

Variations in the effective anisotropy have been described as driving force for spin-flop magnetic transitions in spin-orbit mediated $J_{eff} = 1/2$ systems [33, 229, 230, 255, 256]. The strong SO interaction takes the system away from the isotropic Heisenberg picture of the magnetic exchange, into an anisotropic regime where the magnetic spin direction is mainly dictated by the lattice geometry. The intimate interlace between these two degrees of freedom, results in a collinear antiferromagnetic order with the mangetic moments pointing along the c-axis when θ is above a critical value, and canted antiferromagnetism within the ab-plane wherein is below.

According to the investigations conducted by Kim *et al.* [251], the critical values for the spin-flop transition happen to be $\theta \sim 0.21\pi$ and $\eta = 0.27$ for $Sr_3Ir_2O_7$. From the progressive decrease of θ upon applied pressure deduced from RIXS data, we found that this transition from collinear to canted antiferromagnetism may occur at a critical pressure $P_0 \sim 18$ GPa, in broad agreement with the $P_c^R \sim 14$ GPa observed by Raman spectroscopy [241]. Parallel DFT calculations predicts a 3% of epitaxial compression strain at the critical flip point. Extrapolating from the compression of the ab lattice parameters observed in the

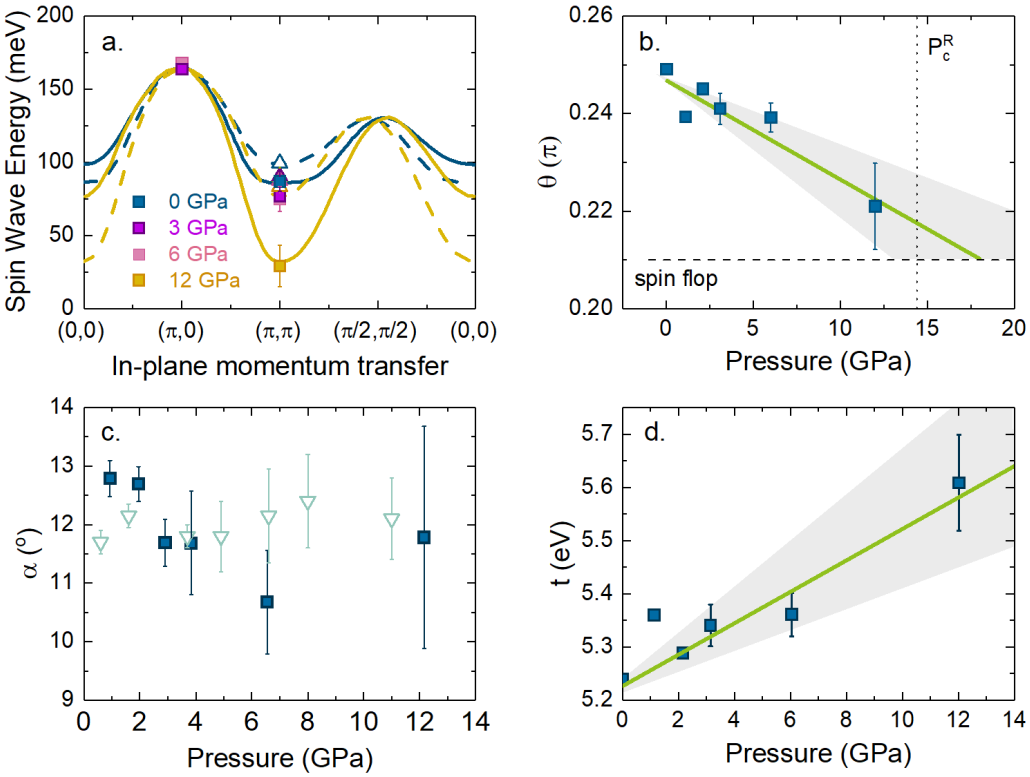

Figure 5.17 *Modeling of HP-RIXS spectra of $Sr_3Ir_2O_7$ within the linear spin wave model [253]. a) Fitted values of spin-wave energy dispersion that best describes the experimental data. Solid and dashed lines (full and empty symbols) stand for acoustic and optical branches respectively. Values for b) the effective anisotropy θ, c) the rotation angle α and d) the electron hopping constant t, obtained from best fit to the spin wave dispersion for each P point. Shaded area in b) and d) represent the confidence intervals. Open symbols in c) correspond to the values of α determined from single-crystal XRD on $Sr_3Ir_2O_7$ at 200 K within (see Section 5.2.4).*

experimental results shown in Section 5.2.4, we found that the critical point for the spin-flop transition is reached at 18 GPa, as illustrated in Figure 5.18 a).

In order to further confirm this hypothesis, the minimum energy Hamiltonian describing the magnetic structure upon increasing pressure was also calculated within the mean-field approximation and Monte-Carlo simulations. In both cases, a critical value of $P_0^{calc} \sim 18$ GPa for $T \to 0$, was found for the transition from collinear along c to canted-antiferromagnetism within the a-b plane in good agreement with the previous values. Figure 5.19 illustrates the spin-canting process upon increasing pressure obtained from Monte-Carlo simulations. The temperature dependence of $T_N(P)$ was also well described by both methods up to 12 GPa. In Figure 5.18 b) it can be seen a summary of the experimental and

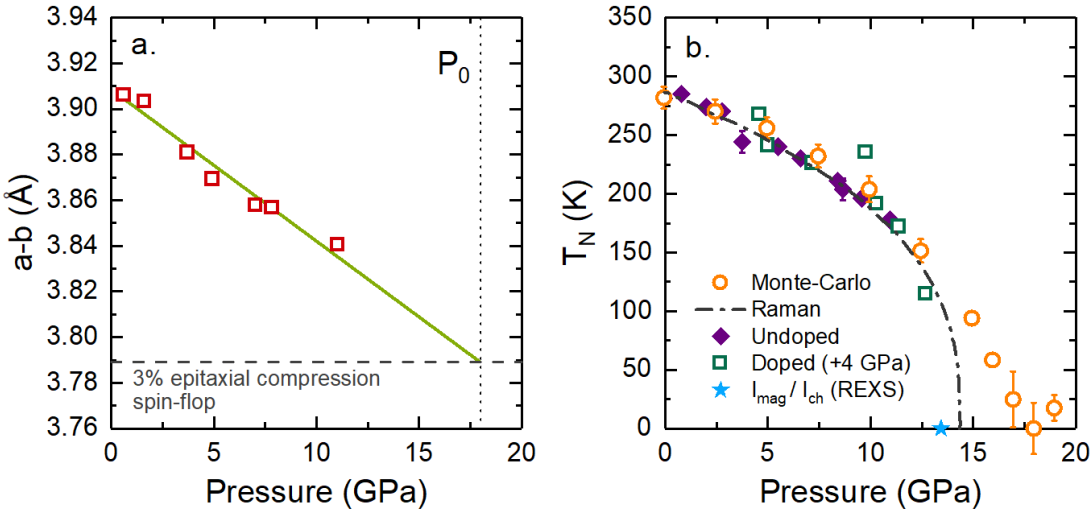

Figure 5.18 *a) Epitaxial compression of the ab-lattice parameters upon increasing pressure obtained from single-crystal XRD and intersection with the predicted value for the spin-flop transition P_0 (3% of epitaxial compression). b) Summary of the evolution of T_N (P) upon pressure from experimental and Monte-Carlo simulations. Raman data adapted from [241].*

calculated values of T_N(P) for doped and undoped $Sr_3Ir_2O_7$ by REXS, Raman scattering and Monte-Carlo simulations on the pure material. The blue star also represents the critical pressure at which the magnetic moment vanishes according to the I_{mag}/I_{charge} ratio.

The difference between the experimental value P_c^R observed by Raman and the critical pressure P_0 predicted by different methods, may rely on the assumptions made for the modelling such as invariant tilt around c or fixed η, since bandwidth broadening upon applied pressure is expected to reduce the Coulomb repulsion). Additionally, the presence of quantum fluctuations affecting the electronic ground state can also be significant in $J_{eff} = 1/2$ at low temperature and are neglected in both, mean-field and Monte-Carlo simulations.

First order staggered magnetization per spin is given by $< m > = S - \epsilon$, where ϵ contemplates quantum fluctuations and S stands for the spin quantum number. By simulating the PT dependence of <m> using the spin-wave dispersion calculated for the RIXS data at different values of pressure, we found that <m> tends to 0 at a critical pressure of $P_{QCP} \sim 20$ GPa for all temperatures, which may be an indication of quantum phase transition (QPT). Although P_{QCP} is significantly highier than P_c^R, it is remarkably close to the first-order structural

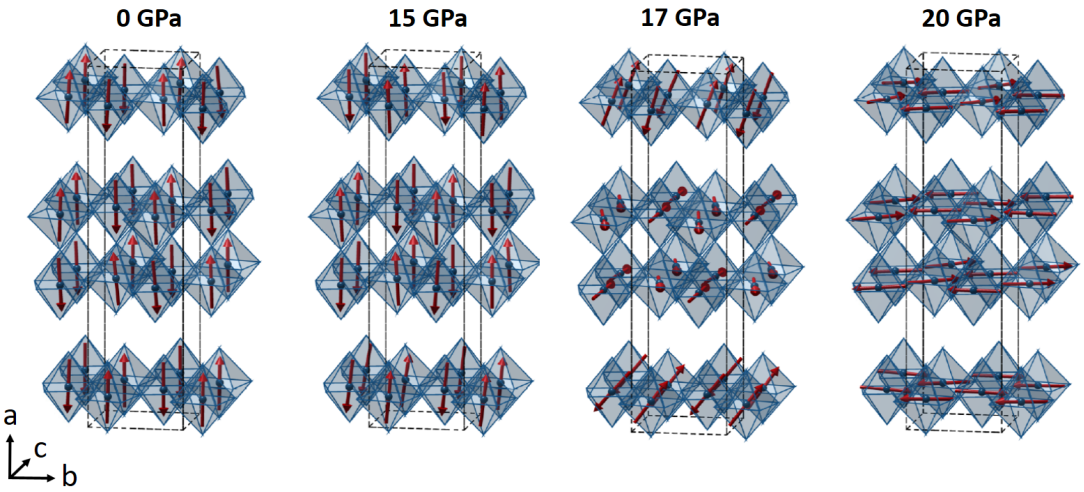

Figure 5.19 *Spin configuration at T = 0 for various pressures, determined from classical Monte-Carlo simulations. A spin-flop transition occurs between 15 and 20 GPa. Unit cell within the monoclinic space group C2/c (No. 15).*

transition observed by PXRD at 20 K (see Figure 5.16) [248].

Another possibility is the presence of a tricritical point at 13 GPa supported by the coincidence between $T_N(P)$ and $T_S(P)$ below 100 K observed in the Raman study [241] close to P_c. This would somehow explain the degradation in the sample quality above 12 GPa, observed in REXS and RIXS experiments.

The presence of a first order structural transition coincident with a potential QPT, could give rise to the existence of a quantum widom line (QWL) in $Sr_3Ir_2O_7$; *i.e.* a line in whose proximity there is continuous evidence of strong quantum fluctuations for all values of PT, until reaching a minimum critical point (P_c, T_c) (dotted vertical line in Fig. 5.16).

Because of the close similarity observed to the phase-diagram of MnSi [257, 258], a final point needs to be made regarding the potential magnetic ground state that may occur between P_c and P_{QCP}. In MnSi, the region delineated by the mismatch of P_c and P_{QCP} seems to present partial electronic order in the shape of helical fluctuations. Whether this or some other exotic quantum behaviour takes place in this region is still to be disclosed. Likewise, experimental observation of the canted two-dimensional antiferromagnetic order predicted to occur in the proximity of 18 GPa remains subject of further experimental investigation.

.

Chapter 6

Final remarks and future prospects

Contents

In this final Chapter, I provide a short summary of the principal results of this thesis. First of all, I enumerate the main characteristics of the HP system designed for conducting REXS experiments on I16, followed by an overview of the future perspectives of the field. In a similar manner, there is a discussion on the major results obtained from studying the magnetic order of $Sr_3Ir_2O_7$ and the doped counterpart $(Sr_{1-x}La_x)_3Ir_2O_7$ under pressure. These results prove the unrivalled potential and versatility of HP-REXS experiments for the study of intermediate to strongly correlated states with competing energy scales in 5d TMOs.

6.1 Novel technological means for HP resonant x-ray studies

With regards to the technological side of the HP-REXS experiments, I have presented the design of a high-pressure system consisting of an asymmetric membrane-driven diamond anvil cell for operation in back-scattering geometry. The cell presents a wide aperture fitting a maximum scattering angle of 100 degrees. The new setup also includes a panoramic dome and a set of fibre optics to measure the level of pressure *in situ* at low-temperature using the luminescence of ruby. These characteristics, remote membrane actuation and low-temperature pressure tuning, are particularly beneficial for the performance of synchrotron experiments, which are often costly and time-limited. The possibility of changing pressure at low temperature eliminates the need to thermally cycle to room temperature with each pressure change, maximising the time efficiency during the experiment.

Different tests demonstrated the successful performance of the setup, including a membrane burst trial and different P-T off-line tests that ensured safe use up to 20 GPa of pressure (for anvils of 500 μm of culet diameter), and down to 30 K of temperature. The compact dimensions of the cell, 57 mm in diameter and *ca.* 20 mm in height, allow easy coupling to other cryostat models available at most of the large research facilities. Simple modifications to the cell body and the dome could ready this design for use at other beamlines. Another key parameter for HP-REXS experiments is the absorption from diamonds. Values of excitation energy below 8 keV were found to be critical using anvils 1.25 mm thick. Nevertheless, measurement at the Ni K-edge (8.333 keV) was successfully

tested on I16.

In spite of the fact that the HP-REXS setup meets the initial project target, a few aspects could be further improved in the future. For example, the measurement of the ruby fluorescence is at times compromised by the progressive lift of the sample chamber with respect to the fibre-tip when inflating the gas membrane to increase pressure. Defocusing and a significant loss of intensity in the ruby signal occurs when the distance between the fibre-tip and the sample chamber grows. Use of either adjustable optics outside the cryostat or alternative pressure gauge methods as the equation of state of gold, were considered to amend this problem. On the one hand, using external optics implies higher complexity and higher cost with respect to the current optical setup. On the other hand, the use of the lattice parameters of gold as pressure scale is significantly more time-consuming in I16 than the measurement employing a ruby, while not resulting in a superior accuracy at low temperature.

The second improvement to explore is the reduction of the pressure cell dimensions. A smaller DAC would allow both scattering in Laue geometry and a reduction of the minimum temperature inside the cryostat. Freeing space makes possible fitting additional shielding stages to improve the thermal insulation. Unfortunately, a reduction of the m-RXS DAC size is not possible without sacrificing the membrane capacity. In order to explore alternatives, a new cell was designed based on a wedge actuating mechanism. The wedge-DAC presents more compact dimensions to operate in transmission. However, full development of this setup requires redesigning the cryostat dome and building an external optical system, which is therefore left to future work.

6.2 Pressure tuning of the magnetic nature of $Sr_3Ir_2O_7$ and $(Sr_{1-x}La_x)_3Ir_2O_7$

This thesis explores the potential HP-REXS experiments have in the study of 5d correlated materials. In particular, the magnetic nature of $Sr_3Ir_2O_7$ and $(Sr_{1-x}La_x)_3Ir_2O_7$ [x = 0.007(1)] was investigated upon the application of static pressure. Analysis of the data revealed that $T_N(P)$ decreased progressively in $\sim$ -10 K/GPa in both pure and doped systems as the pressure was increased up to 12 and 8 GPa respectively. The effect of 0.7% La doping in the magnetic ordering

temperature is equivalent to the application of 4 GPa of static pressure on the pure system. Considering this shift, $T_N(P)$ follows remarkably similar trends in both while remaining consistent with the ordering temperature values estimated from HP Raman spectroscopy data on $Sr_3Ir_2O_7$ [241] (see Fig. 5.16).

A linear decrease in the ordered magnetic moment was also observed in pure and doped samples upon an increase in pressure. Similar application of a 4 GPa shift upwards in pressure on the data set from the doped material and joint analysis with the $Sr_3Ir_2O_7$ data, revealed a linear reduction in the magnetic ordering moment of 8-9% per GPa. Extrapolation of the linear fit that best describes this trend, predicts vanishing of the long range magnetic order in the proximity of 13.5 GPa, in good agreement with the magnetic and structural transitions recently reported by Zhang *et al.* [241].

Change in the correlation length or the realisation of a disordered state are both possible explanations for the loss of ordered magnetic moment. Three-dimensional hkl-analysis of the FWHM shows a concurrent isotropic broadening of the magnetic and charge reflections above $\sim$ 8 GPa. The absence of either a significant shift in the peak positions or a sign of directionality in the FWHM widening, suggests the correlation is constant within the range of pressure explored. Additionally, an alteration of the magnetic structure symmetry is also not possible since no extra reflections were found after mapping the portion of the reciprocal space accessible within the pressure cell limits. There are therefore two possible scenarios which could justify the reduction of the magnetic moment projected along the c-axis. On the one hand, a magnetostriction effect could be contributing to the distortion and the eventual collapse of the crystalline structure upon increasing pressure. Consequently, the sample may break into smaller crystallites which are slightly tilted with respect to each other. This would reduce the coherence of the magnetic order and in turn, the magnitude of the resulting moment. On the other hand, a coordinated distortion of the spins pointing along the c-axis towards the ab-plane may occur, transferring a fraction of the moment to the ab-plane. Unfortunately, the experimental evidence does not allow to establish the prevalence of one these hypothesis over the other since the crystalline quality of the samples was systematically spoiled above $P_c \sim 12$ GPa.

Computational modelling of the spin-wave energy dispersion obtained by RIXS up to 12 GPa in the central (π, π) and boundary $(0, \pi)$ positions of the BZ, reveals

that only a simultaneous decrease in the effective anisotropy θ and an increase of the electronic-hopping constant t can effectively describe the experimental data. The two remaining parameters considered within LSW theory, namely $\eta = J_H/U$ and α, were assumed and predicted to remain constant respectively. The latter is in good agreement with the marginal octahedral rotation observed experimentally by HP-XRD. Changes in the anisotropy term have been described as the precursor of spin-flop transitions in spin-orbit mediated $J_{eff} = 1/2$ systems [33, 229, 230, 255, 256]. Interpolation of the critical values reported by Kim *et al.* [227] within the parameters determined by HP-RIXS data, predicts a potential spin-flop transition at $P_0^{calc} \sim 18$ GPa in $Sr_3Ir_2O_7$. Parallel DFT and Monte-Carlo calculations of the epitaxial compression and the lowest energy magnetic Hamiltonian at which the spin-flop transition may occur, reveal similar critical pressure values in the proximity of 18 GPa, further supporting the spin-canting hypothesis.

As previously discussed, this transition is one of the potential scenarios that could account for the progressive loss of magnetic ordered moment observed by REXS upon increasing pressure. Similarly, direct experimental validation of this mechanism was not possible via HP-RIXS since an analogous consistent degradation of the sample quality occurred in all the experiments above $P_c \sim 12$ GPa.

In the case of the HP-REXS studies conducted on $(Sr_{1-x}La_x)_3Ir_2O_7$ crystalline deterioration occurred at much lower pressure of 8 GPa, well below the 12 GPa observed for the pure system. The disparity between these values is indicative of independence from the PTM as the potential cause of the sample degradation. Nevertheless, considering that 0.7% of La doping reduces the magnetic ordering temperature the same as the application of a 4 GPa of pressure in $Sr_3Ir_2O_7$, crystalline degradation occurs at equivalent levels of strain in doped and pure materials.

The P_0^{calc} values calculated through different methods are in broad agreement with the experimental evidence ($P_c^R \sim 14.4$ GPa [241], $P_{I_{mag}/I_{ch}\to 0} \sim 13.5$ GPa and $P_c \sim 12$ GPa). Different factors may be responsible for this inconsistency. Firstly, $\eta = J_H/U$ may vary given the bandwidth broadening expected upon increasing pressure and the consequent reduction of the local Coulomb repulsion U. Secondly, quantum fluctuations which are neglected in mean-field and Monte-Carlo simulations, can often be significant in $J_{eff} = 1/2$ systems, potentially

leading to an overestimation of the critical pressure values.

Additional PT-modelling of the staggered magnetization per spin <m> which considers quantum fluctuations predicts a quantum critical point at $P_{QCP} \sim 20$ GPa for all temperatures. This may point towards the existence of a quantum phase transition (QPT). In a similar manner to what occurs in MnSi [257, 258], the presence of both a tricritical point at P_c and a region of quantum criticality at higher pressure are compatible. The area delimited by the mismatch between P_c and P_{QCP} may be the realm of exotic quantum behaviour. Further work is certainly required to obtain experimental evidence of the electronic order in this area and to prove the potential canted two-dimensional antiferromagnetic order predicted in this study.

6.3 Final discussion and future developments

This thesis demonstrates the substantial potential of REXS in the study of electron correlated materials under high-pressure conditions. In particular, HP-REXS results are extremely advantageous for the investigation of magnetism in single-crystals, which is otherwise often compromised by the larger sample volumes needed in neutron scattering. Therefore, the development of this technique opens the door to a new tantalizing territory of physics full of exciting phenomena. The encouraging experimental results obtained from investigating the magnetic order of $Sr_3Ir_2O_7$ are just a single example of the vast number of materials that can be studied using HP-REXS. Compounds containing 5d elements are a vibrant arena for investigating intermediate to strongly correlated states with competing energy scales.

The design of high-pressure instrumentation specifically dedicated to REXS experiments is rather scarce. Mostly challenged by the strong absorption from the diamond anvils in the range of energies commonly exploited (< 13 keV) and due to the spatial restrictions imposed by the cryogenic environment often required to observe the electron-correlation phenomena. Nevertheless, recent technological developments are bringing researchers closer to meeting these ambitious demands. The instruments proposed here are a clear example of it.

In addition to the m-RXS setup, further developments can be done in the following directions. The wedge-driven design discussed in Section 4.3.2 could

be a good alternative for operating in transmission geometry and for coupling with a CCR unit. Pressure cells of smaller dimensions are crucial in order to fit within the limited space available inside this type of compact cryostat. More bulky cryogenic units are able to reach lower temperatures and to accommodate larger pressure cells. However, they heavily restrict the angular freedom provided by a 6-axis kappa diffractometer, a key aspect in REXS experiments which aims to maximise the number of accessible diffraction angles. Another remarkable contribution is the incorporation of wide-angle partially perforated anvils that contradicting general intuition, present remarkably high strength in spite of the large volume of anvil material removed from them to reduce the beam absorption. This type of anvils would grant access to materials presenting a lower energy absorption edge below 8 keV.

Another important development for the field is the assessment of the accuracy of the applied pressure scales under cryogenic conditions. Traditionally, the focus of high-pressure research has been on achieving high-temperature conditions for geological studies. Given the relative novelty of high-pressure cryogenic investigations, it is therefore crucial to re-evaluate the reliability of the pressure gauges employed at low-temperature.

Aside from the factors which strictly involve high-pressure instrumentation, a natural extension of HP-REXS studies is the addition of magnetic fields necessary to probe the broader three-dimensional space of (H, P, T). Materials such as the Berylco alloy which was utilised in the construction of most of the cell parts presented in this thesis, show very low magnetic-permeability and are useful for this purpose.

Another interesting upgrade is the capability of tuning the angular polarisation of the incident beam. This opens the possibility of recovering the lost geometrical sensitivity due to the confinement of the sample within the pressure cell that impedes the rotation around the scattering vector (azimuthal scan). In this way, variations in the projection of the magnetic moment with respect to the incident beam polarisation can be proved keeping the sample steady.

Finally, the advent of the 4th generation synchrotron radiation sources is expected to significantly improve the counting statistics of HP-REXS studies, which will drastically reduce the acquisition time and enhance the sensitivity, enabling detection of weaker electronic correlations. Combining all these developments

holds much potential for future investigations in the field of intermediate to strongly correlated materials.

6.4 Conclusions

- On the technical side of this thesis, a new high-pressure setup was designed to perform HP-REXS experiments on I16, a world-class beamline to study strong to moderate electronic correlations.
- The new system consists of a membrane-driven pressure cell (m-RXS DAC), a set of optics and a panoramic dome for x-ray scattering in Bragg geometry through a 100° solid angle aperture.
- Pressure can be continuously tuned by inflating a metallic gas-membrane at low temperature and a system of optical fibres is used to excite and collect the fluorescence of ruby as pressure gauge.
- The HP-REXS setup is able to operate at a maximum pressure of 20 GPa using anvils of 500 μm in culet diameter and between ambient and 30 K of temperature.
- The m-RXS DAC is only 56 mm in diameter and *ca.* 20 mm in height, allowing easy coupling with the most common cryostat models available in large research facilities.
- The minimum excitation energy at which the diamond absorption becomes critical lies just above 8 keV for anvils 1.25 mm thick. Collection of resonant scattered reflections at the Ni K-edge (8.333 keV) was possible and tested by studying $AgNiO_2$ under pressure on I16.
- An additional pressure cell based on a wedge-driving mechanism was partially developed.
- The wedge-DAC presents a more compact design with respect to the membrane-driven counterpart. It aims to operate in Laue -transmission- geometry and to lower the minimum temperature accessible.
- The extra space made available by the wedge-DAC with respect to the m-RXS cell can be used to accommodate additional shielding stages improving

the thermal insulation of the cryostat. Full development and testing of this prototype is subject of future research.

- On the scientific part of this thesis, the magnetic behaviour of $Sr_3Ir_2O_7$ and 0.7% La doped $(Sr_{1-x}La_x)_3Ir_2O_7$ was studied by REXS between atmospheric and 12 GPa of pressure.

- The application of static pressure suppresses the magnetic ordering temperature T_N in both, doped and undoped systems, at a rate of -10 K per GPa applied.

- The effect of 0.7% La doping in the magnetic ordering temperature is equivalent to the application of 4 GPa of pressure on the pure system.

- A linear reduction of the magnetic ordering moment of $-$ 8-9%/GPa occurred within the range of pressure explored. Extrapolation of the linear fit that best describes this trend, predicts the long range magnetic order vanishes at $P_{I_{mag}/I_{ch}\to 0} \sim 13.5$ GPa.

- Neither a change in the correlation length of the magnetic order (3-D FWHM analysis) or the alteration of the magnetic structure symmetry seem to be responsible for the loss of magnetic moment.

- Rather magnetostriction effects or a coordinated distortion of the spins pointing along the c-axis towards the ab-plane may be the cause of the magnetic order reduction.

- Experimental evidence for coordinated spin distortion was not possible since the crystalline quality of the samples was systematically spoiled in the proximity of 12 GPa.

Appendix A

Technical drawings for the m-RXS DAC

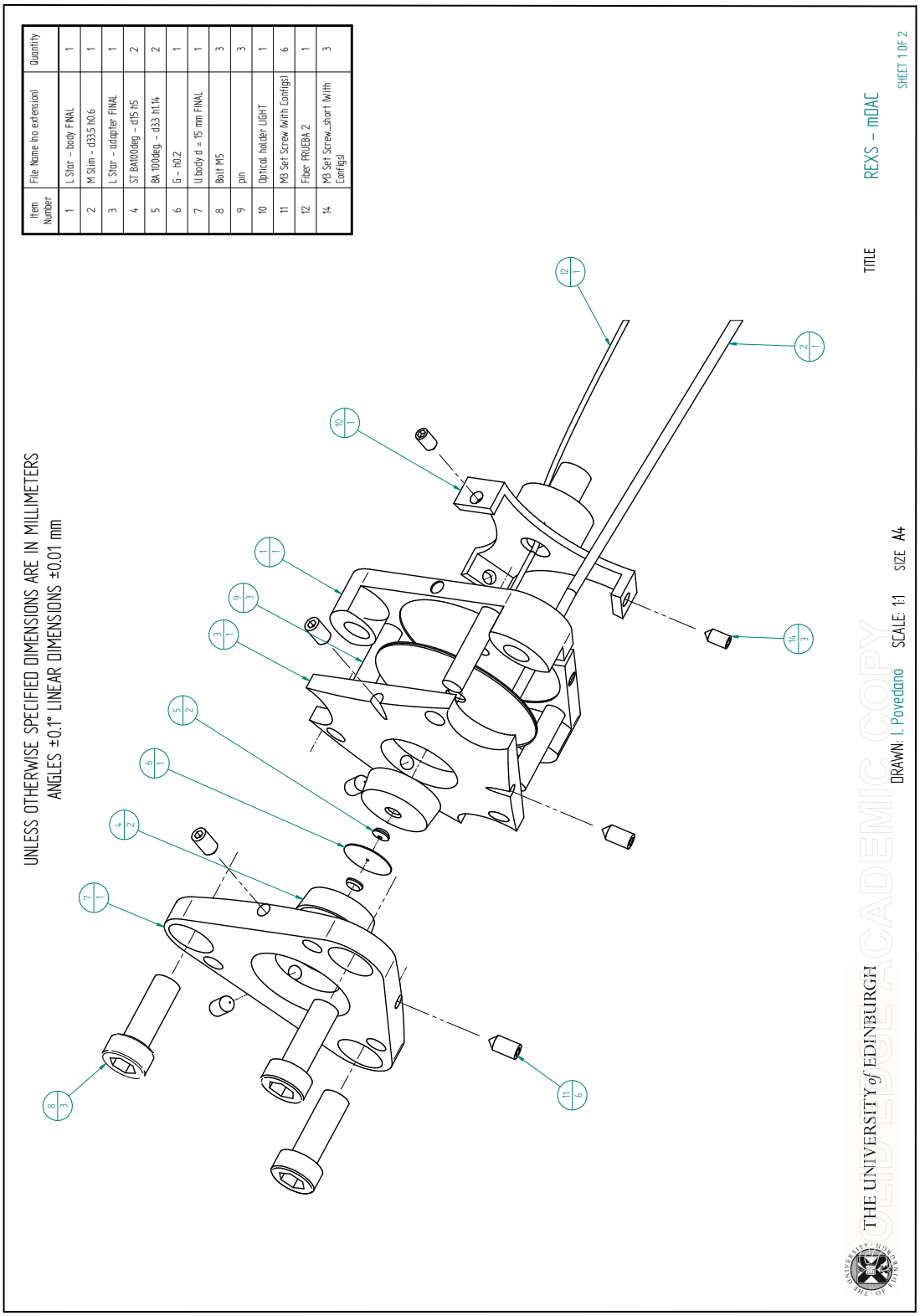

Figure A.1 *Exploded view of the membrane DAC for REXS experiments.*

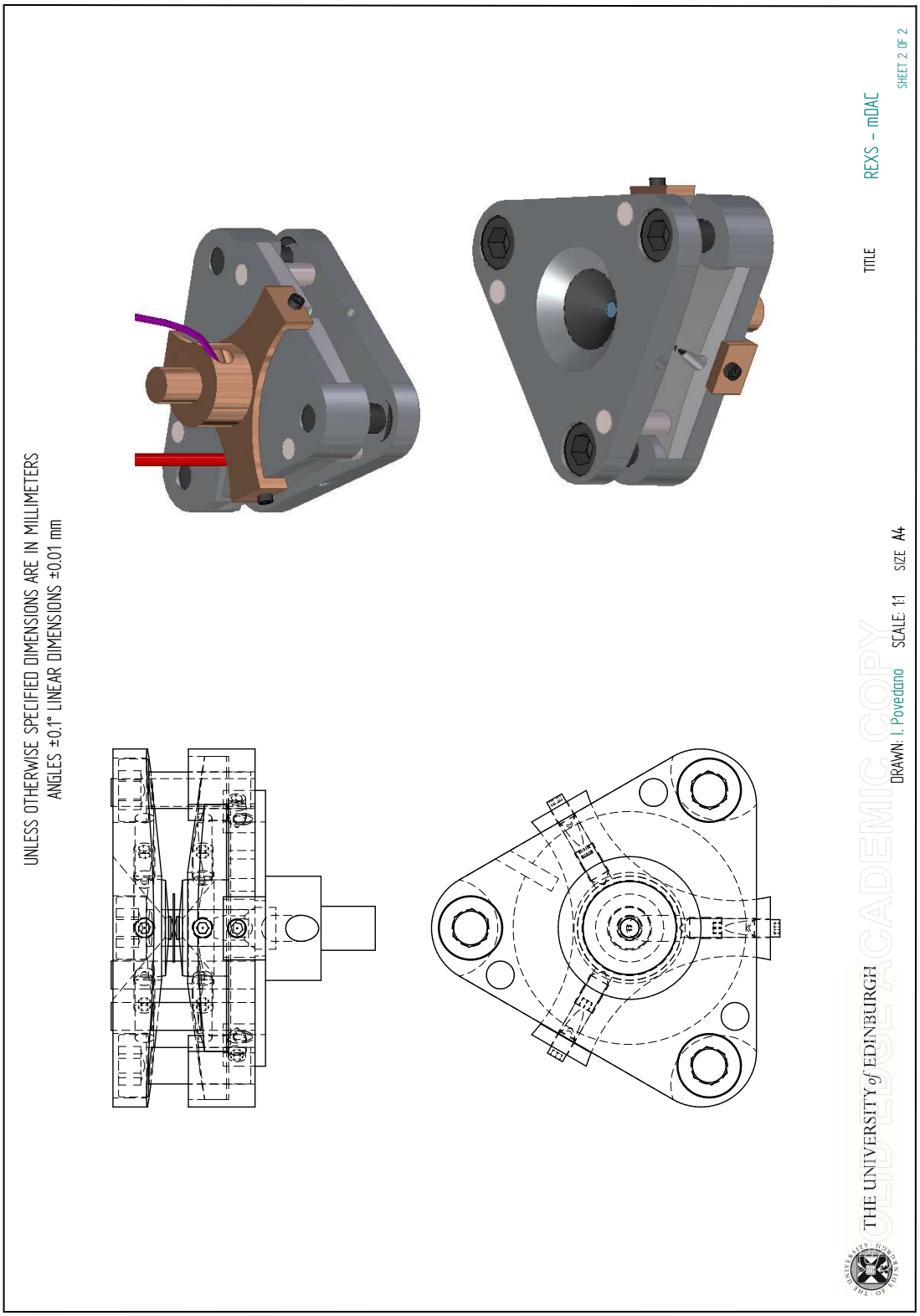

Figure A.2 *Assembly of the membrane DAC for REXS experiments.*

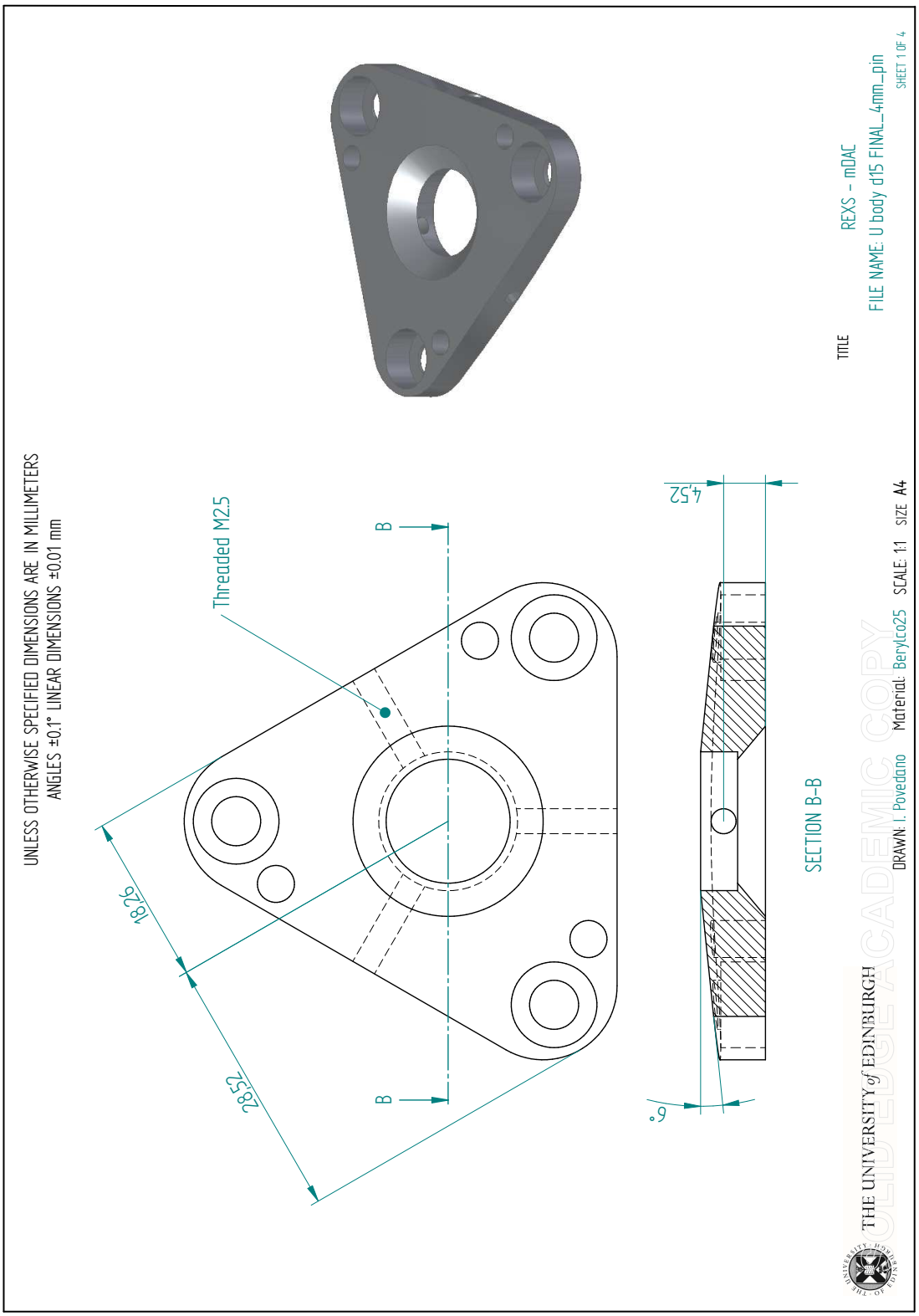

Figure A.3 *Upper body. Sheet 1 of 4.*

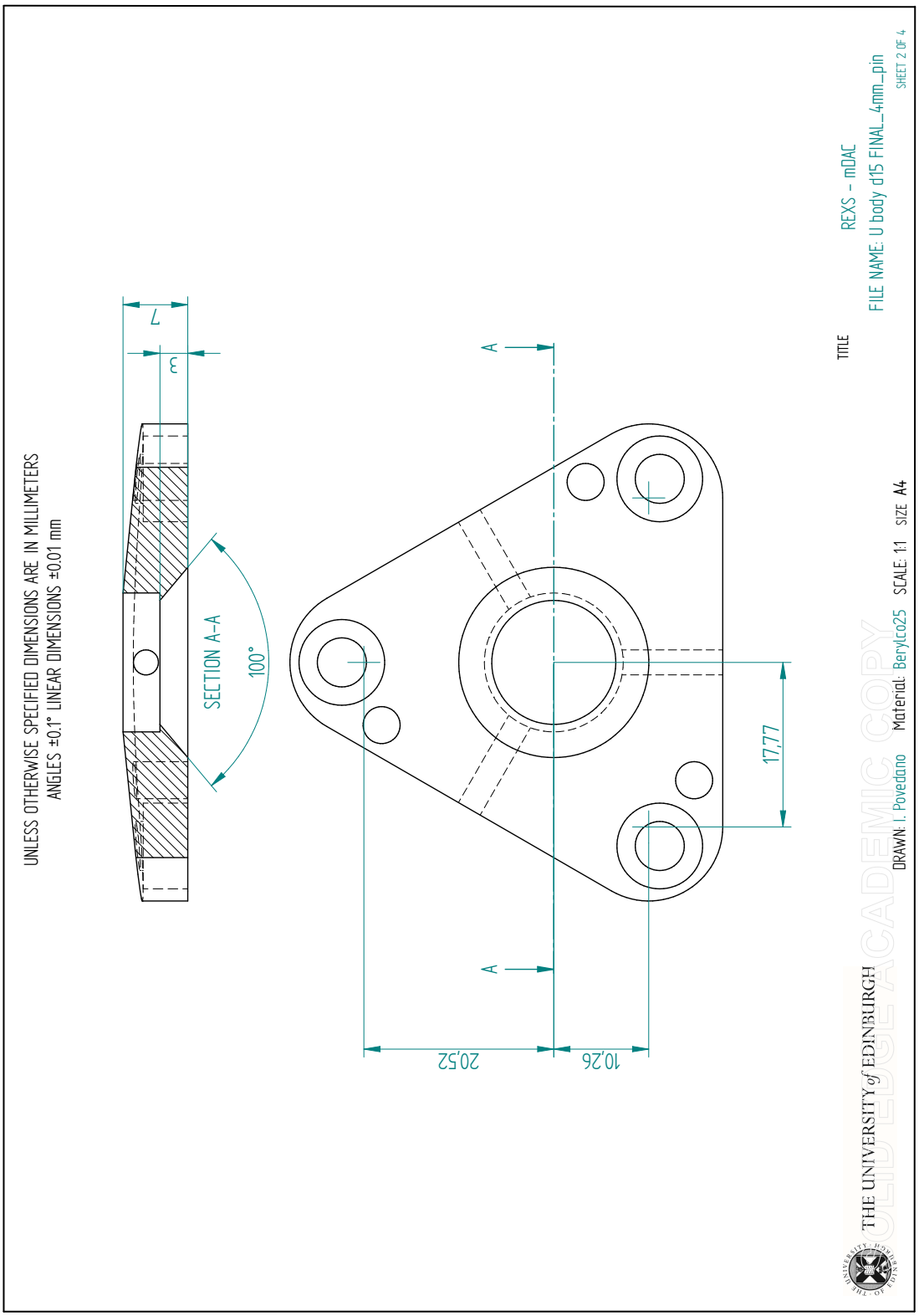

Figure A.4 *Upper body. Sheet 2 of 4*

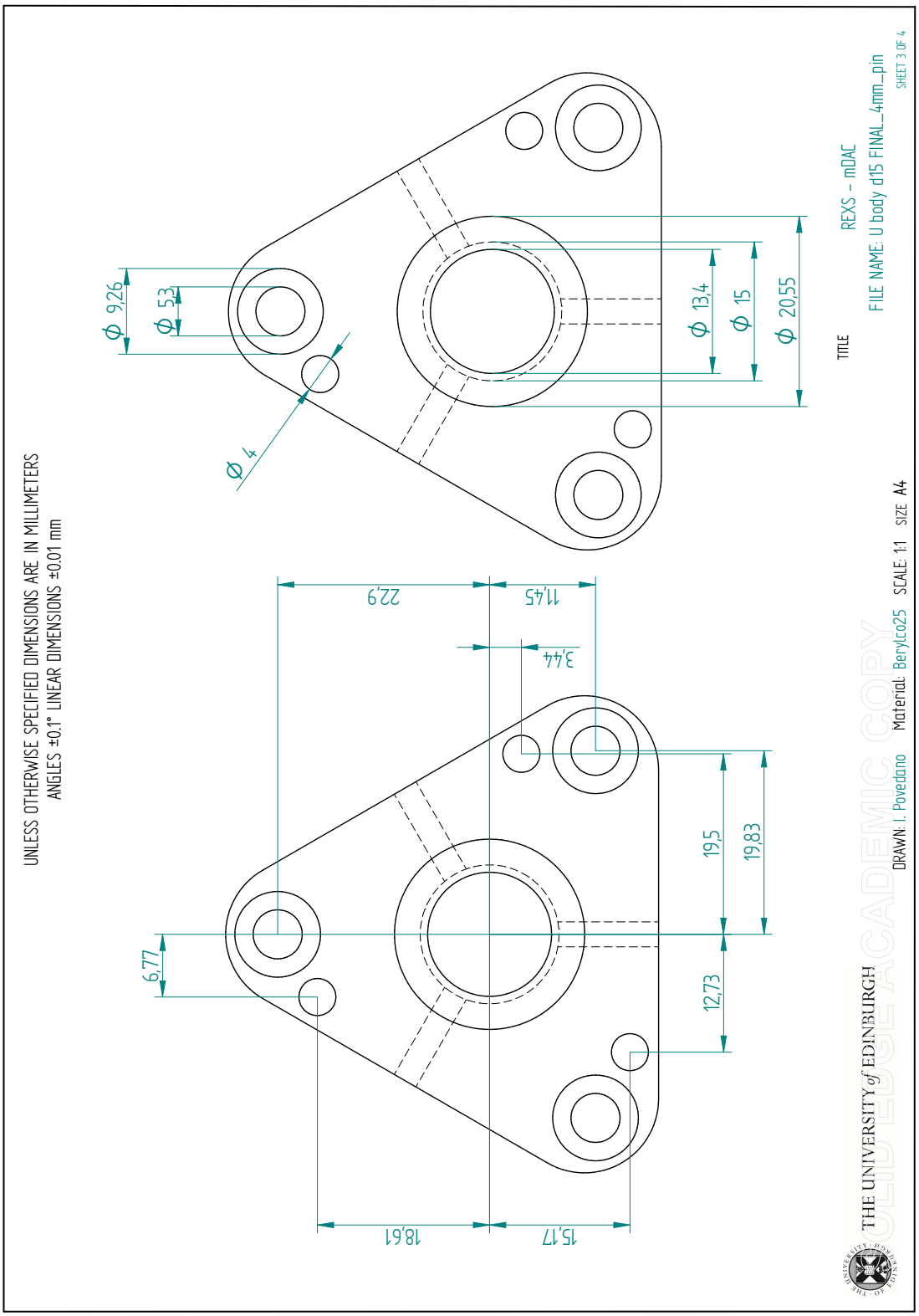

Figure A.5 *Upper body. Sheet 3 of 4*

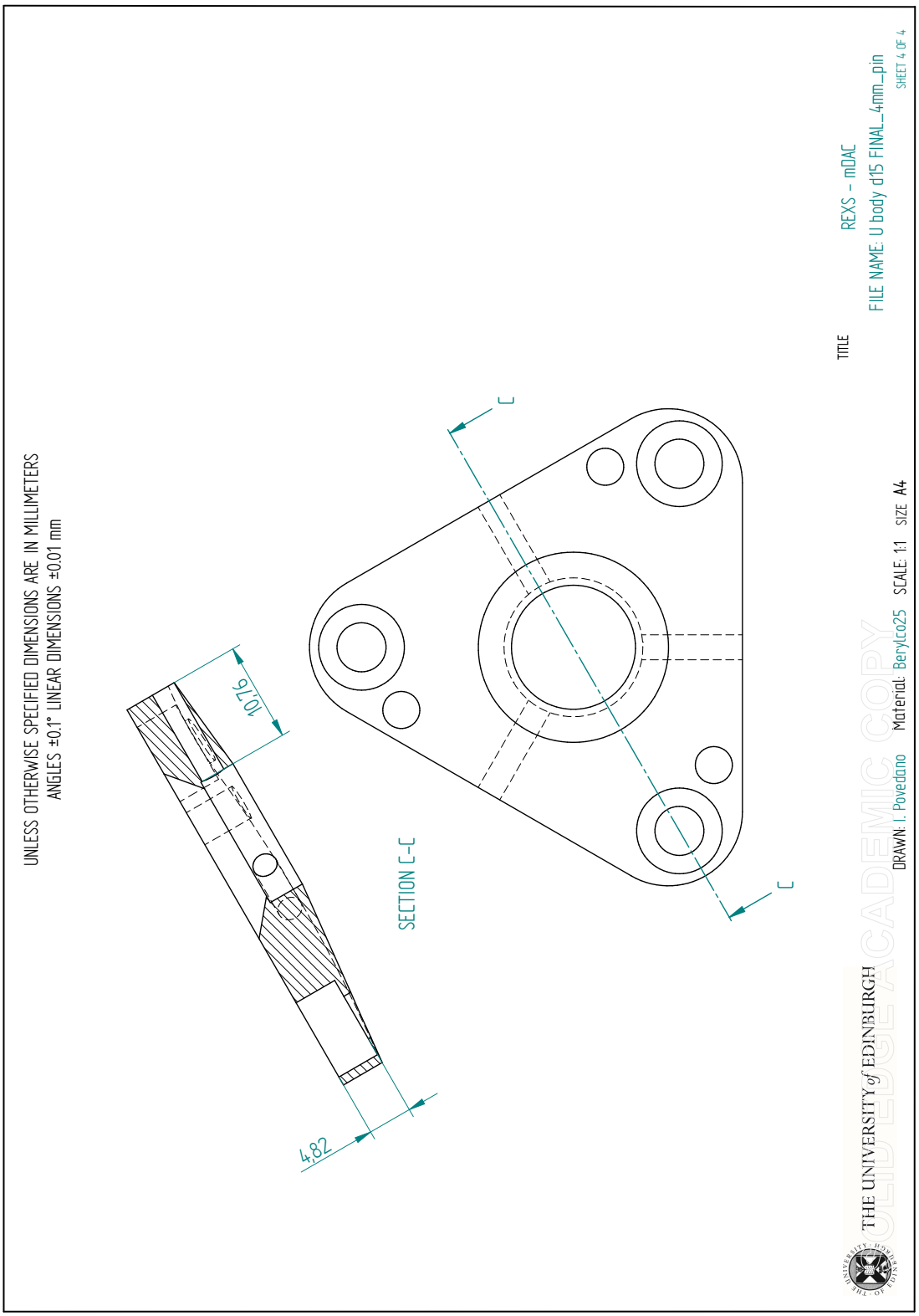

Figure A.6 *Upper body. Sheet 4 of 4*

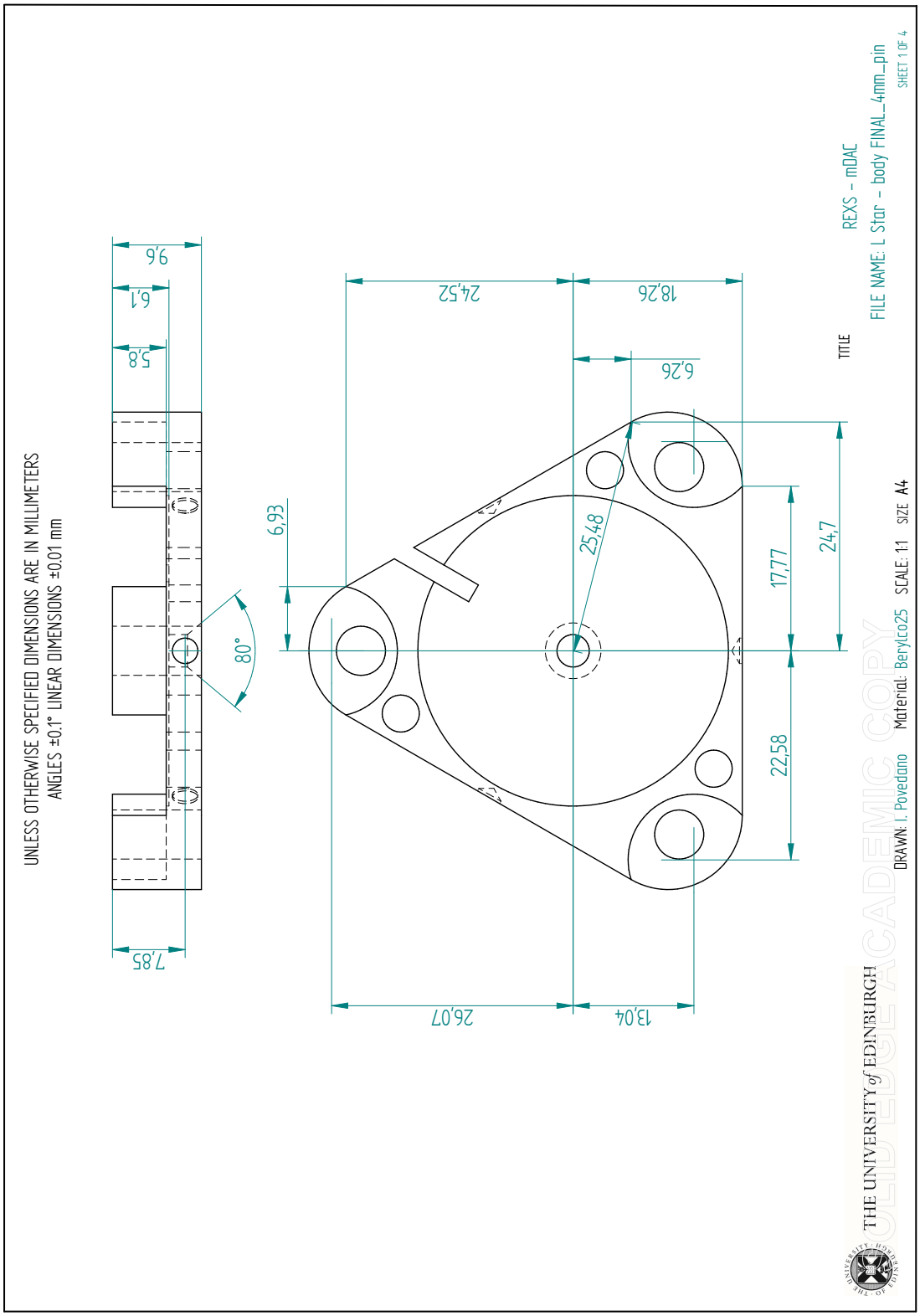

Figure A.7 *Lower body. Sheet 1 of 4.*

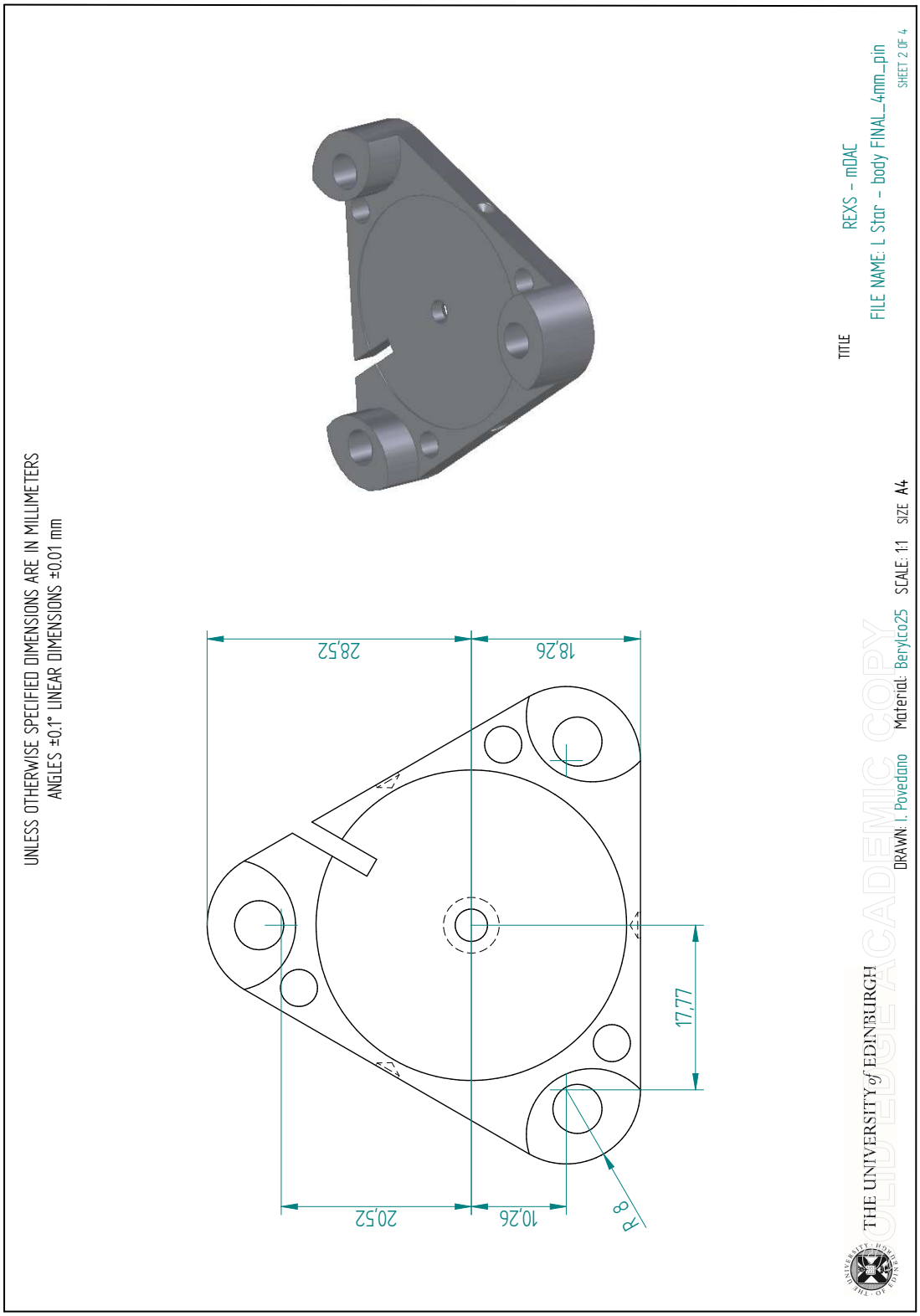

Figure A.8 *Lower body. Sheet 2 of 4.*

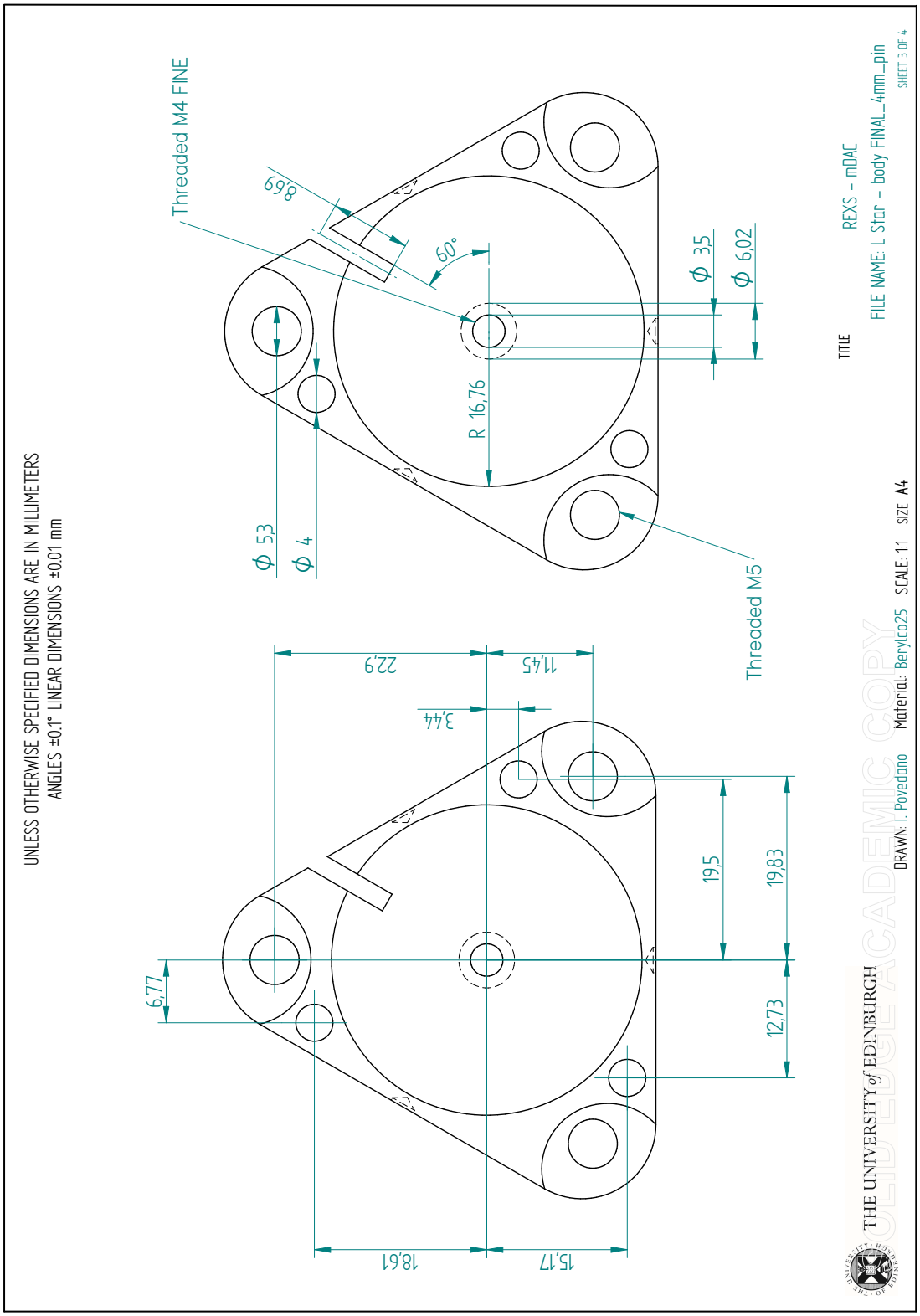

Figure A.9 *Lower body. Sheet 3 of 4.*

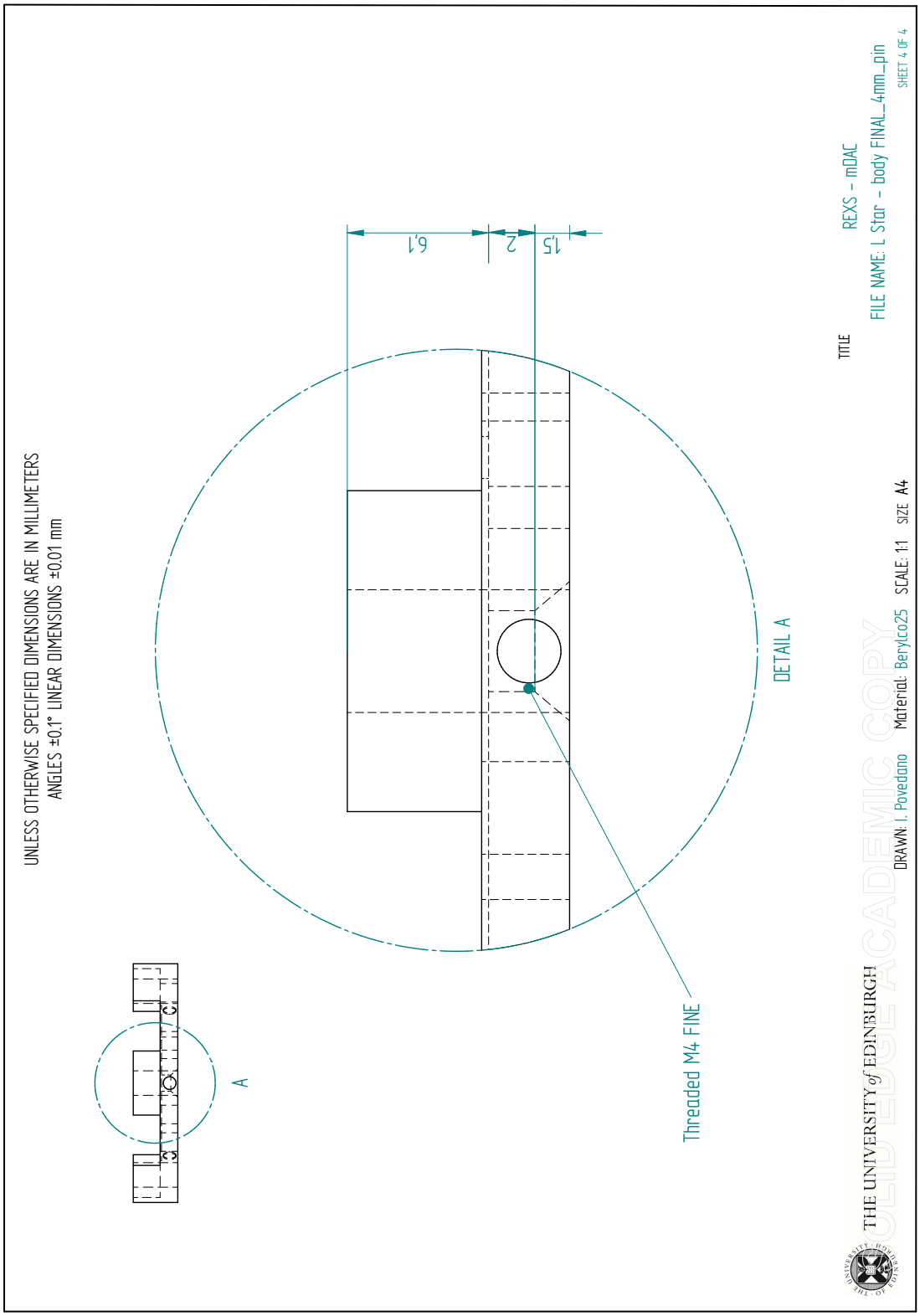

Figure A.10 *Lower body. Sheet 4 of 4.*

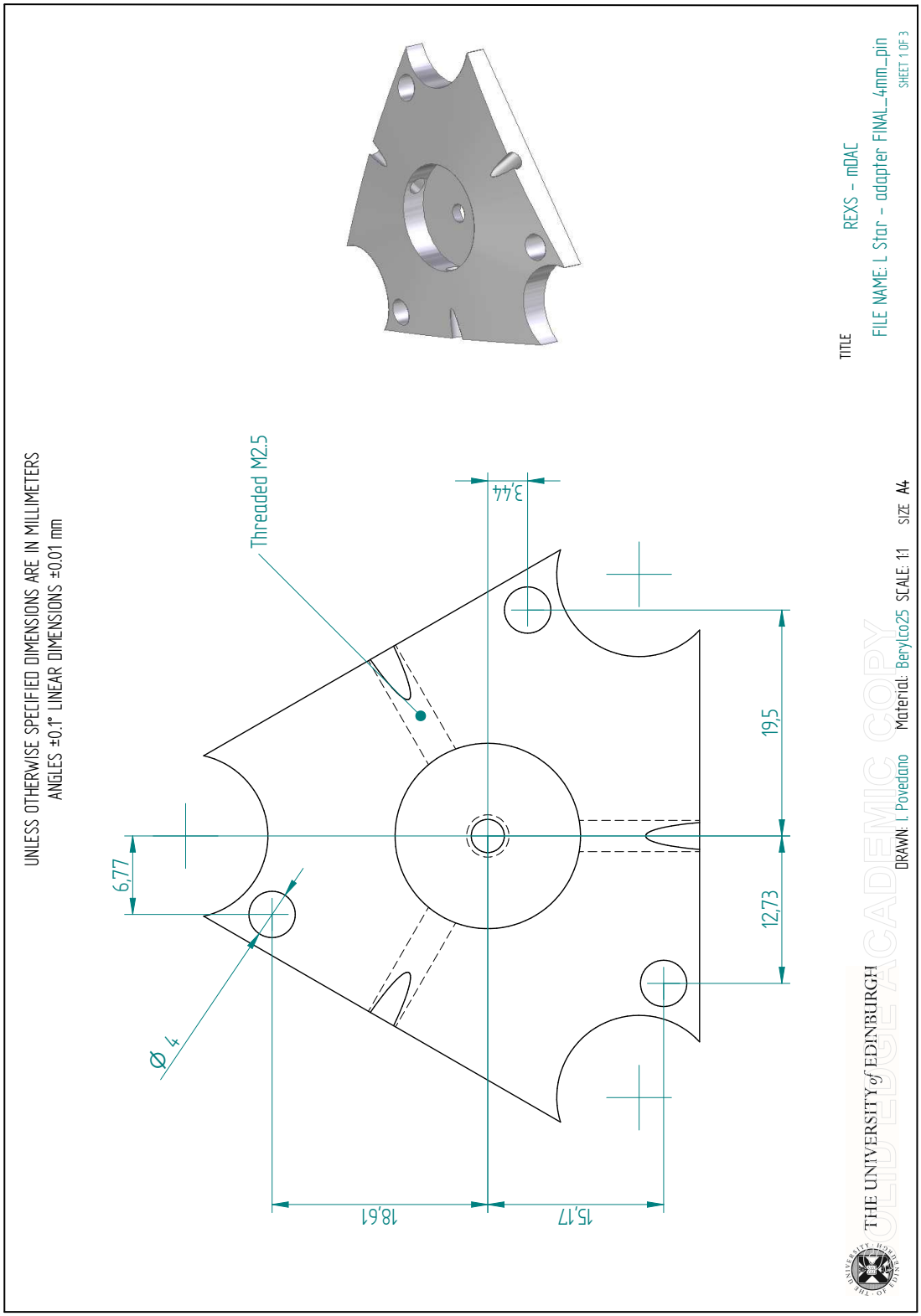

Figure A.11 *Piston-star. Sheet 1 of 3.*

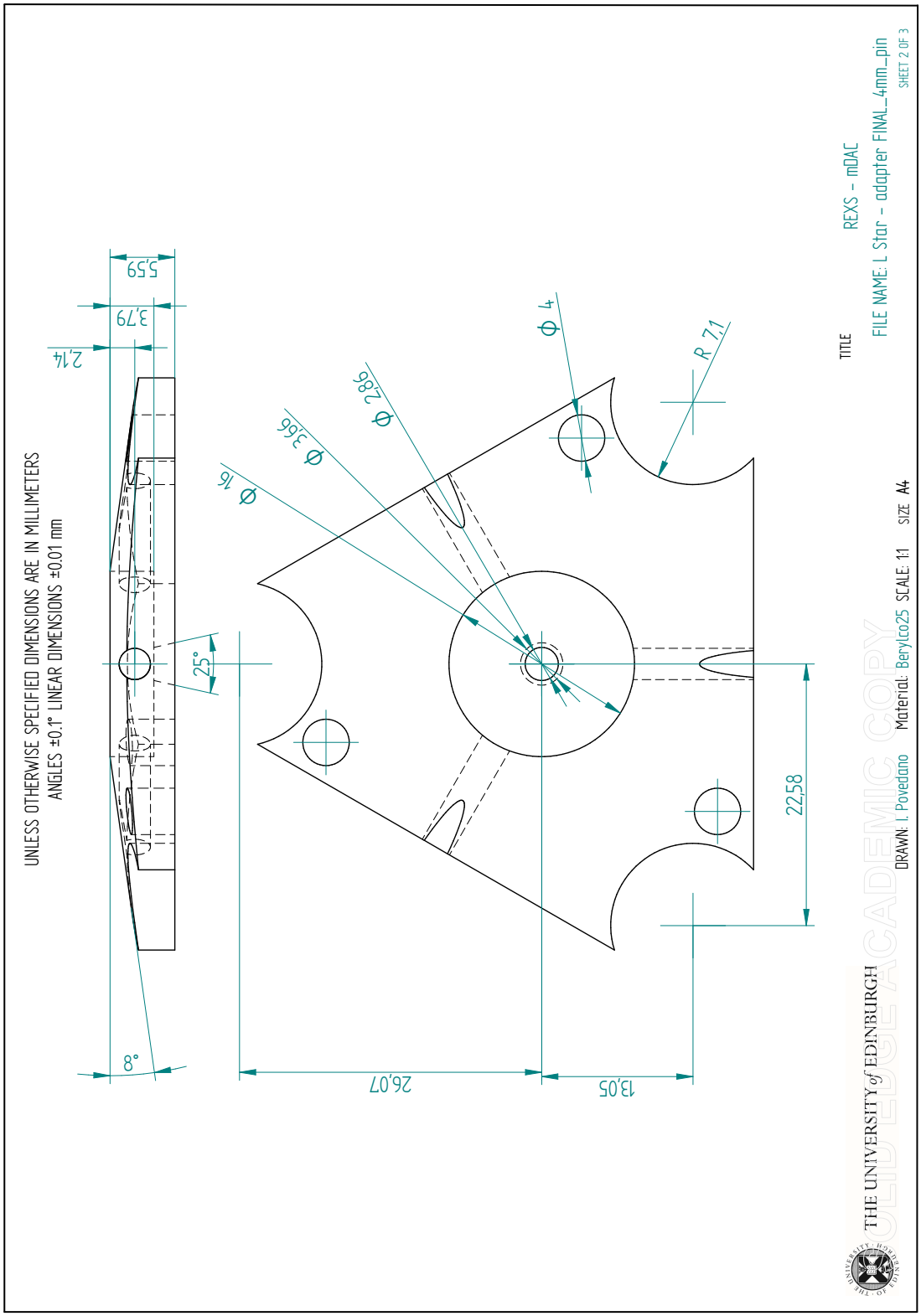

Figure A.12 *Piston-star. Sheet 2 of 3.*

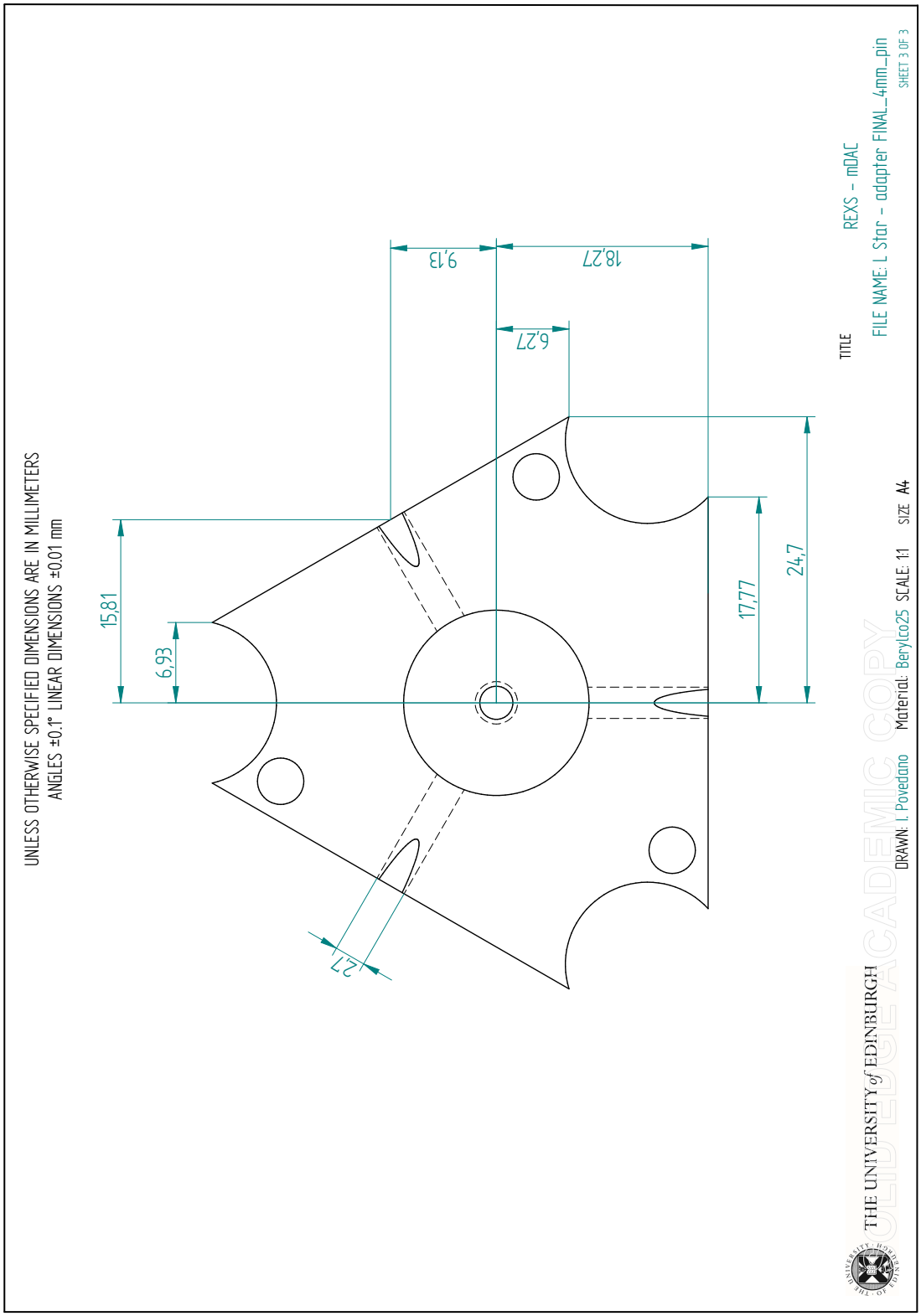

Figure A.13 *Piston-star. Sheet 3 of 3.*

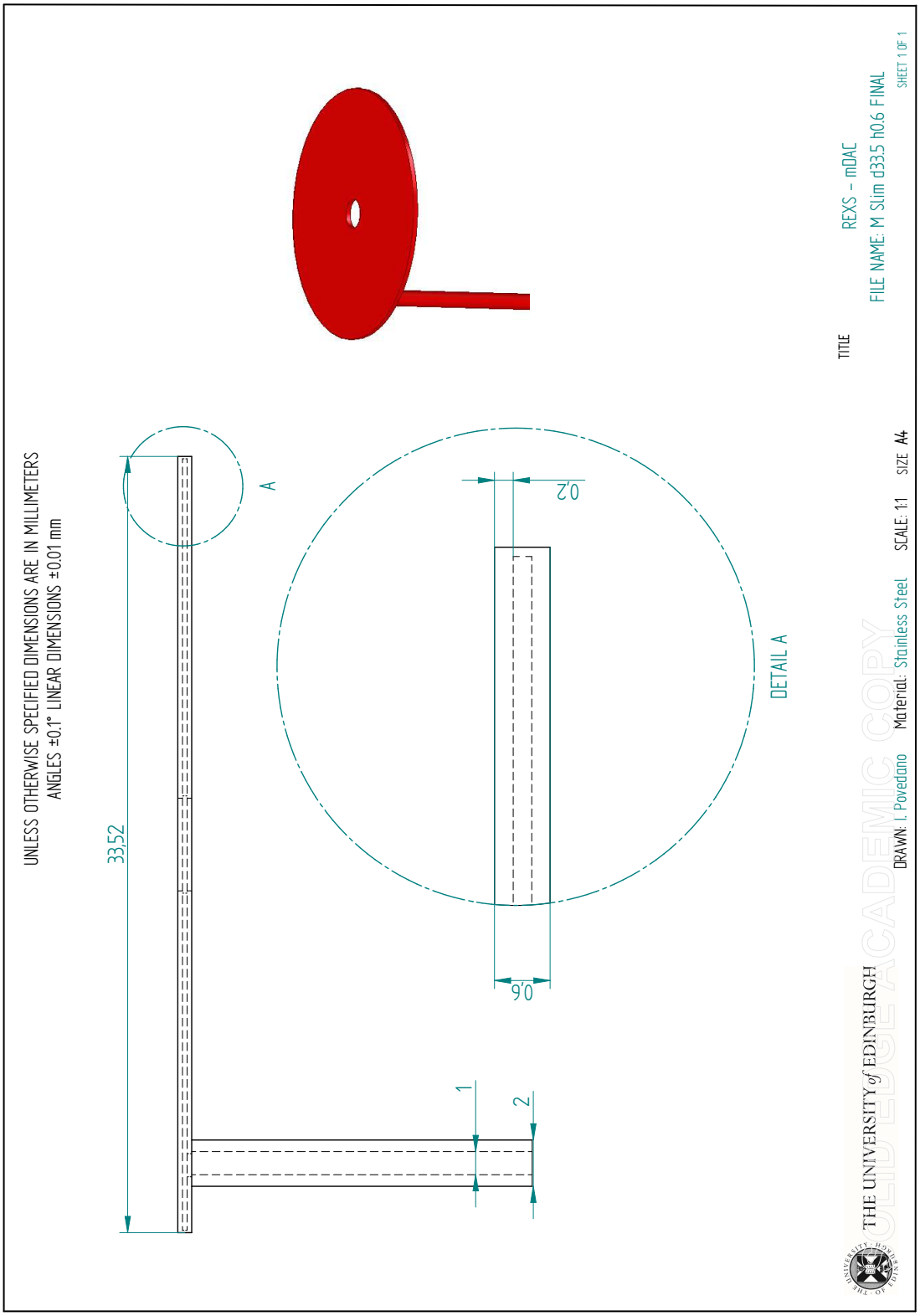

Figure A.14 *Slim membrane.*

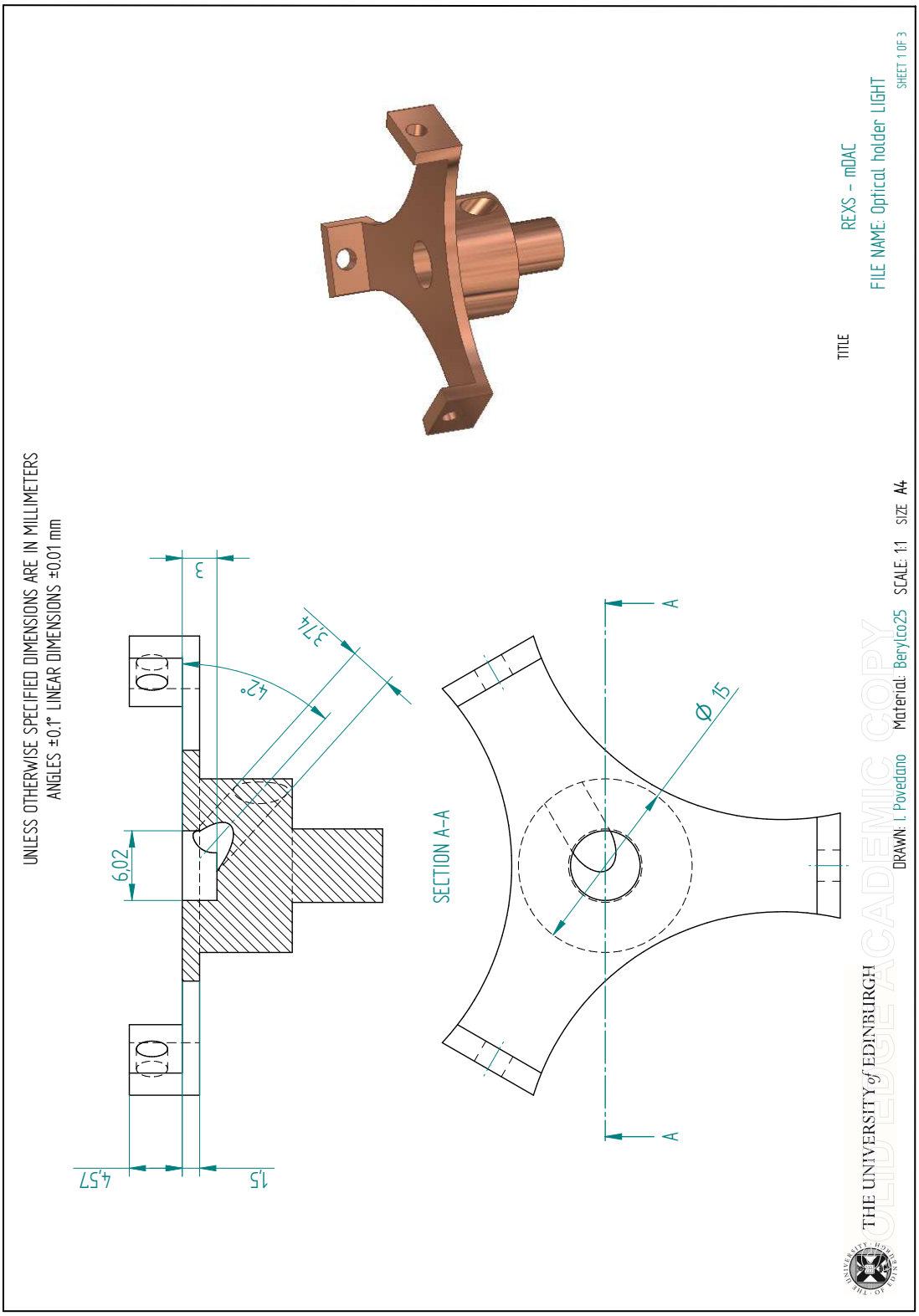

Figure A.15 *Optical holder. Sheet 1 of 3.*

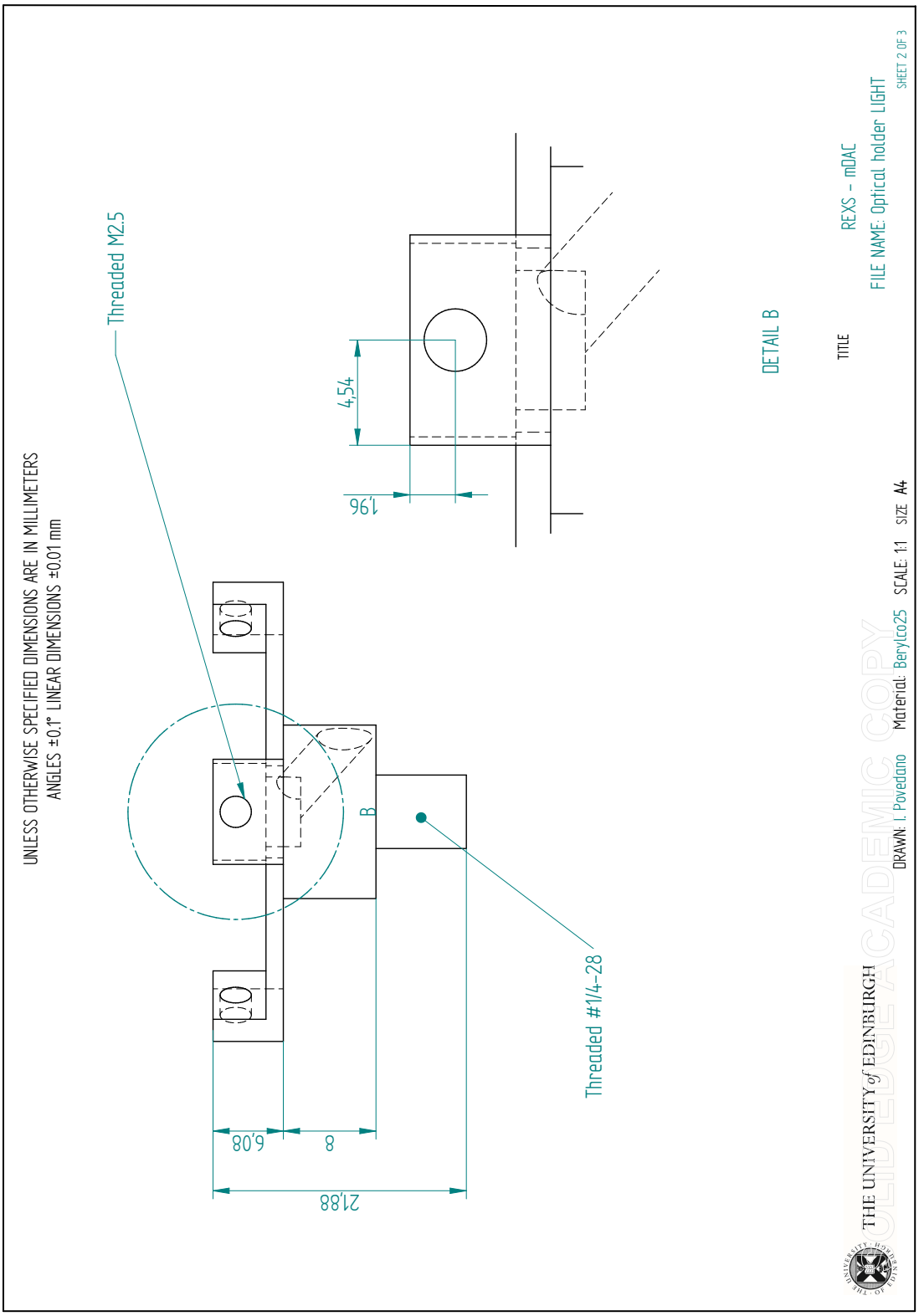

Figure A.16 *Optical holder. Sheet 2 of 3.*

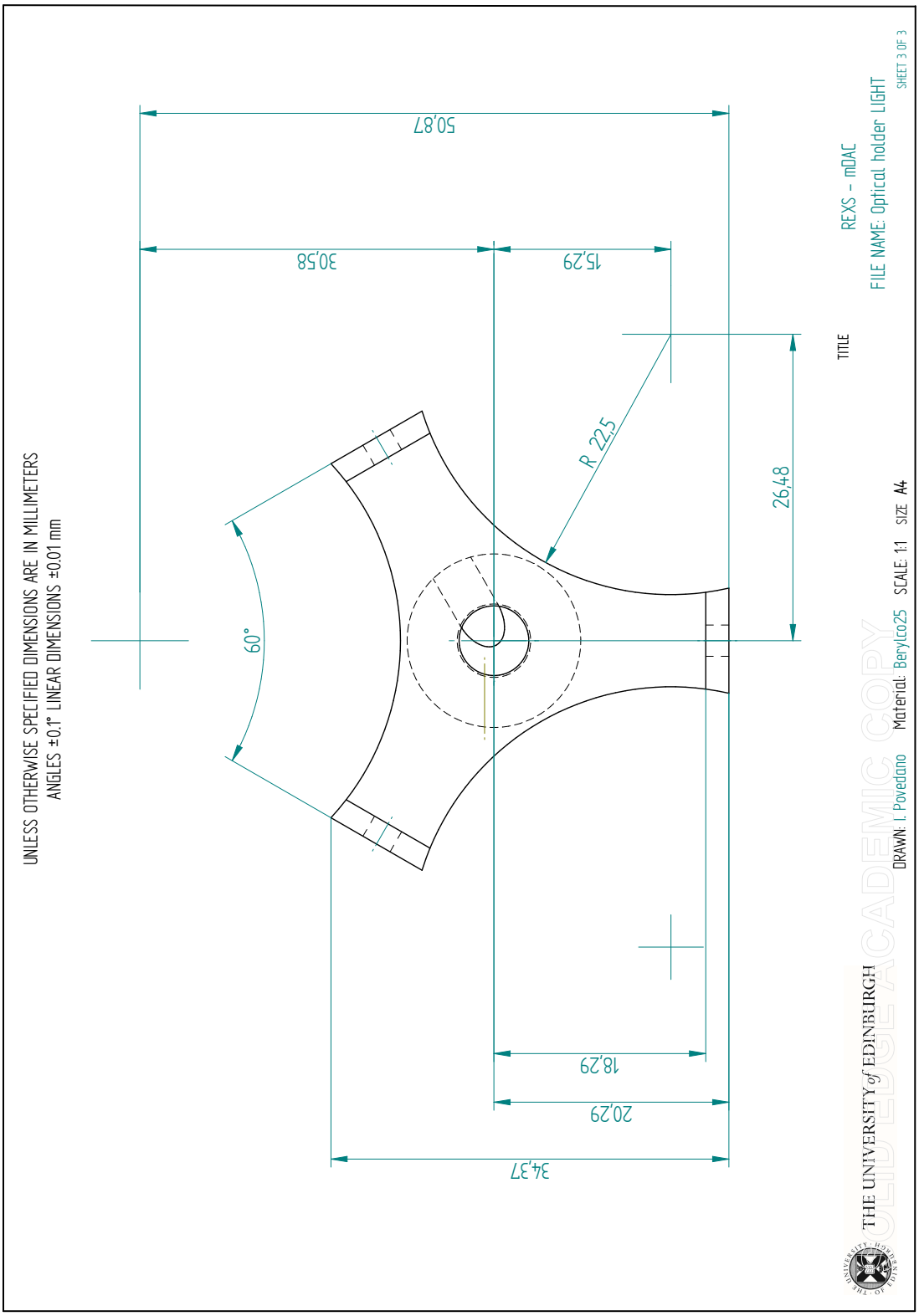

Figure A.17 *Optical holder. Sheet 3 of 3.*

Appendix B

Technical drawings for the thin-cut diamonds

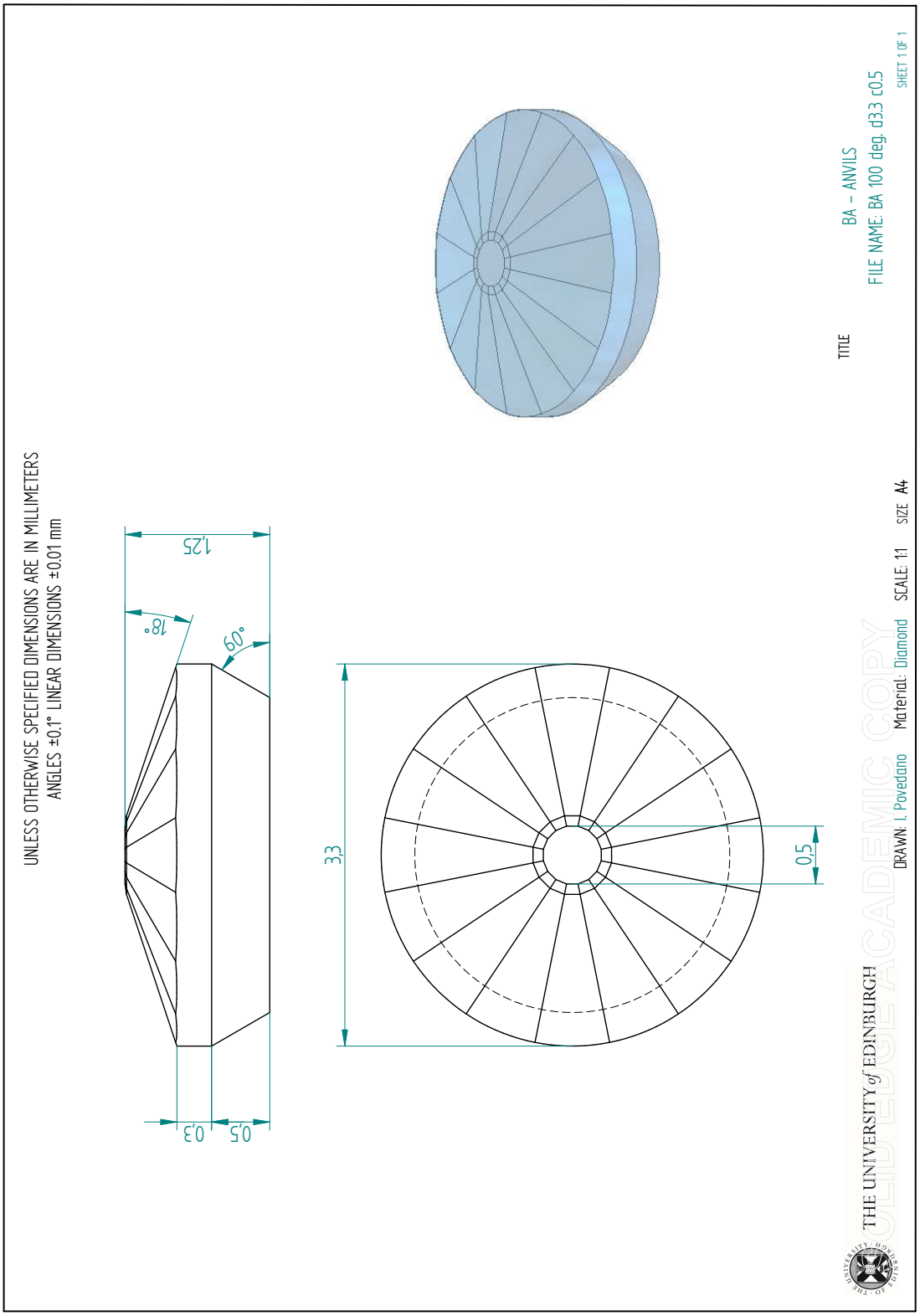

Figure B.1 *BA anvils 0.5 mm culet.*

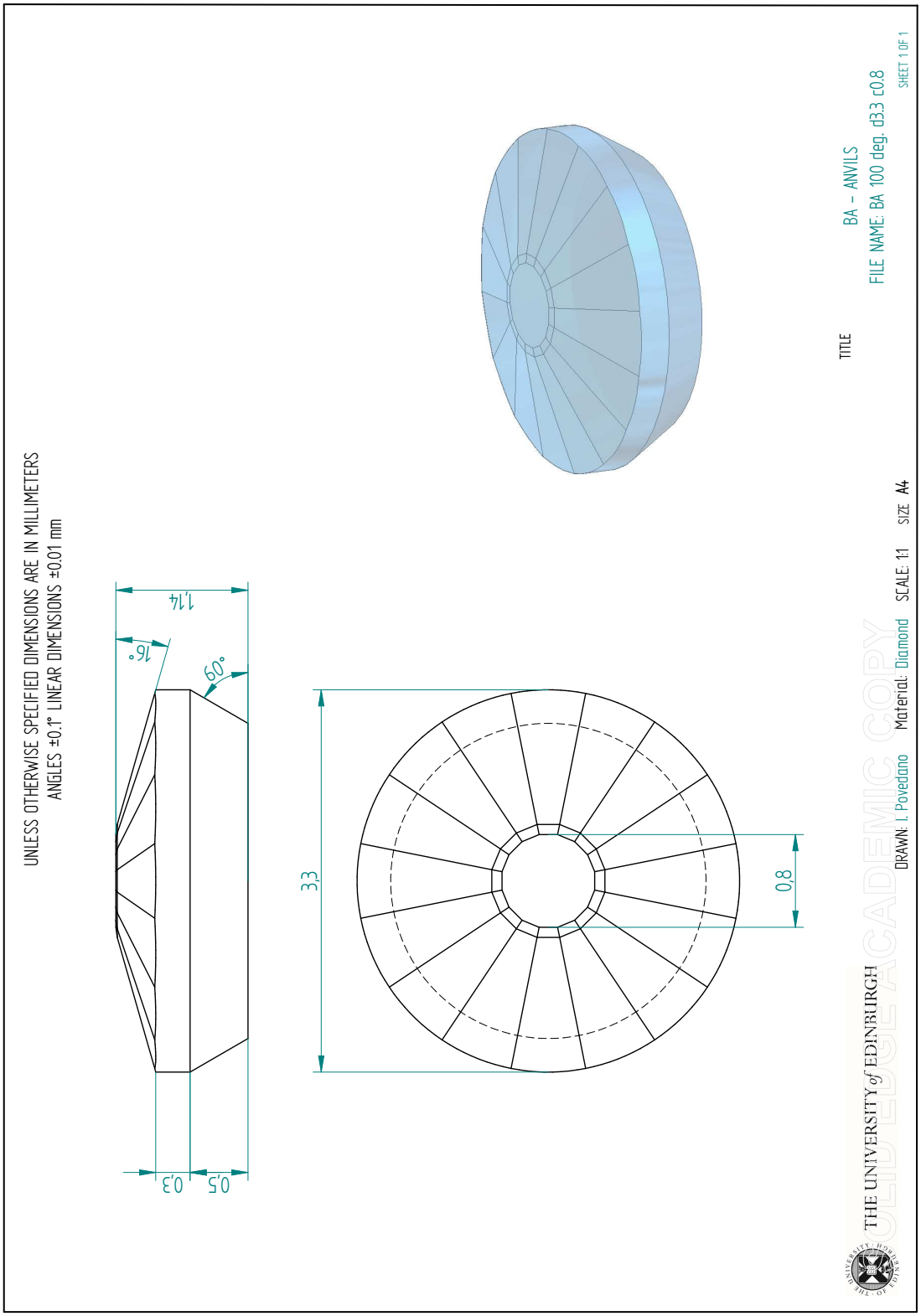

Figure B.2 *BA anvils 0.8 mm culet.*

Appendix C

Technical drawings for the early design I: m-RXS prototype

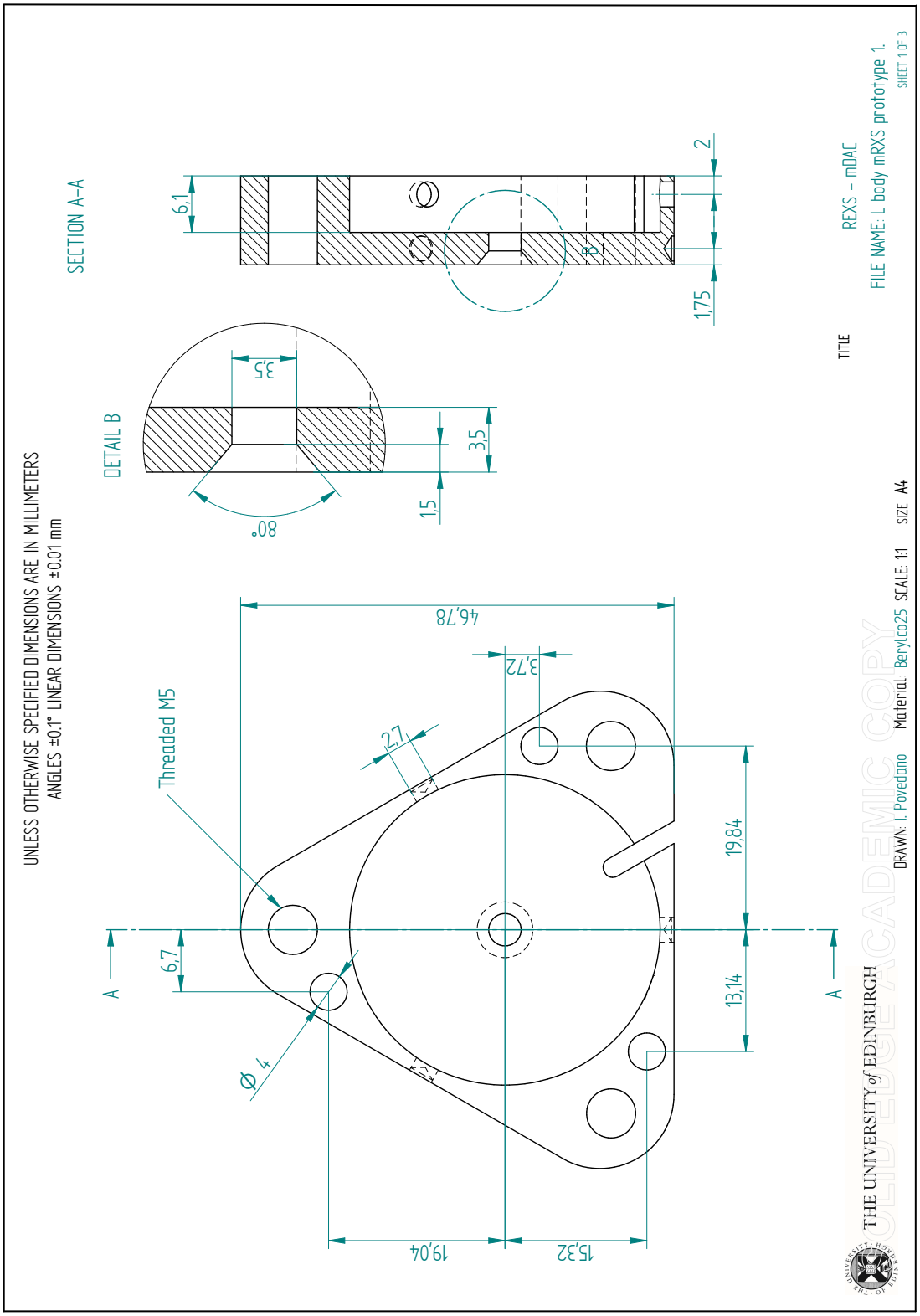

Figure C.1 *Lower body mRXS prototype 1. Sheet 1 of 3.*

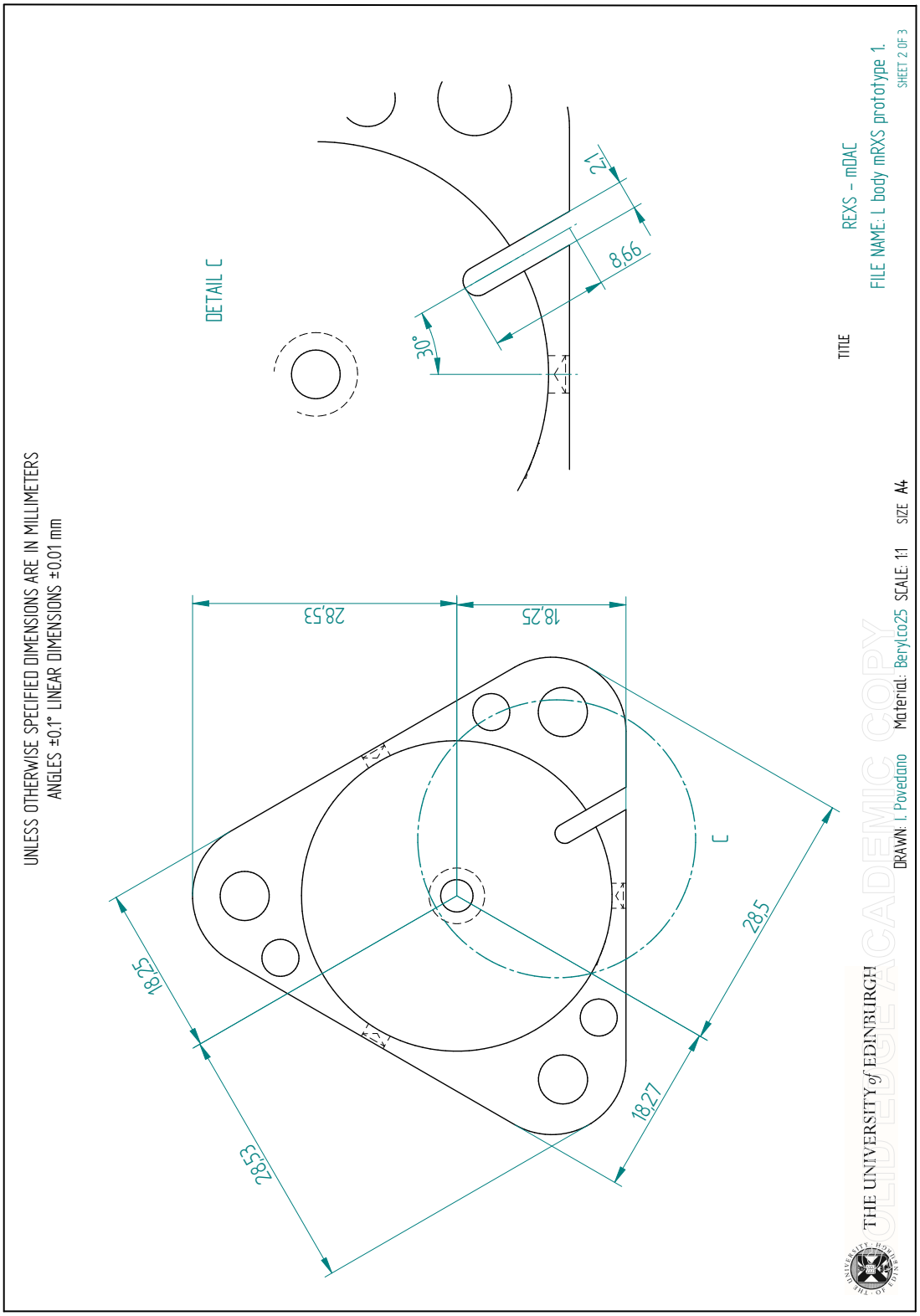

Figure C.2 *Lower body mRXS prototype 1. Sheet 2 of 3.*

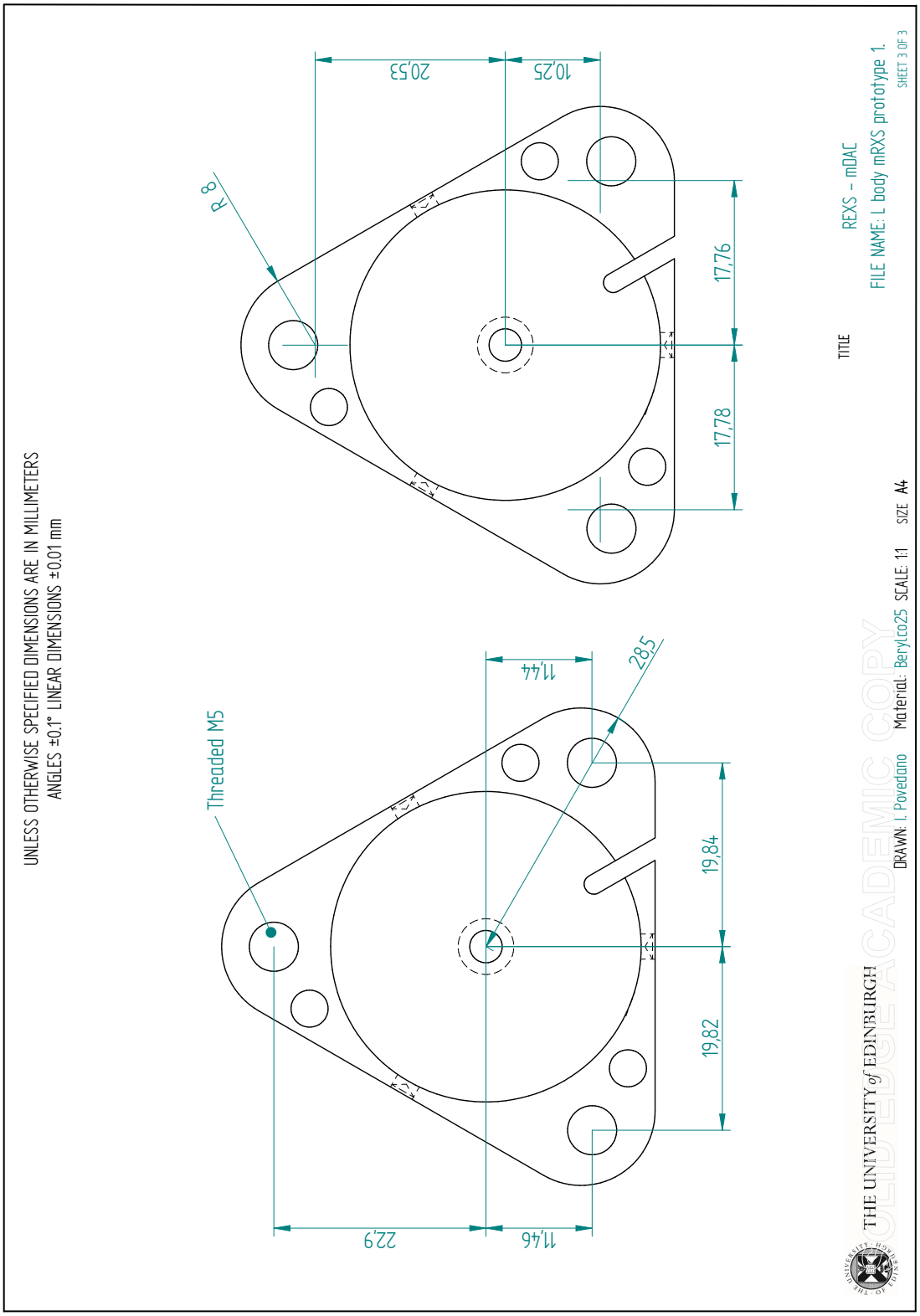

Figure C.3 *Lower body mRXS prototype 1. Sheet 3 of 3.*

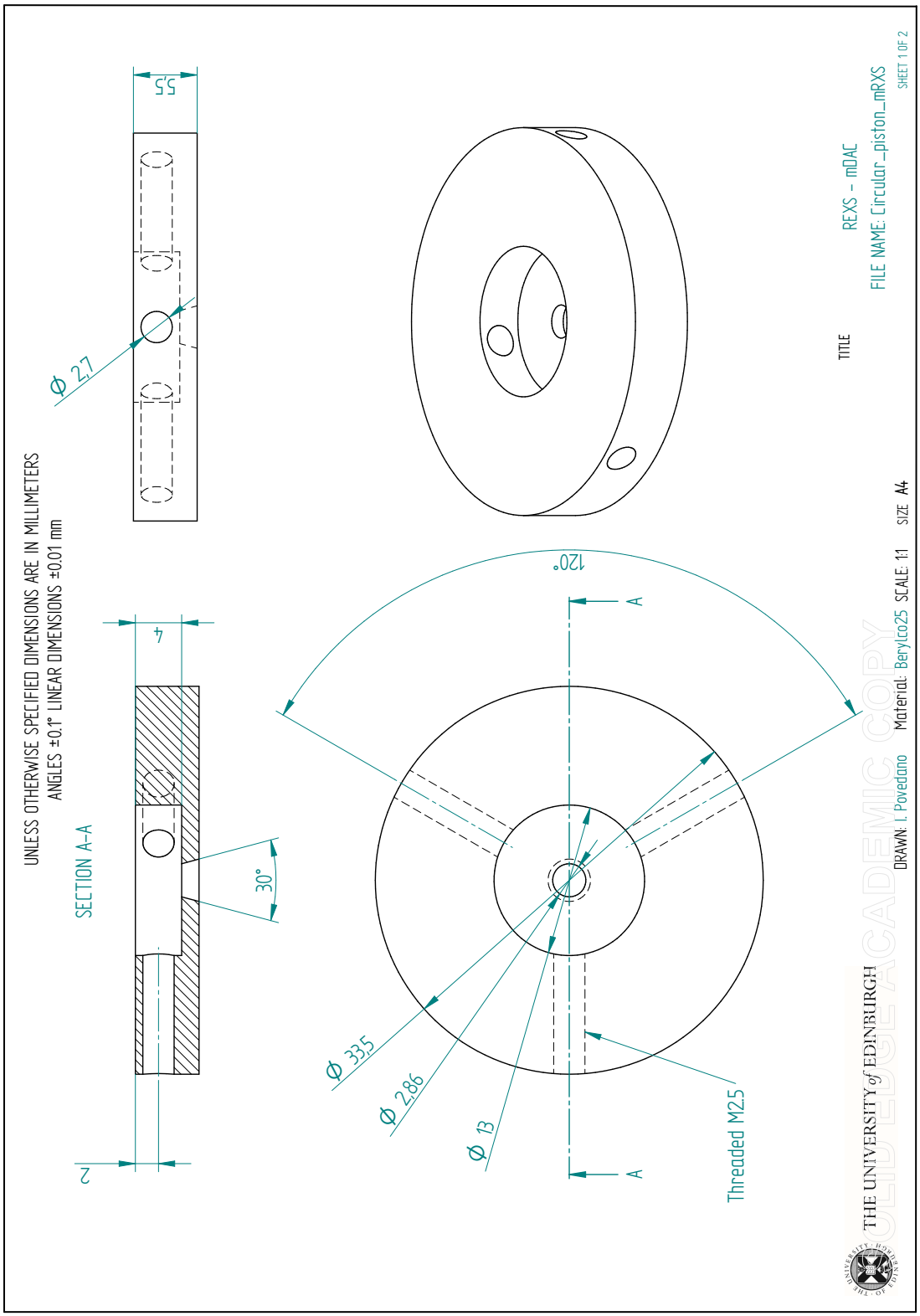

Figure C.4 *Circular Piston mRXS prototype 1. Sheet 1 of 1.*

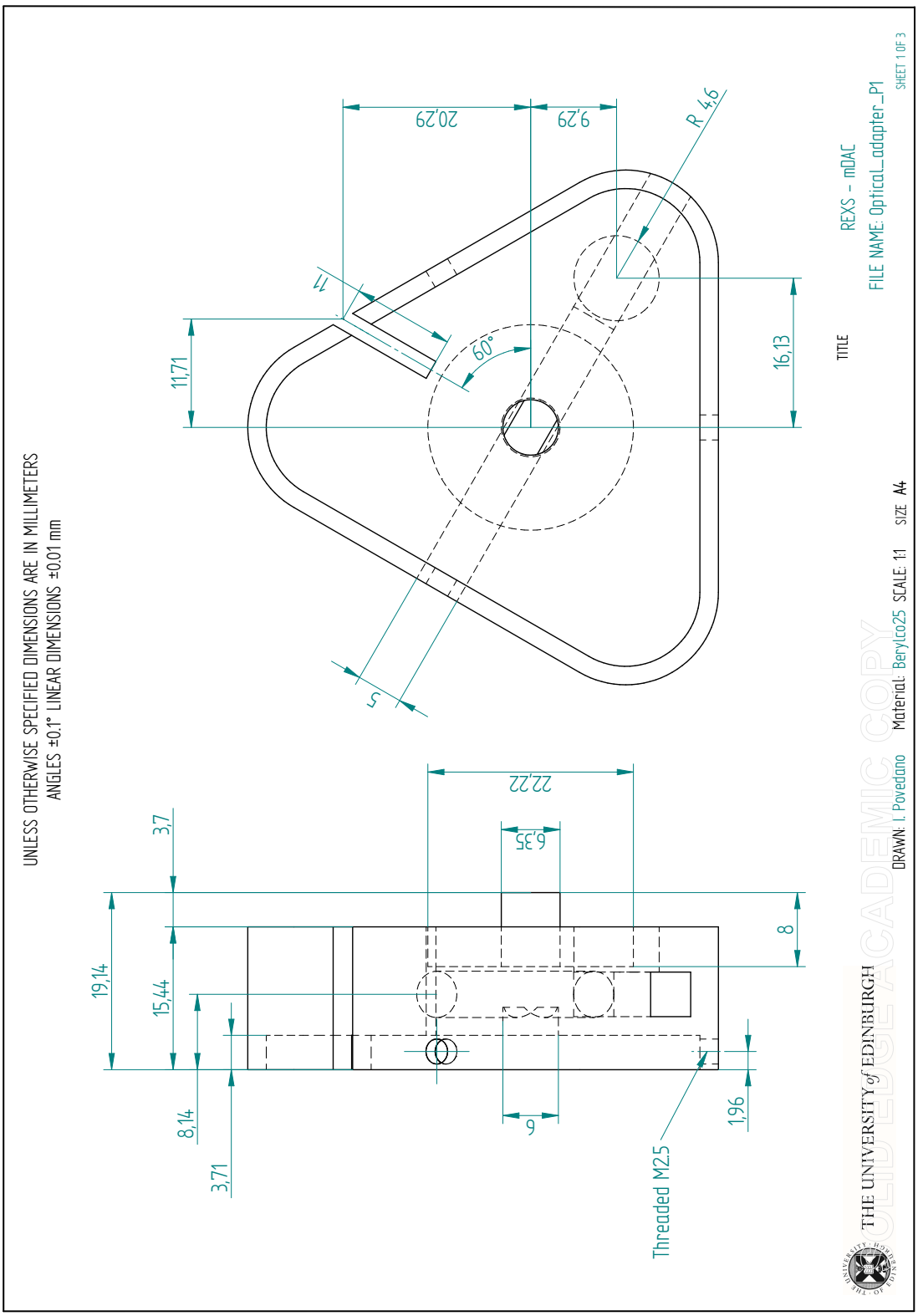

Figure C.5 *Optical holder prototype 1. Sheet 1 of 3.*

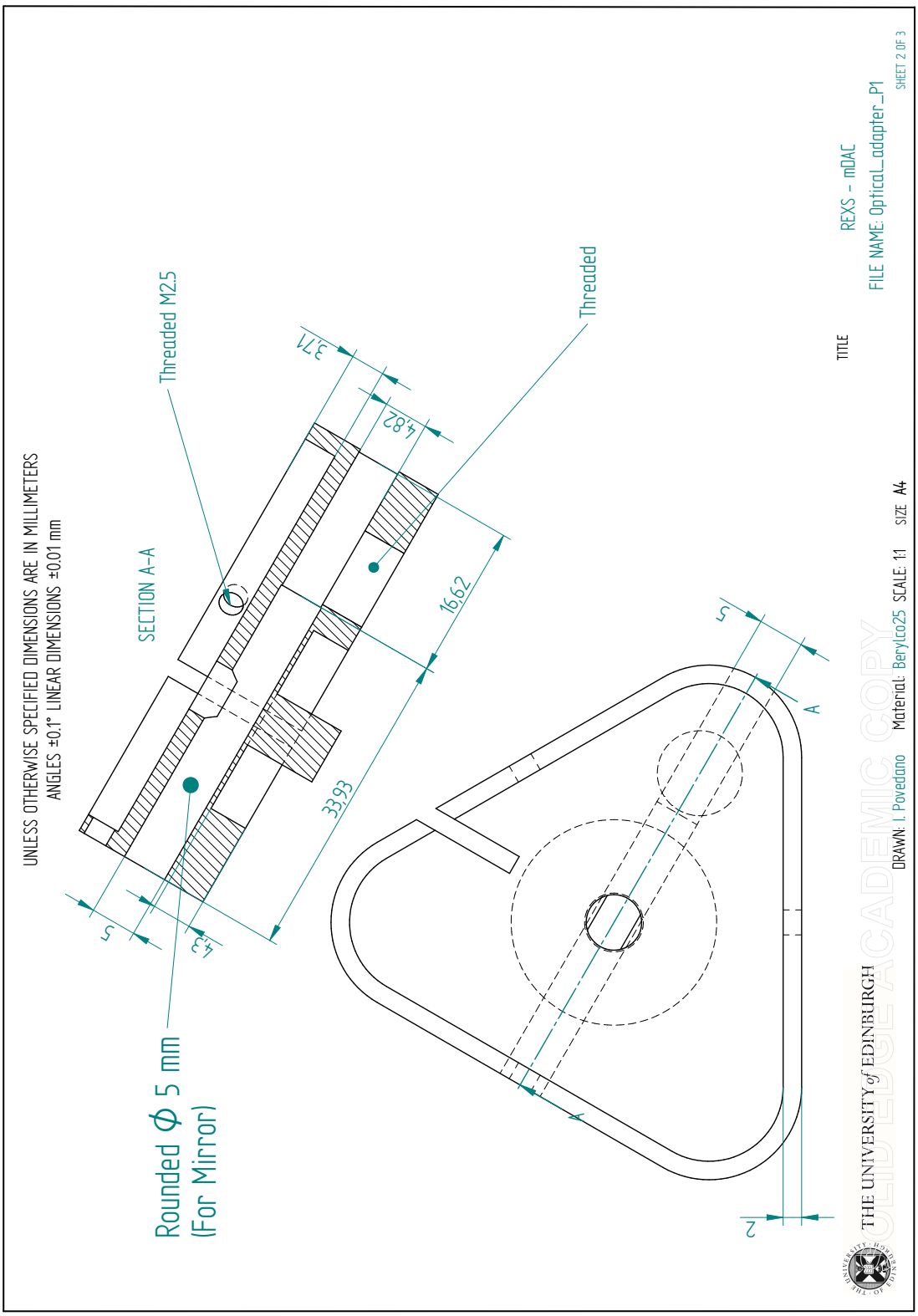

Figure C.6 *Optical holder prototype 1. Sheet 2 of 3.*

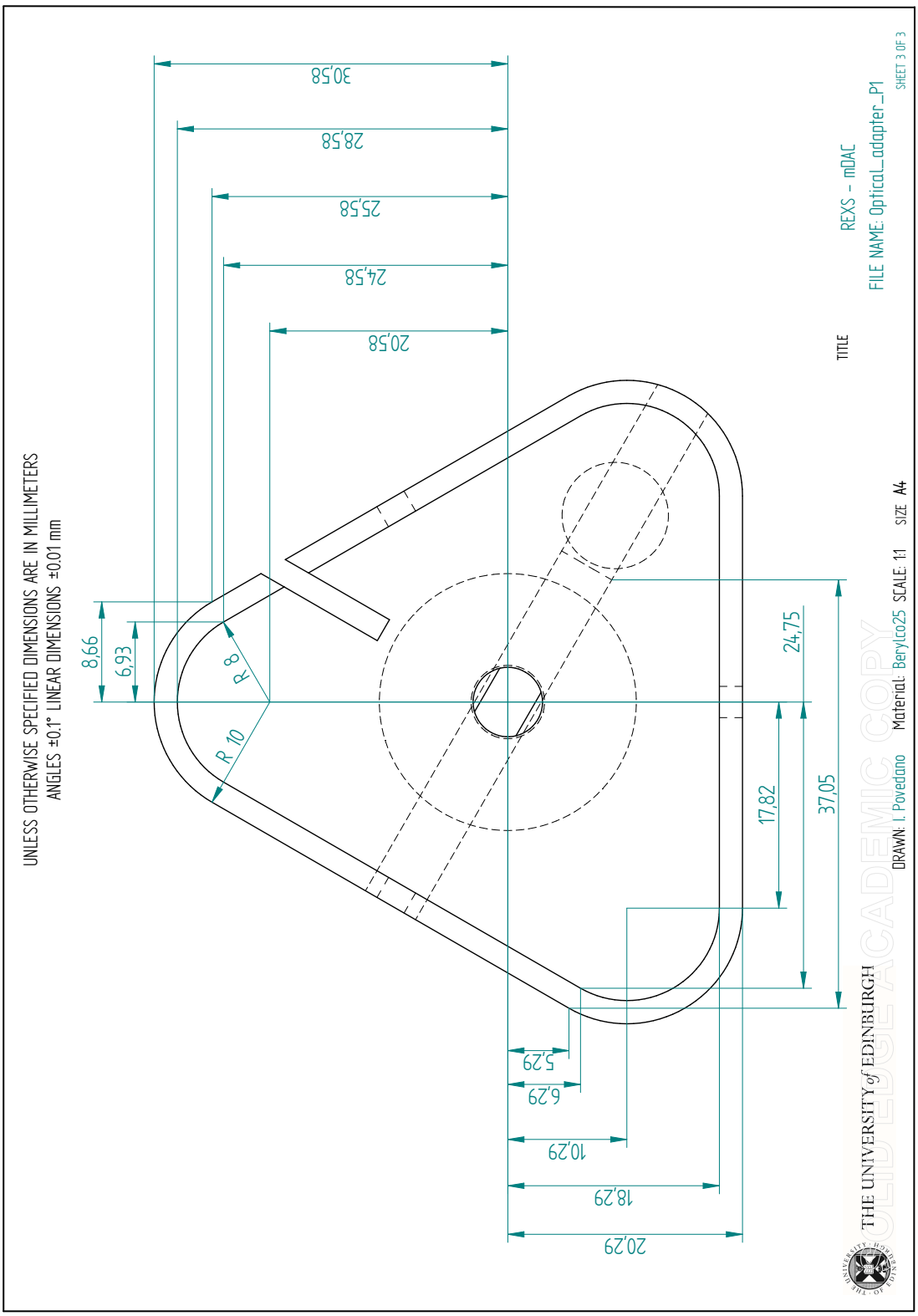

Figure C.7 *Optical holder prototype 1. Sheet 3 of 3.*

Appendix D

Technical drawings for the early design II: wedge-DAC prototype

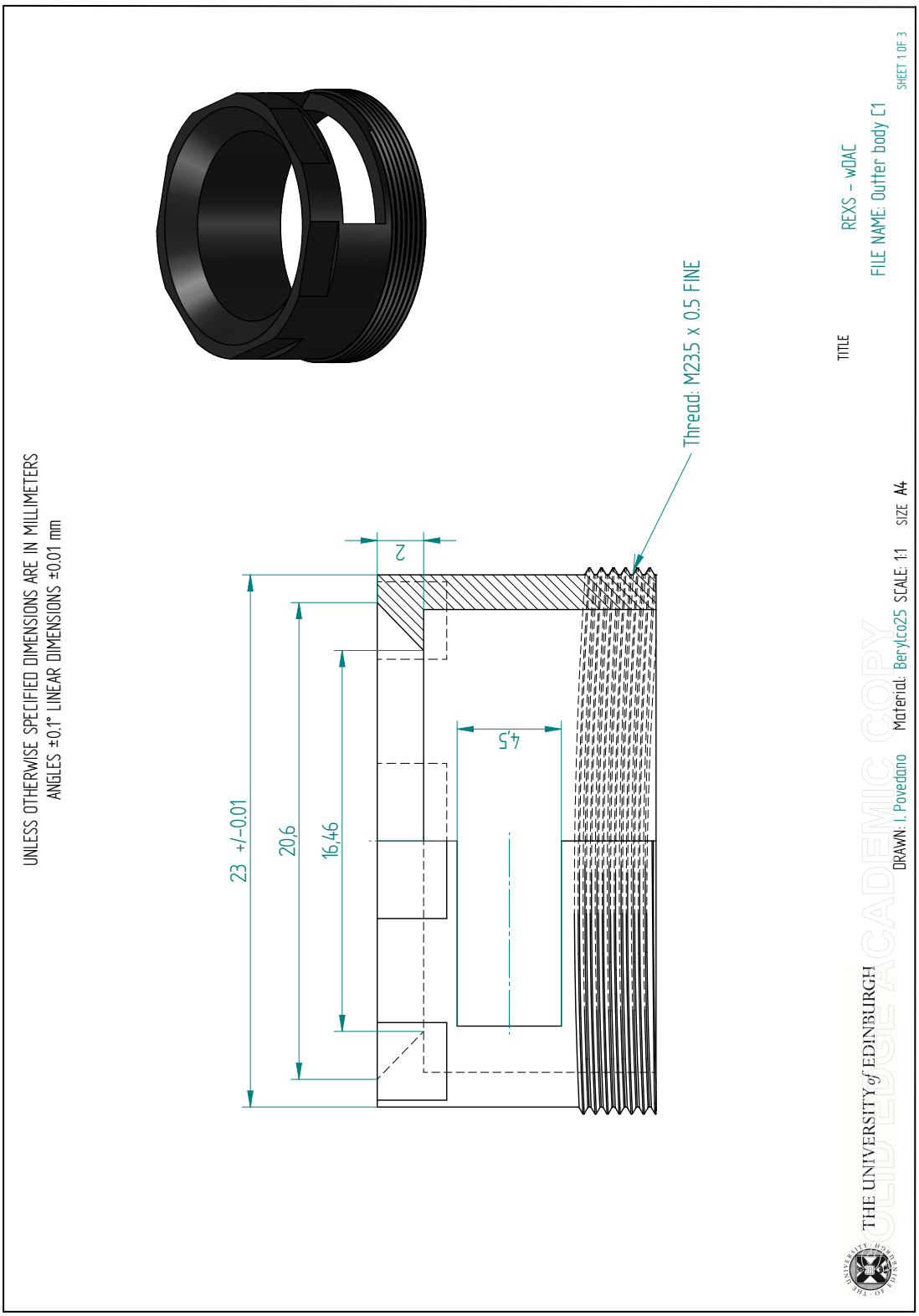

Figure D.1 *Outer body. Sheet 1 of 3.*

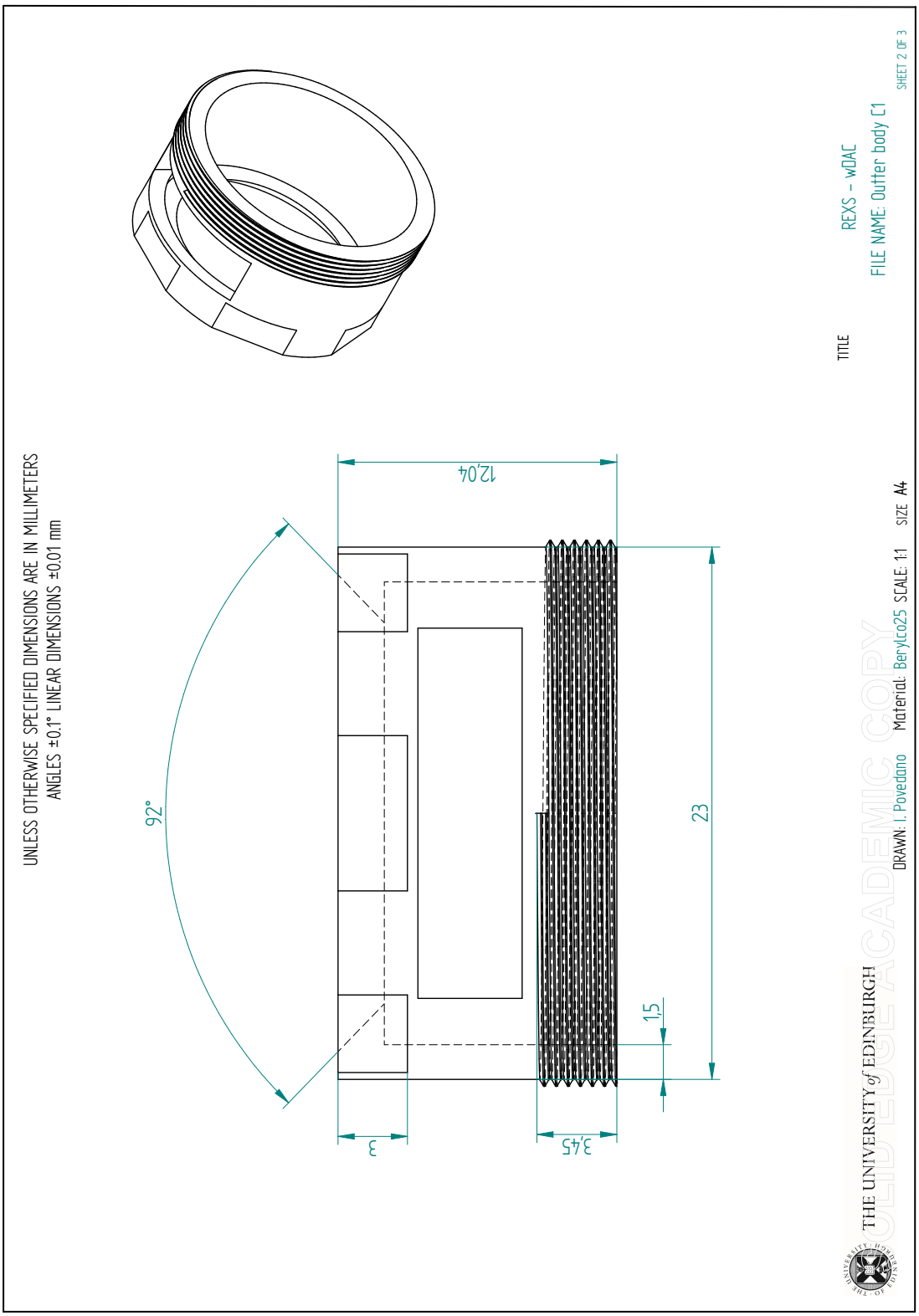

Figure D.2 *Outer body. Sheet 2 of 3.*

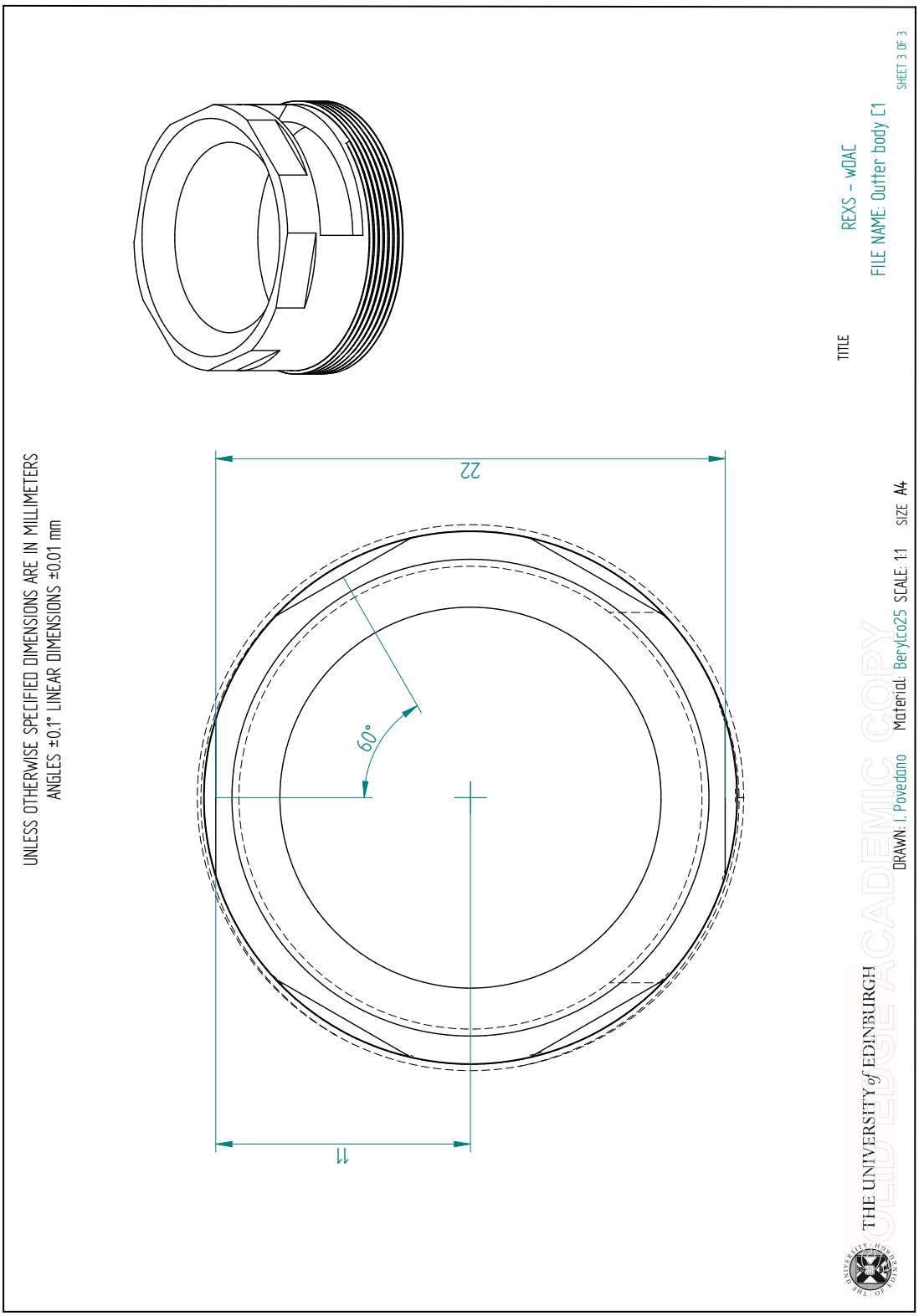

Figure D.3 *Outer body. Sheet 3 of 3.*

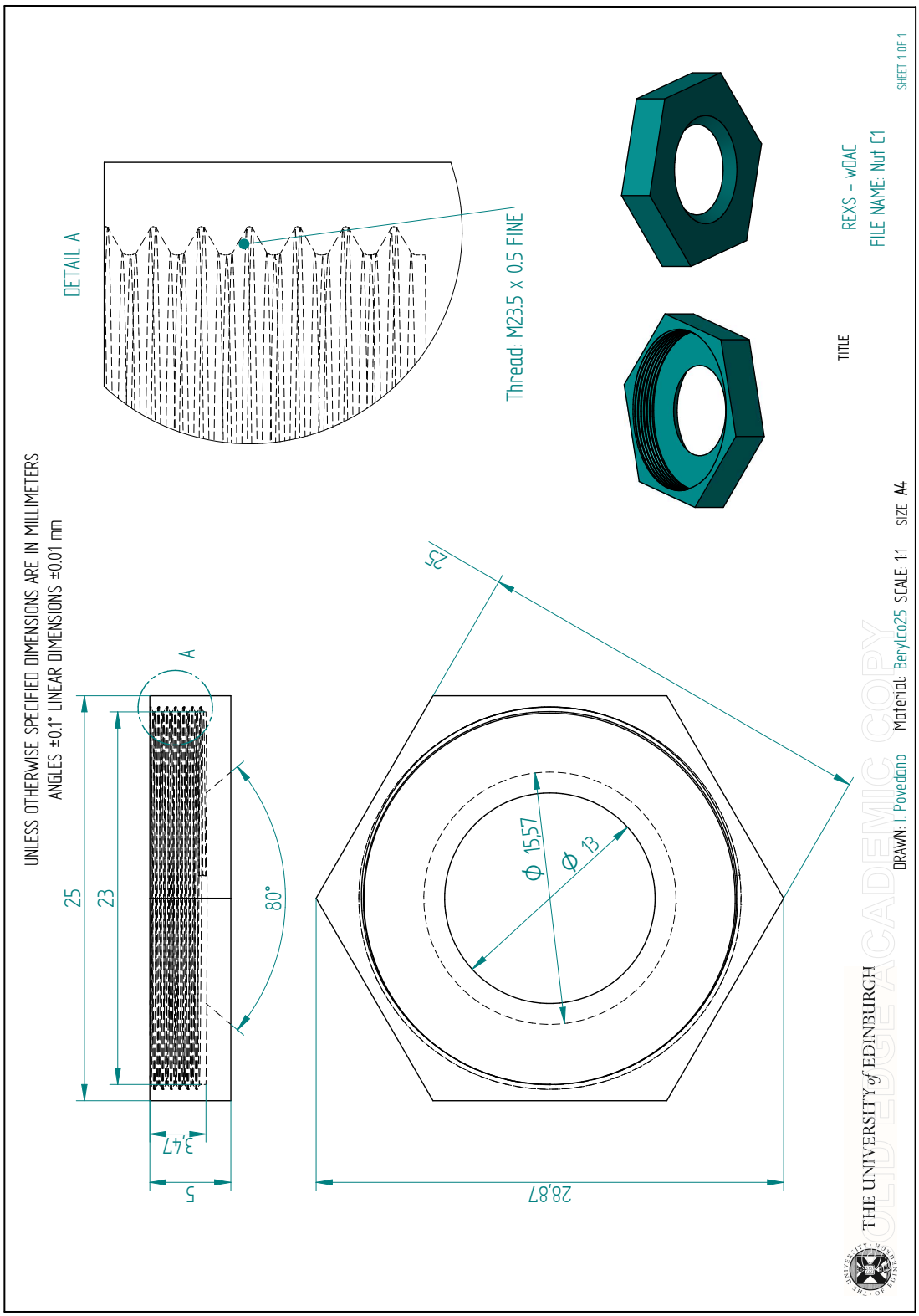

Figure D.4 *Nut. Sheet 1 of 1.*

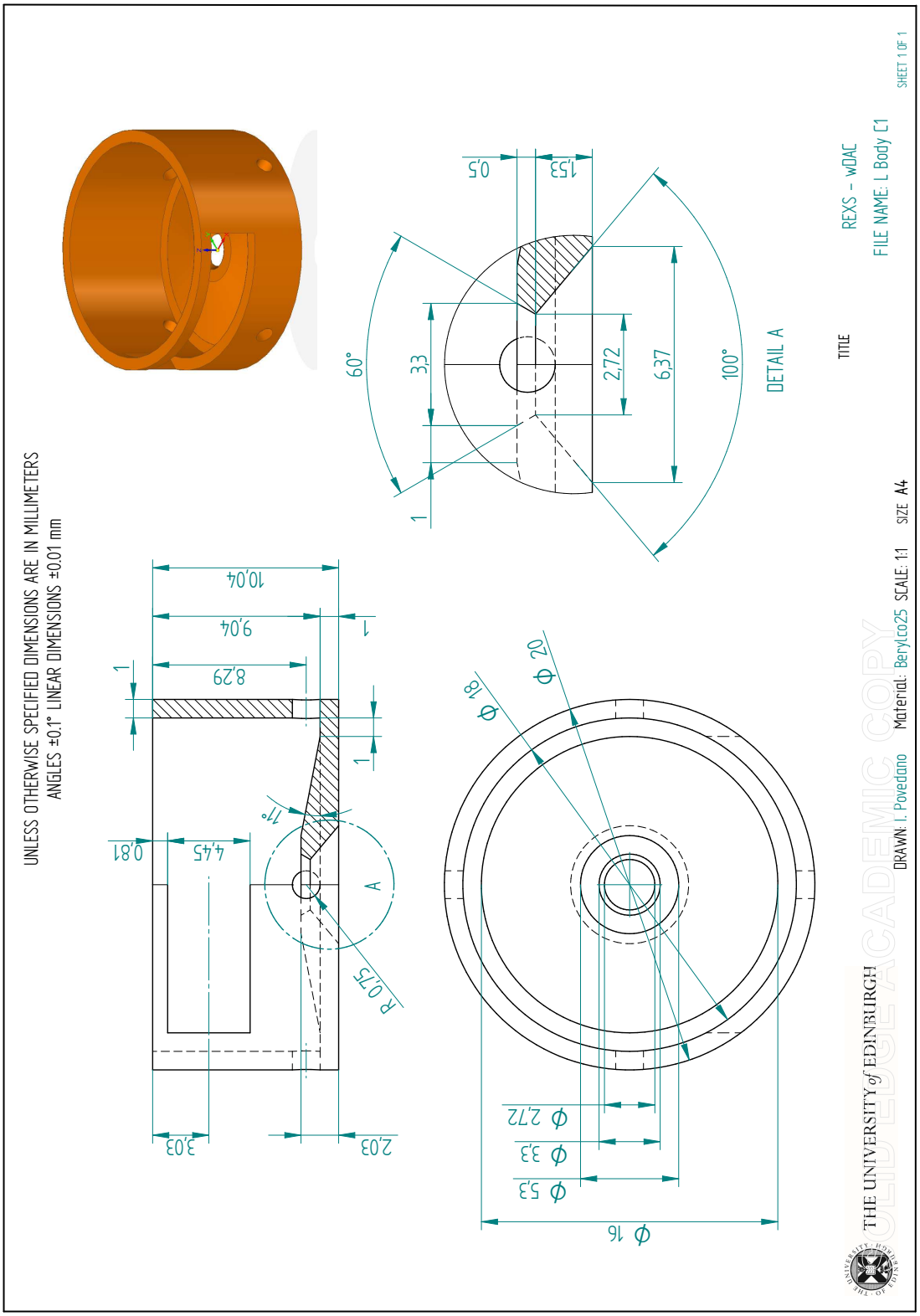

Figure D.5 *Lower body. Sheet 1 of 1.*

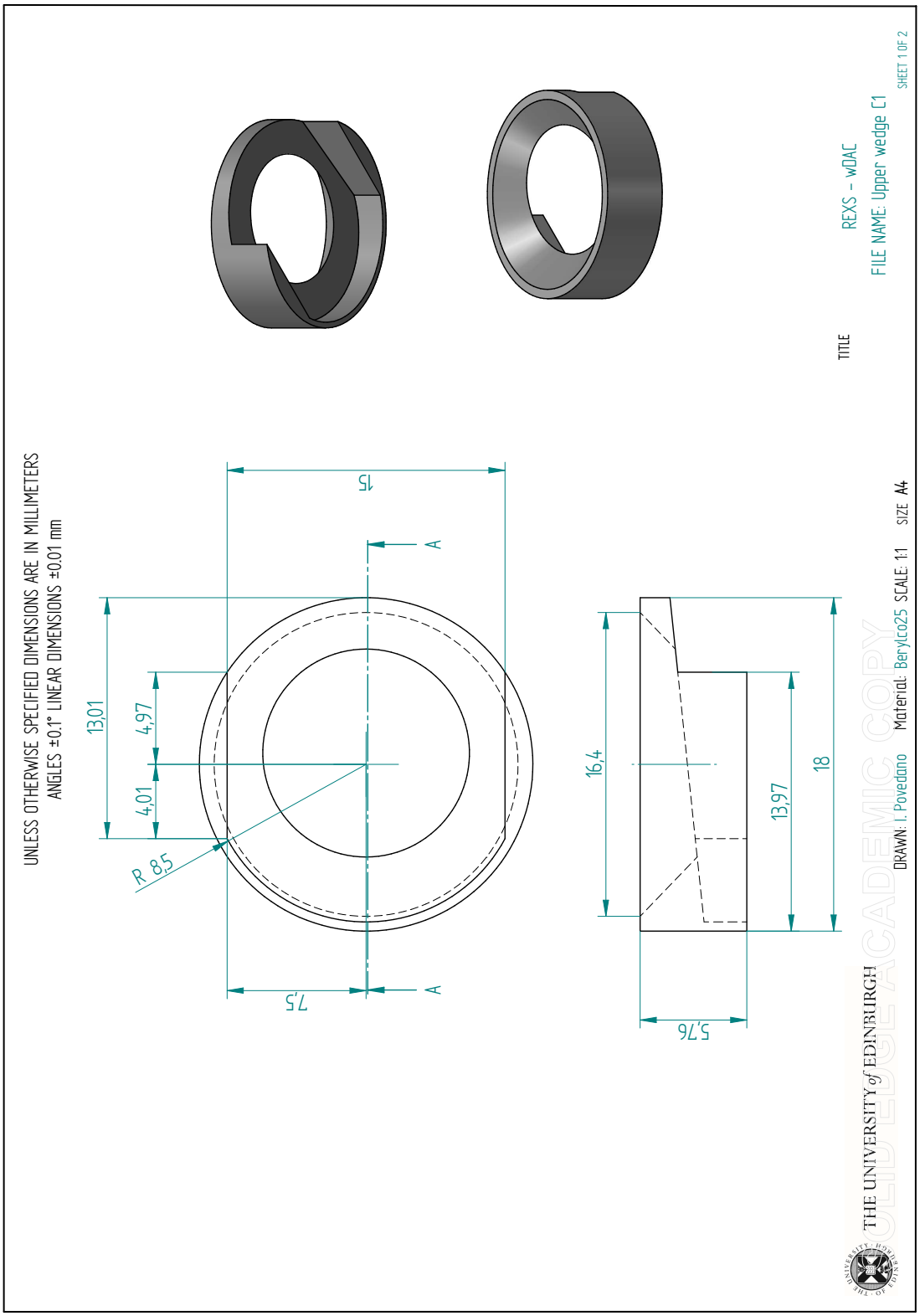

Figure D.6 *Upper wedge. Sheet 1 of 2.*

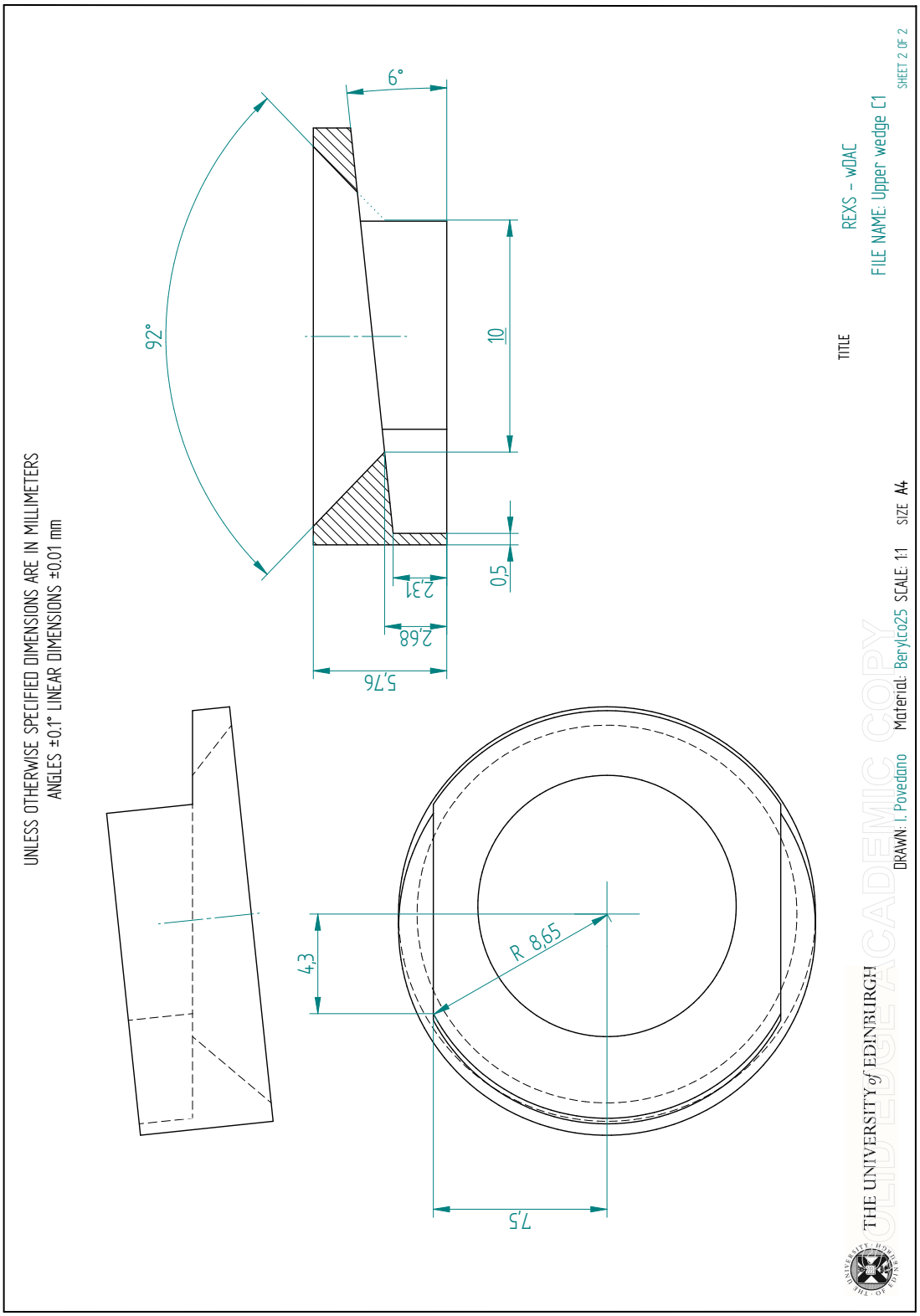

Figure D.7 *Upper wedge. Sheet 2 of 2.*

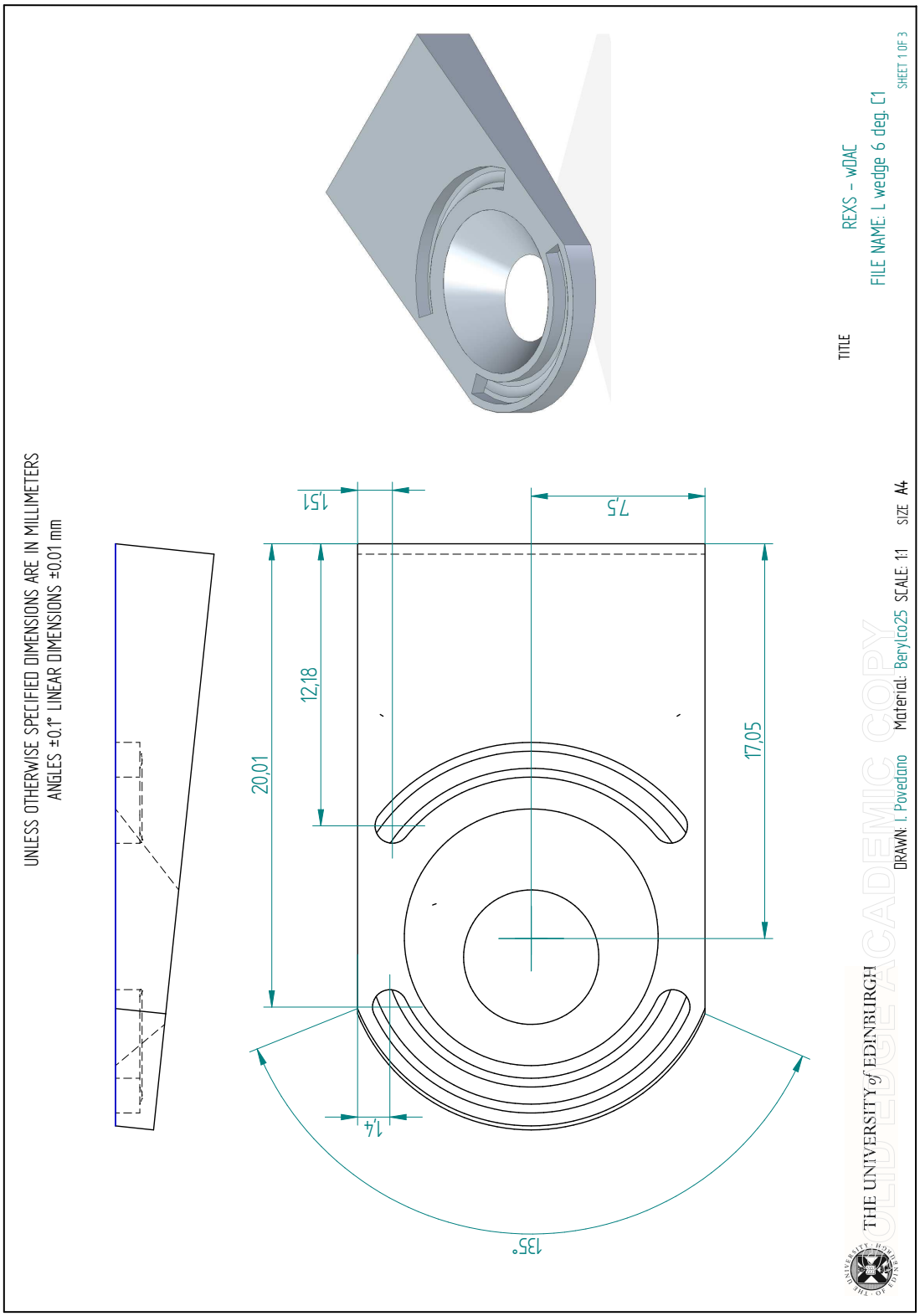

Figure D.8 *Lower wedge. Sheet 1 of 3.*

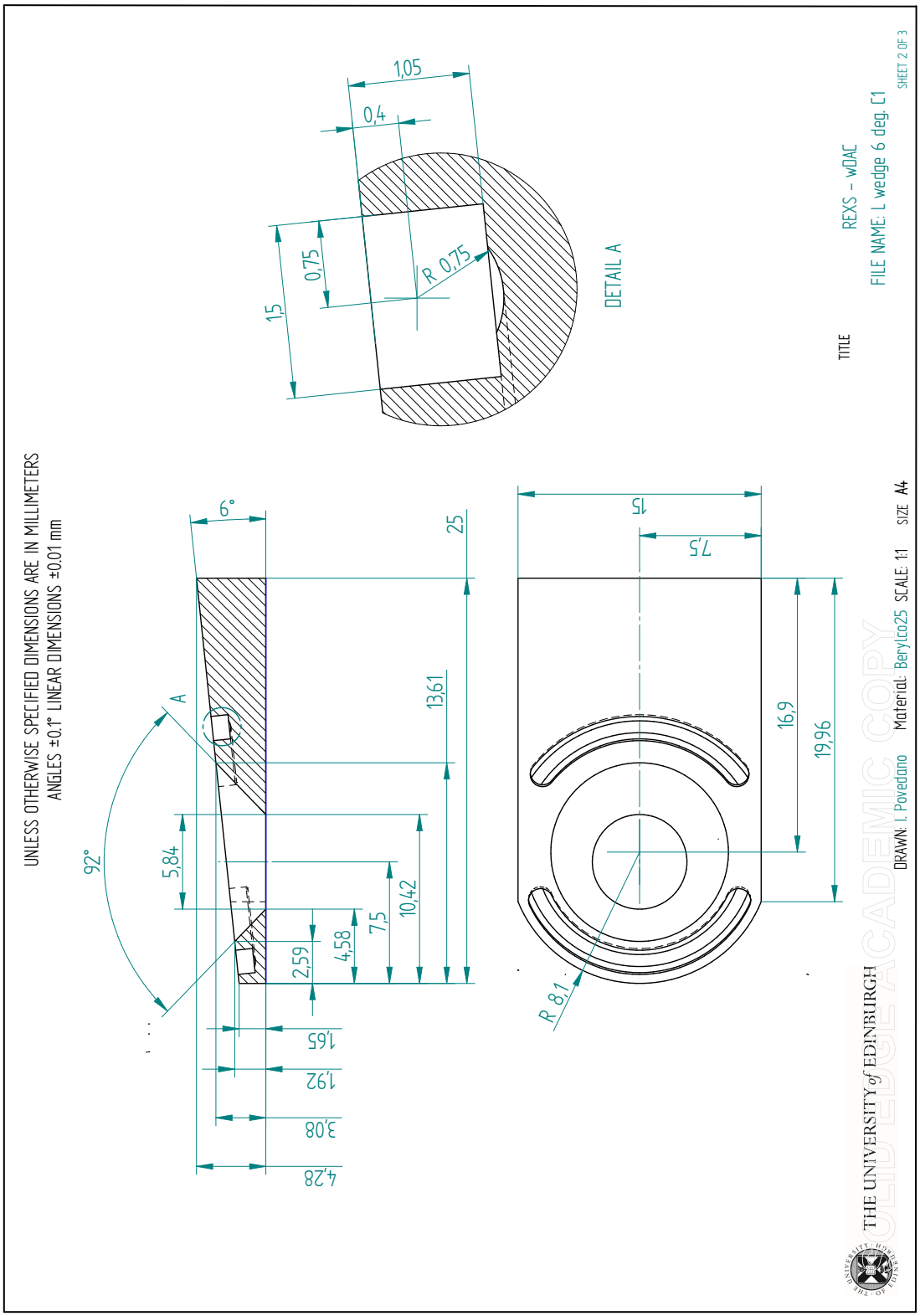

Figure D.9 *Lower wedge. Sheet 2 of 3.*

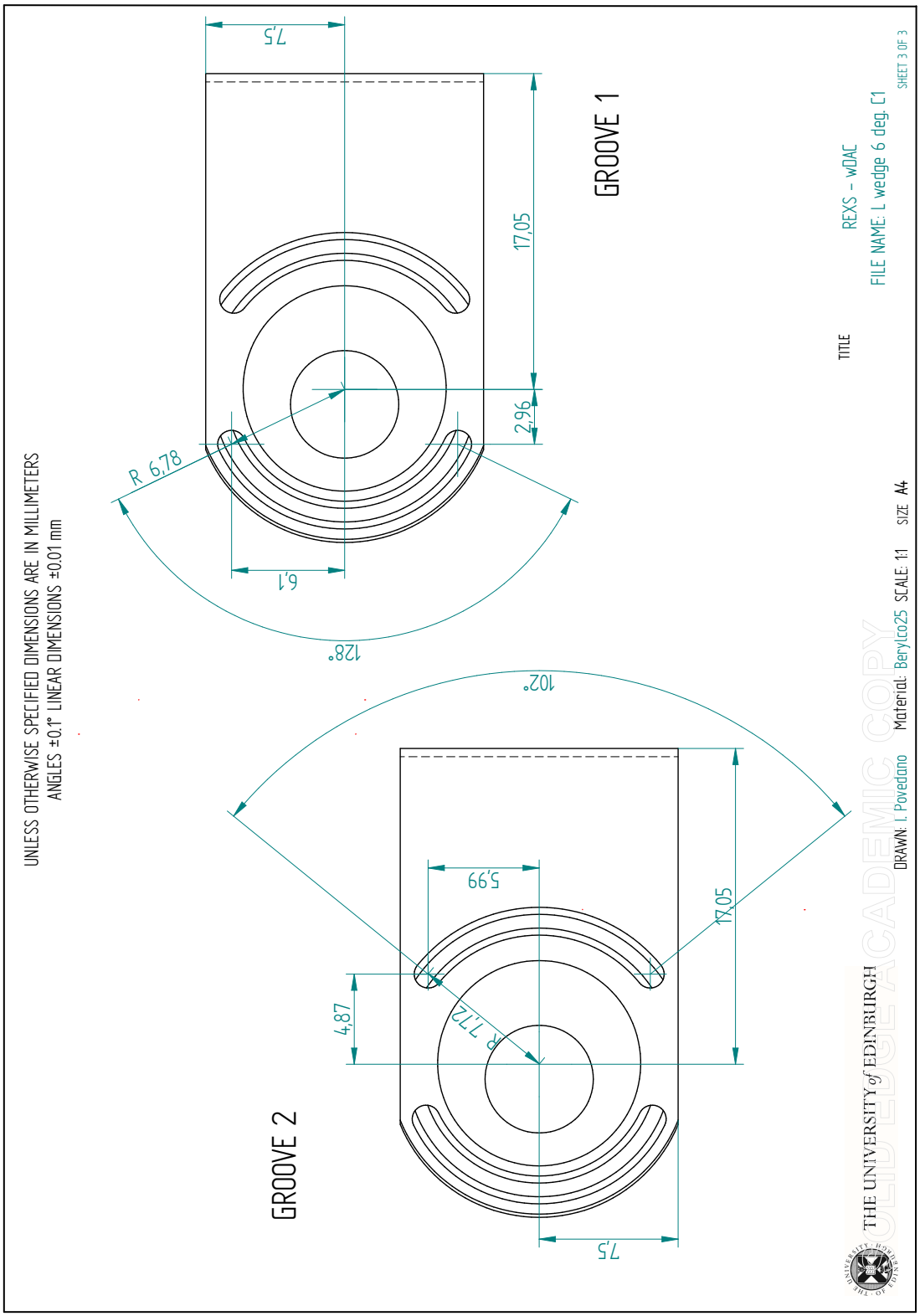

Figure D.10 *Lower wedge. Sheet 3 of 3.*

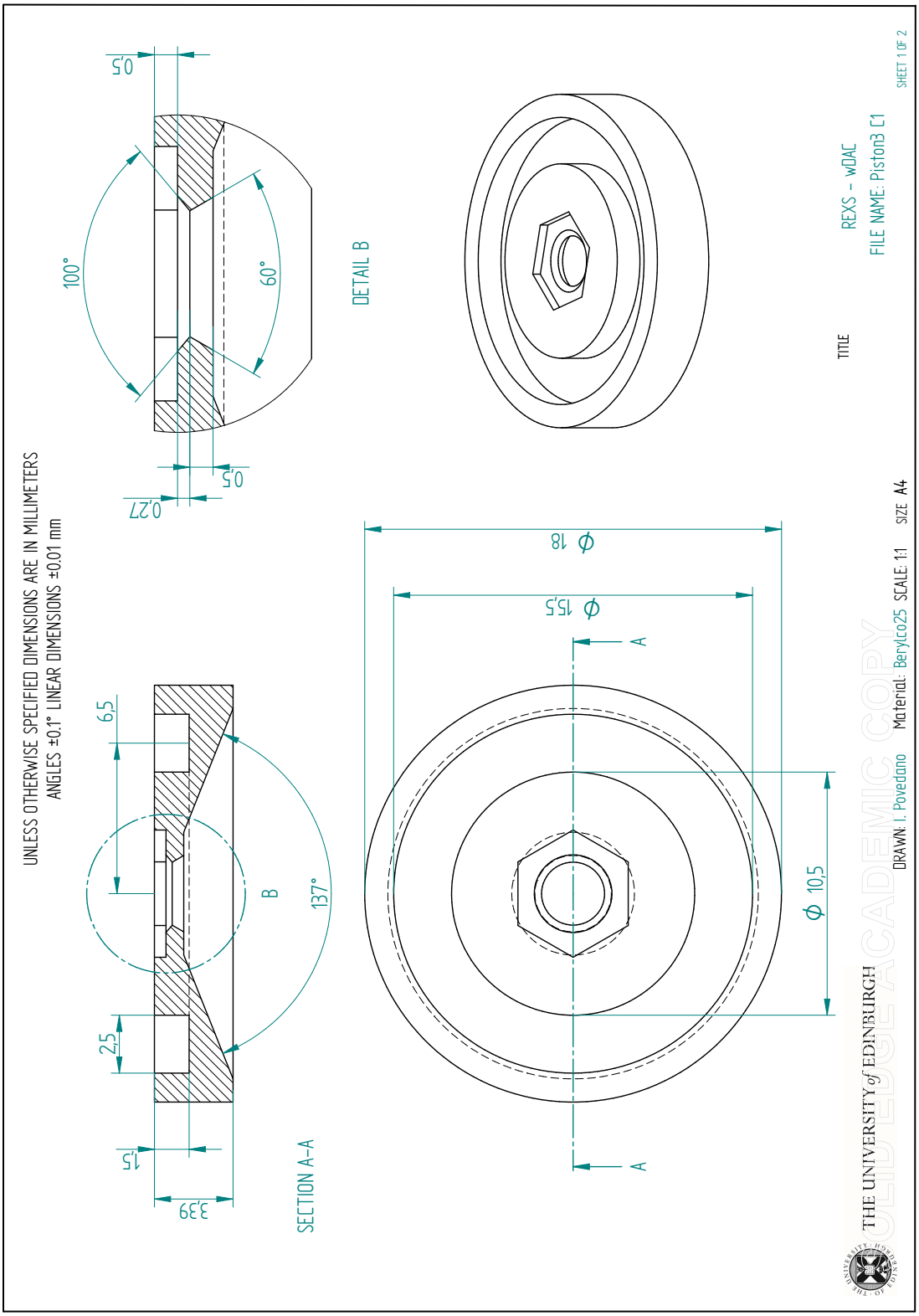

Figure D.11 *Piston. Sheet 1 of 2.*

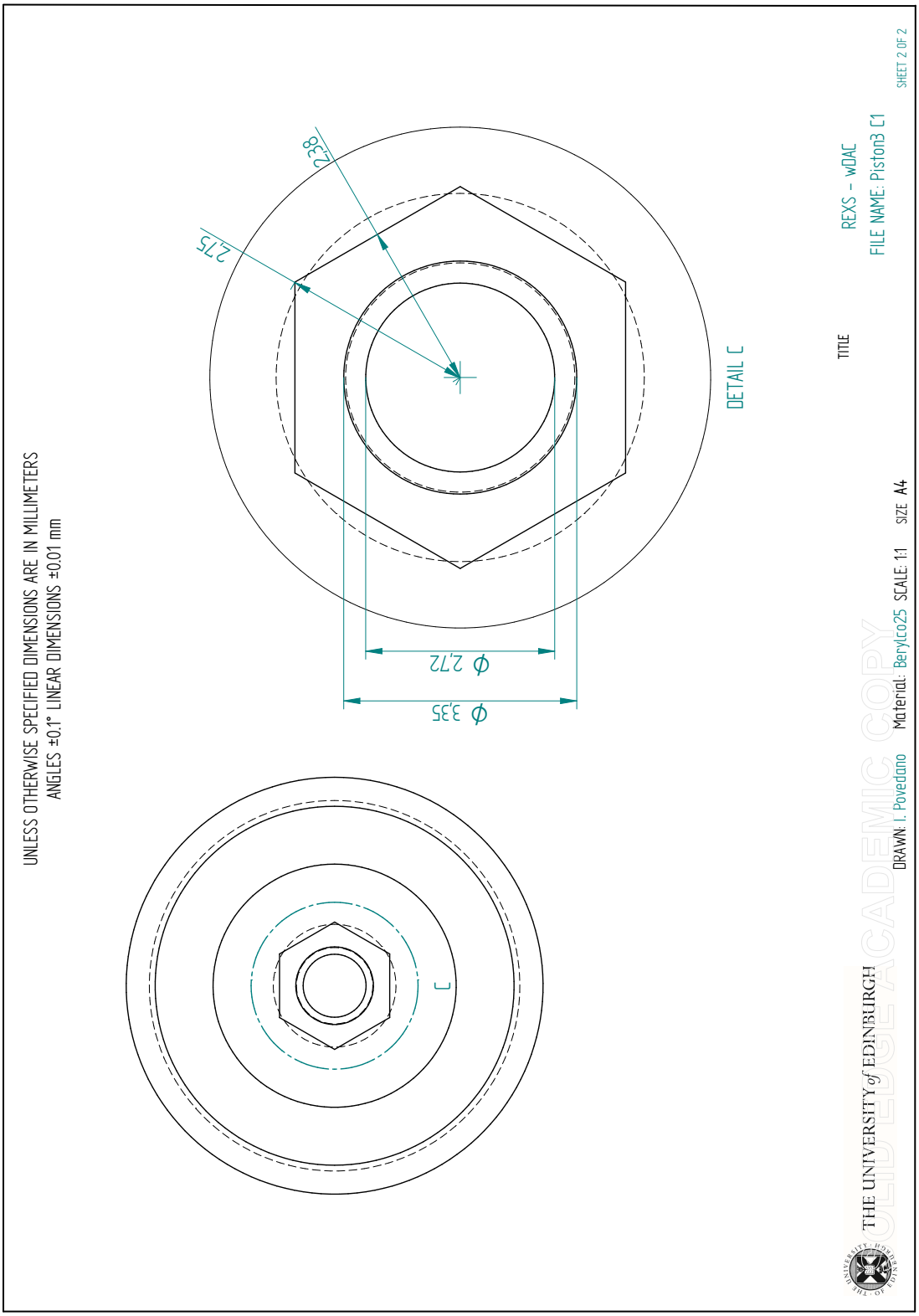

Figure D.12 *Piston. Sheet 2 of 2.*

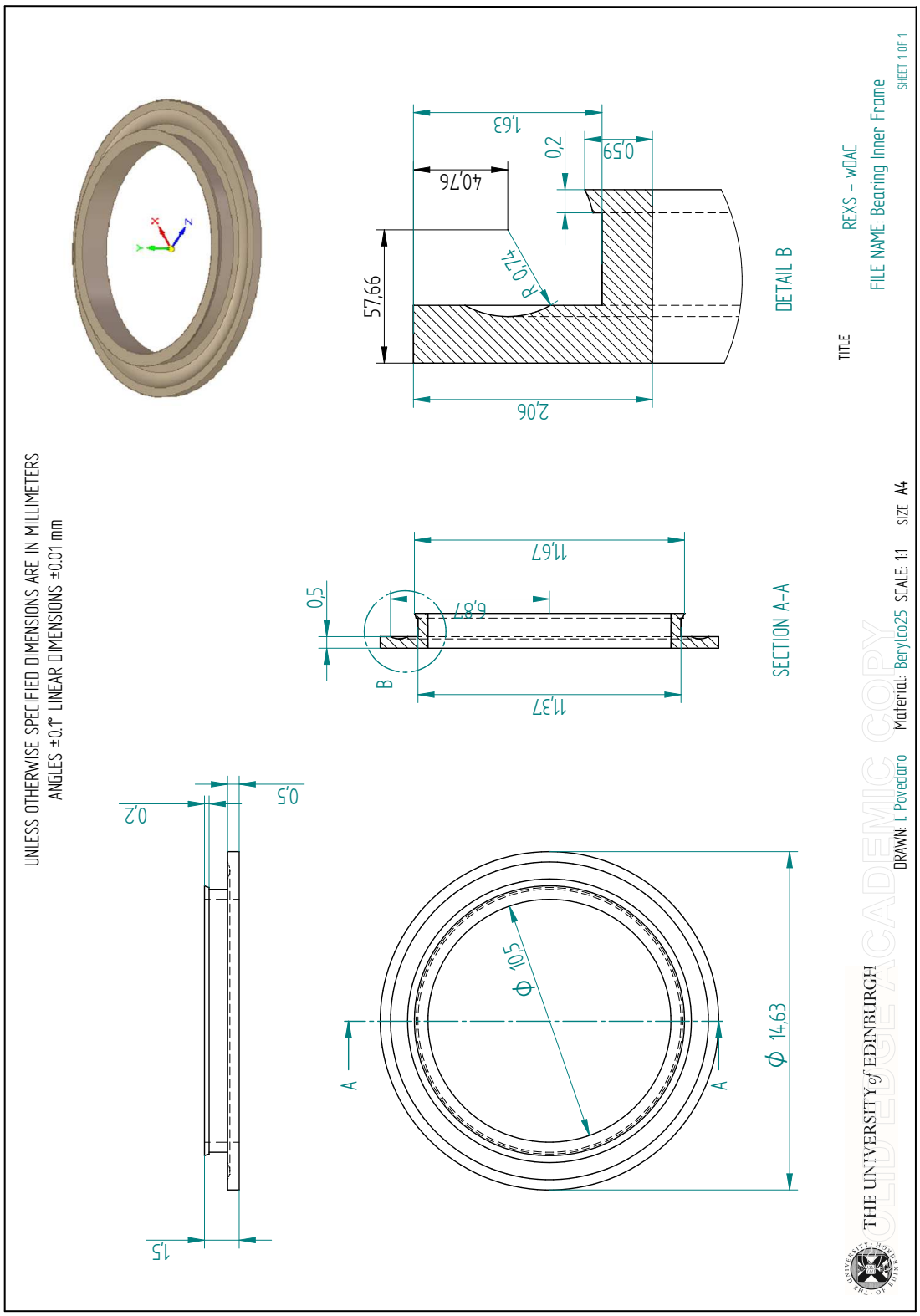

Figure D.13 *Inner bearing frame. Sheet 1 of 1.*

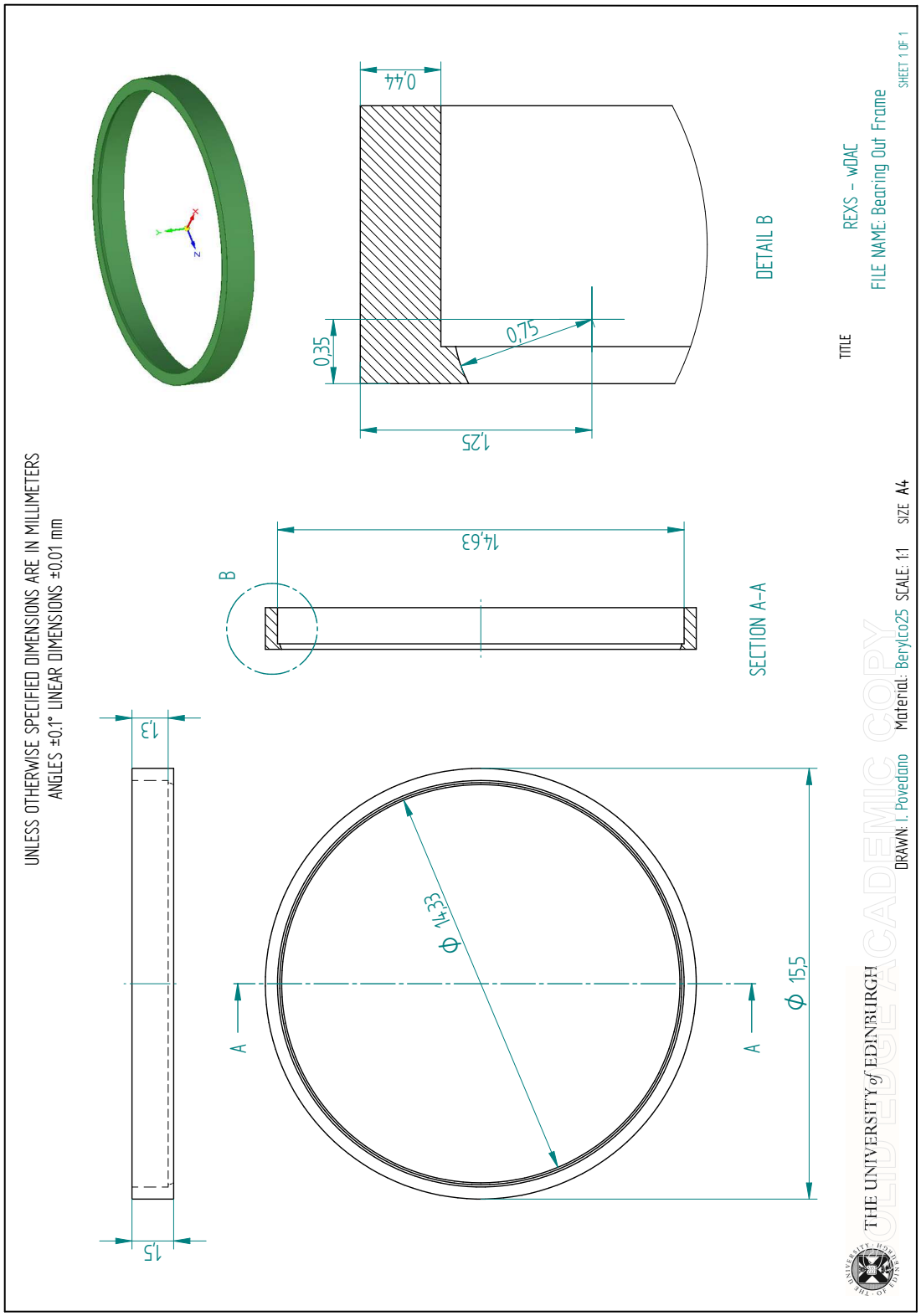

Figure D.14 *Outer bearing frame. Sheet 1 of 1.*

Appendix E

Technical drawings for the dome and the cryostat/CCR

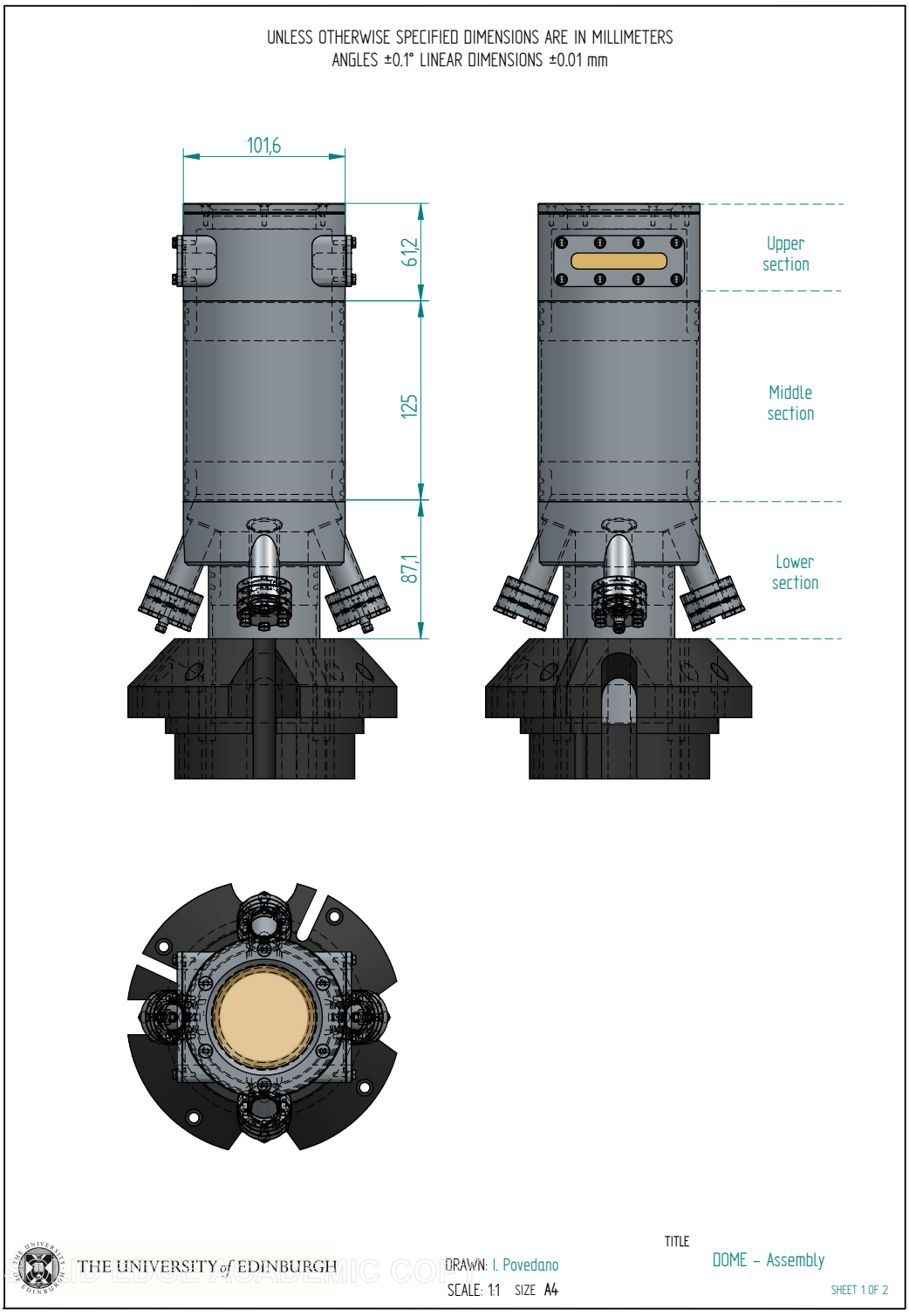

Figure E.1 *Drawings of the dome designed for HP-REXS experiments and detail of the main sections of the body.*

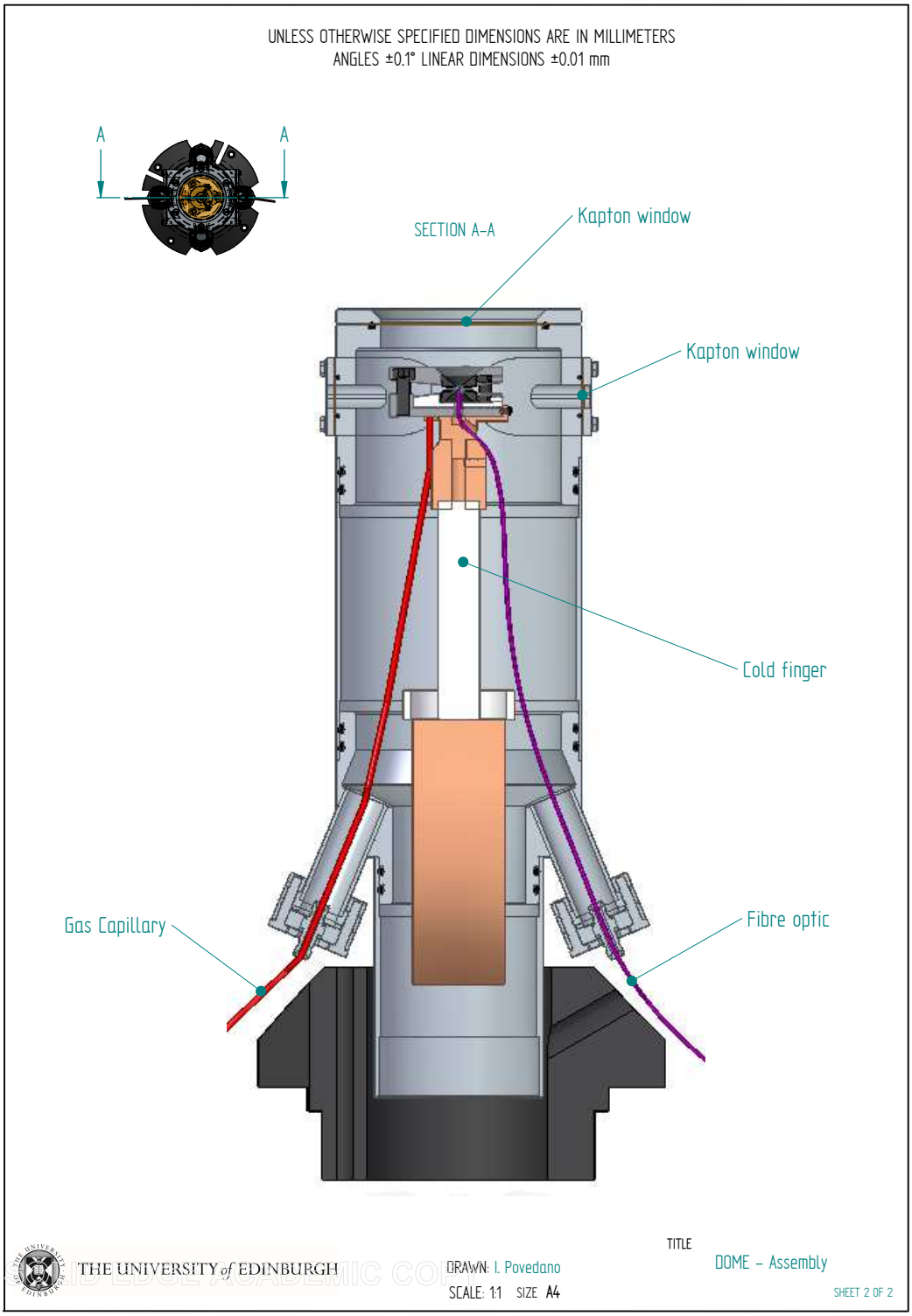

Figure E.2 *Section view of the assembly of the dome designed for HP-REXS experiments, cryostat and membrane cell with detail of the main components.*

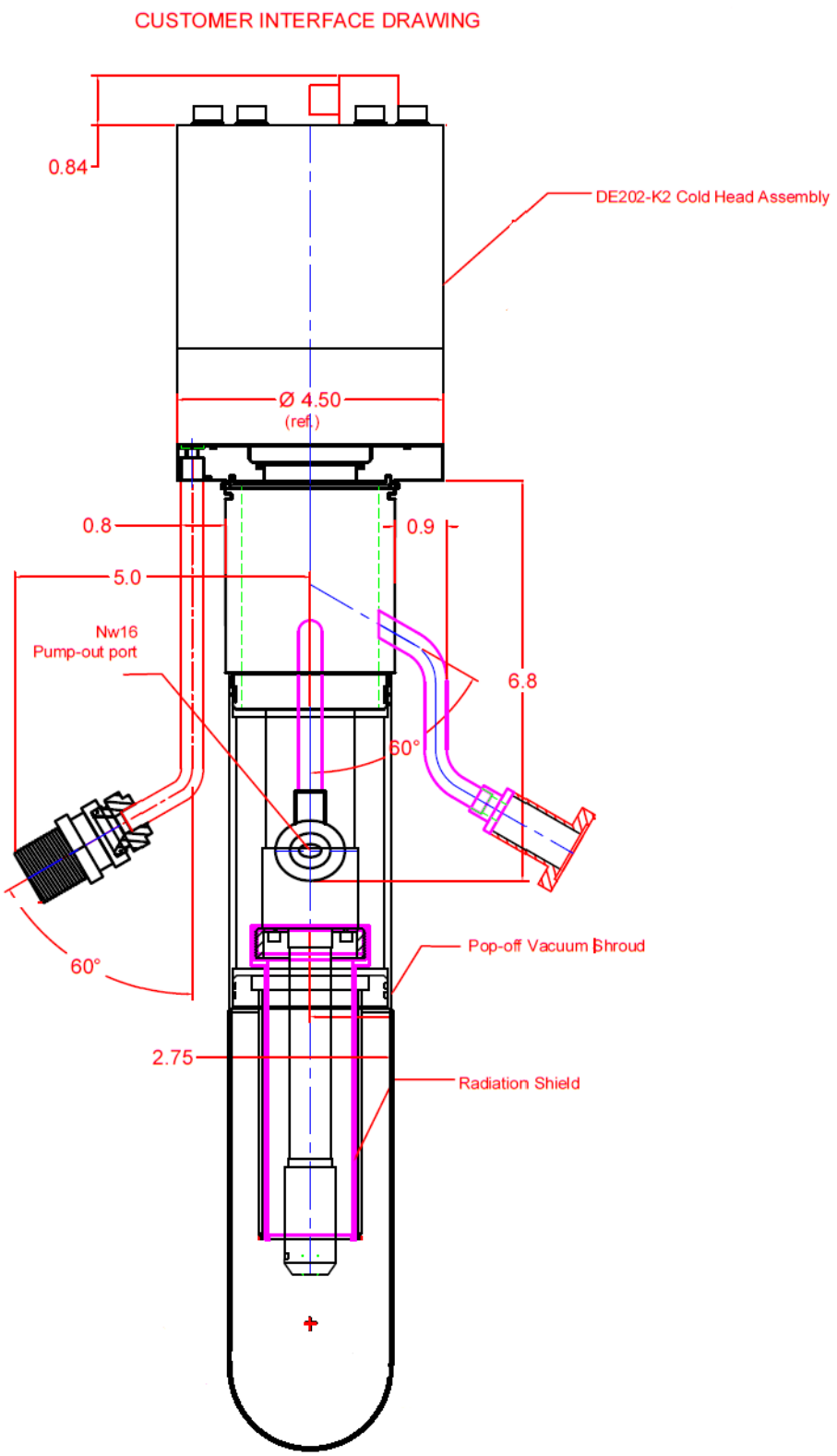

Figure E.3 *Drawings of the 4 K closed cycle cryostat (D-202N).*

Appendix F

Publications

JOURNAL OF SYNCHROTRON RADIATION

ISSN 1600-5775

Received 28 July 2019
Accepted 3 December 2019

Edited by V. Favre-Nicolin, CEA and Université Joseph Fourier, France

Keywords: high-pressure; resonant X-ray scattering; DAC; instrumentation development; low temperature.

High-pressure developments for resonant X-ray scattering experiments at I16

I. Povedano,[a,b]* A. Bombardi,[b,c] D. G. Porter,[b] M. Burt,[b] S. Green[b] and K. V. Kamenev[a]

[a]School of Engineering and Centre for Science at Extreme Conditions, The University of Edinburgh, Edinburgh EH9 3FD, UK, [b]Diamond Light Source Ltd, Harwell Science and Innovation Campus, Didcot OX11 3PU, UK, and [c]Clarendon Laboratory, Department of Physics, University of Oxford, Parks Road, Oxford OX1 3PU, UK. *Correspondence e-mail: isabel.povedano@diamond.ac.uk

An experimental setup to perform high-pressure resonant X-ray scattering (RXS) experiments at low temperature on I16 at Diamond Light Source is presented. The setup consists of a membrane-driven diamond anvil cell, a panoramic dome and an optical system that allows pressure to be measured *in situ* using the ruby fluorescence method. The membrane cell, inspired by the Merrill–Bassett design, presents an asymmetric layout in order to operate in a back-scattering geometry, with a panoramic aperture of 100° in the top and a bottom half dedicated to the regulation and measurement of pressure. It is specially designed to be mounted on the cold finger of a 4 K closed-cycle cryostat and actuated at low-temperature by pumping helium into the gas membrane. The main parts of the body are machined from a CuBe alloy (BERYLCO 25) and, when assembled, it presents an approximate height of 20–21 mm and fits into a 57 mm diameter. This system allows different materials to be probed using RXS in a range of temperatures between 30 and 300 K and has been tested up to 20 GPa using anvils with a culet diameter of 500 µm under quasi-cryogenic conditions. Detailed descriptions of different parts of the setup, operation and the developed methodology are provided here, along with some preliminary experimental results.

1. Introduction

A plethora of phenomena such as multiferroicity (Lee *et al.*, 2013), metal–insulator transitions (Calder *et al.*, 2012), charge-ordering (Pascut *et al.*, 2011), solving the magnetic structure of frustrated magnets (Agrestini *et al.*, 2008; Biffin *et al.*, 2014) or the distribution of magnetic domains (Fabrizi *et al.*, 2010; Waterfield-Price *et al.*, 2016) have been understood using the resonant X-ray scattering (RXS) technique. The RXS technique is based on the enhancement of the magnetic scattering cross-section that occurs when the energy of the incoming beam is tuned to the proximity of an absorption edge of the magnetic element of interest (Gibbs *et al.*, 1988; Hill & McMorrow, 1996). During the resonant process, electrons from a specific electronic level in the core are promoted to a virtual state near the Fermi level and immediately decay (Blume & Gibbs, 1988), emitting a photon with the same energy as the incident one. This powerful combination of spectroscopic information via the access to the specific projection of the electronic density of states and crystallographic capability via the sensitivity to periodic arrangements of electrons and magnetic moments in crystalline materials provides a unique source of information that has proven invaluable in understanding many complex electronic phenomena.

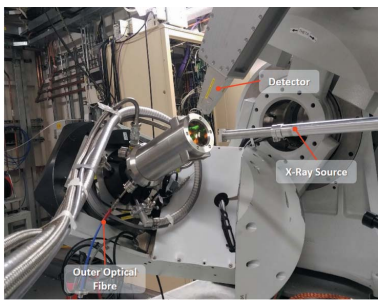

All the electronic arrangements mentioned above are particularly sensitive to the spatial distribution of the atoms involved in the correlation. By applying pressure we can induce changes in the crystal lattice, varying the orbital overlapping – distance and angle between atomic orbitals – and therefore we may affect directly the relative strength and in some cases the relative sign of the magnetic exchange interactions. Thus, using pressure, new exciting ground states can become accessible, such as for the case of the recently achieved high-temperature superconductivity on LaH_{10} (Drozdov *et al.*, 2019), the pressure-induced ferroelectricity in $GdMn_2O5$ (Poudel *et al.*, 2015) or the tuning of the metal–insulator transition in Ca_2RuO_4 (Nakamura, 2007).

Historically, the device most commonly used for high-pressure (HP) experiments due to its compact design and large range of pressures reachable is the diamond anvil cell (DAC). In a DAC, the sample, a single crystal in RXS experiments, is placed between the flat tips of two opposed diamond anvils and confined in the hole of a metallic gasket. In this chamber, pressure is generated by applying force on the anvils (see Fig. 1). In order to generate isotropic pressure, the sample space is also filled with a pressure-transmitting media (PTM) (gas, liquid or solid) which helps to maintain hydrostatic conditions. Additionally, we place a pressure marker in the sample chamber – a substance with a well known response to applied pressure such as an *in situ* pressure gauge.

Despite the potential of the combination of HP and RXS, there are not many examples in the literature using these two techniques, mainly due to the technical difficulties associated with the experimental setup, discussed in the next section, and the fact that the enhancement of the resonant signal is large only for dipolar transitions from electrons in the core towards semi-occupied electronic levels responsible for the magnetic properties of the material, in the presence of a strong spin–orbit coupling. Only under these conditions is the enhancement of the resonant signal large, facilitating the detection of the scattered signal. Most of these phenomena require low temperature to stabilize the electron-correlated state, which makes the manipulation of a DAC more complex due to the need of mechanisms for remote actuation. Additionally, the increase of the dissipation in the transmitted force due to the increased friction at low temperature, the limited space available inside the cryogenic equipment and the possible variations in the thermal contractions of the different parts of the cell represent further challenges. Moreover, most of the resonant edges of interest occur at energies below 13 keV, where the absorption of the diamond anvils can be high enough to compromise the detection of the weak scattered signal (Sapelkin & Bayliss, 2001). Nonetheless, the newly found interest towards 5*d* transition metal compounds showing a large increase of the signal at energies where the diamonds are relatively transparent, together with further improvement of the synchrotron capabilities that allow a reduced beam size with high flux, reactivates the attention of the condensed matter community towards the HP-RXS experiments. For these reasons, the design of tailored HP instrumentation compatible with the demands of RXS is needed.

In this paper, we present a new HP-RXS setup to perform experiments in back-scattering configuration within 30–300 K and up to 20 GPa of pressure on I16, the Materials and Magnetism beamline at Diamond Light Source (Collins *et al.*, 2010). The new setup includes a membrane-driven DAC, an optical system to measure pressure *in situ* and a custom-designed panoramic dome. Some of the preliminary tests performed are also shown, proving the feasibility of this experimental approach.

2. HP setup for RXS

In order to design a high-pressure setup for RXS we need to overcome the following technical challenges.

We need a pressure cell with a large opening in order to maximize the scattering angle and, therefore, with access to reciprocal space while maintaining its mechanical strength.

It must be compact enough to operate at low temperature for two reasons: the limited space inside cryogenic devices and the fact that the smaller the mass inside the cryostat the easier it is to reach thermal equilibrium. Ideally, it should be machined from material that has high thermal conductivity and low thermal expansion, while remaining mechanically strong at low temperature. The design must also provide the means of changing and measuring pressure *in situ* in the whole range of temperature. Finally, it is necessary to reach a compromise between the dimensions of diamond anvils and sample. The smaller the culets of the anvils, the higher the pressure we can access, but the smaller the size of the crystal that we can fit in the sample chamber and therefore the scattered signal we obtain. Additionally, the detection of the scattered peaks also depends on the contribution of the diamond scattering into the background noise and the absorption of radiation by the diamond anvils, which changes significantly with the incident X-ray energy and becomes particularly critical below 7 keV (Sapelkin & Bayliss, 2001).

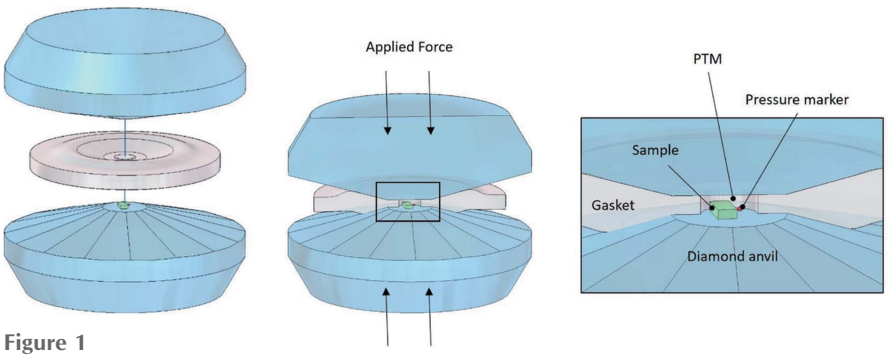

Figure 1
Illustration of the assembly and the main components of a diamond anvil cell: opposed diamond anvils, metallic gasket and sample space. The image on the right also shows in detail the elements placed in the sample chamber: sample, PTM and pressure marker.

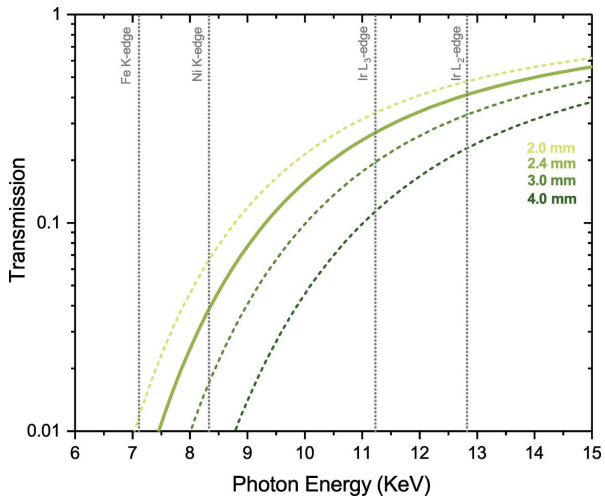

Figure 2
X-ray transmission (note the logarithmic scale) through diamond anvils of thickness between 1.0 and 2.0 mm for the range of energy between 6 and 15 keV calculated from Henke *et al.* (1993). We consider that the total thickness that the X-rays need to cross is twice the thickness of one anvil. For the anvils employed in our experiments, 1.2 mm thick, the X-rays need to go through a total thickness of 2.4 mm of anvil material (solid line). The dotted vertical lines represent some of the most common resonant edges of interest.

In Fig. 2, we can see how the thickness of the anvils plays a key role in the feasibility of the HP-RXS experiments. Small changes in the thickness result in significant variations in the transmitted signal. The anvils employed in our cell are a thinner version of the commercially available Boheler–Almax cut (Boehler & Hantsetters, 2004), with a final thickness of 1.2 mm. If we consider the total path of the incident and outgoing photons, the X-rays travel through a minimum thickness of 2.4 mm when perpendicular to the diamond face. Under these conditions, the minimum energy accessible without a huge reduction of the incident beam is just above 7.5 keV (solid line in Fig. 2). Other authors found a good solution using wide-angle partially drilled anvils in Laue geometry (Feng *et al.*, 2014; Wang *et al.*, 2016). In this case, a conical partial perforation of 60° reduces the total thickness of diamond crossed by the X-ray beam under 1 mm. However, for the back-scattering configuration chosen for the present design, such a solid angle limits considerably the access to the reciprocal space.

In the following sections, we describe the different parts of the experimental setup for HP-RXS experiments, including a detailed description of its operation.

2.1. Cell design

The proposed system was designed for use with the instrumentation available on I16, in particular a 4 K closed-cycle cryostat (D-202N) mounted on a Newport six-circle kappa goniometer. Keeping in mind the limited space available to host the cell, we designed a membrane-driven DAC inspired by the Merrill–Basset idea (Merrill & Bassett, 1974) with three pins for alignment and three screws as the locking mechanism. In Fig. 3, we can see a cross-sectional and a exploded view of the CAD model of the cell.

The material chosen for constructing the upper and lower body (parts 10 and 3 in Fig. 3), the piston (6) and the cryostat holder (2) is a CuBe alloy, BERYLCO25 from NGK (NGK-alloys, 2019), which combines non-magnetic behaviour with good thermal conductivity and mechanical high strength at low temperature (LT).

The cell presents an asymmetric design, with a panoramic aperture of 100° in the top part and a bottom half dedicated to the regulation and measurement of pressure. Unlike the original Merrill–Basset design, where the force is generated by tightening the locking screws (11 in Fig. 3), our design includes a gas membrane (4) that pushes the piston (6) and transmits the force towards the sample cavity. The gas membrane is hosted within the bottom half of the cell body avoiding the use of any additional fastening mechanism that would increase the overall thickness of the cell. When assembled, the cell is approximately 20–21 mm high, and fits into a circle of external diameter of 57 mm (circumference tangential to the triangular profile). This latter requirement is largely imposed by the required area of the gas membrane in order to reach the target

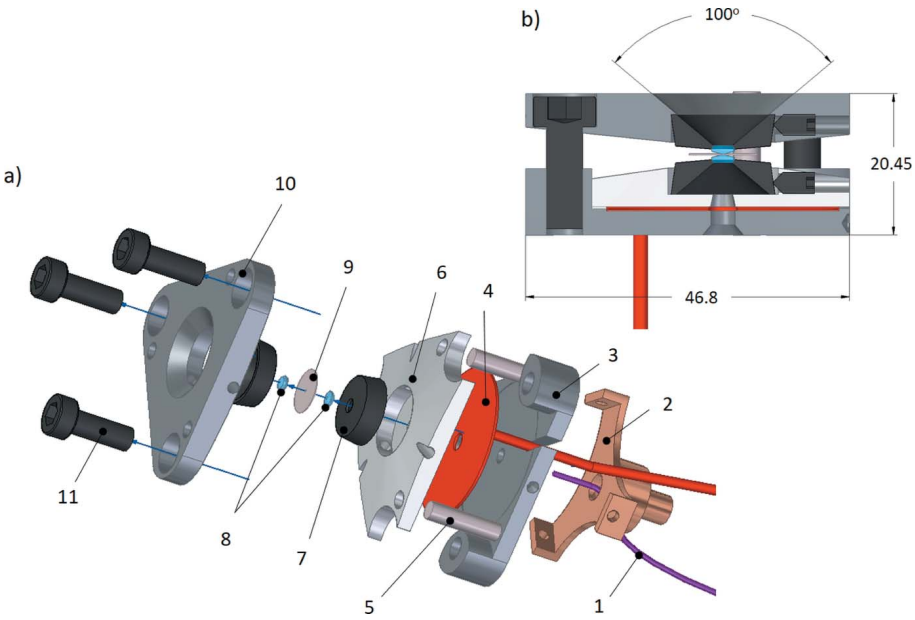

Figure 3
(*a*) Exploded view of the CAD model of the pressure cell. (1) Fibre optic, (2) cryostat adapter, (3) lower-body, (4) gas membrane, (5) alignment pin, (6) piston, (7) tungsten carbide seats, (8) diamond anvils, (9) gasket, (10) upper body and (11) M5 locking screws. (*b*) Section view of the cell with key dimensions in mm (opening angle in degrees).

pressure in the sample chamber. Taking into account the definition of pressure, $P = F/A$, we considered the target average pressure of 16 GPa at the anvil level, 120 bar in the membrane (36% under the safe limit of the gas controller, 190 bar) and oversized culets of 900 µm (12% larger than the maximum culet size considered for real experimental conditions) in order to compensate for the loss of force due to the friction between the various moving parts of the cell. Although the mechanism of pneumatic actuation was first proposed by Letoullec *et al.* (1988), our membrane design is more similar to the style of double-sided diaphragms (Daniels & Ryschkewitsch, 1983; Sinogeikin *et al.*, 2015). Our membranes are much more compact as they are built by welding two circular pieces of stainless steel foil, each 0.2 µm thick, with a final external diameter of 33.5 mm (35% smaller than the American counterparts) and with an inner hole of 4 mm. After use, the total thickness of the membrane changes to 0.5–0.7 mm. Attached to one of the faces is a metallic capillary (1 mm outer diameter) to introduce the gas and generate the force. For assessing the safe pressure limit of the membrane, a controlled burst test found a failure pressure of 850 bar, more than 600 bar over the maximum intended working pressure employed during our experiments.

We considered two options for the geometry of the experiment with the scattering plane crossing the diamond anvils. In Fig. 4(*a*) we show the Bragg geometry (back-scattering), where the reflected X-rays are collected though the same side of the cell through which the incident beam hits the sample; and in Fig. 4(*b*) the Laue configuration (transmission), where the scattered light is collected from the side opposite to the exciting beam. In Bragg geometry, we can use thicker samples, which are easier to prepare, and which also provide access to the high-angle region of the reciprocal space richer in reflections. In Laue geometry, the alignment of the sample in the beam is easier to conduct; the drop in the intensity of the transmitted signal due to the presence of the sample is larger than in the back-scattering geometry. This is the approach followed by Feng *et al.* (2014), using partially perforated diamonds to reduce the diamond absorption in transmission geometry. However, moving back to the comparison between Bragg and Laue configurations, in our particular case, to reach the same target pressure in transmission we would need a larger cell body in order to accommodate a larger membrane. Thus to obtain a symmetric scattering angle in both sides of the cell while keeping the same area in the membrane, its external diameter would be significantly larger. Under these conditions, the sample chamber would be easily above the centre of rotation without possibility of adjustment. For this reason, we found the back-scattering configuration as the most convenient for coupling with our current instrumentation arrangement.

Alternative designs with the scattering plane across the metallic gasket to avoid the absorption of radiation of the diamond anvils have been proposed by other authors (Kernavanois *et al.*, 2005). In these cells, a wider scattering angle can be accessed as well as absorption edges of lower energy. Despite these advantages, they employ beryllium as the gasket material, which is widely known for its toxicity and requires special dedicated handling instrumentation which is not currently compatible with the regulations at Diamond.

The back-scattering configuration leaves free the bottom face of the cell that can be employed for hosting the optics needed for the pressure measurement using the ruby fluorescence method (Piermarini *et al.*, 1975). To this end, we developed an optical system that consists of two sections: a bifurcated fibre in the external part of the cryostat, made of six individual laboratory-grade cores, 300 µm in diameter and 2.5 m long, assembled in two legs (5 + 1) from Ocean Optics; and a single core fibre (1 mm thick) inside the cryogenic device. The three ends of the bifurcated fibre are connected through SMA connectors to a 532 nm diode laser, a portable spectrometer from Ocean Optics (MayaPro4000) and the single core fibre inside the cryostat. The end of the inner fibre in the proximity of the sample chamber is a manually polished free end with no fitting.

A number of alternative models for the optical setup were tested including additional mirrors and collimation lenses. However, the loss of light due to the transfer between different optical elements was found to be larger than in the system adapted for our cell and described above.

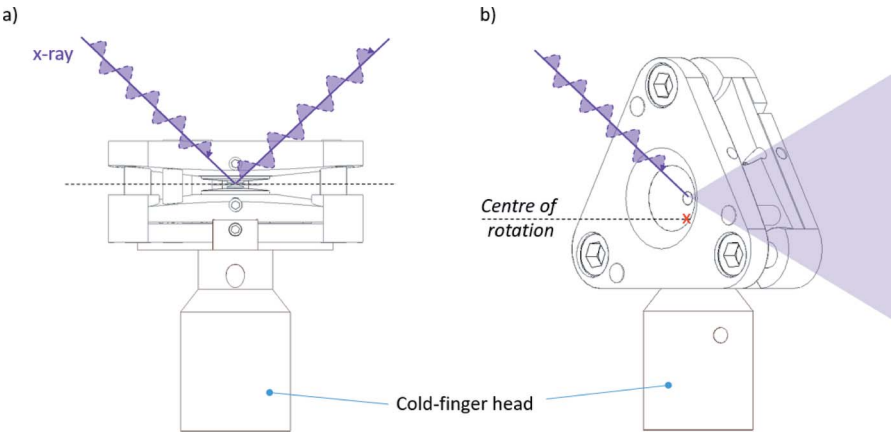

Figure 4
View of the back-scattering (*a*) and transmission (*b*) configurations.

2.2. Panoramic dome

In addition to the pressure cell, a panoramic dome has been designed specifically for the HP-RXS experiments. The dome is machined from steel 304L; it presents a cylindrical structure divided into three sections with a total height of 27.3 cm over the base of the cryostat and 10.2 cm in diameter. The possibility of assembling the dome in three separate parts allows its top section to be easily replaced to accommodate different experimental geome-

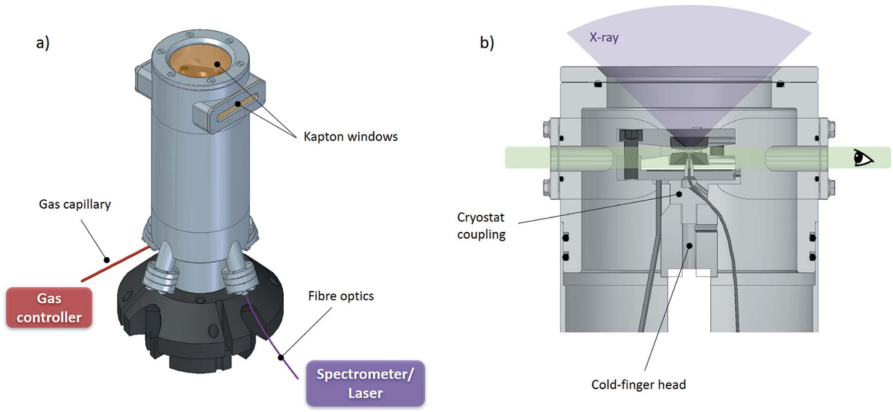

Figure 5
CAD-model of (*a*) the cryostat dome with details of the feed-throughs dedicated to the gas capillary and the fibre optics and the different optical windows. (*b*) Section view with details of the interior of the cryostat in the proximity of the pressure cell. Shaded areas represent the scattering angle at the top and lateral optical access at the bottom.

tries. In Fig. 5, we show a CAD model with some of the main features of the design.

In this first version of the dome, the upper section is specifically designed for experiments in back-scattering with three kapton windows: a panoramic aperture at the top for the scattering of the X-rays and two lateral windows for optical access. Kapton and beryllium are the only reliable materials employed for windows in cryogenic devices due to their low absorption of X-rays. Kapton allows visual examination of the cell while showing a reasonable durability to conduct the experiments and offers a reasonable transmission above 7 keV. The lower section of the dome presents four fitting ports, one of them dedicated to the insertion of the gas capillary for pressure regulation and the second one for the fibre optics. In order to prevent large oscillations of temperature when pumping gas into the membrane, the gas capillary is attached to the first stage of the cryostat so the gas is pre-cooled before reaching the cell body. In Fig. 6, we provide a photograph of the real pressure cell and the setup for HP-RXS experiments.

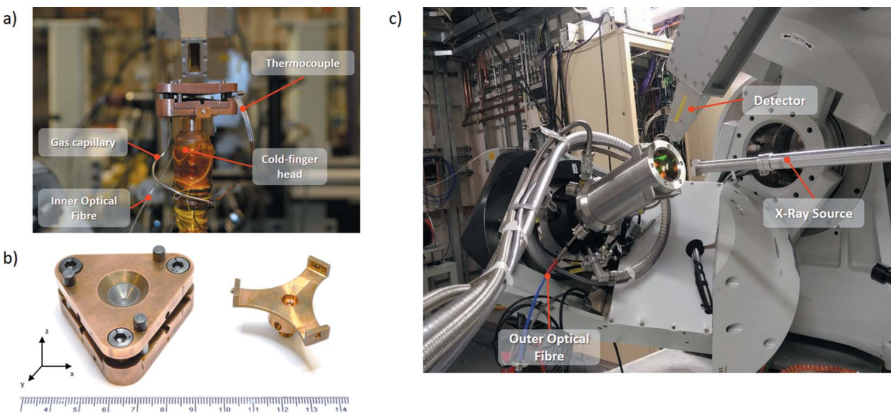

Figure 6
Pictures of the setup for HP-RXS experiments. (*a*) Pressure cell mounted on the cold finger. Detail of the thermo-couple, optical fibre, gas capillary and cold-finger head. (*b*) Pressure cell and cryostat coupling piece. (*c*) HP-RXS setup on I16. Detail of the X-ray source, optical fibre and detector.

2.3. Loading and operation

In order to perform an HP-RXS experiment, we start by loading the pressure cell. First, the sample is placed as described before between the two tips of the diamond anvils, centred in the hole of a pre-indented metallic gasket (see Fig. 1). Once the sample is in the desired orientation, we include the pressure marker and the PTM in the sample chamber. Then, the cell is clamped by tightening the three M5 screws and mounted on the head of the cold finger. Once the cell is mounted on the cryostat, the next step is the alignment of the sample in the centre of rotation of the diffractometer. In a first approximation, with the cryostat open as in Fig. 6(*a*), we adjust the sample position optically by using a set of cameras in different orientations. Then, using the X-ray beam, we scan the gasket hole along the three directions of the space x, y and z, looking for a drop in the diffuse scattering from the diamond due to the presence of the sample. In order to look for a drop along the z axis [see system of coordinates in Fig. 6(*b*)], assuming the sample is flat and parallel to the diamond tips, we rotate the cell $\pm 5^{\circ}$ around an axis normal to z. Then, with the sample tilted, we scan along the z axis and we update the sample position to the point where the absorption is at its maximum. Now we are in a position to start looking for diffraction peaks. After finding a couple of reflections with their corresponding *hkl* indices, we can build an orientation matrix to navigate in the reciprocal space and to reach the position of the reflections of interest.

Once the alignment of the sample at room temperature is complete, we can start cooling down the system. Due to the limited space inside the cryostat we need to operate without any sort of thermal shielding but the actual dome. This limits the minimum temperature reachable to 30.5 K, with an approximate cooling time of 2.5 h (see Fig. 7). The increased base temperature is due mainly to the mass of the cell and the absence of the thermal shield. A temperature difference is observed between the head of the cold finger and the cell body (Fig. 7, inset).

During the cooling process, the height of the sample changes due to the thermal contraction of the different parts of the cryostat. This height variation is reproducible, so it is possible to estimate the correction in sample height based on the measured sample temperature. In order to produce a reliable temperature variation, the cryostat is held at base temperature while the sample temperature is

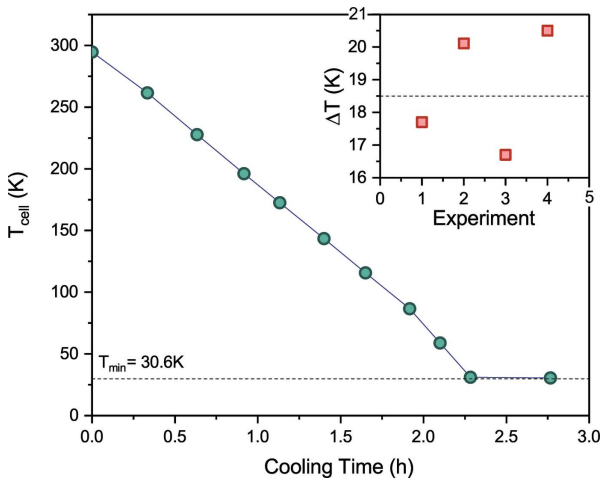

Figure 7
Cooling time of the cell mounted inside the cryostat from ambient to base temperature. The dashed line shows the minimum temperature reached. The inset shows the temperature difference, ΔT (K), between the top of the cold finger and the cell body for different experiments. The dashed line in the inset shows the average value of the temperature difference.

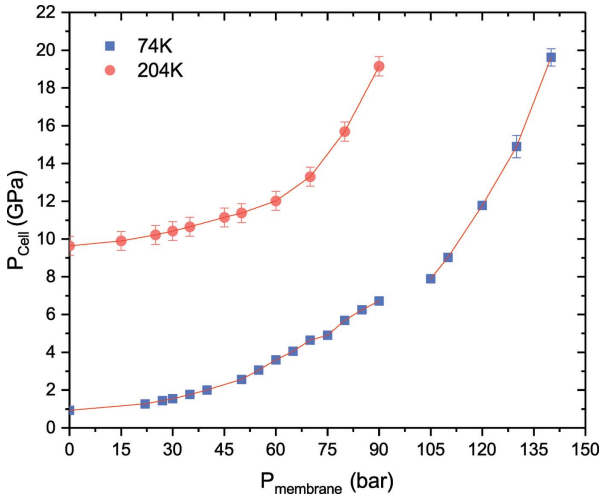

Figure 8
Results of the pressure test performed at 74 K and 204 K with blue squares and red dots, respectively. Pressure in the cell in GPa as a function of the pressure in the membrane in bars. The first determined using the ruby fluorescence technique, the second regulated using a GE Druck PACE5000 gas controller. The cell was prepared using 4:1 methanol:ethanol as PTM and it was closed initially at 1 GPa. The test was performed in the first place at 74 K reaching a maximum pressure close to 20 GPa. Then the pressure in the membrane was released and the test was repeated at 204 K.

controlled using a heater. Therefore, even for the cases when a particularly low temperature is not required, initially the system needs to be cooled down to base temperature. When the target temperature in the cell is reached, we can look for the reflections resulting from the electronic correlation of interest, realign the sample position using the signal of the peak under study (x, y, z scans described above maximizing the peak intensity) and start the RXS experiment.

Pressure is controlled by pumping helium gas into the membrane that pushes up the piston increasing the force in the sample chamber. In Fig. 8, we can see the evolution of the level of pressure in the cell against the pressure in the membrane for two different temperatures. The two pressure tests were performed using anvils with culets of 500 µm, 4:1 methanol:ethanol (ME) as PTM and a steel gasket (initially 200 µm thick) pre-indented down to 107 µm thickness. The cell was loaded with a piece of ruby at an initial pressure of 1 GPa and mounted on the cryostat. Then, the temperature was stabilized, firstly at 74 K and the pressure was increased, reaching a maximum value close to 20 GPa measured by the ruby fluorescence method and corrected to the actual temperature. After that, the pressure in the membrane was released and the test was repeated at 204 K. In both cases, we found a deterioration of the ruby signal (broadening of the peaks and loss of intensity) at the same critical pressure that can be attributed to the lost of hydrostaticity at these conditions and to the fact that the sample chamber is further away from the fibre optics tip as we keep on increasing pressure by inflating the membrane.

Additionally to the pressure experiment, extra tests were performed in order to further develop the correct experimental methodology, determining the time required to stabilize the system when carrying out small variations of temperature and to explore the possibility of using gold as an alternative for pressure determination. In order to do so, we prepared the membrane cell using anvils with culets of 800 µm, a steel gasket indented down to 116 µm and drilled with a 500 µm hole in the centre of the indentation. Then, the cell was loaded with gold and ruby using 4:1 ME as PTM. Several pressure–temperature (P–T) points were reached observing that for temperature increments of 5–10 K a stabilization time of 35–40 min is required in order to reach the thermal equilibrium. This long stabilization time is an expected consequence of the temperature difference observed between the head of the cold finger and the cell body (see Fig. 7, inset), that could be improved using better insulation from the exterior, improving further the thermal contact between the cell and the cold finger and miniaturizing the cell.

For several of the experimental P–T points reached, we measured the level of pressure using the dependence of the ruby fluorescence shift applying the temperature correction from Datchi *et al.* (2007) and the equation of state of gold from Holzapfel *et al.* (2001). The results obtained can be seen in Fig. 9. For the gold scale, the values of pressure were obtained by averaging the lattice parameters calculated from the position of the reflections (511), (531) and (442) and applying the equation of state mentioned.

Both methods provide reasonably similar values of pressure up to 4 GPa, from where we observed an underestimation from ruby with respect to the gold gauge. This discrepancy between the two approaches might be the result of a combination of deviatoric stress arising from the solidification of the pressure medium (non-hydrostaticity) (Torikachvili *et al.*, 2015) and the fact that the crystal of ruby and the piece of gold might not be exposed to the same stress due to the pressure gradient along the sample chamber (Mao, 1978).

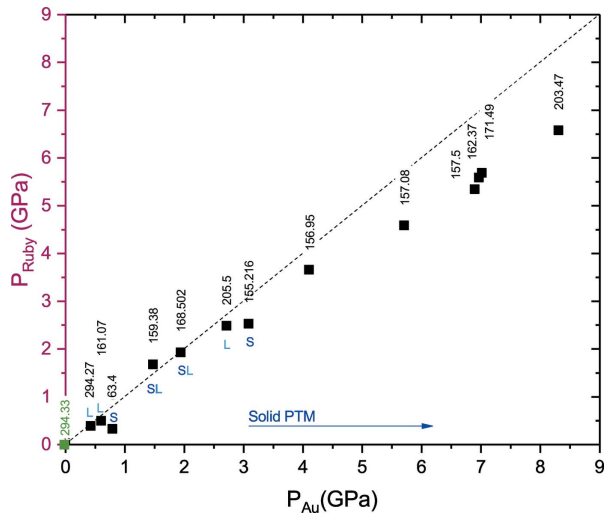

Figure 9
Comparative measurement of pressure for different experimental conditions using the pressure shift of the R1 luminescence line of ruby (Datchi *et al.*, 2007) and the equation of state of gold from Holzapfel *et al.* (2001). All the pressure points were acquired using the same loading for different temperature and pressure conditions. The temperature for each point is given (vertical) above the each data point. 'S' and 'L' stand for the state of the pressure media (4:1 methanol:ethanol), 'solid' or 'liquid', respectively. The first point in green corresponds to the reference for ruby and gold at room conditions.

In favour of experimental simplicity, the ruby gauge is more convenient. At the moment, the gas control unit for the membrane is placed inside the experimental hutch and cannot be controlled remotely from the control room. Therefore, pressure-tuning requires switching off the beam, entering the hutch and manually operating the gas membrane. Once we are inside the hutch, whereas the ruby method allows the level of pressure to be estimated directly in a few seconds, the use of gold requires exiting the hutch once again, interlocking, switching on the beam, aligning at the gold position and acquiring the diffraction pattern. In some cases, we may need to repeat this sequence of steps several times until reaching the aimed level of pressure, increasing significantly the time employed (from minutes to hours compared with the ruby method). A second aspect that makes the use of gold less suitable is the fact that the addition of extra components in the sample chamber represents an extra source of background noise that in some cases may be critical when trying to detect particularly weak resonant signals. For our particular experimental conditions and for the reasons just mentioned, we consider the ruby fluorescence a better approach to estimate pressure.

We also experienced some issues due to the chemical reactivity of the different substances present in the sample chamber when exposed to the X-ray radiation that hampered our progress in establishing the correct experimental method. On several occasions we observed photon-induced chemical reactions in the sample chamber that degraded the quality of the sample and prevented us from observing the signals of interest. We tried different loading combinations of PTM (4:1 ME, 1:1 *n*-pentene:isopentane, Silicone oil, Daphne oil 7373, NaCl, KCl) and substances employed to fix the sample position (Vaseline, vacuum grease and superglue), finding that not the loading combination but only the attenuation of the beam was effective in preventing the reactions from happening. At the energy range employed in our experiments (8–13 keV), the absorption cross-section of X-rays is larger than for higher energy, making the lighter elements in the transmitting media more prone to undergo chemical reactions. Helium gas loading was also considered to reduce the reactivity of the sample chamber components. However, a contraction in the chamber volume to 5–10% of the initial value at HP–LT is expected when using stainless steel gaskets (Feng *et al.*, 2010), which requires initial thin samples, 10 µm × 10 µm × 5 µm, that would not take full advantage of the full flux of the focused beam. A number of HP-RXS studies in the literature consider 4:1 ME as the best option for PTM (Feng *et al.*, 2010, 2014; Wang *et al.*, 2016, 2019). On the other hand, only 6 GPa of pressure at 200 K are sufficient to solidify He (Mao *et al.*, 1988; Loubeyre *et al.*, 1993). Thus, it is not clear that He provides a significant improvement in hydrostaticity over 4:1 ME at LT. The attenuation of the incident beam down to 2% of the full intensity seems to be enough to avoid the degradation of 4:1 ME loadings and was adopted as the preferred methodology. Besides the attenuation of the beam, the use of steel as the gasket material was also found to be the most adequate for our experiments. The emission lines of Fe, $K_{\alpha 2}$ (6.390 keV) and $K_{\beta 1}$ (7.057 keV), are far enough from the range of energy employed in our experiments in order to discriminate completely from the signal using the detector energy threshold. Other gasket materials such as Re, commonly used for the higher-pressure range, were found not suitable for this reason.

3. Experimental application

An HP-RXS study on the magnetic order of $Sr_3Ir_2O_7$ was conducted on I16 using the developed instrumentation. $Sr_3Ir_2O_7$ is an intermediate case (n = 2) of the Ruddlesden–Popper (RP) series of layered iridates $Sr_{n+1}Ir_nO_{3n+1}$ that presents tetragonal structure at ambient conditions (*I*4/*mmm*, a = 3.9026 Å, c = 20.9300 Å) (Subramanian *et al.*, 1994) and magnetic order at relatively high temperature (T_N = 285 K) (Boseggia *et al.*, 2012). In this family of compounds the interplay between the octahedral crystal field and the strong spin–orbit coupling at the Ir^{4+} ($5d^5$) sites combined with the layered structure give rise to a rich landscape of fascinating properties (Moon *et al.*, 2008).

In particular, $Sr_3Ir_2O_7$ is specially suitable for the HP-RXS study for several reasons. Firstly, the Ir L_3 absorption edge (11.215 keV) falls within the energy range where the diamond anvil absorption is not so strong to compromise the observation of magnetic reflections, as it is the case for other elements, *i.e.* rare-earths. Secondly, this kind of perovskite structures presents a natural tendency of the transition metal oxygen octahedra to rotate and distort under a small compression, that may affect the strength and sign of the magnetic exchange interactions. Finally, the relatively high ordering temperature

makes easier the experimental conditions for this first experiment.

The full results of this study are beyond the scope of this paper and are to be published in a separate document. Hence, in Fig. 10 (left) we show the magnetic reflection (0.5, 0.5, 34) and the Bragg peak (1, 1, 34) collected at 2.4 GPa and 150 K using the experimental setup described here. In Fig. 10 (right) we can see a comparison between the energy scan collected under the same experimental conditions at the magnetic reflection (0.5, 0.5, 34) and the fluorescence of the sample acquired in transmission geometry at 2.2 GPa and 200 K using a different system (Jin *et al.*, 2017). The measured intensity of the magnetic reflections in this system is about one-tenth of that of an average charge reflection. This same ratio applies for the loss of intensity observed when introducing the samples in the pressure cell with respect to the bare crystal. The collection time for these measurements was usually 1 s per point, obtaining a typical signal-to-noise ratio of 2:1 for the magnetic signals.

In summary, we have developed a high-pressure system for HP-RXS experiments on I16. It includes an asymmetric membrane-driven diamond anvil cell for operation in back-scattering geometry, with a solid opening angle of 100°. The system is fitted with a set of fibre optics that connects the external and internal part of the cryostat, allowing the measurement of pressure *in situ* using the luminescence of ruby. This setup has been tested for pressures up to 20 GPa and temperatures down to 30.6 K. A study on the magnetic order of $Sr_3Ir_2O_7$ was conducted and some of the experimental data obtained are shown, proving the viability of the proposed methodology. The compactness of the cell allows to potentially couple it to other cryostat models available at most large facilities. Simple modifications of the cell body and the dome could be easily done to accommodate it for use at other beamlines. Although a size reduction of the cell body is not possible without weakening the membrane capacity, exploring alternatives to reduce the dimensions of the pressure cell that would allow operation in transmission geometry and reaching lower values of minimum temperature would be convenient. We also consider that the addition of a more complex external setup for the measurement of the ruby fluorescence would improve the system's reliability and ease of use. It is not clear whether or not the increase in hydrostaticity of helium over 4:1 methanol:ethanol as the PTM is significant in the low-temperature regime. However, further insight into this question would also be of interest to the future developments.

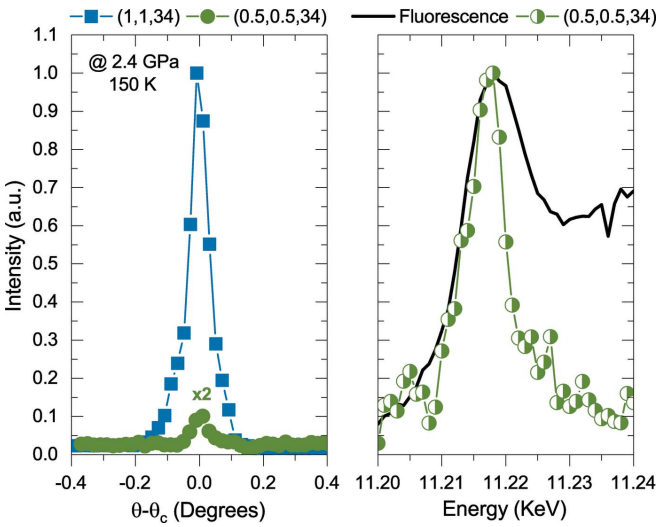

Figure 10
(*a*) Measurement of the magnetic and Bragg reflections (0.5, 0.5, 34) (green dots) and (1, 1, 34) (blue squares) of $Sr_3Ir_2O_7$ collected at 2.4 GPa and 150 K. (*b*) Energy scan on the magnetic peak (0.5, 0.5, 34) (half-filled green dots) collected under the same conditions. The solid black line shows the fluorescence collected from a different sample of the same batch at 2.2 GPa and 200 K in transmission, using an alternative setup more limited in temperature.

Acknowledgements

We would like to thank Diamond Light Source for the beam times granted under proposals MT-17731, MT-19890, MT-20778 and NT-21376; Dr Larissa S. I. Veiga and Dr James G. Vale for the collaboration in the RXS study on $Sr_3Ir_2O_7$ and Dr Robin Perry for providing the samples employed. We acknowledge the support provided by Mr David McCabe, Mr Robert Pocock and the I15 and I19 beamline staff at Diamond.

Funding information

This work was co-funded by The University of Edinburgh and Diamond Light Source under the studentship STU0076-CT-1049.

References

Agrestini, S., Mazzoli, C., Bombardi, A. & Lees, M. R. (2008). *Phys. Rev. B*, **77**, 140403.
Biffin, A., Johnson, R. D., Kimchi, I., Morris, R., Bombardi, A., Analytis, J. G., Vishwanath, A. & Coldea, R. (2014). *Phys. Rev. Lett.* **113**, 197201.
Blume, M. & Gibbs, D. (1988). *Phys. Rev. B*, **37**, 1779–1789.
Boehler, R. & De Hantsetters, K. (2004). *High. Press. Res.* **24**, 391–396.
Boseggia, S., Springell, R., Walker, H. C., Boothroyd, A. T., Prabhakaran, D., Wermeille, D., Bouchenoire, L., Collins, S. P. & McMorrow, D. F. (2012). *Phys. Rev. B*, **85**, 184432.
Calder, S., Garlea, V. O., McMorrow, D. F., Lumsden, M. D., Stone, M. B., Lang, J. C., Kim, J.-W., Schlueter, J. A., Shi, Y. G., Yamaura, K., Sun, Y. S., Tsujimoto, Y. & Christianson, A. D. (2012). *Phys. Rev. Lett.* **108**, 257209.
Collins, S. P., Bombardi, A., Marshall, A. R., Williams, J. H., Barlow, G., Day, A. G., Pearson, M. R., Woolliscroft, R. J., Walton, R. D., Beutier, G., Nisbet, G., Garrett, R., Gentle, I., Nugent, K. & Wilkins, S. (2010). *AIP Conf. Proc.* **1234**, 303–306.
Daniels, W. B. & Ryschkewitsch, M. G. (1983). *Rev. Sci. Instrum.* **54**, 115–116.
Datchi, F., Dewaele, A., Loubeyre, P., Letoullec, R., Le Godec, Y. & Canny, B. (2007). *High. Press. Res.* **27**, 447–463.
Drozdov, A. P., Kong, P. P., Minkov, V. S., Besedin, S. P., Kuzovnikov, M. A., Mozaffari, S., Balicas, L., Balakirev, F. F., Graf, D. E., Prakapenka, V. B., Greenberg, E., Knyazev, D. A., Tkacz, M. & Eremets, M. I. (2019). *Nature*, **569**, 528–531.

Fabrizi, F., Walker, H. C., Paolasini, L., de Bergevin, F., Fennell, T., Rogado, N., Cava, R. J., Wolf, T., Kenzelmann, M. & McMorrow, D. F. (2010). *Phys. Rev. B*, **82**, 024434.
Feng, Y., Jaramillo, R., Wang, J., Ren, Y. & Rosenbaum, T. F. (2010). *Rev. Sci. Instrum.* **81**, 041301.
Feng, Y., Wang, J., Palmer, A., Aguiar, J. A., Mihaila, B., Yan, J.-Q., Littlewood, P. B. & Rosenbaum, T. F. (2014). *Nat. Commun.* **5**, 4218.
Gibbs, D., Harshman, D. R., Isaacs, E. D., McWhan, D. B., Mills, D. & Vettier, C. (1988). *Phys. Rev. Lett.* **61**, 1241–1244.
Henke, B., Gullikson, E. & Davis, J. (1993). *At. Data Nucl. Data Tables*, **54**, 181–342.
Hill, J. P. & McMorrow, D. F. (1996). *Acta Cryst.* A**52**, 236–244.
Holzapfel, W. B., Hartwig, M. & Sievers, W. (2001). *J. Phys. Chem. Ref. Data*, **30**, 515–529.
Jin, H., Woodall, C. H., Wang, X., Parsons, S. & Kamenev, K. V. (2017). *Rev. Sci. Instrum.* **88**, 035103.
Kernavanois, N., Deen, P. P., Paolasini, L. & Braithwaite, D. (2005). *Rev. Sci. Instrum.* **76**, 083909.
Lee, N., Vecchini, C., Choi, Y. J., Chapon, L. C., Bombardi, A., Radaelli, P. G. & Cheong, S.-W. (2013). *Phys. Rev. Lett.* **110**, 137203.
Letoullec, R., Pinceaux, J. P. & Loubeyre, P. (1988). *High. Press. Res.* **1**, 77–90.
Loubeyre, P., LeToullec, R., Pinceaux, J. P., Mao, H. K., Hu, J. & Hemley, R. J. (1993). *Phys. Rev. Lett.* **71**, 2272–2275.
Mao, H. K. (1978). *Science*, **200**, 1145–1147.
Mao, H. K., Hemley, R. J., Wu, Y., Jephcoat, A. P., Finger, L. W., Zha, C. S. & Bassett, W. A. (1988). *Phys. Rev. Lett.* **60**, 2649–2652.
Merrill, L. & Bassett, W. A. (1974). *Rev. Sci. Instrum.* **45**, 290–294.
Moon, S. J., Jin, H., Kim, K. W., Choi, W. S., Lee, Y. S., Yu, J., Cao, G., Sumi, A., Funakubo, H., Bernhard, C. & Noh, T. W. (2008). *Phys. Rev. Lett.* **101**, 226402.
Nakamura, F. (2007). *J. Phys. Soc. Jpn*, **76**, A96–A99.
NGK-alloys (2019). *NGK*, http://www.ngk-alloys.com.
Pascut, G. L., Coldea, R., Radaelli, P. G., Bombardi, A., Beutier, G., Mazin, I. I., Johannes, M. D. & Jansen, M. (2011). *Phys. Rev. Lett.* **106**, 157206.
Piermarini, G. J., Block, S., Barnett, J. D. & Forman, R. A. (1975). *J. Appl. Phys.* **46**, 2774–2780.
Poudel, N., Gooch, M., Lorenz, B., Chu, C. W., Kim, J. W. & Cheong, S. W. (2015). *Phys. Rev. B*, **92**, 144430.
Sapelkin, A. V. & Bayliss, S. C. (2001). *High. Press. Res.* **21**, 315–329.
Sinogeikin, S. V., Smith, J. S., Rod, E., Lin, C., Kenney-Benson, C. & Shen, G. (2015). *Rev. Sci. Instrum.* **86**, 072209.
Subramanian, M., Crawford, M. & Harlow, R. (1994). *Mater. Res. Bull.* **29**, 645–650.
Torikachvili, M. S., Kim, S. K., Colombier, E., Bud'ko, S. L. & Canfield, P. C. (2015). *Rev. Sci. Instrum.* **86**, 123904.
Wang, Y., Feng, Y., Cheng, J.-G., Wu, W., Luo, J. L. & Rosenbaum, T. F. (2016). *Nat. Commun.* **7**, 13037.
Wang, Y., Rosenbaum, T. F. & Feng, Y. (2019). *IUCrJ*, **6**, 507–520.
Waterfield Price, N., Johnson, R. D., Saenrang, W., Maccherozzi, F., Dhesi, S. S., Bombardi, A., Chmiel, F. P., Eom, C.-B. & Radaelli, P. G. (2016). *Phys. Rev. Lett.* **117**, 177601.

Bibliography

[1] Povedano, I., Bombardi, A., Porter, D. G., Burt, M., Green, S. & Kamenev, K. V. High-pressure developments for resonant x-ray scattering experiments at I16. *Journal of Synchrotron Radiation* **27**, 351–359 (2020).

[2] Povedano, I., Vale, J. G., Rossi, M., Veiga, L. S. I., Boseggia, S., Faure, Q., Giles, E. C., Perry, R. S., Porter, D. G., McMorrow, D. F., Kamenev, K. V., Moretti-Sala, M. & Bombardi, A. Pressure-induced spin flop transition in the spin-orbit Mott insulator $Sr_3Ir_2O_7$ (submitted).

[3] Lee, N., Vecchini, C., Choi, Y. J., Chapon, L. C., Bombardi, A., Radaelli, P. G. & Cheong, S.-W. Giant tunability of ferroelectric polarization in $GdMn_2O_5$. *Physical Review Letters* **110**, 137203 (2013).

[4] Calder, S., Garlea, V. O., McMorrow, D. F., Lumsden, M. D., Stone, M. B., Lang, J. C., Kim, J.-W., Schlueter, J. A., Shi, Y. G., Yamaura, K., Sun, Y. S., Tsujimoto, Y. & Christianson, A. D. Magnetically driven metal-insulator transition in $NaOsO_3$. *Physical Review Letters* **108**, 257209 (2012).

[5] Pascut, G. L., Coldea, R., Radaelli, P. G., Bombardi, A., Beutier, G., Mazin, I. I., Johannes, M. D. & Jansen, M. Direct observation of charge order in triangular metallic $AgNiO_2$ by single-crystal resonant x-ray scattering. *Physical Review Letters* **106**, 157206 (2011).

[6] Agrestini, S., Mazzoli, C., Bombardi, A. & Lees, M. R. Incommensurate magnetic ground state revealed by resonant x-ray scattering in the frustrated spin system $Ca_3Co_2O_6$. *Physical Review B* **77**, 140403 (2008).

[7] Biffin, A., Johnson, R., Kimchi, I., Morris, R., Bombardi, A., Analytis, J., Vishwanath, A. & Coldea, R. Noncoplanar and counterrotating incommensurate magnetic order stabilized by kitaev interactions in $\gamma - Li_2IrO_3$. *Physical Review Letters* **113**, 197201 (2014).

[8] Donnerer, C., Rahn, M. C., Schierle, E., Perry, R. S., Veiga, L. S. I., Nisbet, G., Collins, S. P., Prabhakaran, D., Boothroyd, A. T. & McMorrow, D. F. Selective probing of magnetic order on tb and ir sites in stuffed $Tb_2Ir_2O_7$

using resonant x-ray scattering. *Journal of Physics: Condensed Matter* **31**, 344001 (2019).

[9] Fabrizi, F., Walker, H. C., Paolasini, L., de Bergevin, F., Fennell, T., Rogado, N., Cava, R. J., Wolf, T., Kenzelmann, M. & McMorrow, D. F. Electric field control of multiferroic domains in $Ni_3V_2O_8$ imaged by x-ray polarization-enhanced topography. *Physical Review B* **82**, 024434 (2010).

[10] Price, N. W., Johnson, R., Saenrang, W., Maccherozzi, F., Dhesi, S., Bombardi, A., Chmiel, F., Eom, C.-B. & Radaelli, P. Coherent magnetoelastic domains in multiferroic $BiFeO_3$ films. *Physical Review Letters* **117**, 177601 (2016).

[11] Feng, Y., Silevitch, D. M. & Rosenbaum, T. F. A compact bellows-driven diamond anvil cell for high-pressure, low-temperature magnetic measurements. *Review of Scientific Instruments* **85**, 033901 (2014).

[12] Wang, Y., Rosenbaum, T. F., Palmer, A., Ren, Y., Kim, J.-W., Mandrus, D. & Feng, Y. Strongly-coupled quantum critical point in an all-in-all-out antiferromagnet. *Nature Communications* **9**, 2953 (2018).

[13] Breznay, N. P., Ruiz, A., Frano, A., Bi, W., Birgeneau, R. J., Haskel, D. & Analytis, J. G. Resonant x-ray scattering reveals possible disappearance of magnetic order under hydrostatic pressure in the kitaev candidate $\gamma - Li_2IrO_3$. *Physical Review B* **96**, 020402 (2017).

[14] Feng, Y., Jaramillo, R., Srajer, G., Lang, J. C., Islam, Z., Somayazulu, M. S., Shpyrko, O. G., Pluth, J. J., k. Mao, H., Isaacs, E. D., Aeppli, G. & Rosenbaum, T. F. Pressure-tuned spin and charge ordering in an itinerant antiferromagnet. *Physical Review Letters* **99**, 137201 (2007).

[15] Feng, Y., Palmer, A., Wang, Y., Silevitch, D. M. & Rosenbaum, T. F. Direct probe of fermi surface evolution across a pressure-induced quantum phase transition. *Physical Review B* **91**, 155142 (2015).

[16] Feng, Y., Wang, J., Jaramillo, R., van Wezel, J., Haravifard, S., Srajer, G., Liu, Y., Xu, Z.-A., Littlewood, P. B. & Rosenbaum, T. F. Order parameter fluctuations at a buried quantum critical point. *Proceedings of the National Academy of Sciences* **109**, 7224–7229 (2012).

[17] Wang, J., Feng, Y., Jaramillo, R., van Wezel, J., Canfield, P. C. & Rosenbaum, T. F. Pressure tuning of competing magnetic interactions in intermetallic $CeFe_2$. *Physical Review B* **86**, 014422 (2012).

[18] Kernavanois, N., Deen, P. P., Paolasini, L. & Braithwaite, D. Pressure device for resonant magnetic x-ray scattering. *Review of Scientific Instruments* **76**, 083909 (2005).

[19] Braithwaite, D., Paolasini, L., Deen, P., Kernavanois, N., Yakhou, F., Canfield, P. & Lapertot, G. High-pressure resonant magnetic x-ray diffraction and transport experiments in $Ce(Fe_{1-x}Co_x)_2$. *Physica B: Condensed Matter* **378-380**, 782–783 (2006).

[20] Paolasini, L., Detlefs, C., Mazzoli, C., Wilkins, S., Deen, P. P., Bombardi, A., Kernavanois, N., de Bergevin, F., Yakhou, F., Valade, J. P., Breslavetz, I., Fondacaro, A., Pepellin, G. & Bernard, P. ID20: a beamline for magnetic and resonant x-ray scattering investigations under extreme conditions. *Journal of Synchrotron Radiation* **14**, 301–312 (2007).

[21] Collins, S. P., Bombardi, A., Marshall, A. R., Williams, J. H., Barlow, G., Day, A. G., Pearson, M. R., Woolliscroft, R. J., Walton, R. D., Beutier, G., Nisbet, G., Garrett, R., Gentle, I., Nugent, K. & Wilkins, S. Diamond beamline I16 (materials & magnetism). 303 (AIP, 2010).

[22] Witczak-Krempa, W., Chen, G., Kim, Y. B. & Balents, L. Correlated quantum phenomena in the strong spin-orbit regime. *Annual Review of Condensed Matter Physics* **5**, 57–82 (2014).

[23] Ngai, J., Walker, F. & Ahn, C. Correlated oxide physics and electronics. *Annual Review of Materials Research* **44**, 1–17 (2014).

[24] Keimer, B., Kivelson, S. A., Norman, M. R., Uchida, S. & Zaanen, J. From quantum matter to high-temperature superconductivity in copper oxides. *Nature* **518**, 179–186 (2015).

[25] Moritomo, Y., Asamitsu, A., Kuwahara, H. & Tokura, Y. Giant magnetoresistance of manganese oxides with a layered perovskite structure. *Nature* **380**, 141–144 (1996).

[26] Spaldin, N. A. & Ramesh, R. Advances in magnetoelectric multiferroics. *Nature Materials* **18**, 203–212 (2019).

[27] Frano, A., Blanco-Canosa, S., Schierle, E., Lu, Y., Wu, M., Bluschke, M., Minola, M., Christiani, G., Habermeier, H. U., Logvenov, G., Wang, Y., van Aken, P. A., Benckiser, E., Weschke, E., Tacon, M. L. & Keimer, B. Long-range charge-density-wave proximity effect at cuprate/manganate interfaces. *Nature Materials* **15**, 831–834 (2016).

[28] Wen, J.-J., Huang, H., Lee, S.-J., Jang, H., Knight, J., Lee, Y. S., Fujita, M., Suzuki, K. M., Asano, S., Kivelson, S. A., Kao, C.-C. & Lee, J.-S. Observation of two types of charge-density-wave orders in superconducting $La_{2-x}Sr_xCuO_4$. *Nature Communications* **10**, 3269 (2019).

[29] Pincini, D. *On the hierarchy of electronic and magnetic energy scales in novel 3d , 4d and 5d transition metal oxides probed by x-ray techniques.* Ph.D. thesis, University College London (2018).

[30] Hubbard, J. Electron correlations in narrow energy bands. *Proceedings of the Royal Society of London. Series A. Mathematical and Physical Sciences* **276**, 238–257 (1963).

[31] Hubbard, J. Electron correlations in narrow energy bands iii. an improved solution. *Proceedings of the Royal Society of London. Series A. Mathematical and Physical Sciences* **281**, 401–419 (1964).

[32] Cao, G., Xin, Y., Alexander, C. S., Crow, J. E., Schlottmann, P., Crawford, M. K., Harlow, R. L. & Marshall, W. Anomalous magnetic and transport behavior in the magnetic insulator $Sr_3Ir_2O_7$. *Physical Review B* **66**, 214412 (2002).

[33] Wang, Q., Cao, Y., Waugh, J. A., Park, S. R., Qi, T. F., Korneta, O. B., Cao, G. & Dessau, D. S. Dimensionality-controlled mott transition and correlation effects in single-layer and bilayer perovskite iridates. *Physical Review B* **87**, 245109 (2013).

[34] Kim, B. J., Jin, H., Moon, S. J., Kim, J.-Y., Park, B.-G., Leem, C. S., Yu, J., Noh, T. W., Kim, C., Oh, S.-J., Park, J.-H., Durairaj, V., Cao, G. & Rotenberg, E. Novel J_{eff} =1/2 Mott state induced by relativistic spin-orbit coupling in Sr_2IrO_4. *Physical Review Letters* **101**, 076402 (2008).

[35] Crawford, M. K., Subramanian, M. A., Harlow, R. L., Fernandez-Baca, J. A., Wang, Z. R. & Johnston, D. C. Structural and magnetic studies of Sr_2IrO_4. *Physical Review B* **49**, 9198–9201 (1994).

[36] Cao, G., Bolivar, J., McCall, S., Crow, J. E. & Guertin, R. P. Weak ferromagnetism, metal-to-nonmetal transition, and negative differential resistivity in single-crystal Sr_2IrO_4. *Physical Review B* **57**, R11039–R11042 (1998).

[37] Cao, G., Crow, J., Guertin, R., Henning, P., Homes, C., Strongin, M., Basov, D. & Lochner, E. Charge density wave formation accompanying ferromagnetic ordering in quasi-one-dimensional $BaIrO_3$. *Solid State Communications* **113**, 657–662 (2000).

[38] Shanavas, K. V., Popović, Z. S. & Satpathy, S. Theoretical model for Rashba spin-orbit interaction in d electrons. *Physical Review B* **90**, 165108 (2014).

[39] Francisco, E. & Pueyo, L. Theoretical spin-orbit coupling constants for 3d ions in crystals. *Physical Review B* **37**, 5278–5288 (1988).

[40] Mattheiss, L. F. Electronic structure of RuO_2, OsO_2 and IrO_2. *Physical Review B* **13**, 2433–2450 (1976).

[41] Kane, C. L. & Mele, E. J. Z_2 topological order and the quantum spin hall effect. *Physical Review Letters* **95**, 146802 (2005).

[42] Hsieh, D., Qian, D., Wray, L., Xia, Y., Hor, Y. S., Cava, R. J. & Hasan, M. Z. A topological dirac insulator in a quantum spin hall phase. *Nature* **452**, 970–974 (2008).

[43] Kargarian, M. & Fiete, G. A. Topological crystalline insulators in transition metal oxides. *Physical Review Letters* **110**, 156403 (2013).

[44] Wan, X., Turner, A. M., Vishwanath, A. & Savrasov, S. Y. Topological semimetal and fermi-arc surface states in the electronic structure of pyrochlore iridates. *Physical Review B* **83**, 205101 (2011).

[45] Xu, S.-Y., Belopolski, I., Alidoust, N., Neupane, M., Bian, G., Zhang, C., Sankar, R., Chang, G., Yuan, Z., Lee, C.-C., Huang, S.-M., Zheng, H., Ma, J., Sanchez, D. S., Wang, B., Bansil, A., Chou, F., Shibayev, P. P., Lin, H., Jia, S. & Hasan, M. Z. Discovery of a Weyl fermion semimetal and topological fermi arcs. *Science* **349**, 613–617 (2015).

[46] Quan, Y. M., Zou, L. J., Liu, D. Y. & Lin, H. Q. Competition between crystal field splitting and Hund's rule coupling in two-orbital magnetic metal-insulator transitions. *The European Physical Journal B* **85**, 55 (2012).

[47] Kim, B. J., Ohsumi, H., Komesu, T., Sakai, S., Morita, T., Takagi, H. & Arima, T. Phase-sensitive observation of a spin-orbital Mott state in Sr_2IrO_4. *Science* **323**, 1329–1332 (2009).

[48] Moon, S. J., Jin, H., Kim, K. W., Choi, W. S., Lee, Y. S., Yu, J., Cao, G., Sumi, A., Funakubo, H., Bernhard, C. & Noh, T. W. Dimensionality Controlled Insulator-Metal Transition and Correlated Metallic State in 5d Transition Metal Oxides ($n = 1, 2$, and ∞). *Physical Review Letters* **101**, 226402 (2008).

[49] Cao, G. & Schlottmann, P. The challenge of spin–orbit-tuned ground states in iridates: a key issues review. *Reports on Progress in Physics* **81**, 042502 (2018).

[50] Ye, F., Chi, S., Cao, H., Chakoumakos, B. C., Fernandez-Baca, J. A., Custelcean, R., Qi, T. F., Korneta, O. B. & Cao, G. Direct evidence of a zigzag spin-chain structure in the honeycomb lattice: A neutron and x-ray diffraction investigation of single-crystal Na_2IrO_3. *Physical Review B* **85**, 180403 (2012).

[51] Liu, X., Berlijn, T., Yin, W.-G., Ku, W., Tsvelik, A., Kim, Y.-J., Gretarsson, H., Singh, Y., Gegenwart, P. & Hill, J. P. Long-range magnetic ordering in Na_2IrO_3. *Physical Review B* **83**, 220403(R) (2011).

[52] Clancy, J. P., Gretarsson, H., Sears, J. A., Singh, Y., Desgreniers, S., Mehlawat, K., Layek, S., Rozenberg, G. K., Ding, Y., Upton, M. H., Casa, D., Chen, N., Im, J., Lee, Y., Yadav, R., Hozoi, L., Efremov, D., van den

Brink, J. & Kim, Y.-J. Pressure-driven collapse of the relativistic electronic ground state in a honeycomb iridate. *npj Quantum Materials* **3**, 35 (2018).

[53] Takayama, T., Krajewska, A., Gibbs, A. S., Yaresko, A. N., Ishii, H., Yamaoka, H., Ishii, K., Hiraoka, N., Funnell, N. P., Bull, C. L. & Takagi, H. Pressure-induced collapse of the spin-orbital mott state in the hyperhoneycomb iridate $\beta - Li_2IrO_3$. *Physical Review B* **99**, 125127 (2019).

[54] Veiga, L. S. I., Etter, M., Glazyrin, K., Sun, F., Escanhoela, C. A., Fabbris, G., Mardegan, J. R. L., Malavi, P. S., Deng, Y., Stavropoulos, P. P., Kee, H.-Y., Yang, W. G., van Veenendaal, M., Schilling, J. S., Takayama, T., Takagi, H. & Haskel, D. Pressure tuning of bond-directional exchange interactions and magnetic frustration in the hyperhoneycomb iridate $\beta - Li_2IrO_3$. *Physical Review B* **96**, 140402 (2017).

[55] Veiga, L. S. I., Glazyrin, K., Fabbris, G., Dashwood, C. D., Vale, J. G., Park, H., Etter, M., Irifune, T., Pascarelli, S., McMorrow, D. F., Takayama, T., Takagi, H. & Haskel, D. Pressure-induced structural dimerization in the hyperhoneycomb iridate $\beta - Li_2IrO_3$ at low temperatures. *Physical Review B* **100**, 064104 (2019).

[56] Majumder, M., Manna, R., Simutis, G., Orain, J., Dey, T., Freund, F., Jesche, A., Khasanov, R., Biswas, P., Bykova, E., Dubrovinskaia, N., Dubrovinsky, L., Yadav, R., Hozoi, L., Nishimoto, S., Tsirlin, A. & Gegenwart, P. Breakdown of magnetic order in the pressurized kitaev iridate $\beta - Li_2IrO_3$. *Physical Review Letters* **120**, 237202 (2018).

[57] Takayama, T., Kato, A., Dinnebier, R., Nuss, J., Kono, H., Veiga, L., Fabbris, G., Haskel, D. & Takagi, H. Hyperhoneycomb iridate $\beta - Li_2IrO_3$ as a platform for kitaev magnetism. *Physical Review Letters* **114**, 077202 (2015).

[58] Hu, K., Zhou, Z., Wei, Y.-W., Li, C.-K. & Feng, J. Bond ordering and phase transitions in Na_2IrO_3 under high pressure. *Physical Review B* **98**, 100103(R) (2018).

[59] Hermann, V., Ebad-Allah, J., Freund, F., Jesche, A., Tsirlin, A. A., Gegenwart, P. & Kuntscher, C. A. Optical signature of the pressure-induced dimerization in the honeycomb iridate $\gamma - Li_2IrO_3$. *Physical Review B* **99**, 235116 (2019).

[60] Biesner, T., Biswas, S., Li, W., Saito, Y., Pustogow, A., Altmeyer, M., Wolter, A. U. B., Bchner, B., Roslova, M., Doert, T., Winter, S. M., Valentí, R. & Dressel, M. Detuning the honeycomb of $\alpha - RuCl_3$: Pressure-dependent optical studies reveal broken symmetry. *Physical Review B* **97**, 220401(R) (2018).

[61] Hermann, V., Altmeyer, M., Ebad-Allah, J., Freund, F., Jesche, A., Tsirlin, A. A., Hanfland, M., Gegenwart, P., Mazin, I. I., Khomskii, D. I., Valentí, R. & Kuntscher, C. A. Competition between spin-orbit coupling, magnetism, and dimerization in the honeycomb iridates: $\alpha - Li_2IrO_3$ under pressure. *Physical Review B* **97**, 020104(R) (2018).

[62] Sun, F., Zheng, H., Liu, Y., Sandoval, E. D., Xu, C., Xu, J., Jin, C. Q., Sun, C. J., Yang, W. G., Mao, H. K., Mitchell, J. F., Kolmogorov, A. N. & Haskel, D. Electronic and structural response to pressure in the hyperkagome-lattice $Na_3Ir_3O_8$. *Physical Review B* **98**, 085131 (2018).

[63] Simutis, G., Barbero, N., Rolfs, K., Leroy-Calatayud, P., Mehlawat, K., Khasanov, R., Luetkens, H., Pomjakushina, E., Singh, Y., Ott, H.-R., Mesot, J., Amato, A. & Shiroka, T. Chemical and hydrostatic-pressure effects on the kitaev honeycomb material Na_2IrO_4. *Physical Review B* **98**, 104421 (2018).

[64] Banerjee, A., Bridges, C. A., Yan, J.-Q., Aczel, A. A., Li, L., Stone, M. B., Granroth, G. E., Lumsden, M. D., Yiu, Y., Knolle, J., Bhattacharjee, S., Kovrizhin, D. L., Moessner, R., Tennant, D. A., Mandrus, D. G. & Nagler, S. E. Proximate kitaev quantum spin liquid behaviour in a honeycomb magnet. *Nature Materials* **15**, 733–740 (2016).

[65] Wang, Z., Guo, J., Tafti, F. F., Hegg, A., Sen, S., Sidorov, V. A., Wang, L., Cai, S., Yi, W., Zhou, Y., Wang, H., Zhang, S., Yang, K., Li, A., Li, X., Li, Y., Liu, J., Shi, Y., Ku, W., Wu, Q., Cava, R. J. & Sun, L. Pressure-induced melting of magnetic order and emergence of a new quantum state in $\alpha - RuCl_3$. *Physical Review B* **97**, 245149 (2018).

[66] Savary, L., Moon, E.-G. & Balents, L. New type of quantum criticality in the pyrochlore iridates. *Physical Review X* **4**, 041027 (2014).

[67] Kondo, T., Nakayama, M., Chen, R., Ishikawa, J. J., Moon, E.-G., Yamamoto, T., Ota, Y., Malaeb, W., Kanai, H., Nakashima, Y., Ishida, Y., Yoshida, R., Yamamoto, H., Matsunami, M., Kimura, S., Inami, N., Ono, K., Kumigashira, H., Nakatsuji, S., Balents, L. & Shin, S. Quadratic Fermi node in a 3D strongly correlated semimetal. *Nature Communications* **6**, 10042 (2015).

[68] Hirata, Y., Nakajima, M., Nomura, Y., Tajima, H., Matsushita, Y., Asoh, K., Kiuchi, Y., Eguiluz, A. G., Arita, R., Suemoto, T. & Ohgushi, K. Mechanism of enhanced optical second-harmonic generation in the conducting pyrochlore-type $Pb_2Ir_2O_{7-x}$ oxide compound. *Physical Review Letters* **110**, 187402 (2013).

[69] Bouchard, R. & Gillson, J. A new family of bismuth — precious metal pyrochlores. *Materials Research Bulletin* **6**, 669–679 (1971).

[70] Liu, W., Han, H., Ling, L., Ma, L., Pi, L., Zhang, L. & Zhang, Y. Localization induced by pressure in pyrochlore $Bi_2Ir_2O_7$. *Ceramics International* **43**, 17100–17103 (2017).

[71] Tafti, F. F., Ishikawa, J. J., McCollam, A., Nakatsuji, S. & Julian, S. R. Pressure-tuned insulator to metal transition in $Eu_2Ir_2O_7$. *Physical Review B* **85**, 205104 (2012).

[72] Ueda, K., Kaneko, R., Ishizuka, H., Fujioka, J., Nagaosa, N. & Tokura, Y. Spontaneous hall effect in the weyl semimetal candidate of all-in all-out pyrochlore iridate. *Nature Communications* **9**, 3032 (2018).

[73] Als-Nielsen, J. & McMorrow, D. *Elements of Modern X-ray Physics* (John Wiley & Sons, Inc., 2011).

[74] Willmott, P. *An Introduction to Synchrotron Radiation* (Wiley John + Sons, 2019). URL https://www.ebook.de/de/product/35687937/philip_willmott_an_introduction_to_synchrotron_radiation.html.

[75] Christou, C., Kempson, V., Dunkel, K. & Piel, C. The pre-injector linac for the diamond light source. *Proceedings of LINAC, Lbeck, Germany* 84–86 (2004).

[76] Bergevin, F. D. & Brunel, M. Diffraction of x-rays by magnetic materials. i. general formulae and measurements on ferro- and ferrimagnetic compounds. *Acta Crystallographica Section A* **37**, 314–324 (1981).

[77] Blume, M. Magnetic scattering of x rays (invited). *Journal of Applied Physics* **57**, 3615–3618 (1985).

[78] Blume, M. & Gibbs, D. Polarization dependence of magnetic x-ray scattering. *Physical Review B* **37**, 1779–1789 (1988).

[79] Hannon, J. P., Trammell, G. T., Blume, M. & Gibbs, D. X-ray resonance exchange scattering. *Physical Review Letters* **61**, 1245–1248 (1988).

[80] Hill, J. P. & McMorrow, D. F. X-ray resonant exchange scattering: Polariztaion dependence and correlation function. *Acta Crystallographica Section A Foundations of Crystallography* **52**, 236–244 (1996).

[81] Altarelli, M. Resonant x-ray scattering: A theoretical introduction. In *Magnetism: A Synchrotron Radiation Approach*, 201–242 (Springer Berlin Heidelberg, 2006).

[82] Iwanenko, D. & Pomeranchuk, I. On the maximal energy attainable in a betatron. *Physical Review* **65**, 343–343 (1944).

[83] Elder, F. R., Gurewitsch, A. M., Langmuir, R. V. & Pollock, H. C. Radiation from electrons in a synchrotron. *Physical Review* **71**, 829–830 (1947).

[84] Gould, R. J. High-energy photons from the compton-synchrotron process in the crab nebula. *Phys. Rev. Lett.* **15**, 577–579 (1965). URL https://link.aps.org/doi/10.1103/PhysRevLett.15.577.

[85] Haas, M., Chini, R., Meisenheimer, K., Stickel, M., Lemke, D., Klaas, U. & Kreysa, E. On the far-infrared emission of quasars. *The Astrophysical Journal* **503**, L109–L113 (1998).

[86] Mobilio, B. F. M. C., Settimio (ed.) *Synchrotron Radiation* (Springer-Verlag GmbH, 2014). URL https://www.ebook.de/de/product/23042819/synchrotron_radiation.html.

[87] Joly, Y., Matteo, S. D. & Bunău, O. Resonant x-ray diffraction: Basic theoretical principles. *The European Physical Journal Special Topics* **208**, 21–38 (2012).

[88] Paolasini, L. Resonant and magnetic x-ray diffraction. In *Synchrotron Radiation*, 361–387 (Springer Berlin Heidelberg, 2014).

[89] Lovesey, S., Balcar, E., Knight, K. & Fernandez-Rodriguez, J. Electronic properties of crystalline materials observed in x-ray diffraction. *Physics Reports* **411**, 233–289 (2005).

[90] Matteo, S. D., Joly, Y. & Natoli, C. R. Detection of electromagnetic multipoles by x-ray spectroscopies. *Physical Review B* **72**, 144406 (2005).

[91] Matteo, S. D. Dipole-quadrupole spherical tensors in resonant x-ray diffraction. *Journal of Physics: Conference Series* **211**, 012008 (2010).

[92] Dmitrienko, V. E. & Ovchinnikova, E. N. Resonant x-ray diffraction: 'forbidden' Bragg reflections induced by thermal vibrations and point defects. *Acta Crystallographica Section A Foundations of Crystallography* **56**, 340–347 (2000).

[93] Dmitrienko, V. E. & Ovchinnikova, E. N. Resonant x-ray diffraction: Forbidden bragg reflections induced by atomic displacements. *Structural Chemistry* **13**, 397–404 (2002).

[94] Dmitrienko, V. E., Ovchinnikova, E. N. & Ishida, K. X-ray spectroscopy of thermally distorted electronic states in crystals. *Journal of Experimental and Theoretical Physics Letters* **69**, 938–942 (1999).

[95] Collins, S. P., Laundy, D., Dmitrienko, V. E., Mannix, D. & Thompson, P. Evidence for two mechanisms of temperature-dependent forbidden resonant diffraction in ZnO. *Physica Scripta* **T115**, 10651067 (2005).

[96] Finkelstein, K. D., Shen, Q. & Shastri, S. Resonant x-ray diffraction near the iron K-edge in hematite α-Fe_2O_3. *Physical Review Letters* **69**, 1612–1615 (1992).

[97] Templeton, D. H. & Templeton, L. K. Tetrahedral anisotropy of x-ray anomalous scattering. *Physical Review B* **49**, 14850–14853 (1994).

[98] Dmitrienko, V. E. & Ovchinnikova, E. N. Chirality-induced `forbidden' reflections in x-ray resonant scattering. *Acta Crystallographica Section A Foundations of Crystallography* **57**, 642–648 (2001).

[99] Hahn, T. *International tables for crystallography - Volume A: Space-group symmetry, vol. A of International Tables for Crystallography (Book 1))* (Published for the International Union of Crystallography by Springer, Dordrecht, Netherlands, 2005).

[100] Dudzik, E., Dhesi, S. S., Collins, S. P., Drr, H. A., van der Laan, G., Chesnel, K., Belakhovsky, M., Marty, A., Samson, Y. & Goedkoop, J. B. X-ray resonant magnetic scattering from FePd thin films. *Journal of Applied Physics* **87**, 5469–5471 (2000).

[101] Ukleev, V., Yamasaki, Y., Morikawa, D., Kanazawa, N., Okamura, Y., Nakao, H., Tokura, Y. & hisa Arima, T. Coherent resonant soft x-ray scattering study of magnetic textures in FeGe. *Quantum Beam Science* **2**, 3 (2018).

[102] Zhu, Z., Strempfer, J., Rao, R., Occhialini, C., Pelliciari, J., Choi, Y., Kawaguchi, T., You, H., Mitchell, J., Shao-Horn, Y. & Comin, R. Anomalous antiferromagnetism in metallic RuO_2 determined by resonant x-ray scattering. *Physical Review Letters* **122**, 017202 (2019).

[103] Gibbs, D., Moncton, D. E., D'Amico, K. L., Bohr, J. & Grier, B. H. Magnetic x-ray scattering studies of holmium using synchrotron radiation. *Physical Review Letters* **55**, 234–237 (1985).

[104] Bridgman, P. W. *Collected experimental papers* (Harvard University Press, 1964).

[105] Bridgman, P. W. Biographical. NobelPrize.org (1946). URL https://www.nobelprize.org/prizes/physics/1946/bridgman/biographical/. Last visited: 12.04.2019.

[106] Rieke, H. H. & Chilingarian, G. V. Chapter 8 equipment and techniques used in compaction studies. In *Compaction of Argillaceous Sediments*, vol. 16 of *Developments in Sedimentology*, 353 – 398 (Elsevier, 1974). URL http://www.sciencedirect.com/science/article/pii/S0070457108707787.

[107] Tennant, S. On the nature of the diamond. *Philosophical Transactions of the Royal Society of London* **87**, 123–127 (1797).

[108] Bundy, F. P., Hall, H. T., Strong, H. M. & Wentorf, R. H. Man-made diamonds. *Nature* **176**, 51–55 (1955).

[109] Bovenkerk, H. P., Bundy, F. P., Chrenko, R. M., Codella, P. J., Strong, H. M. & Wentorf, R. H. Errors in diamond synthesis. *Nature* **365**, 19–19 (1993).

[110] Weir, C. E., Lippincott, E. R., Van Valkenburg, A. & Bunting, E. N. Infrared studies in the 1- to 15-micron region to 30,000 atmospheres. *J. Res. Natl. Bur. Stand.* **63A**, 55 (1959).

[111] Jamieson, J. C., Lawson, A. W. & Nachtrieb, N. D. New device for obtaining x-ray diffraction patterns from substances exposed to high pressure. *Review of Scientific Instruments* **30**, 1016–1019 (1959).

[112] Piermarini, G. High pressure x-ray crystallography with the diamond cell at NIST/NBS. *Journal of Research of the National Institute of Standards and Technology* **106**, 889 (2001).

[113] Bassett, W. A., Takahashi, T. & Stook, P. W. X-ray diffraction and optical observations on crystalline solids up to 300 kbar. *Review of Scientific Instruments* **38**, 37–42 (1967).

[114] Piermarini, G. J. & Block, S. Ultra high pressure diamond-anvil cell and several semiconductor phase transition pressures in relation to the fixed point pressure scale. *Review of Scientific Instruments* **46**, 973–979 (1975).

[115] Valkenburg, A. V. Diamond high-pressure windows. *Diamond Research* 17–19 (1964).

[116] Valkenburg, A. V. Visual observations of single crystal transitions under true hydrostatic pressures up to 40 kilobar. *Conference Internationale sur-les-Hautes Pressions. Le Creusot, Saone-et-Loire, France* (1965).

[117] Piermarini, G. J. & Braun, A. B. Crystal and molecular structure of CCl_4 III: A high pressure polymorph at 10 kbar. *The Journal of Chemical Physics* **58**, 1974–1982 (1973).

[118] Besson, J. M. & Pinceaux, J. P. Melting of helium at room temperature and high pressure. *Science* **206**, 1073–1075 (1979).

[119] Takemura, K. Pressure scales and hydrostaticity. *High Pressure Research* **27**, 465–472 (2007).

[120] Mao, H. K. High-pressure physics: Sustained static generation of 1.36 to 1.72 megabars. *Science* **200**, 1145–1147 (1978).

[121] Mao, H. K. & Bell, P. M. *Carnegie Inst. Washington* **74**, 402 (1975).

[122] Ruoff, A. L., Xia, H., Luo, H. & Vohra, Y. K. Miniaturization techniques for obtaining static pressures comparable to the pressure at the center of the earth: X-ray diffraction at 416 GPa. *Review of Scientific Instruments* **61**, 3830–3833 (1990).

[123] Dubrovinskaia, N., Dubrovinsky, L., Solopova, N. A., Abakumov, A., Turner, S., Hanfland, M., Bykova, E., Bykov, M., Prescher, C., Prakapenka, V. B., Petitgirard, S., Chuvashova, I., Gasharova, B., Mathis, Y.-L., Ershov, P., Snigireva, I. & Snigirev, A. Terapascal static pressure generation with ultrahigh yield strength nanodiamond. *Science Advances* **2**, e1600341 (2016).

[124] Sakai, T., Yagi, T., Irifune, T., Kadobayashi, H., Hirao, N., Kunimoto, T., Ohfuji, H., Kawaguchi-Imada, S., Ohishi, Y., Tateno, S. & Hirose, K. High pressure generation using double-stage diamond anvil technique: problems and equations of state of rhenium. *High Pressure Research* **38**, 107–119 (2018).

[125] Dewaele, A., Loubeyre, P., Occelli, F., Marie, O. & Mezouar, M. Toroidal diamond anvil cell for detailed measurements under extreme static pressures. *Nature Communications* **9**, 2913 (2018).

[126] Jenei, Z., O'Bannon, E. F., Weir, S. T., Cynn, H., Lipp, M. J. & Evans, W. J. Single crystal toroidal diamond anvils for high pressure experiments beyond 5 megabar. *Nature Communications* **9**, 3563 (2018).

[127] O'Bannon, E. F., Jenei, Z., Cynn, H., Lipp, M. J. & Jeffries, J. R. Contributed review: Culet diameter and the achievable pressure of a diamond anvil cell: Implications for the upper pressure limit of a diamond anvil cell. *Review of Scientific Instruments* **89**, 111501 (2018).

[128] Lawson, A. W. & Riley, N. A. An x-ray camera for obtaining powder pictures at high pressures. *Review of Scientific Instruments* **20**, 763–765 (1949).

[129] Lawson, A. W. & Tang, T.-Y. A diamond bomb for obtaining powder pictures at high pressures. *Review of Scientific Instruments* **21**, 815–815 (1950).

[130] Piermarini, G. J. & Weir, C. E. A diamond cell for x-ray diffraction studies at high pressures. *JOURNAL OF RESEARCH of the National Bureau of StandardsA. Physics and Chemistry* **66A**, 325–331 (1962).

[131] Merrill, L. & Bassett, W. A. Miniature diamond anvil pressure cell for single crystal x-ray diffraction studies. *Review of Scientific Instruments* **45**, 290–294 (1974).

[132] Block, S., Weir, C. W. & Piermarini, G. J. High-pressure single-crystal studies of ice VI. *Science* **148**, 947–948 (1965).

[133] Weir, C. E., Piermarini, G. J. & Block, S. Instrumentation for single crystal x-ray diffraction at high pressures. *Review of Scientific Instruments* **40**, 1133–1136 (1969).

[134] Keller, R. & Holzapfel, W. B. Diamond anvil device for x-ray diffraction on single crystals under pressures up to 100 kilobar. *Review of Scientific Instruments* **48**, 517–523 (1977).

[135] Schiferl, D. 50-kilobar gasketed diamond anvil cell for single-crystal x-ray diffractometer use with the crystal structure of sb up to 26 kilobars as a test problem. *Review of Scientific Instruments* **48**, 24–30 (1977).

[136] Schiferl, D., Jamieson, J. C. & Lenko, J. E. 90-kilobar diamond-anvil high-pressure cell for use on an automatic diffractometer. *Review of Scientific Instruments* **49**, 359–364 (1978).

[137] Koepke, J., Dieterich, W., Glinnemann, J. & Schulz, H. Improved diamond anvil high-pressure cell for single-crystal work. *Review of Scientific Instruments* **56**, 2119–2122 (1985).

[138] Ahsbahs, H. Diamond-anvil high-pressure cell for improved single-crystal x-ray diffraction measurements. *Review of Scientific Instruments* **55**, 99–102 (1984).

[139] Hawke, R. S., Syassen, K. & Holzapfel, W. B. An apparatus for high pressure raman spectroscopy. *Review of Scientific Instruments* **45**, 1598–1601 (1974).

[140] Syassen, K. & Holzapfel, W. B. High-pressure–low-temperature x-ray power diffractometer. *Review of Scientific Instruments* **49**, 1107–1111 (1978).

[141] Gubser, D. U. & Webb, A. W. High-pressure effects on the superconducting transition temperature of aluminum. *Physical Review Letters* **35**, 104–107 (1975).

[142] Endo, S., Mishima, O., Ohno, Y. & Kawamura, T. Diamond-anvil cell equipped with a worm gear intensifier for pressure generation at low temperature. *Japanese Journal of Applied Physics* **21**, L702–L704 (1982).

[143] Shaw, R. W. & Nicol, M. Simple low-temperature press for diamond-anvil high pressure cells. *Review of Scientific Instruments* **52**, 1103–1104 (1981).

[144] Daniels, W. B. & Ryschkewitsch, M. G. Simple double diaphragm press for diamond anvil cells at low temperatures. *Review of Scientific Instruments* **54**, 115–116 (1983).

[145] Kobayashi, T. Diamond-anvil high-pressure cell for optical spectroscopy at low temperature. *Review of Scientific Instruments* **56**, 255–259 (1985).

[146] Silvera, I. F. & Wijngaarden, R. J. Diamond anvil cell and cryostat for low-temperature optical studies. *Review of Scientific Instruments* **56**, 121–124 (1985).

[147] Mao, H.-K. & Hemley, R. J. Energy dispersive x-ray diffraction of micro-crystals at ultra high pressures. *High Pressure Research* **14**, 257–267 (1996).

[148] Mao, H. K. Phonon density of states of iron up to 153 gigapascals. *Science* **292**, 914–916 (2001).

[149] Toullec, R. L., Loubeyre, P., Pinceaux, J. P., Mao, H. K. & Hu, J. A system for doing low temperature-high pressure single crystal x-ray diffraction with a synchrotron source. *High Pressure Research* **6**, 379–388 (1991).

[150] Toullec, R. L., Loubeyre, P., Pinceaux, J. P., Mao, H. K. & Hu, J. Single crystal x-ray diffraction with a synchrotron source in a mDAC at low temperature. *High Pressure Research* **8**, 691–696 (1992).

[151] Torchio, R., Marini, C., Kvashnin, Y. O., Kantor, I., Mathon, O., Garbarino, G., Meneghini, C., Anzellini, S., Occelli, F., Bruno, P., Dewaele, A. & Pascarelli, S. Structure and magnetism of cobalt at high pressure and low temperature. *Physical Review B* **94**, 024429 (2016).

[152] Yamawaki, H., Fujihisa, H., Sakashita, M., Nakayama, A. & Aoki, K. Powder x-ray diffraction study of the volume change of ice VIII under high pressure. *Physica B: Condensed Matter* **344**, 260–264 (2004).

[153] Loubeyre, P., LeToullec, R., Pinceaux, J. P., Mao, H. K., Hu, J. & Hemley, R. J. Equation of state and phase diagram of solid ^{4}He from single-crystal x-ray diffraction over a large P-T domain. *Physical Review Letters* **71**, 2272–2275 (1993).

[154] Mao, H. K., Shu, J., Shen, G., Hemley, R. J., Li, B. & Singh, A. K. Elasticity and rheology of iron above 220 GPa and the nature of the earth's inner core. *Nature* **396**, 741–743 (1998).

[155] Zhao, J. Y., Bi, W., Sinogeikin, S., Hu, M. Y., Alp, E. E., Wang, X. C., Jin, C. Q. & Lin, J. F. A compact membrane-driven diamond anvil cell and cryostat system for nuclear resonant scattering at high pressure and low temperature. *Review of Scientific Instruments* **88**, 125109 (2017).

[156] Mao-type diamond anvil cells for x-ray experiments. URL https://duffy.princeton.edu/laboratory/diamond-anvil-cells. Last visited: 16.05.2019.

[157] Jin, H., Woodall, C. H., Wang, X., Parsons, S. & Kamenev, K. V. A novel diamond anvil cell for x-ray diffraction at cryogenic temperatures manufactured by 3D printing. *Review of Scientific Instruments* **88**, 035103 (2017).

[158] Kano, M., Kurita, N., Hedo, M., Uwatoko, Y., Tozer, S. W., Suzuki, H. S., Onimaru, T. & Sakakibara, T. Electrical resistivity measurements on $PrPb_3$ under high pressures. *Journal of the Physical Society of Japan* **76**, 56–57 (2007).

[159] Giriat, G., Wang, W., Attfield, J. P., Huxley, A. D. & Kamenev, K. V. Turnbuckle diamond anvil cell for high-pressure measurements in a superconducting quantum interference device magnetometer. *Review of Scientific Instruments* **81**, 073905 (2010).

[160] Cosier, J. & Glazer, A. M. A nitrogen-gas-stream cryostat for general x-ray diffraction studies. *Journal of Applied Crystallography* **19**, 105–107 (1986).

[161] Brochier, D. Cryostat temprature variable pour mesures neutroniques ou optiques. *Tech. Report* **77** (1977).

[162] Almax-easylabs. URL https://www.almax-easylab.com/DiamondSelectionPage.aspx. Last visited: 23.05.2019.

[163] Boehler, R. & Hantsetters, K. D. New anvil designs in diamond-cells. *High Pressure Research* **24**, 391–396 (2004).

[164] Dunstan, D. J. & Spain, I. L. Technology of diamond anvil high-pressure cells: I. principles, design and construction. *Journal of Physics E: Scientific Instruments* **22**, 913–923 (1989).

[165] Henke, B., Gullikson, E. & Davis, J. X-ray interactions: Photoabsorption, scattering, transmission, and reflection at e = 50-30,000 eV, z = 1-92. *Atomic Data and Nuclear Data Tables* **54**, 181–342 (1993).

[166] Henke website for calculation of x-ray transmission. URL http://henke.lbl.gov/optical_constants/filter2.html. Last visited: 24.05.2019.

[167] Dadashev, A., Pasternak, M. P., Rozenberg, G. K. & Taylor, R. D. Applications of perforated diamond anvils for very high-pressure research. *Review of Scientific Instruments* **72**, 2633–2637 (2001).

[168] Irifune, T., Kurio, A., Sakamoto, S., Inoue, T. & Sumiya, H. Ultrahard polycrystalline diamond from graphite. *Nature* **421**, 599–600 (2003).

[169] Ishimatsu, N., Matsumoto, K., Maruyama, H., Kawamura, N., Mizumaki, M., Sumiya, H. & Irifune, T. Glitch-free x-ray absorption spectrum under high pressure obtained using nano-polycrystalline diamond anvils. *Journal of Synchrotron Radiation* **19**, 768–772 (2012).

[170] Nazare, M. H. *Properties, Growth and Applications of Diamond (Emis Datareviews Series, 26)* (The Institution of Engineering and Technology, 2000).

[171] Eremets, M. I. *High Pressure Experimental Methods* (OUP Oxford, 1996).

[172] Araldite rapid glue. URL https://www.go-araldite.com/products/epoxy-adhesives/araldite-rapid-24ml-syringe. Last visited: 27.11.2019.

[173] Hysol 9514 glue. URL https://www.loziska.com/store/9514-en.pdf. Last visited: 27.11.2019.

[174] Loctite double-bubble glue. URL https://www.henkel-adhesives.com/ee/en/product/structural-adhesives/loctite_double_bubble.html. Last visited: 27.11.2019.

[175] Stycast 2851 glue. URL https://www.henkel-adhesives.com/de/en/product/encapsulants/loctite_stycast_2851ft.html. Last visited: 27.11.2019.

[176] Lin, J.-F., Shu, J., kwang Mao, H., Hemley, R. J. & Shen, G. Amorphous boron gasket in diamond anvil cell research. *Review of Scientific Instruments* **74**, 4732–4736 (2003).

[177] Merkel, S. & Yagi, T. X-ray transparent gasket for diamond anvil cell high pressure experiments. *Review of Scientific Instruments* **76**, 046109 (2005).

[178] Materials property data - matweb. URL http://www.matweb.com/. Last visited: 30.05.2019.

[179] Specac press. URL https://www.specac.com/en/products/sample-prep/hydraulic-press/manual/manual. Last visited: 27.12.2019.

[180] AEP load cell. URL www.aeptransducers.com/load-cells/73-cbs.html. Last visited: 27.12.2019.

[181] Torikachvili, M. S., Kim, S. K., Colombier, E., Bud'ko, S. L. & Canfield, P. C. Solidification and loss of hydrostaticity in liquid media used for pressure measurements. *Review of Scientific Instruments* **86**, 123904 (2015).

[182] Klotz, S., Chervin, J.-C., Munsch, P. & Marchand, G. L. Hydrostatic limits of 11 pressure transmitting media. *Journal of Physics D: Applied Physics* **42**, 075413 (2009).

[183] Kenichi, T. & Singh, A. K. High-pressure equation of state for Nb with a helium-pressure medium: Powder x-ray diffraction experiments. *Physical Review B* **73**, 224119 (2006).

[184] Feng, Y., Jaramillo, R., Wang, J., Ren, Y. & Rosenbaum, T. F. Invited article: High-pressure techniques for condensed matter physics at low temperature. *Review of Scientific Instruments* **81**, 041301 (2010).

[185] Wang, Y., Rosenbaum, T. F. & Feng, Y. X-ray magnetic diffraction under high pressure. *IUCrJ* **6**, 507–520 (2019).

[186] Wang, Y., Feng, Y., Cheng, J.-G., Wu, W., Luo, J. L. & Rosenbaum, T. F. Spiral magnetic order and pressure-induced superconductivity in transition metal compounds. *Nature Communications* **7**, 13037 (2016).

[187] Jaramillo, R., Feng, Y., Wang, J. & Rosenbaum, T. F. Signatures of quantum criticality in pure Cr at high pressure. *Proceedings of the National Academy of Sciences* **107**, 13631–13635 (2010).

[188] Syassen, K. Ruby under pressure. *High Pressure Research* **28**, 75–126 (2008).

[189] McCumber, D. E. & Sturge, M. D. Linewidth and temperature shift of the R lines in ruby. *Journal of Applied Physics* **34**, 1682–1684 (1963).

[190] Ragan, D. D., Gustavsen, R. & Schiferl, D. Calibration of the ruby R1 and R2 fluorescence shifts as a function of temperature from 0 to 600 K. *Journal of Applied Physics* **72**, 5539–5544 (1992).

[191] Datchi, F., Dewaele, A., Loubeyre, P., Letoullec, R., Godec, Y. L. & Canny, B. Optical pressure sensors for high-pressure–high-temperature studies in a diamond anvil cell. *High Pressure Research* **27**, 447–463 (2007).

[192] Weinstein, B. A. Ruby thermometer for cryobaric diamond-anvil cell. *Review of Scientific Instruments* **57**, 910–913 (1986).

[193] Vos, W. L. & Schouten, J. A. On the temperature correction to the ruby pressure scale. *Journal of Applied Physics* **69**, 6744–6746 (1991).

[194] Li-Wen, X., Rong-Zheng, C. & Chang-Qing, J. Measurement of R line fluorescence in ruby using the diamond anvil cell at low temperature. *Chinese Physics Letters* **17**, 555–557 (2000).

[195] Yamaoka, H., Zekko, Y., Jarrige, I., Lin, J.-F., Hiraoka, N., Ishii, H., Tsuei, K.-D. & Mizuki, J. Ruby pressure scale in a low-temperature diamond anvil cell. *Journal of Applied Physics* **112**, 124503 (2012).

[196] Adams, D. M., Appleby, R. & Sharma, S. K. Spectroscopy at very high pressures. X. use of ruby R-lines in the estimation of pressure at ambient and at low temperatures. *Journal of Physics E: Scientific Instruments* **9**, 1140–1144 (1976).

[197] Nakano, K., Akahama, Y., Ohishi, Y. & Kawamura, H. Ruby scale at low temperatures calibrated by the NaCl gauge: Wavelength shift of ruby R1 fluorescence line at high pressure and low temperature. *Japanese Journal of Applied Physics* **39**, 1249–1251 (2000).

[198] Hess, N. J. & Exarhos, G. J. Temperature and pressure dependence of laser induced fluorescence in Sm:YAG—a new pressure calibrant. *High Pressure Research* **2**, 57–64 (1989).

[199] Holzapfel, W. B., Hartwig, M. & Sievers, W. Equations of state for cu, ag, and au for wide ranges in temperature and pressure up to 500 GPa and above. *Journal of Physical and Chemical Reference Data* **30**, 515–529 (2001).

[200] Dewaele, A., Loubeyre, P. & Mezouar, M. Equations of state of six metals above 94 GPa. *Physical Review B* **70**, 094112 (2004).

[201] Fei, Y., Ricolleau, A., Frank, M., Mibe, K., Shen, G. & Prakapenka, V. Toward an internally consistent pressure scale. *Proceedings of the National Academy of Sciences* **104**, 9182–9186 (2007).

[202] Bridgman, P. W. The measurement of hydrostatic pressures up to 20,000 kilograms per square centimeter. *Proceedings of the American Academy of Arts and Sciences* **47**, 321–343 (1911).

[203] Wang, C. Electrical resistance of manganin coil to 7 kbar and 200 degrees. *Review of Scientific Instruments* **38**, 24–26 (1967).

[204] Oxford Instruments Cryojet - Cryostream-800. URL https://www.oxcryo.com/product/cryostream-800. Last visited: 18.10.2019.

[205] Solid edge CAD software. URL https://solidedge.siemens.com/en/. Last visited: 27.12.2019.

[206] Gibbs, D., Harshman, D. R., Isaacs, E. D., McWhan, D. B., Mills, D. & Vettier, C. Polarization and resonance properties of magnetic x-ray scattering in holmium. *Physical Review Letters* **61**, 1241–1244 (1988).

[207] Klotz, S. *Techniques in High Pressure Neutron Scattering* (Taylor & Francis Ltd., 2012). URL https://www.ebook.de/de/product/21177355/stefan_klotz_techniques_in_high_pressure_neutron_scattering.html.

[208] Haberl, B., Dissanayake, S., Wu, Y., Myles, D. A. A., dos Santos, A. M., Loguillo, M., Rucker, G. M., Armitage, D. P., Cochran, M., Andrews, K. M., Hoffmann, C., Cao, H., Matsuda, M., Meilleur, F., Ye, F., Molaison, J. J. & Boehler, R. Next-generation diamond cell and applications to single-crystal neutron diffraction. *Review of Scientific Instruments* **89**, 092902 (2018).

[209] Shermadini, Z., Khasanov, R., Elender, M., Simutis, G., Guguchia, Z., Kamenev, K. & Amato, A. A low-background piston–cylinder-type hybrid high pressure cell for muon-spin rotation/relaxation experiments. *High Pressure Research* **37**, 449–464 (2017).

[210] Walker, I. R. Nonmagnetic piston–cylinder pressure cell for use at 35 kbar and above. *Review of Scientific Instruments* **70**, 3402–3412 (1999).

[211] Uwatoko, Y., Todo, S., Ueda, K., Uchida, A., Kosaka, M., Mori, N. & Matsumoto, T. Material properties of Ni Cr Al alloy and design of a 4 GPa class non-magnetic high-pressure cell. *Journal of Physics: Condensed Matter* **14**, 11291–11296 (2002).

[212] Simmons, J., Azizi, A., Daeumer, M. & Schiffres, S. Schiffreslocal thermal conductivity mapping of selective laser melted 316l stainless steel. In *Annual International Solid Freeform Fabrication Symposium - An Additive Manufacturing Conference* (2018).

[213] Materials property data - Azom. URL https://www.azom.com/properties/. Last visited: 30.09.2019.

[214] Lu, J., Toplosky, V. J., Goddard, R. E. & Han, K. Low temperature physical properties of Co35Ni20Cr10Mo alloy MP35N. *Cryogenics* **86**, 106–111 (2017).

[215] Walker, I. Considerations on the selection of alloys for use in pressure cells at low temperatures. *Cryogenics* **45**, 87–108 (2005).

[216] NGK-Beryllium Cooper Alloys. URL http://www.ngk-alloys.com/NGK_Berylco_Catalogue_En.pdf. Last visited: 01.10.19.

[217] Carobronze - Beryllium Cooper Alloys. URL http://www.frwcarobronze.fr/Beryllium_en. Last visited: 01.10.19.

[218] Sinogeikin, S. V., Smith, J. S., Rod, E., Lin, C., Kenney-Benson, C. & Shen, G. Online remote control systems for static and dynamic compression and decompression using diamond anvil cells. *Review of Scientific Instruments* **86**, 072209 (2015).

[219] Aoki, K., Kakudate, Y., Yoshida, M., Usuba, S., Tanaka, K. & Fujiwara, S. Wedge-driven and miniature diamond-anvil cells for high-pressure optical and x-ray diffraction studies. *Japanese Journal of Applied Physics* **26**, 2107–2110 (1987).

[220] Nowell, H., Barnett, S. A., Christensen, K. E., Teat, S. J. & Allan, D. R. I19, the small-molecule single-crystal diffraction beamline at diamond light source. *Journal of Synchrotron Radiation* **19**, 435–441 (2012).

[221] Aligent. CrysAlis PRO (Aligent Technologies Ltd., Yarton, Oxfordshire, England. (2014). URL https://www.rigaku.com/products/smc/crysalis. Last visited: 02.11.2019.

[222] Petříček, V., Dušek, M. & Palatinus, L. Crystallographic computing system JANA2006: General features. *Zeitschrift fr Kristallographie - Crystalline Materials* **229** (2014). URL http://jana.fzu.cz/.

[223] Hunter, E. C. *Exploration of novel correlated electronic states in 5d transition metal oxides*. Ph.D. thesis, The University of Edinburgh (2016).

[224] Toby, B. H. R factors in Rietveld analysis: How good is good enough? *Powder Diffraction* **21**, 67–70 (2006).

[225] Souri, M., Terzic, J., Johnson, J. M., Connell, J. G., Gruenewald, J. H., Thompson, J., Brill, J. W., Hwang, J., Cao, G. & Seo, A. Electronic and optical properties of la-doped $Sr_3Ir_2O_7$ epitaxial thin films. *Physical Review Materials* **2**, 024803 (2018).

[226] Hao, L., Meyers, D., Dean, M. & Liu, J. Novel spin-orbit coupling driven emergent states in iridate-based heterostructures. *Journal of Physics and Chemistry of Solids* **128**, 39–53 (2019).

[227] Kim, B. H., Khaliullin, G. & Min, B. I. Magnetic couplings, optical spectra, and spin-orbit exciton in 5d electron Mott insulator Sr_2IrO_4. *Physical Review Letters* **109**, 167205 (2012).

[228] Zhao, J. G., Yang, L. X., Yu, Y., Li, F. Y., Yu, R. C., Fang, Z., Chen, L. C. & Jin, C. Q. High-pressure synthesis of orthorhombic $SrIrO_3$ perovskite and its positive magnetoresistance. *Journal of Applied Physics* **103**, 103706 (2008).

[229] Okada, Y., Walkup, D., Lin, H., Dhital, C., Chang, T.-R., Khadka, S., Zhou, W., Jeng, H.-T., Paranjape, M., Bansil, A., Wang, Z., Wilson, S. D. & Madhavan, V. Imaging the evolution of metallic states in a correlated iridate. *Nature Materials* **12**, 707–713 (2013).

[230] Park, H. J., Sohn, C. H., Jeong, D. W., Cao, G., Kim, K. W., Moon, S. J., Jin, H., Cho, D.-Y. & Noh, T. W. Phonon-assisted optical excitation in the narrow bandgap Mott insulator $Sr_3Ir_2O_7$. *Physical Review B* **89**, 155115 (2014).

[231] Zhang, H., Haule, K. & Vanderbilt, D. Effective J = 1/2 insulating state in Ruddlesden-Popper iridates: An LDA + DMFT study. *Physical Review Letters* **111**, 246402 (2013).

[232] Ding, Y., Yang, L., Chen, C.-C., Kim, H.-S., Han, M. J., Luo, W., Feng, Z., Upton, M., Casa, D., Kim, J., Gog, T., Zeng, Z., Cao, G., kwang Mao, H. & van Veenendaal, M. Pressure-induced confined metal from the mott insulator $Sr_3Ir_2O_7$. *Physical Review Letters* **116**, 216402 (2016).

[233] Wojek, B. M., Berntsen, M. H., Boseggia, S., Boothroyd, A. T., Prabhakaran, D., McMorrow, D. F., Rønnow, H. M., Chang, J. & Tjernberg, O. The insulator $Sr_3Ir_2O_7$ studied by means of angle-resolved photoemission spectroscopy. *Journal of Physics: Condensed Matter* **24**, 415602 (2012).

[234] King, P. D. C., Takayama, T., Tamai, A., Rozbicki, E., Walker, S. M., Shi, M., Patthey, L., Moore, R. G., Lu, D., Shen, K. M., Takagi, H. & Baumberger, F. Spectroscopic indications of polaronic behavior of the

strong spin-orbit insulator $Sr_3Ir_2O_7$. *Physical Review B* **87**, 241106(R) (2013).

[235] Porras, J., Bertinshaw, J., Liu, H., Khaliullin, G., Sung, N. H., Kim, J.-W., Francoual, S., Steffens, P., Deng, G., Sala, M. M., Efimenko, A., Said, A., Casa, D., Huang, X., Gog, T., Kim, J., Keimer, B. & Kim, B. J. Pseudospin-lattice coupling in the spin-orbit mott insulator Sr_2IrO_4. *Physical Review B* **99**, 085125 (2019).

[236] Kim, J., Casa, D., Upton, M. H., Gog, T., Kim, Y.-J., Mitchell, J. F., van Veenendaal, M., Daghofer, M., van den Brink, J., Khaliullin, G. & Kim, B. J. Magnetic excitation spectra of Sr_2IrO_4 probed by resonant inelastic x-ray scattering: Establishing links to cuprate superconductors. *Physical Review Letters* **108**, 177003 (2012).

[237] Li, L., Kong, P. P., Qi, T. F., Jin, C. Q., Yuan, S. J., DeLong, L. E., Schlottmann, P. & Cao, G. Tuning the $J_{eff} = 1/2$ insulating state via electron doping and pressure in the double-layered iridate $Sr_3Ir_2O_7$. *Physical Review B* **87**, 235127 (2013).

[238] Swift, M. W., Porter, Z., Wilson, S. D. & de Walle, C. G. V. Electron doping in $Sr_3Ir_2O_7$: Collapse of band gap and magnetic order. *Physical Review B* **98**, 081106(R) (2018).

[239] Vale, J. G. & Hunter, E. C. Putative magnetic quantum criticality in $(Sr_{1-x}La_x)_3Ir_2O_7$. *Physical Review B* **98**, 100406(R) (2018).

[240] Zocco, D. A., Hamlin, J. J., White, B. D., Kim, B. J., Jeffries, J. R., Weir, S. T., Vohra, Y. K., Allen, J. W. & Maple, M. B. Persistent non-metallic behavior in Sr_2IrO_4 and $Sr_3Ir_2O_7$ at high pressures. *Journal of Physics: Condensed Matter* **26**, 255603 (2014).

[241] Zhang, J., Yan, D., Yesudhas, S., Deng, H., Xiao, H., Chen, B., Sereika, R., Yin, X., Yi, C., Shi, Y., Liu, Z., Prschke, E. M., Chen, C.-C., Chang, J., Ding, Y. & kwang Mao, H. Lattice frustration in spin-orbit mott insulator $Sr_3Ir_2O_7$ at high pressure. *npj Quantum Materials* **4**, 23 (2019).

[242] Boseggia, S., Springell, R., Walker, H. C., Boothroyd, A. T., Prabhakaran, D., Collins, S. P. & McMorrow, D. F. On the magnetic structure of $Sr_3Ir_2O_7$: an x-ray resonant scattering study. *Journal of Physics: Condensed Matter* **24**, 312202 (2012).

[243] Boseggia, S., Springell, R., Walker, H. C., Boothroyd, A. T., Prabhakaran, D., Wermeille, D., Bouchenoire, L., Collins, S. P. & McMorrow, D. F. Antiferromagnetic order and domains in $Sr_3Ir_2O_7$ probed by x-ray resonant scattering. *Physical Review B* **85**, 184432 (2012).

[244] Dhital, C., Khadka, S., Yamani, Z., de la Cruz, C., Hogan, T. C., Disseler, S. M., Pokharel, M., Lukas, K. C., Tian, W., Opeil, C. P., Wang, Z. &

Wilson, S. D. Spin ordering and electronic texture in the bilayer iridate $Sr_3Ir_2O_7$. *Physical Review B* **86**, 100401(R) (2012).

[245] Hogan, T., Bjaalie, L., Zhao, L., Belvin, C., Wang, X., de Walle, C. G. V., Hsieh, D. & Wilson, S. D. Structural investigation of the bilayer iridate $Sr_3Ir_2O_7$. *Physical Review B* **93**, 134110 (2016).

[246] Subramanian, M., Crawford, M. & Harlow, R. Single crystal structure determination of double layered strontium iridium oxide $Sr_3Ir_2O_7$. *Materials Research Bulletin* **29**, 645–650 (1994).

[247] Matsuhata, H., Nagai, I., Yoshida, Y., Hara, S., ichi Ikeda, S. & Shirakawa, N. Crystal structure of $Sr_3Ir_2O_7$ investigated by transmission electron microscopy. *Journal of Solid State Chemistry* **177**, 3776–3783 (2004).

[248] Donnerer, C., Feng, Z., Vale, J. G., Andreev, S. N., Solovyev, I. V., Hunter, E. C., Hanfland, M., Perry, R. S., Rønnow, H. M., McMahon, M. I., Mazurenko, V. V. & McMorrow, D. F. Pressure dependence of the structure and electronic properties of $Sr_3Ir_2O_7$. *Physical Review B* **93**, 174118 (2016).

[249] Zhao, Z., Wang, S., Qi, T. F., Zeng, Q., Hirai, S., Kong, P. P., Li, L., Park, C., Yuan, S. J., Jin, C. Q., Cao, G. & Mao, W. L. Pressure induced second-order structural transition in $Sr_3Ir_2O_7$. *Journal of Physics: Condensed Matter* **26**, 215402 (2014).

[250] Donnerer, C., Sala, M. M., Pascarelli, S., Rosa, A. D., Andreev, S. N., Mazurenko, V. V., Irifune, T., Hunter, E. C., Perry, R. S. & McMorrow, D. F. High-pressure insulator-to-metal transition in $Sr_3Ir_2O_7$ studied by x-ray absorption spectroscopy. *Physical Review B* **97**, 035106 (2018).

[251] Kim, J., Said, A. H., Casa, D., Upton, M. H., Gog, T., Daghofer, M., Jackeli, G., van den Brink, J., Khaliullin, G. & Kim, B. J. Large spin-wave energy gap in the bilayer irdate $Sr_3Ir_2O_7$: Evidence for enhanced dipolar interactions near the Mott metal-insulator transition. *Physical Review Letters* **109**, 157402 (2012).

[252] Sala, M. M., Schnells, V., Boseggia, S., Simonelli, L., Al-Zein, A., Vale, J. G., Paolasini, L., Hunter, E. C., Perry, R. S., Prabhakaran, D., Boothroyd, A. T., Krisch, M., Monaco, G., Rønnow, H. M., McMorrow, D. F. & Mila, F. Evidence of quantum dimer excitations in $Sr_3Ir_2O_7$. *Physical Review B* **92**, 024405 (2015).

[253] Rossi, M., Henriquet, C., Jacobs, J., Donnerer, C., Boseggia, S., Al-Zein, A., Fumagalli, R., Yao, Y., Vale, J. G., Hunter, E. C., Perry, R. S., Kantor, I., Garbarino, G., Crichton, W., Monaco, G., McMorrow, D. F., Krisch, M. & Sala, M. M. Resonant inelastic x-ray scattering of magnetic excitations under pressure. *Journal of Synchrotron Radiation* **26**, 1725–1732 (2019).

[254] Ray, S., Vojta, M. & Janssen, L. Quantum critical behavior of two-dimensional fermi systems with quadratic band touching. *Physical Review B* **98**, 245128 (2018).

[255] Jackeli, G. & Khaliullin, G. Mott insulators in the strong spin-orbit coupling limit: From Heisenberg to a quantum compass and Kitaev models. *Physical Review Letters* **102**, 017205 (2009).

[256] Kim, J. W., Choi, Y., Kim, J., Mitchell, J. F., Jackeli, G., Daghofer, M., van den Brink, J., Khaliullin, G. & Kim, B. J. Dimensionality driven spin-flop transition in layered iridates. *Physical Review Letters* **109**, 037204 (2012).

[257] Pfleiderer, C., Reznik, D., Pintschovius, L., v. Lhneysen, H., Garst, M. & Rosch, A. Partial order in the non-fermi-liquid phase of MnSi. *Nature* **427**, 227–231 (2004).

[258] Goko, T., Arguello, C. J., Hamann, A., Wolf, T., Lee, M., Reznik, D., Maisuradze, A., Khasanov, R., Morenzoni, E. & Uemura, Y. J. Restoration of quantum critical behavior by disorder in pressure-tuned (Mn,Fe)Si. *npj Quantum Materials* **2**, 44 (2017).